A new technique for diagnosing pulmonary embolism based on respiratory exchange



Snapper Magor-Elliott

St Edmund Hall

University of Oxford

A thesis submitted for the degree of

Doctor of Philosophy

Michaelmas 2021

Acknowledgements

First and foremost I would like to acknowledge the outstanding supervision of Professor Peter Robbins throughout my studies. He dedicated an enormous amount of time to teaching and never lost patience or enthusiasm. He had worked for a over a decade on the device and modelling required for this thesis and without him this work would not have been possible.

Although he left the laboratory before my arrival, James Mountain's model of the lung was a fundamental basis of this work so I thank him for his previous work.

I would also like to thank Christopher Fullerton for his dedication and hard-work on updating the software required for my work as well as the very friendly atmosphere he created which created an excellent working environment.

On the hardware front, a great many thanks are owed to Professor Grant Ritchie and Graham Richmond for the expertise and determined efforts on the device used for my measurements as well as their personal advice and help on many matters. Many others in their group also deserve my gratitude like John, Nick, Gus and others.

For the work on COVID-19, a great many thanks are owed to David Holdsworth, Rebecca, Kayleigh and all the anaesthetists involved in acquiring the arterial blood sample.

I am also very grateful to Tom Smith and all the Qinetiq staff, without whom the study on the lung under enhanced gravity would not have been possible.

Finally, I thank my family and friends for their support and care, in particular Eunice Chesebe and my mother, Thomasin Magor. Their home schooling and care of me as a child helped give me the inquisitive mind that led me to this juncture. I also thank Will Sargent, Anna Zerio, Rhue Magor and Tim Elliott

for always being happy to volunteer in various tests to help my work and Anna Zerio, George Powell, Tom Versluys and Jase Clarkson for their sage advice.

Please note Chapters 4 and 5 include material and text I previously published as first author [1]. All materials reproduced in this thesis were written and produced by me.

Abstract

This thesis was primarily concerned with whether it would be possible to develop a technique for diagnosing pulmonary embolism without employing ionising radiation. Unfortunately, the COVID-19 pandemic halted experimental work in this area, and so a second aim of this thesis became to determine whether any residual physiological abnormalities in cardiopulmonary function could be detected in patients who had recovered from acute COVID-19 infection. Chapter 1 provides a brief introduction to the hypotheses and goals of the research contained within the thesis. Chapter 2 outlines the key concepts explored by this thesis and reviews relevant literature relating to cardiopulmonary physiology, gas exchange, pulmonary embolism and COVID-19. Chapter 3 describes a pre-existing molecular flow sensing technology and model of the lungs that form the basis of the work in the following chapters. Chapter 4 covers development of a novel model of the circulation and body gas stores which gives estimates of blood gas states across the circulation (and allows recirculation when connected to a model of the lung). This model is validated in Chapter 5, with good reproduction of measured changes demonstrated using a number of experiments that perturb the storage of body gases. Chapter 6 presents a small study collecting gas exchange measurements from hospital patients with suspected pulmonary embolism. Significant differences are observed between pulmonary embolism positive and negative patients when circulatory model estimates of blood gas state are compared with measurements of blood gases from a venous cannula. Chapter 7 extracts data from a cohort of pulmonary embolism negative patients to further investigate the ability of the proposed method to correctly estimate blood gas states in health. In Chapter 8, data were collected from participants who had recovered from COVID-19 infection and

several pathological changes to model lung parameters are shown to scale with the severity of initial COVID-19 infection. Chapter 9 presents validation work using enhanced gravity to induce changes in the distribution of lung compliance but not deadspace. The pre-existing lung model successfully disentangled these two sources of expired gas profile smearing. Finally, Chapter 10 concludes this thesis with a summary of my findings, their implications and potential future avenues of research.

Contents

1 Introduction **1**

1.1 Research motivation 1

1.2 Primary research question 2

1.3 Thesis outline 5

2 Literature review **7**

2.1 Cardiopulmonary physiology 8

2.1.1 Circulation 9

2.1.1.1 Heart structure 9

2.1.1.2 Vessel structure 10

2.1.1.3 Capillary gas exchange 11

2.1.1.4 Circulatory mechanics 11

2.1.2 Ventilation 13

2.1.2.1 Lung structure 13

2.1.2.2 Gas exchange in the lung 14

2.1.2.3 Mechanics of ventilation 14

2.1.3 The effect of gravity on pulmonary ventilation and perfusion 16

2.2 Body and blood storage of respiratory gases 16

2.2.1 Gas physics and chemistry 16

2.2.2 Inert gases (nitrogen) 17

2.2.3 Carbon dioxide 18

2.2.4 Oxygen 20

2.2.5 Interrelated nature of carbon dioxide and oxygen storage 21

2.3 Existing mathematical models of the circulation and body gas stores 22

2.3.1 Carbon dioxide . . . 22
2.3.2 Oxygen . . . 23
2.3.3 Nitrogen . . . 23
2.3.4 Shortcomings of all previous models . . . 23
2.4 Pulmonary embolism . . . 24
2.4.1 Pulmonary embolism mechanism and aetiology . . . 24
2.4.2 Pulmonary embolism diagnosis . . . 24
2.4.2.1 Existing techniques . . . 24
2.4.2.2 Flaws of existing techniques and the dangers of ionising radiation . . . 25
2.4.2.3 Pulmonary embolism in pregnant women . . . 26
2.4.3 Attempts at using blood and respiratory measurements to diagnose pulmonary embolism . . . 28
2.4.3.1 Using blood samples alone to diagnose pulmonary embolism 29
2.4.3.2 Using estimates of alveolar gas alone to diagnose pulmonary embolism . . . 30
2.4.3.3 Comparing blood and respiratory measurements to diagnose pulmonary embolism . . . 30
2.4.3.4 Limitations of these techniques . . . 31
2.5 Coronavirus disease 2019 . . . 32
2.5.1 COVID-19 emergence, transmission and significance . . . 32
2.5.2 COVID-19 symptoms . . . 33
2.5.3 COVID-19 diagnosis . . . 34
2.5.4 COVID-19 pathology . . . 34
2.5.5 COVID-19 risk factors . . . 35
2.5.6 COVID-19 treatment . . . 36
2.5.7 Long term effects of COVID-19 . . . 36
2.6 Summary . . . 37

3 Pre-existing technology **39**

3.1 Introduction . . . 39
3.2 Measurement of respiratory exchange . . . 40

3.2.1 History and current commercial devices . . . 40
3.2.2 The molecular flow sensing device . . . 42
3.3 Inhomogeneity in the lung . . . 45
3.3.1 Previous attempts to measure lung inhomogeneity . . . 45
3.3.2 Log-normal lung model . . . 46
3.3.3 Parameter estimation from molecular flow sensor experimental data using the log-normal lung . . . 47
3.4 Experimental measurement protocol . . . 49
3.4.1 Success in detecting increases in lung inhomogeneity parameters associated with respiratory disease . . . 50
3.5 Limitations of log-normal lung . . . 51
3.5.1 Importance of considering blood gas stores and recirculation . . . 52
3.5.2 Modelling of the circulatory system within the log-normal lung . . . 52
3.5.2.1 Recirculation modelling during the washout . . . 53
3.5.2.2 Estimating the pulmonary arterial gas content input during air breathing . . . 54
3.6 Shortcomings related to the circulatory system and thesis objectives . . . 55
3.7 Summary . . . 56

4 Circulatory and body gas stores modelling 57
4.1 Introduction . . . 57
4.2 CBGS model construction and execution . . . 58
4.2.1 CBGS model general description . . . 58
4.2.2 Construction of model for standard man . . . 59
4.2.3 Scaling the CBGS model to individuals . . . 64
4.2.4 Solubilities and partition coefficients . . . 64
4.2.5 Gas exchange between circulation and body tissues . . . 67
4.2.5.1 Equilibration between tissue and blood for inert gases . . . 68
4.2.5.2 Equilibration between tissue and blood using the blood model . . . 69
4.2.6 Setting initial conditions . . . 70
4.2.7 CBGS execution . . . 72

4.2.7.1 Modelling blood flow using plug flow . . . 73
4.2.8 CBGS implementation . . . 76
4.3 CBGS discussion . . . 76
4.4 Combining the CBGS with the LNL . . . 80
4.5 CBGS summary . . . 80

5 Circulatory and body gas stores model validation 81
5.1 Introduction . . . 81
5.2 Methods . . . 82
5.2.1 Simulation of previously reported studies . . . 82
5.2.1.1 Nitrogen literature measurements . . . 82
5.2.1.2 Carbon dioxide literature measurements . . . 82
5.2.1.3 Oxygen literature measurements . . . 83
5.2.2 Experimental validation . . . 83
5.2.2.1 Data collection . . . 83
5.2.2.2 Nitrogen perturbations . . . 84
5.2.2.3 Carbon dioxide perturbations . . . 84
5.2.2.4 Oxygen perturbations . . . 85
5.2.2.5 Data analysis . . . 85
5.3 Results . . . 87
5.3.1 General model properties . . . 87
5.3.2 Nitrogen validation . . . 90
5.3.3 Carbon dioxide validation . . . 92
5.3.4 Oxygen validation . . . 98
5.3.5 Experimental validation results summary . . . 100
5.4 Discussion . . . 101

6 Detection of pulmonary malperfusion 104
6.1 Introduction . . . 104
6.2 Methods . . . 106
6.2.1 Blood sampling site selection . . . 106
6.2.2 R-line construction and blood sample comparison . . . 107

6.2.3 Blood sampling testing . . . 110
6.2.4 Pulmonary embolism diagnosis experimental method . . . 111
6.3 Results . . . 113
6.3.1 Log-normal lung parameters recovered . . . 114
6.3.2 Pulmonary embolism diagnosis using the blood R-line error . . . 116
6.4 Discussion . . . 118

7 Validation of model prediction of blood R lines in health 121
7.1 Introduction . . . 121
7.2 Methods . . . 122
7.3 Results . . . 122
7.4 Discussion . . . 124

8 Effect of COVID-19 on the cardiopulmonary system 128
8.1 Introduction . . . 128
8.2 Methods . . . 129
8.2.1 Data collection . . . 129
8.2.2 Modelling . . . 131
8.2.3 Statistical analysis . . . 131
8.3 Results . . . 134
8.3.1 σ_{Cl} results . . . 137
8.3.2 σ_{Cd} results . . . 138
8.3.3 σ_{DS} results . . . 139
8.3.4 ϵ_B results . . . 140
8.3.5 f_{DS}^{pred} results . . . 141
8.3.6 f_{FRC}^{pred} results . . . 142
8.3.7 Pa_{CO2} results . . . 143
8.3.8 Aa_{grad} results . . . 144
8.4 Discussion . . . 145

9 The lung under enhanced gravity 150
9.1 Introduction . . . 150
9.2 Methods . . . 151

9.2.1 Experimental methods . . . 151
9.2.2 Statistical methods . . . 153
9.3 Results . . . 153
9.4 Discussion . . . 156

10 Conclusions **158**
10.1 Summary of findings . . . 158
10.2 Future work . . . 160
10.2.1 Further work on pulmonary embolism . . . 160
10.2.2 Further work on COVID-19 . . . 161
10.2.3 Other potential applications of the CBGS model . . . 161
10.3 Concluding remarks . . . 163

A Arterial tree values **164**

Bibliography **167**

Chapter 1

Introduction

1.1 Research motivation

Lung alveoli, together with the blood vessels supplying them, perform the crucial function of gas exchange between the blood and atmosphere. Pulmonary embolism (PE) occurs when an obstruction lodges in an artery supplying the lung and cuts off blood flow to the accompanying alveoli. Hence, depending upon the blockage location and the extent of the alveoli it affects, PE can result in significant gas exchange interference. The obstruction typically originates from a venous thromboembolism, a blood clot, elsewhere in the circulation dislodging and passing through the heart to block a pulmonary (lung) artery. Other causes of obstruction are possible, such as the rarer amniotic fluid embolism which can occur in pregnancy if amniotic fluid enters the maternal blood stream. PE is one of the most common human cardiovascular diseases, in the EU accounting for around 5 deaths per 1000 for men and around 10 deaths per 1000 for women between the ages of 15-55 [2] and 12.5 % of sudden deaths between ages 5-35 [3].

Efficient diagnosis of PE is important both for the prompt provision of treatment and to avoid detrimental over-treatment. The classic signs and symptoms are also the most frequently presenting complaint in ambulatory admissions: breathlessness with or without chest pain. Diagnosis of PE is problematic because only a small subset of these patients are PE-positive because these symptoms are shared by many other conditions. The underlying pathology for some of the underlying conditions can be diagnosed rapidly, for example pneumonia, heart attack and pneumothorax. However, hospitals are left

with a large collection of patients with similar symptoms for whom PE remains just one of several possible diagnoses.

To manage these issues, National Institute for Health and Care Excellence (NICE) guidance recommends partitioning this group into high index and low index suspicion groups for PE [4]. For high likelihood patients, prompt referral for computed tomography pulmonary angiogram (CTPA) or ventilation/perfusion (V/Q) scintigraphy scans is recommended. Unfortunately, both these main PE investigations involve radiation exposure, skilled radiologists and waiting times. Consequently, for the low likelihood group, a gateway screening test is recommended: D-dimer (which only requires a simple venous blood sample). However, this test is unsatisfactory due to its low specificity where chronic inflammation and many other conditions can result in a positive test [5]. Furthermore, it cannot be used in pregnancy, during which time PEs are also more frequent. Consequently, a large number of PE negative patients are sent for CTPA or V/Q scans and exposed unnecessarily to ionising radiation. PE screening technology that is superior to the D-dimer test but which does not involve radiation exposure (and can be administered by unspecialised clinical staff) would be of significant clinical utility.

1.2 Primary research question

Gas exchange in the alveoli modulates the partial pressures of expired (breathed out the mouth) gases such that they are different from those in the surrounding air that is inspired (breathed in). Continued gas exchange is dependent upon the presence of perfusion, the flow of fresh blood past the alveoli due to the pumping of the heart, and ventilation, the flow of fresh air in and then out the lungs as a result of breathing. PE results in alveolar regions of the lung that are ventilated with air but not perfused with blood. In these regions gas exchange is compromised and the gas will more closely resemble inspired air, therefore affecting the expired gas partial pressures to some degree.

The overarching hypothesis of this thesis is that detailed measurement of the profiles (shape of the partial pressures over time) by which respiratory and/or tracer gases emerge from the lung contain information on the health and functioning of the blood vessels in the lungs. In particular that expired gas profiles can be used to estimate alveolar volumes of

the lung that are ventilated but not perfused (as found in PE). If successful, this technique could be used to diagnose PE without the need to irradiate the patient.

There have been a number of previous attempts to diagnose PE by detecting alveolar regions of the lung that are ventilated but unperfused [6, 7]. In short, these techniques were predicated on comparing measurements of arterial blood gas samples (Pa_{gas}) to the end tidal respiratory gases at the mouth (PET_{gas}). The end tidal gas, the last gas that leaves the mouth during an expiration, is assumed to have originated in the alveoli, and thus be representative of alveolar gas. These techniques then assume the presence of a PE when Pa_{gas} is different to PET_{gas} because a blockage means there are regions of lung where alveolar gases do not equilibrate with blood, and thus have a lower CO_2 and higher O_2 partial pressure (closer to that of air).

Some of these techniques have been encouraging but all have ultimately proved inadequate [6]. The two main problems have been: i) the need for an arterial catheter to be inserted into the patient, and most importantly ii) an assumption that end tidal CO_2 partial pressure is a reliable measure of the arterial CO_2 partial pressure in the absence of PE (i.e. $E(PET_{gas}) = E(Pa_{gas})$, where E denotes the expected value). The reasons these are problems are i) inserting an arterial catheter requires specialist medical intervention and is not a procedure that can be done by the admitting physician or nurse and ii) even in good health the assumption around the equality of end tidal and arterial blood gases is not valid for a variety of physiological reasons (most crucially that end-tidal gas is not a good estimate of alveolar gas; see Chapter 2).

The aim of this thesis is to use a respiratory approach that removes any assumption of end tidal and arterial gases being equal and instead calculates, in the absence of a PE, what the blood gas partial pressures should be from more detailed measurements and analyses of the respired gas. The proposed technique also removes the need to measure arterial blood directly, as it can predict for blood which has varying degrees of venous admixture, so can use blood from a warmed hand vein. The central assumption of the method is that in the absence of PE the mixed venous point for partial pressures P_{CO_2} and P_{O_2} will fall on the line of potential gas content values as blood changes from arterial to venous. If PE is present the expectation is that the measured venous blood P_{CO_2}, P_{O_2} point will lie above the P_{CO_2}, P_{O_2} predicted R line as model blood transitions from

arterial to venous.

The gas profiles at the mouth must be measured very accurately as the information they provide on the pulmonary vasculature will necessarily be very subtle. As such, this work relies on a novel prototype device for measuring respired gas exchange with unparalleled accuracy [8]. Even accurate raw gas profiles do not give clear indication on the health of the vasculature and can vary significantly based on lung pathophysiology. Therefore, in order to reliably recover information on the health of the vasculature one must also reliably estimate the status of the lung and its ventilation. Using a highly accurate molecular flow sensing (MFS) device combined with a computational model of the lungs (LNL), clinically relevant information on the health of the airways has been recovered [9]. For useful information on the health of the pulmonary vasculature to be recovered more accurate predictions of the inflow of gas concentrations into the pulmonary artery are required. This could be achieved through modelling the circulation and body gas stores (CBGS) to account for recirculation and account for dynamic changes in tissue gas storage.

Thus, this work aims to test whether detailed measurements of venous blood and expired gas profiles could be used in conjunction with a novel computational model of the cardiopulmonary system as a whole (heart, circulation and lungs) to diagnose PE. The proposed approach is not intended to entirely replace clinical imaging techniques, which offer advantages such as determining the anatomical location and number of PE. The proposed approach cannot provide this information, which is required in rare cases where vascular surgery must be performed (to treat the PE). Instead, the proposed approach is intended for use in screening to rule out a significant proportion of PE negative patients, thus reducing the number of patients unnecessarily referred for clinical imaging. It could also remove the need for all PE positive screened patients to have ionising imaging if the approach can distinguish between PE severities (as most PE can be treated with anticoagulant drugs). As a non-invasive and non-ionising procedure, it would be safe for the patient and simple for the operator. The automation of the computational fitting would remove the need for specialists and provide diagnostic results in less than an hour.

1.3 Thesis outline

In this section I briefly outline the structure of this thesis.

Firstly, relevant literature is covered in Chapter 2. This includes a review of cardiopulmonary physiology, its pathology and diagnosis of disease in this system. Storage of gases in the body and prior models that have attempted to reproduce dynamic changes in human gas storage are described.

Next, Chapter 3 outlines the existing technology and modelling used as the foundation of this thesis: the prototype device used to measure gas exchange at the mouth and the prior computational modelling of the lung that used this highly accurate measurement as an input. The need for modelling of the circulation and body gas to achieve the aims of this thesis is explained.

Chapter 4 describes the modelling of the circulation and body gas stores I developed to complement the existing modelling of the lung and how they are combined.

In Chapter 5, validation of this model is discussed. The physiological ideal of inserting pulmonary artery catheters was not ethically permissible in healthy volunteers. Instead, validation was undertaken by: i) comparing model predictions with previously published data and ii) comparing model predictions with experimental data for transients in gas exchange at the mouth following changes in alveolar gas composition.

Having validated the model, in Chapter 6 I explore the experimental protocol to estimate pulmonary malperfusion, as seen in PE, using healthy volunteers. This involved a venous sampling protocol planned for use in a PE diagnosis clinical trial. Having refined a methodology, I investigate whether this model and device can be used to diagnose pulmonary embolism in a small clinical study.

As a result of the COVID-19 pandemic the research on PE was cut short. Chapter 7 describes results from a cohort of healthy military personnel (only including here those who were not admitted to hospital for COVID-19) who had arterial samples taken concomitantly to breath gas analysis. This provided an alternative route to further validate and investigate this method's feasibility as a diagnostic technique for PE.

As a result of the pandemic, one of the few areas in which respiratory experiments were acceptable ethically was in those who had recovered from COVID-19, both due to the high interest in this information and the low risk of reinfection for these participants.

Thus, Chapter 8 describes experimental work on a cohort of military personel who had recovered from COVID-19. These participants undertook a breathing protocol using the aforementioned device and modelling to probe whether this method could detect lingering pathological changes after recovery from acute infection (which may play a role in long COVID).

In Chapter 9, further validation of the lung and circulatory modelling is achieved through exposing volunteers to enhanced gravity and investigating the model's parameters under these conditions. Gravity is known to cause dramatic changes in certain physiological characteristics estimated by the model parameters whilst others should remain unchanged.

This thesis conclude with Chapter 10, where findings are summarised and potential future directions are discussed.

Chapter 2

Literature review

Chapter 1 outlined the aim of this thesis: to develop a technology for diagnosing pulmonary embolism based on respiratory exchange. This method will rely on combining a detailed physiological model of the lungs, circulation and body gas stores with careful measurements of respiratory gases at the mouth and venous blood samples. This Chapter will review the fundamental science and literature that forms the basis of this work.

First, cardiopulmonary physiology must be explored to inform the design of the model of the lungs, circulation and body gas stores described in Chapter 3 and 4. This includes the structure of the circulation, the mechanics of blood flow and capillary exchange. The structure of the lungs, the mechanics of air flow and the exchange of gases in the lungs are also briefly described.

Secondly, the significant stores of nitrogen, carbon dioxide and oxygen in the body tissues and the nature of this storage is described. In addition, blood gas chemistry and physiological mechanisms for gas homeostasis (maintenance of equilibrium of these stores) are outlined.

Following on from this, I explore existing models of the circulation and storage of body gases for nitrogen, carbon dioxide and oxygen in the literature and explain their shortcomings.

Next, pathological changes to the cardiopulmonary system with pulmonary embolism (PE) are described. The reasons for the additional PE burden in pregnancy are outlined. The shortcomings and risks inherent in existing diagnostic techniques are explained. Finally, this section describes how all these issues are compounded in pregnant women.

I finalise the discussion on PE by covering previous attempts to avoid ionising radiation through using respiratory and blood gas measurements to diagnose PEs. The reasons for the failure of these to gain widespread clinical adoption are explored and the potential solutions suggested. These include improved modelling of recirculation and body gas stores which is an important goal of this thesis.

During the course of this thesis the COVID-19 pandemic began. This resulted in the direction of the thesis needing to be changed as human experimental work on PE had to cease. However, experimental work on COVID-19 was possible. In this final section, the COVID-19 pandemic and its associated pathology is briefly described.

2.1 Cardiopulmonary physiology

Many living cells require a constant oxygen and nutrient supply to release energy via oxidative respiration [10]. This in turn produces carbon dioxide and other waste products. For unicellular organisms simple diffusion directly from the surroundings is sufficient. As complex and large multicellular organisms (metazoans) evolved, efficient respiratory exchange became compromised due to the reducing surface area to volume ratio. This is an issue when respiratory exchange relies purely on diffusion because the time t it would take a particle to travel a given distance x in one specific direction increases according to the Stokes-Einstein Law that can be simplified to: $t = kx^2$, where k is a constant [11, 12]. Thus, although fast over small distances diffusion would be insufficient to supply the deeper sections of the larger organism [10]. Furthermore, many multicellular organisms developed clusters of specialised cells with complex structures that allow them to react to environmental challenges more rapidly at the expense of faster metabolisms (e.g. muscle). These faster metabolisms demanded even greater gas exchange rates.

Without a solution this would leave these cells without a fresh supply of oxygen and a means to remove excess carbon dioxide. In order to overcome these limits of diffusion, many metazoans evolved circulatory systems that utilise convection/bulk flow for rapid shuttling of body fluid containing the desired gases and nutrients and specialised gas exchange organs such as the lungs that utilise convection of fresh air (or external fluid for aquatic animals) to maintain optimal exchange. In essence the cardiovascular system is

simply a collection of vessels and pumps that work both independently and in concert to ensure efficient supply and removal of substances around the entire organism. However, once delivered, diffusion remains the fundamental means of transport between tissue and circulating medium.

Depending on the metabolic demands and size of the organism the cardiopulmonary system varies [13]. In humans, the cardiopulmonary system consists of the heart, lungs, airways and blood vessels in a closed circulation, separated from the tissue and tissue fluid by vessel walls. This closed nature allows higher pressures, faster supply and greater control of distribution of blood supply. The functions of the human cardiopulmonary system are many: to exchange respiratory gases efficiently, clotting to close wounds, rapid transport of immune system components, global signalling, thermoregulation, and to provide nutrients and remove waste. For the purposes of this thesis I will focus on the gas exchange function of the cardiopulmonary system: to provide oxygen for metabolism and remove the waste product, carbon dioxide.

2.1.1 Circulation

2.1.1.1 Heart structure

The human heart is located in the chest cavity protected by the pericardial sac and the ribs. Humans possess a closed double circulation; two primary pumps and circulations connected in series. The right heart pumps blood into the pulmonary circulation, which in turn feeds into the left heart which then pumps blood through the systemic circulation back to the right heart to complete the closed circuit. In terms of gas exchange the cycle can be viewed as beginning with the the right heart providing blood via the pulmonary arteries to the lungs for gas exchange (oxygenation and removal of carbon dioxide). The pulmonary veins then supply this oxygenated blood to the left heart which then does work to re-pressurise the blood for transport around the body via the systemic circulation. After deoxygenation and addition of carbon dioxide in the tissues, blood then returns to the right heart via the systemic veins and the process is repeated.

To fulfil this purpose the heart consists of 4 muscular chambers (2 in both the left and right heart): right atrium, right ventricle, left atrium and left ventricle. The two atria assist in filling the ventricles more rapidly. The two ventricles contract to generate

strong pressures that pump the blood out of the heart through one way semi-lunar valves. At the cellular level, around 75% of the heart tissue volume consists of cardiomyocytes [14], specialised muscle cells electrically coupled via intercalated discs (syncytium) to facilitate rythmic contraction. The electrical coupling of the cells allows them to contract in unison. These cardiomyocytes surround a scaffolding of collagen which forms the junction between the atria and ventricles and prevents depolarisation passing between atria and ventricles in an uncontrolled manner. Healthy heart beats are synchronised by pacemaker cells located in the sino-atrial node and the atrio-ventricular node which depolarise and contract spontaneously and regularly at a higher natural rhythm than the rest of the heart. Finally, there are conducting cells that allow the electrical signal to propagate in a controlled manner from atria to ventricles and aid in distributing the excitation across the ventricles.

2.1.1.2 Vessel structure

The blood vessels can be divided into three main sections: arteries, capillaries and veins. All these vessels have an inner lining of endothelial cells. Arteries and veins also have a second layer of concentrically organised smooth muscle cells and a third layer of collagenous extracellular matrix to maintain the form and rigidity of the vessel. Arteries are relatively small calibre pipes with thick smooth muscle walls that carry blood out from the heart under high and varying pressures. The arteries can store energy, expanding and recoiling during each contraction and relaxation of the ventricles in order to smooth the pressure profile over the heartbeat and provide more continuous blood flow. Arteries branch into smaller and smaller vessels that feed into capillaries which have the smallest diameter, sometimes only a single red blood cell wide, and extremely thin walls to facilitate their role in exchanging gases and nutrients/waste with their attendant tissue. Finally, the veins carry blood away from the capillaries to the heart. Veins have the largest calibre cross sections, walls of intermediate thickness and one way valves to facilitate their role in returning low pressure blood to the heart. Together veins hold around 60% of the blood in the circulatory system[15] and those with smooth muscle contract and relax in response to pressure changes to enable continued function in the face of changes in overall circulatory volume and volume distribution (e.g. with postural changes) in a process called delayed

compliance. Further divisions include: arterioles (which are small arteries linking the arteries and capillaries) and venules (which are small veins bridging the large veins and capillaries).

2.1.1.3 Capillary gas exchange

The cardiovascular system supplies tissues of the body with blood containing the nutrients and gases needed to support life. Despite the red blood cells being contained within this closed circuit it can be considered open to exchange of smaller molecules such as gases, fluids, nutrients and waste products along most of the extent of its capillary network. This network infiltrates all tissues in the body such that almost all cells in vertebrate bodies are within 50-100 um of a capillary [16]. The blood flow here is also relatively slow. As a result, in most cases it is reasonable to assume that tissues are in equilibrium with the venous blood that carries blood out of their suppliant capillaries.

2.1.1.4 Circulatory mechanics

Heamodynamics, the dynamics of blood flow, are explained mechanistically by Darcy's Law: fluids flow down pressure gradients from regions of high pressure to areas of low pressure [17]. Specifically, Darcy's law states that blood flow $\dot{Q}$ is linearly proportional to the pressure difference between the two points and inversely proportional to the resistance R, i.e. $\dot{Q} = \frac{\Delta P}{R}$. Thus, in the cardiovascular system the flow across the capillaries will be greater when there is a greater pressure difference between the arterial and venous pressures of the suppliant vessels (the perfusion pressure).

As described previously, the pumping action of the heart over the cardiac cycle (the set cyclical sequence of muscular contractions over the four chambers of the heart) raises the pressure of the blood in the arteries. Venous pressure is usually very small and thus the pressure difference across the entire circulation can be estimated simply from the arterial pressure. Total body blood flow, often referred to as the cardiac output, is therefore proportional to the total arterial blood pressure divided by the total vascular resistance. The cardiac output can also be defined as the stroke volume (the blood volume emptied for each heart beat) multiplied by the heart rate (the number of heart beats in a given time period).

The resistance is primarily caused by the friction of the blood flowing next to the vessel walls. Blood passage can be approximated by laminar flow; parallel streams where the fastest blood is that in the centre (as it is furthest from the centre but also experiences friction as it moves past slower blood) and the slowest blood is adjacent to the vessel walls themselves. With laminar flow, resistance, R, is defined from Poiseuille's Law by: $R \propto \frac{L\eta}{r^4}$, where L is vessel length, η is viscosity of the fluid and r is vessel radius [18]. Thus a significant determinant of vessel resistance, and in turn rate of blood flow, is the vessel radius and to a lesser extent the vessel length. Therefore, the main site of resistance in the circulation is the small arteries and arterioles. This is because although the capillaries are very narrow (giving a smaller r), they are in parallel and their total cross-sectional area is enormous and they are very short (so have a low L value). This allows the arteries and arterioles to control the blood flow distribution across the body tissues through constricting and relaxing their smooth muscle. The viscosity of blood will remain constant unless the ratio of red blood cells to blood plasma, referred to as the haematocrit, changes. Blood flow is more chaotic near branches in the vessels (and with pathological changes in vessel lumen) where turbulent flow can dominate.

Total blood flow can be increased via autonomic innervation, circulating hormones and through increased venous return to the heart. The sympathetic cardiac accelerator nerves innervate the sino-atrial node and atrio-ventricular node to increase heart rate (positive chronotropic effect) whilst the parasympathetic vagus nerve innervates the sino-atrial node to decrease heart rate (negative chronotropic effect). Contrastingly, the increased venous return to the heart increases the stroke volume but not the heart rate. Increases in venous return are primarily caused by skeletal muscle contraction combined with venous one way valves acting as an effective pump during exercise. The increased return of blood to the heart via the veins stretches the cardiac muscle and enhances the strength of the contraction on the subsequent heart beat (and thus stroke volume) via the Frank-Starling Law [19].

The distribution of blood flow to different tissues and organs can be moderated significantly through a number of mechanisms. The arterioles and arteries that supply given tissues can have their radius increased (vasodilation) or decreased (vasoconstriction) through local, neuronal and hormonal control. An example of redistribution of blood flow

through vasomotion is during exercise. During exercise there is an integrated and co-ordinated cardiovascular response to increase total perfusion (cardiac output). However there is also a preferential increase in flow to muscle, and more specifically to the muscle that is being utilised. This is primarily caused by local metabolites signalling the muscle arterioles to vasodilate (metabolic hyperaemia). There is also capillary recruitment through neuronal based relaxation of precapillary schincters (which keep many capillary beds empty at rest).

2.1.2 Ventilation

2.1.2.1 Lung structure

The lungs are highly specialised organs which perform the crucial function of gas exchange with the surroundings [20]. The structure of the airways is well suited to this function and can be separated into three general zones: respiratory, transitional and conducting.

The respiratory zone has a large surface area with which blood can flow in close apposition to alveolar gas, allowing for rapid diffusion of gases across this surface. Theoretically, this results in the blood that leaves the lungs being essentially equilibrated with the outside world. In order to achieve this function the alveolar ducts of the respiratory zone consist of millions of tiny alveoli with thin (single cell layer) epithelial walls surrounded by capillaries. Capillaries are thin vessels with a single celled endothelial wall. Thus, only a thin, two cell layer, separates air and blood across an enormous internal surface area of around 29 - 69 m^2 [21]. Thus, a relatively small blood volume is distributed over this large surface area. These details of the anatomy are all adaptations to overcome the limitations of diffusion.

Fresh air must be provided to the alveoli in order for the diffusion gradient and gas exchange to be maintained. The conducting zone is made up of larger calibre airways (from the trachea to the terminal bronchioles) that deliver and remove breathed air through a series of branching tubes which become increasingly short, narrow and numerous as they approach the alveoli from the mouth and nose. Whereas diffusion plays a crucial role for gas molecule movement in the alveoli, the dominant mechanism of gas movement in the conducting zone is convection. Liquids are relatively dense and viscous. Therefore, liquid bulk convection systems, such as the human circulatory system and gills of aquatic

animals, have evolved to be unidirectional to avoid having to do work to reverse the direction of flow [13]. Air is both less viscous and less dense than blood. Therefore, it is not particularly energetically expensive to do work to accelerate air into and then back out of the lungs through breathing. Thus, the human cardiopulmonary system relies on unidirectional flow of blood past the alveoli and bidirectional flow of air in and out of the conducting zone of the lungs to maintain diffusion gradients. The conducting zone primarily serves to distribute air between the outside world and alveoli. However, it also has an important role in protecting the alveoli through removing pathogens and large particles, and warming and humidifying the inspired air. As there are no alveoli in this zone it does not contribute to gas exchange and constitutes the anatomic dead space of the lung. The conducting zones also have their own vascular supply called the bronchial circulation. Unlike the pulmonary circulation, this serves to supply the conducting tissues with their nutrient and oxygen requirements and not to exchange gas with the atmosphere.

The transitory zone is marked by the appearance of alveoli, and thus gas exchange, in the respiratory bronchioles. The transitory airways continue to channel air deeper into the lung until the alveolar ducts of the respiratory zone. As such, a portion of their volume can also be considered dead space regarding gas exchange.

2.1.2.2 Gas exchange in the lung

The alveoli of the respiratory zone are responsible for extracting oxygen from the lungs and depositing carbon dioxide into the air spaces. This process is achieved entirely by simple diffusion which is highly efficient due to the large (alveolar) surface area to (air and blood) volume ratio and the ventilation providing fresh gas to maintain the diffusion gradient.

2.1.2.3 Mechanics of ventilation

The mechanics of ventilation can also be approximated similarly to laminar flow in the circulation: pressure differences between sections of a closed pipe cause convection of air from one region to another. The lungs are enclosed within the airtight thoracic cavity, surrounded by the rib cage and the diaphragm muscle [22]. In between the lung and the cavity are two pleura separated by a thin layer of fluid. The two pleura have no anatomical

connections [23] but are held securely together by sub-atmospheric intrapleural pressure [24]. They do not directly contact each other due to repulsion by polar phospholipids on each membrane [25] which provide a well lubricated surface for movement to support breathing. The lung alveoli have an inward elastic recoil tendency such that they collapse without the balancing force from the pleura connected to the thoracic cavity. When a human relaxes the breathing apparatus, the outward recoil of the ribcage is equal and opposite to the inward recoil of the lungs. These opposing forces result in a negative intrapleural pressure at the end of expiration of around -5 cmH_2O [26].

During inspiration the intercostal muscles of the ribs and the diaphragm contract to expand the thoracic cavity against the increasing elastic recoil force of the alveoli. This decreases the intrapleural pressure to around -8 cmH_2O and increases the pressure difference across the lung wall (transpulmonary pressure), causing the alveoli to expand. This alveolar expansion reduces the pressure in the alveoli below the atmospheric pressure of zero. These notably small pressure differences cause air to flow from the mouth into the alveoli. To complete the breathing cycle at rest (eupnea) the diaphragm and intercostal muscles relax during expiration and the elastic inward recoil of the lung reduces the cavity volume until the force equals the natural outward elastic tendency of the ribcage and diaphragm. The lower cavity volume raises the alveolar pressure above atmospheric and causes air to flow out the lung. The remaining volume in the lungs at the end of relaxed expiration is referred to as functional residual capacity (FRC) and is the volume around which the lungs usually return close to during expiration [27]. During heavy exercise intercostal and abdominal muscles can contract to increase the speed of expiration by actively reducing thoracic volume.

Closer to the mouth, the airways are subjected to thoracic pressure changes and are reinforced with cartilage to prevent collapse or significant changes in volume. This helps ensure the majority of changes in lung volume occur in the alveoli (advantageous as they are the only site of gas exchange) and not the large airway deadspace. It is worth noting that deeper into the lungs there are conducting airways that have no cartilage reinforcement and do expand and relax during the breathing cycle. This means the anatomical dead space does vary slightly over a human breath.

2.1.3 The effect of gravity on pulmonary ventilation and perfusion

Human lungs consist of a small tissue mass occupying a large volume of compliant alveoli filled with air. The air can readily redistribute itself. As such, when exposed to gravity the weight of the lung causes it to deform. When standing on Earth the human lung experiences an increasing gradient of pleural pressure down the lung as the weight of the lung compresses the basal alveoli and stretches the apical alveoli [28]. As more negative pleural pressures cause greater opening of the alveoli, the base of the lung has smaller alveolar volumes and the apex of the lung has larger alveolar volumes. Alveoli have a non-linear relationship between pressure and volume and smaller alveoli at the base of the lung are on a more compliant section of the pressure-volume curve and thus expand more for the same decrease in pressure during inspiration. Thus, the bottom of the lungs are better ventilated than the apex. The perfusion of the lungs is also affected by gravity as the weight of the fluid means it more readily flows downwards towards the base of the lungs whilst greater pressures are required to pump blood to the apices of the lungs. As a result, the perfusion follows a similar trend to the ventilation but it is even greater in magnitude such that ventilation and perfusion are most unmatched at the vertical extremes of the lungs. The gravity dependent differences in alveolar volume and compliance, and different perfusion to alveoli are important sources of inhomogeneity in the lung. Along with anatomical mismatches, gravity dependent ventilation perfusion mismatch ($\dot{V}/\dot{Q}$ ratio) is another form of inhomogeneity in the lungs.

2.2 Body and blood storage of respiratory gases

2.2.1 Gas physics and chemistry

Gases are stored and circulated within the body in a variety of ways: i) in gaseous form in the airways, ii) in physical solution within the tissue, tissue fluids and blood, and in some cases iii) chemically combined with biological molecules [29]. Total gas stores in the body can be rapidly adjusted by changing the ventilation of the lungs whilst the circulatory system can modulate the overall storage as well as its distribution across the body.

Physiological conditions usually involve a mix of gases in the inspired atmosphere such that the total pressure exerted by a gaseous mixture can be broken down into partial pressures (P_x) for each gas, x. When these gases are in contact with a liquid (in the lungs the surface fluid of the alveoli) some gas dissolves up until the equilibrium point where the tendency of gas molecules to leave the fluid is equal to tendency for gas molecules to dissolve into it. The partial pressure in the liquid and the gas phase are defined as the same at this point. The actual concentration (the number of molecules per unit of liquid volume) of an inert gas in the liquid phase at this point is determined by a physical property of the gas and the liquid it is dissolving into: the solubility coefficient. Various physical properties influence this, for example, the polarity of the liquid and the gas in question. In addition, many gases reversibly bind and react with biological molecules which greatly influences the content of these gases in the liquid phase as it removes the tendency for these gases to exit into the gaseous phase and thus shifts the equilibrium such that greater amounts of gas are stored. An important concept for this thesis is the dissociation curve for each gas which accounts for all of these effects. The dissociation curve for a gas defines the relationship between the concentration of the gas in the blood/tissue and the partial pressure of the gas in gaseous mixture or solution to which it is exposed.

In terms of function, the body gas stores play an important role in regulating and buffering acidity, and providing vital gas stores to maintain homeostasis (keeping physically dissolved gas levels within narrow limits) in the face of temporary supply changes. For oxygen the stores can supply more oxygen to meet demand in the face of briefly reduced supply and for carbon dioxide the stores sequester the additional metabolically produced toxic waste product. In the following sections I detail the storage of inert gases, such as nitrogen, and the more complex storage and reactions of the metabolic gases: carbon dioxide and oxygen.

2.2.2 Inert gases (nitrogen)

Inert gases do not undergo chemical reactions under a given set of conditions. Due to the dynamic conditions in physiology this definition can be obtuse. Weathersby [30] uses the assumption that biologically inert gases obey Henry's law: dissolved gas content is

directly proportional to the partial pressure of the gas phase [31]. Thus, if the gas obeys Henry's Law the concentration is equal to the solubility coefficient multiplied by the partial pressure for the given gas.

Nitrogen is the most abundant atmospheric gas and fulfils this requirement. Nitrogen is metabolically inactive and has little active use biologically. Nevertheless, nitrogen dissolves from inhaled gas into the liquid phase of the lungs and is carried around the body in solution by the cardiovascular system where it equilibrates with the rest of the body. Nitrogen is non-polar, and thus relatively insoluble in water, so the diffusion of nitrogen from air to water is relatively slow. Nitrogen has several fold greater storage in fat that water [30].

2.2.3 Carbon dioxide

Impressively, the body of a 70 kg human stores the equivalent of around 120 L (in gaseous form at one atmosphere of pressure) of carbon dioxide [32, 33]. Over 90% of this carbon dioxide is stored as carbonate in bone where it forms mineral crystals crucial to giving bone its properties of hardness and rigidity [34, 33]. In other tissues and blood almost all carbon dioxide is stored as bicarbonate and physically dissolved in solution [29]. Bicarbonate and hydrogen ions are produced as part of a reversible reaction between water and carbon dioxide to produce carbonic acid. This reaction is strongly catalysed by the metalloenzyme (contains a metallic zinc ion) carbonic anhydrase [35]. Carbonic acid releases hydrogen ions (depending upon the solutions pH) which must be buffered in some way for the reversible reaction to continue to store carbon dioxide as bicarbonate. Excess hydrogen ions can be buffered by amino groups. These are found on both the amino termini of proteins and histidine (an amino acid) residues within proteins. As a result most of the buffering capacity is intracellular.

In blood, carbon dioxide is mostly stored as bicarbonate in the plasma but haemoglobin also plays an important direct role by binding directly to carbon dioxide to form carbaminohaemoglobin. Haemoglobin is only found in red blood cells and carbaminohaemoglobin accounts for around 10% of blood storage of carbon dioxide [36]. Haemoglobin in the red blood cells also indirectly contributes to carbon dioxide storage through its role as the primary buffer of hydrogen ions released by carbonic

acid [35]. Haemoglobin is an excellent buffer because it possesses a large number of the aforementioned histidine groups. Albumin and phosphate also play an important role in sequestering hydrogen ions. To allow the reversible reaction to continue to produce carbonic acid the bicarbonate produced in the red blood cells is removed into the blood plasma through anionic exchange with chloride ions through a process named the Hamburger shift [37].

Binding to oxygen changes haemoglobin's allosteric state (its 3-dimensional shape) [35]. The affinity of haemoglobin for carbon dioxide (to form carbaminohaemoglobin) depends upon the allosteric state where the deoxygenated state has greater affinity for carbon dioxide and the oxygenated state has a lower affinity for carbon dioxide [38]. This is named the Haldane effect and it means at lower oxygen concentrations the blood carries more carbon dioxide per unit volume for any given carbon dioxide partial pressure. The allosteric conformations of haemoglobin also have different dissociation constants for histidine residue binding to protons which affects the storage of CO_2 as bicarbonate. Indeed, this effect on the buffering of protons accounts for around half of the allosteric interaction that causes the Haldane effect [39].

Carbon dioxide is produced by living cells through respiration. Overall, the rate of carbon dioxide removal must equal the rate of production to maintain homeostasis. However, in reality the removal of carbon dioxide often does not match production (which itself can vary significantly) and the body stores perform the important function of buffering these changes over the short term. High levels of carbon dioxide in the stores, hypercapnia, cause acidosis [40]. Severe acidosis results in reduced ventilation and enhanced parasympathetic nervous depression of cardiac output [41]. If the partial pressure of carbon dioxide goes above 10 kPa this can lead to seizures, unconsciousness and death [42]. Contrastingly, if carbon dioxide storage in the body drops alkalinity will be raised.

Therefore, regulation of carbon dioxide stores is an important component of homeostasis. In the shorter term the stores of carbon dioxide in the blood and non-osseous tissues are controlled by changes in ventilation and/or cardiac output [29]. Hyperventilation and hypoventilation change the partial pressure in the alveoli and therefore the concentration of carbon dioxide in the systemic blood that supplies the

tissues [43]. Although changes in ventilation are capable of rapidly changing body CO_2 stores, persistent changes in ventilation result in much longer term perturbation of CO_2 equilibrium. Indeed, research on pigs has demonstrated that even 48 hours after alveolar CO_2 is modified through changes in ventilation a new equilibrium is not fully reached [44]. Over the course of minutes and seconds the total cardiac output and its distribution will be offset by tissue metabolisms to determine whether gas stores are increased or decreased in each tissue. Over the longer term the skeleton and the kidneys play an important role in the storage of carbon dioxide. Starting around a day after a change in inspired carbon dioxide the kidneys help regulate total body stores and a new equilibrium is reached in around a week [45, 46]. This is achieved by changing both renal reabsorption of bicarbonate ions and renal excretion of hydrochloric acid (which affects the concentration of bicarbonate held for a given partial pressure of carbon dioxide through changing the hydrogen ion concentration and thus affecting the reversible conversion of carbon dioxide into bicarbonate). Bone carbonate stores do not have a simple response to changes in carbon dioxide due to the simultaneous effect on acidity caused by carbon dioxide changes [47]. If carbon dioxide is increased this generates more hydrogen ions in the blood and reduces pH which causes a decrease in bone carbonate storage. After 10 days when the pH is returned to normal the carbon dioxide storage slowly increases again to above normal values [34].

2.2.4 Oxygen

Unlike carbon dioxide, most oxygen is stored in the blood with the equivalent of approximately 1.2 L of gaseous oxygen stored in the blood of a 70 kg man in an atmosphere at sea level [29, 48]. The same man would store only around 0.3 L of oxygen in the remaining tissues [29, 48]. Due to the greater atmospheric oxygen content and the smaller total body store of oxygen, the gaseous oxygen held in the lungs compromises a much larger share of total body molecular oxygen content than is the case for carbon dioxide.

The amount of oxygen stored in solution in both blood and tissue is relatively low due to oxygen's low physical solubility. Most body oxygen is stored through binding to the haem proteins haemoglobin and myoglobin. Haem proteins are named for their ferrous Fe^{2+} ion prosthetic group which directly binds to oxygen [49]. The importance

of oxygen binding proteins for oxygen storage is demonstrated by animals adapted to prolonged breath holding, such as seals, which have more haemoglobin, blood volume and myoglobin [50, 51]. In humans, myoglobin is largely limited to slow twitch skeletal and cardiac muscle cells where it may serve as an emergency oxygen store during exercise [52] and facilitates faster diffusion of oxygen from the cell membrane to the mitochondria in these metabolically demanding tissues [53].

Haemoglobin is only present in red blood cells and has four ferrous ions each of which can bind an oxygen molecule. The multiple binding sites allow haemoglobin to show cooperative homotropic binding qualities where each oxygen ligand bound to haemoglobin makes it easier for the next oxygen molecule to bind through conformational protein transitions [54]. Haemoglobin also displays heterotropic characteristics with carbon dioxide and hydrogen ions, reducing its affinity for oxygen via the Bohr effect [55]. As mentioned previously oxygen also affects haemoglobin's affinity for carbon dioxide (both through haemoglobin directly binding to carbon dioxide and indirectly by changing its affinity for hydrogen ions). Thus the total blood content for carbon dioxide and oxygen can only be estimated accurately from their partial pressures if both interrelationships through the Bohr and Haldane effects are considered.

Homeostasis of oxygen stores ensures life preserving reserves of oxygen for when activity is increased or if exchange is briefly interrupted (e.g. through breath holding). Regulation of these stores on the time scale of seconds is achieved by changing ventilation and cardiac output to modulate the rate of supply from the lungs to the demand from metabolically active tissues. Over days, body storage of oxygen is regulated by changes in blood haemoglobin content [56]. Haemoglobin concentration is modulated by levels of the haemoglobin stimulating hormone erythropoeitin. Increased erythropoietin release is one of the most important physiological changes during human acclimatisation to high altitude hypoxia (low oxygen).

2.2.5 Interrelated nature of carbon dioxide and oxygen storage

Body storage of both carbon dioxide and oxygen is interrelated for several reasons. First, the ability of blood haemoglobin to bind and store both gases depends on the concentration of the other gas according to the Haldane [38] and Bohr [55] effects. Secondly, homeostatic

processes aimed at regulating the store of one gas, such as ventilation and perfusion changes, tend to influence the other gas as well [57]. Thirdly, oxygen consumption and carbon dioxide production rates are linked through the respiration reaction so the gases can be considered to be functions of one another [57, 58]. Finally, metabolic rate is reduced by extreme levels of either gas [59, 43].

2.3 Existing mathematical models of the circulation and body gas stores

Storage of various body gases has been modelled in the literature to some degree. Here I will investigate the existing models in the literature for carbon dioxide, oxygen and nitrogen, and their limitations.

2.3.1 Carbon dioxide

Several models of body CO_2 storage have been reported in the literature [29, 32, 60, 61, 62]. One of the simplest forms these take is a single tissue compartment that equilibrates with the lungs via an immediate (zero volume) blood circulation [32, 61]. The capacitance of this compartment could be assigned a value such that the profile of experimentally measured carbon dioxide accumulation or clearance over time could be reproduced. However, studies demonstrate that these single compartment models are inadequate to describe experimentally measured blood CO_2 changes, as there are multiple time constants apparent in experimental data which a single compartment cannot reproduce [29, 32, 62].

Some multi-compartment models in the literature include a small set of compartments and a simplified single large arterial and venous vessel supply [32, 60]. These models perform better than single compartment models. Over time periods longer than ~ 30 min they can closely reproduce experimental data [32, 60]. However, they reproduce poorly the effect of CO_2 storage in shorter experiments lasting less than 15 minutes. Their fit to the data is only improved with post hoc manipulations such as unrealistic redistributions in perfusion, unrealistic changes in metabolism or arbitrary changes in the tissue CO_2 solubility in a subset of tissues to match that of water [63]. Post hoc manipulations like

these are problematic when physiologically accurate model outputs are required under different conditions and for different participants.

2.3.2 Oxygen

For whole body O_2 stores, the only dynamic model which I am aware of is that of Cherniack and Longobardo [64]. They incorporated O_2 solubilities into the CO_2 model of Farhi and Rahn [32]. This model reproduced experimental perturbations in body O_2 stores over a 3-min period poorly unless O_2 consumption was reduced at a specific time point. While such a model summarises the specific experiment, it clearly cannot be used to predict responses more generally for other scenarios.

2.3.3 Nitrogen

Multicompartmental nitrogen body gas store models exist, such as the Baker and Farmery model [65]. Their model consists of four hypothetical compartments (muscle, fat, vessel poor and vessel rich) of varying solubilities supplied by parallel vessels with no circulatory delay. Blood immediately exits the 'heart' passes through arteries of zero volume and then immediately exits the parallel venous tree. The main issues with this model are the lack of transport delays, the model only considers nitrogen and it relates to purely hypothetical compartments.

2.3.4 Shortcomings of all previous models

The accuracy of a storage model is substantially determined by the capacitance of its stores for each gas. This depends upon the number of compartments (or the number of rate constants), and their composition and size (which needs to be scalable to the individual). None of the pre-existing models are satisfactory for the purpose of this thesis because they suffer from an inability to reproduce experimental results over short periods less than 15 minutes (the time period over which the proposed protocol will be run). Reasons for this inadequacy could include incorrect number and capacitance of stores as well as the failure to include circulatory transit times which can delay recirculation of gases by an average of $\sim$ a minute. Of those that do include transport delays, they have

been essentially concerned with the anaesthetic gases [66, 67].

2.4 Pulmonary embolism

2.4.1 Pulmonary embolism mechanism and aetiology

Pulmonary embolism, where an obstruction occurs in a pulmonary artery or arteriole, is a life threatening condition due to its interference with the critical function of gaseous exchange. A pulmonary embolism is usually caused by a deep vein thrombus (DVT) partially dislodging (embolization) and migrating to the lungs where it then blocks one of the pulmonary arteries or arterioles [68]. If the blockage of pulmonary circulation is sufficiently extensive it can cause hypoxia, haemodynamic instability and death. Evidently, the aetiology of PE is closely linked to DVT. The three main risk factors for DVT are reduced perfusion, abnormal blood clotting and damage to veins.

2.4.2 Pulmonary embolism diagnosis

2.4.2.1 Existing techniques

PE typically presents with relatively non-specific clinical features such as shortness of breath and chest pain [69]. These symptoms are a very common patient complaint and are shared by many other pathologies. As a result, the possibility of PE is considered in a large group of patients for whom PE is the underlying disease in only a small subset. Nevertheless, the possibility of PE must be seriously considered both due to the aforementioned risk of mortality and because PE is treatable through administration of anticoagulants. Indeed, efficient diagnosis of PE and prompt provision of treatment can reduce PE related mortality by over two thirds [70]. Correct diagnoses can also help avoid overtreatment and the concomitant risks of anticoagulant drugs [71].

In contrast to pathologies like myocardial infarction there is no single test which is both sensitive and specific for PE [69, 72]. Instead, according to National Institute for Health and Care Excellence (NICE) guidance, several methods are used whereby negative PE patients are removed from the clinical pathway using the fastest and lowest risk diagnostic techniques wherever possible [4]. To begin with, clinical assessment and scoring tests are

used to assess whether a patient suffering from the classic symptoms of breathlessness and chest pain may have PE. Chest X-rays may also be taken to exclude other causes. Then the patients suspected of having PE are separated into two groups: PE likely and PE unlikely (high and low probability groups).

Low likelihood patients start with a preliminary screening test which requires only a venous blood sample to investigate levels of the fibrin proteolytic product: D-dimer [73]. D-dimer is a biomarker for inflammation and a negative test allows patients with low likelihood of PE to be quickly removed from the clinical pathway. The D-dimer test has a high negative predictive value for low likelihood patients.

However, in the case of high likelihood patients the risk of a false negative from using this test is unacceptably high (between ten and twenty percent) [74]. Consequently, high likelihood patients and those with a failed D-dimer test are immediately referred for the more definitive PE diagnostic techniques: V/Q scintigraphy and Computed Tomography Pulmonary Angiography (CTPA) [71]. V/Q scintigraphy is a radiopharmaceutical technique that uses comparative imaging of inhaled radionuclide xenon and venous infusions of technetium-labelled albumin to compare the distributions of ventilation and perfusion in the lungs. CTPA relies on repeated slice X-ray imaging of a radiocontrast substance infused intravenously. Both have excellent clinical negative predictive value [75]. However, with its recent utilisation of 64 multiple detectors, CTPA gives higher resolution in smaller branches of the airways [76] and is considered superior when the possibility of other lung diseases is suspected.

2.4.2.2 Flaws of existing techniques and the dangers of ionising radiation

The current pathway for PE diagnosis suffers from several issues. Unfortunately, both definitive PE investigations involve ionising radiation exposure, waiting for scanning equipment availability and treatment with anticoagulants during the interim. Ionising radiation consists of either subatomic particles or electromagnetic waves with sufficient energy to detach the electrons of molecules they come into contact with. Depending upon the dose, time period over which it is applied and the quality of the radiation this ionisation can cause significant damage to biological tissues [77]. Above 1 Gy radiation causes burns and above 10 Gy severe acute radiation poisoning. Below 1 Gy the main

risk is caused by ionising energy damaging DNA which can lead to cancerous mutations. CTPA delivers up to around 50 mGy to the chest and V/Q scans deliver around 0.28-0.51 mGy [78]. With small radiation doses like these it is difficult to precisely quantify the increased cancer risk [77] but it undeniably raises relative cancer risk. For comparison, a single hour of travel on a high-altitude aeroplane delivers a radiation dose of around 0.002 mGy [79].

Due to the most comprehensive PE investigations involving radiation exposure, skilled radiologists and waiting times, suspected PE patients are separated into two groups with an initial D-dimer screening of lower likelihood patients to reduce patient load and risk. However, the D-dimer test suffers from low specificity as many inflammatory conditions including trauma and infection can cause a positive test [80, 5]. In fact, D-dimer testing is capable of excluding PE in only 14-32% of outpatients without any other known conditions and less than 5% of patients with known comorbidities [81]. Therefore, due to both PE's non-specific symptoms and D-dimer assay being a relatively non-specific screening mechanism many patients are added to the high risk pathway. Amongst the high likelihood patients sent for ionising scans, only a small proportion of around 0.3 are PE positive [74, 82, 83], with the remainder unnecessarily exposed to radiation. Clearly, a superior screening test would be beneficial.

2.4.2.3 Pulmonary embolism in pregnant women

Pregnancy compounds all of the aforementioned issues. In pregnancy the risk of PE is greater, the diagnosis of PE is more problematic and overtreatment is more harmful.

All three of the risk factors for DVT and thus PE are raised in pregnancy [84]. First, perfusion is reduced both due to weight of the foetus and uterus inhibiting venous outflow from the extremities and because of reduced maternal activity reducing venous return. Secondly, damage to veins can occur during normal delivery or as a result of perinatal surgery. Thirdly and most importantly, the blood is altered to a hypercoagulated state as a result of pregnancy-associated hormonal changes to blood clotting factors. The hypercoagulated state likely evolved to protect pregnant women from the leading cause of maternal death during childbirth before modern medicine: haemorrhage [84, 85]. Less frequently, the PE can be caused by amniotic fluid entering the maternal bloodstream.

Together these risk factors raise the incidence of maternal PE to 1 in 1000 [86], 4–10 times the risk in non-pregnant women [87, 88]. Risk of DVT increases prior to many anatomical changes of pregnancy in the first trimester [89] but is at its greatest in the post-partum period [88]. The risk is especially high following pregnancy-related surgery. Due to its prevalence and severity, PE remains the primary cause of pregnancy-related mortality in more economically developed nations where maternal haemorrhage is now effectively treated [90, 91, 92].

Diagnosis of PE in pregnant women is further complicated by the classic signs and symptoms of PE being co-indicated in pregnancy [93]. As a result, clinical scoring assessments are not validated in pregnant cohorts [78, 94]. In addition, the gateway D-dimer test loses its diagnostic accuracy [95] due to a physiological increase during pregnancy [96], especially in the third trimester [97], followed by a sharp decrease below normal values for several weeks post-partum [98]. The ionising radiation present in the two definitive PE diagnostic techniques is particularly hazardous to the maternal breast tissue and foetus [99]. Due to the repeated X-ray scans, CTPA exposes the patient to a higher overall radioactive dose than V/Q scintigraphy [100, 75]. However, the radiocontrast substance infused in CTPA is not radioactive in of itself, unlike the technetium-labelled albumin in V/Q scintigraphy which the maternal circulatory system will bring in close apposition to the foetus. Consequently, phantom studies suggest 64-CTPA is safer for the foetus [101, 102] but considerably more dangerous for the pregnant woman's breast tissue with a radiation dose of around 20-60 mGy [103]. Indeed, some estimates place the risk of causing breast cancer in young women as high as 1 in every 143 CTPA scans [104]. For this reason, the lower dose V/Q scintigraphy has been recommended as the initial diagnostic tool in pregnant women with suspected PE [75]. However, the optimal PE diagnostic strategy during pregnancy remains hotly debated and the clinician must decide between irradiating the foetus or breast tissue. It has been proposed that the concern surrounding radiation exposure in pregnancy causes enough reluctance to utilise the diagnostic techniques that it limits timely positive PE diagnoses and treatment, resulting in higher mortality [105].

Finally, precautionary treatment in suspected maternal PE is not recommended as overtreatment results in needless risk to both mother and foetus and makes child birth

riskier because of anticoagulant pharmaceutical side-effects. Therefore, accurate and objective PE investigations are even more important when PE is suspected in pregnant women.

In summary, pregnant women are at a higher risk of suffering a PE, have fewer first-level PE screening techniques available to them, are more likely to have PE symptoms whilst having no pulmonary malperfusion and are more vulnerable to the radiation risks inherent in current diagnostic techniques.

2.4.3 Attempts at using blood and respiratory measurements to diagnose pulmonary embolism

As outlined previously, an accurate PE technique that does not involve radiation exposure, is easy to use, is non-invasive and low cost would be of significant clinical utility. Even if only a screening tool, substituting D-dimer with a more specific measure that suffers from fewer false positives would be valuable for groups of young patients who could otherwise be discharged if it were not for the suspicion of PE. Whatever the technique, it would need to have an almost perfect negative predictive value due to the inherent seriousness of falsely discharging a patient with PE.

The pathophysiology of PE necessarily compromises gas exchange in the lungs as regions of the respiratory zone cannot undergo gas exchange with the blood due to vessel blockage. Based on this principle there have been attempts to estimate pulmonary malperfusion through simple measurement of the blood and/or respiratory gases as this would avoid the need for ionising radiation. To understand the basis of these techniques it is useful to consider the hypothetical three compartment model of the lung which has areas divided into: i) perfused and ventilated, ii) perfused but unventilated and iii) ventilated but unperfused [106, 107]. PE afflicted areas fall into the last category and the gas held there will have a composition approximating atmospheric gas (with a higher O_2 and lower CO_2) due to a lack of exchange creating an 'alveolar deadspace' in addition to the existing 'anatomical deadspace' (from the conducting zones). Even in the presence of a PE, blood reaching the systemic arteries has flowed through unblocked areas of the lungs and is exposed to alveoli as normal. Therefore, the gas composition in the systemic arterial blood should not be affected by PE in a same way as the alveolar gas composition.

As such, in PE-influenced regions the alveolar gas partial pressure will be significantly different to the exiting blood gas contents in a manner not present in health. Comparing systemic arterial blood gas contents to alveolar gas partial pressures should be instructive on whether a patient has a PE, with a difference between alveolar and arterial gas implying the presence and size of a blockage.

It is not feasible to directly sample alveolar gas let alone gather information from alveoli in all segments of the lung to probe for PE. Proxies for an aggregate estimate of alveolar gas are often used. Approximations often use partial pressures from a small final volume of gas expired at the mouth, referred to as end-tidal gas (PET_x). As alveoli are located in the deepest sections of the lungs this gas is assumed to be equivalent to alveolar gas. Some studies found in the literature attempted to detect PE using estimates of alveolar gas alone.

Although arterial puncture requires specialised clinicians it is administered regularly in hospitals. In an ideal lung where ventilation and perfusion are perfectly matched the alveolar and systemic arterial gas partial pressures (Pa_x) would be equivalent [7]. Some studies relied on arterial sampling alone to estimate the alveolar gas state and detect PE.

Some studies used comparisons of both these readings together to probe for areas of the lung that are ventilated but not perfused as in PE.

2.4.3.1 Using blood samples alone to diagnose pulmonary embolism

As PE affects gas exchange it was hypothesised that measurements of the arterial gas, which has come from the lungs via the right heart, could have diagnostic value. However, despite the deleterious effect on gaseous exchange, systemic arterial blood gas measurements on their own show no significant negative predictive value or specificity [108]. As such arterial blood gas measurements alone are not useful for assessment of suspected PE. Some have attempted to combine measurements of arterial blood oxygen partial pressure with D dimer assays [109] but large and carefully controlled studies have shown this is of little use [108]. Considering the pathophysiology, it is unsurprising these techniques failed. With PE the alveolar regions in which blood still flows are healthy and equilibration occurs as normal, meaning partial pressures in the systemic arteries can approximate healthy values.

2.4.3.2 Using estimates of alveolar gas alone to diagnose pulmonary embolism

Others focused on using estimates of alveolar carbon dioxide partial pressures alone to diagnose PEs through capnography, continuous measurement of the partial pressure of CO_2 at the mouth during the respiratory cycle [110]. Volume capnography ($Vcap$) uses the profile of expired CO_2 to define the end-tidal 'alveolar' portion of the breath with the goal of disentangling anatomic deadspace (from the conducting zones) from the alveolar compartment. Prentice *et al.* calculate that the cutoff value of end-tidal CO_2 that gives 100% sensitivity only has a specificity of 12% [111]. Although this would prevent over a tenth of patients from needing to be irradiated and could be combined with D dimer screening it has not garnered wide scale usage.

2.4.3.3 Comparing blood and respiratory measurements to diagnose pulmonary embolism

Rather than considering the arterial blood or alveolar gas partial pressures in isolation, others have tested comparing blood samples with measurements of expired gases as a technique to detect PE.

Some studies focused on using oxygen partial pressures to diagnose PEs based on observation of a larger alveolar-arterial (A-a) oxygen gas gradient than would be found in health. Several techniques have been suggested using alveolar-arterial (A-a) gradients of oxygen either alone [112] or with a minimum normal value for the partial pressure of arterial carbon dioxide (Pa_{CO_2}) [113], as this is expected to drop with PE due to increased alveolar deadspace (N.B. these do not use estimates of alveolar CO_2). Unfortunately, normal values in any or all of these are insufficient to exclude a potential PE due to unacceptably high rates of both false negatives and false positives [108, 114]. If patients with no history of DVT or PE are excluded and a more restrictive range of normal A-a gradients is used then respiratory methods for PE diagnosis show greater potential as a tool for excluding PE with a false negative rate of around 2-10% [112, 108, 114]. However, using this tighter definition of normal oxygen A-a gradient results in a similar proportion of PE negative patients having abnormal respiratory measurements as those suffering from PE, making it an suboptimal screening tool [114].

Studies using carbon dioxide as the comparison gas calculate the alveolar dead space

fraction ($AVDSf$) by comparing the difference between arterial (Pa_{CO2}) and end-tidal (PET_{CO2}) CO_2 where $AVDSf = (Pa_{CO2} - PET_{CO2})/Pa_{CO2})$ [115, 116]. Alveolar dead space increases in PE, and therefore a greater $AVDSf$ is expected. Meta-analysis of 14 trials using both $Vcap$ alone and $AVDSf$ with over 2,000 total subjects (and a proportion of 0.2 PE-positives) demonstrated that the methods had a sensitivity of 0.8 and a specificity of 0.49 [6]. These results indicate these methods may have potential for screening in low likelihood cohorts, particularly if combined with D dimer testing [7], but ultimately are not good enough to replace CTPA or achieve wide scale adoption.

2.4.3.4 Limitations of these techniques

The failure of these techniques is likely due to issues with the underlying assumptions. First and foremost, end-tidal gas is not truly representative of alveolar gas in normal healthy lungs due to a set of physiological properties such as: the imperfect ventilation/perfusion distribution, transit delays caused by the conducting zone of the airways smearing the output and oscillations in alveolar CO_2 values during the breathing cycle. Secondly, the systemic arterial and alveolar values can vary for reasons such as the ventilation/perfusion distribution and shunt causing pulmonary blood to pass through unventilated areas of the lung (as opposed to the apparent dead space caused by PE). Finally, gas values, particularly those for CO_2, wander as individuals spontaneously vary their rate and depth of respiration, a factor that is often compounded by breathing through respiratory equipment and blood sampling related anxiety. The capnography technique is particularly vulnerable to this effect as it only considers end-tidal estimates of alveolar gas and does not compare this to measured blood samples that would indicate shifting body levels of CO_2.

Aside from diagnostic accuracy, another reason this technique has not successfully transferred to regular clinical use is due to the requirement for measurement of blood gas levels using an arterial catheter. This is impractical and requires specialist administration and a method that could work with venous blood sampling would be more practical.

2.5 Coronavirus disease 2019

Coronavirus Disease 2019 (COVID-19) became a pandemic during the course of conducting the experimental work for this thesis. Research on pulmonary embolism was ordered to cease due to the perceived risks of respiratory research in a clinical setting. When PE work was finally allowed to resume, infection control measures and recruiting clinician time was limited such that we could not acquire the required sample size. However, ethical approval was quickly acquired to work on COVID-19 research using the techniques developed in this thesis and I diverted my experimental efforts accordingly.

2.5.1 COVID-19 emergence, transmission and significance

COVID-19 is caused by the severe acute respiratory syndrome coronavirus 2 (SARS-CoV-2). It emerged in December 2019, Wuhan province, China. In the following 18 months it spread across the globe to almost all territories and countries with 179 million confirmed cases and 3.8 million deaths [117, 118]. It was named for its phylogenetic similarity [119] to the viruses that caused the previous severe acute respiratory syndrome (SARS) outbreak which lasted between 2002-2003 and Middle East respiratory syndrome (MERS) which began in 2012 and has yet to be declared contained. In all three of these coronavirus-caused diseases, zoonotic transmission (infection of humans from other animals) is believed to be the initial trigger of the outbreaks [120, 121].

A key to the high transmission rate of SARS-CoV-2, as with the first SARS virus, is that it utilises human angiotensin converting enzyme 2 (hACE-2) as its host receptor [119, 122, 121]. The host receptor is used by the virus to attach and enter cells through interactions with viral spike glycoproteins. hACE-2 is expressed in the alveolar cells of the lung, the endothelial cells lining the blood vessels, gastrointestinal and liver cells. The fact that hACE-2 is expressed in a wide variety of cells provides many routes for infection. Reports have provided strong evidence that COVID-19 can be spread via respiratory droplets [123] and physical contact with infected individuals or recently contaminated items [124]. Respiratory droplets are readily generated during oral speech [125]. Although not widely reported, the presence of live viruses in faeces implies that faecal transmission is also possible [126]. hACE-2 is an essential gene (i.e. required for survival) meaning

that every human is susceptible to the disease and no genetically immune individuals have been identified [127].

SARS and MERS caused relatively few deaths, 774 and 858 respectively, compared with SARS-CoV-2. This is despite SARS-CoV-2 having a relatively small case fatality rate (CFR) of 2.2% [117, 118] compared to SARS and MERS which have CFRs of 9.6% and 34.4%, respectively [120]. The reason for this is the exceptionally high infectiousness of SARS-CoV-2, leading to a very large number of people being infected. Despite only a small percentage of those infected being hospitalised, high total infection numbers and no pre-existing population immunity have resulted in an extremely high load being placed on healthcare services. Due to the stress placed on hospitals most countries around the globe implemented restrictions or lockdowns of some kind as well as public care measures such as face masks, hand washing and wide scale testing and screening. These strategies were predicated on the principle of reducing direct human contact and movement/travel to reduce the ability of the virus to spread and therefore slow down the rate of infection: 'flattening the curve'. These responses to the pandemic have caused adverse effects on global social and economic health [128, 129]. There are many other negative effects of the pandemic and subsequent restrictions. For instance, approximately 1.6 billion students (94% of the total) globally had their learning disrupted through restrictive measures in the largest disturbance of education in human history [130]. Due to these considerations research into the pathology, treatment and containment of COVID-19 is of significant importance.

2.5.2 COVID-19 symptoms

The most frequently reported clinical symptoms of infection with SARS-CoV-2 are unspecific: fever, breathlessness, fatigue and persistent dry cough [131, 127]. Slightly more specific signs such as loss of smell (anosmia) and taste (dysgeusia) are also common. Less common symptoms are also nonspecific: headaches, chest and abdominal pain, diarrhoea, sore throat and sinus congestion. Around 46% (95% confidence interval 18-74%) of people infected with SARS-CoV-2 are asymptomatic, meaning they never develop the symptoms (not to be confused with the incubation period of disease where the individual is pre-symptomatic but not asymptomatic) [132, 133, 134]. This serves to lower death rate but

increase the efficiency of transmission as carriers unwittingly go about normal activities and spread the virus. Both the high rate of asymptomatic sufferers and the nonspecific nature of COVID-19 symptoms has likely aided the spread of COVID-19 because these symptoms or lack thereof could easily be confused with full health or other common bacterial and viral illnesses such as colds and influenza.

2.5.3 COVID-19 diagnosis

Due to the nonspecific nature of symptoms, diagnosis of COVID-19 cannot be based on symptoms alone. The most effective methods for confirming infection detect SARS-CoV-2 nucleic acid sequences: real-time quantitative reverse transcription polymerase chain reaction (qRT-PCR) using primers which match viral acid sequences and nucleic acid next-generation sequencing (NGS). Other methods are also available such as serology tests for SARS-CoV-2 antigens during the acute infection phase and for antibodies against these antigens which can be used to detect previous infection after the acute phase. Radiological testing of the chest often shows characteristic pulmonary ground-glass opacities (caused by serous fibrinous exudate) related to COVID-19 [135, 136, 137]. However, this is not typically used for diagnosis as chest X rays and CT scans can be normal in early disease [138]. Other clinical tests for aiding prognosis and treatment have been explored. For example, patients with blood tests giving D-dimer concentrations higher than 1 ug/mL showed poor prognosis [139].

2.5.4 COVID-19 pathology

Around 80% of symptomatic COVID-19 cases result in mild disease [140]. Severe disease requires hospitalisation and can lead to death even with the best care available. The primary cause of COVID-19 related morbidity and mortality in adults is acute respiratory distress syndrome (ARDS) and acute lung injury (ALI) [141] although there is some debate as to whether the COVID-19 related version of these syndromes is precisely akin to the previously defined versions [142]. ARDS and ALI result in pulmonary oedema (excess fluid in the lungs) and respiratory failure due to detrimental levels of inflammatory cytokines (a category of signalling molecules that regulate the immune system) being produced. The resulting excessive inflammation causes global lung damage at the level of the deep

airways and alveoli. Together with the pulmonary oedema this extensive damage prevents the lung providing its primary function of respiratory exchange leading to hypoxaemia (low blood oxygen) [143]. Unfortunately, this hypoxaemia can be resistant to treatment with supplementary oxygen as a result of pathological alterations in pulmonary blood flow that are thought to cause marked ventilation/perfusion mismatch and intrapulmonary shunt [144, 145]. The likely underlying cause for the increased intrapulmonary shunt is loss of hypoxic vasoconstriction (which in health helps maintain adequate ventilation/perfusion matching), resulting in inappropriately high perfusion of poorly ventilated lung regions. Autopsies of individuals who died after testing positive for COVID-19 display large viral particle loads in alveolar epithelial cells, decreased air volumes and atrophy of lung lobes [127]. Indeed, one of the findings specific to COVID-19 caused ARDS is direct cellular damage by the virus [143]. Signs of severe inflammation are also common with the peripheral lung adhering to the chest wall. Immune responses such as increased macrophages along with increased serous fluid, haemorrhaging and alveolar lesions are often visible in the lung by microscope. Another common finding was secondary bacterial infections and rarely secondary fungal infections. These are common to other viral pneumonias. Rarely, COVID-19 can also cause viral sepsis which can lead to multiple organ failure.

2.5.5 COVID-19 risk factors

The risk of severe disease and mortality in COVID-19 is affected by many factors including male sex, old age, smoking[146] and underlying health conditions such as obesity[147], hypertension, cancer, cardiovascular and/or chronic respiratory disease [148, 120, 139].

The effect of age on COVID-19 mortality is marked, with a 0.1% CFR in healthy people under 40 and a drastic increase to a CFR of around 9% in people over 80 [149]. One study reports that of 1,591 patients admitted to the intensive care unit with a positive test for SARS-CoV-2 the median age was 63 years old, with an interquartile range of 56 to 70 years [150]. The interquartile range demonstrates how tightly constrained the disease is to older individuals. Remarkably, of this group admitted to intensive care 82% were male.

The underlying cardiovascular comorbidities that raise risk of severe COVID-19 and

death include previous myocardial and cerebral infarctions, coronary heart disease [139] and arrhythmias [148, 120].

Chronic obstructive pulmonary disease (COPD) is linked with significant increases of around twice the morbidity and mortality from COVID-19 [148]. Both past and present smokers have an increased risk of severe disease or death as a result of COVID-19 [148, 146] and 1.2 times the likelihood of requiring mechanical ventilation. This may be due to the increased alveolar expression of hACE-2 caused by smoking [151].

Excessive body fat exacerbates severe lung diseases through its effect on metabolic and inflammatory pathways. Indeed, research before the pandemic indicated that obesity (defined as a body mass index above 30) increases the risk of ARDS [152]. ARDS is the primary cause of COVID-19 related death and obesity has since been linked to a highly significant increase in COVID-19 related morbidity and mortality [153, 147]. To make matters worse, obesity inhibits the innate and adaptive immune systems [154] meaning the efficacy of vaccines may be lower in this population [147].

2.5.6 COVID-19 treatment

Initially, due to its novel nature, the only treatments available for severe COVID-19 were supportive. These included supplementary oxygen, invasive intubation with mechanical ventilation[142] and extracorporeal membrane oxygenation (ECMO) [155]. The timing and use of these techniques has been the source of much debate [142]. Many new treatments have been developed and tested including several drugs [156]. Both antiviral drugs used for HIV and Ebola and blood plasma transfusions from recently infected (and recovered) individuals have been shown to be beneficial [157]. Perhaps most crucially, wide scale vaccination is now available with a large number of the world's population now vaccinated [117, 118].

2.5.7 Long term effects of COVID-19

When I began experimental research on COVID-19, the long term effects were unknown as it was only a very recent phenomenon. However, in the subsequent year and a half there has been much research into the chronic effects of COVID-19. Many patients complained of long lasting effects, dubbed 'long COVID' by the media, that persist after the initial

acute disease phase. Chronic or long term COVID-19 is usually considered to be any signs, symptoms or clinical findings that last more than 3 weeks after onset of SARS-CoV-2 infection [158] and are not caused by the virus itself (which has been cleared from the body by this time) but the damage it causes during infection.

A large scale meta-analysis of 47,910 patients indicates around 80% of COVID-19 survivors develop a wide variety (55) of long term signs, symptoms or pathological clinical findings [159]. Many of these are simply continuations of symptoms present during the acute phase, although novel and nonspecific symptoms also arise during the post-infection phase. The most common are fatigue, headaches, cognitive/neurological issues, hair loss, breathlessness (dyspnea), abnormal chest X-rays/CT scans and elevated D-dimer blood tests [159]. It is thought most 'long COVID' occurs in patients who required significant clinical intervention [159]. However, in one study, abnormal X-rays and CT scans after acute disease recovery showed no correlation with the severity of the acute disease phase [160]. Elucidating the relationship between disease severity and recovery of clinical parameters is yet to be fully explored. Lopez et al. [159] recommend that to improve understanding, future studies stratify by sex, age, ethnicity, pre-COVID-19 comorbidities and the severity of the disease when assessing recovery from COVID-19. This thesis focuses on the most relevant of these when assessing the functional recovery of the lungs from SARS-CoV-2 infection.

2.6 Summary

The aim of this thesis is to develop a technique to diagnose PE without the need for ionising radiation or arterial blood gas sampling. Instead, respiratory exchange measurements at the mouth will be used together with venous blood sampling.

Instead of using end-tidal gas measurements, which are affected by both normal variation in healthy lungs as well as any pathological changes, the technique will use a detailed computational model of the lung that incorporates inhomogeneity and deadspace to estimate both alveolar CO_2 and O_2 (model described in the next Chapter). This model lung is constructed using breath data measurements from a highly accurate prototype device (see next Chapter) and outputs arterial blood partial pressure values every 10 ms

(in accordance with the sampling time of the measurement device; see next Chapter).

Instead of using invasive arterial blood gas samples, the proposed technique will use venous blood gas measurements (of both CO_2 and O_2) and compare these to model blood gas predictions. In order to utilise venous measurements one needs to be able to account for body storage and recirculation of gas. As all existing models of the body gas stores and circulation are inadequate a new model of the circulation and body gas stores (CBGS) is created (see Chapter 4). To remedy the issues of existing models, transit delays are incorporated and a broad set of tissues with physiological capacitances are included. This model also will improve lung model arterial estimates by including recirculation.

The validation stages of this thesis became impossible because of the COVID-19 pandemic. Therefore a switch was made to apply the technology/apparatus to explore lung function post-COVID. This COVID study was also capable of providing some preliminary data towards the validation of the methodology for diagnosing PE.

Chapter 3

Pre-existing technology

3.1 Introduction

The work in this thesis exploits measurement technologies and computational models that have been previously developed within the laboratory. The original purpose behind the development of these two technologies was to enable quantitative assessment of new aspects of lung physiology, particularly in relation to understanding inhomogeneity of function within the lung.

The work developing the measurement technology was directed towards obtaining extremely precise measures of gas exchange at the mouth using a spectroscopic device named the molecular flow sensor (MFS) [8]. The advances in precision provided by the MFS were necessary to allow the measured data to be useful in identifying inhomogeneities within the lung [161].

Prior work developing the computational model of the lung – the log normal lung (LNL) – was to provide a model of the lung that was sufficiently detailed that it could incorporate inhomogeneity, but also sufficiently limited in complexity so that useful parameters could be identified from the gas exchange measurements made at the mouth by the MFS [9].

For the device and model to be clinically useful cardiopulmonary parameters must be estimated for a given participant. The process by which the parameters are estimated from the measured breathing data involves non-linear optimisation. While it is conceptually simple to solve the forward problem of calculating model outputs with known parameter

values, it is much harder to solve the inverse problem of estimating the parameter values from a model output.

The experimental measurement protocol that has been used in conjunction with the MFS and LNL technologies to estimate heterogeneity is a 'nitrogen washout', consisting of 10 min of air breathing, followed by 5 min of breathing pure oxygen. When this protocol is measured using the MFS and modelled using the LNL it can provide clinically useful measures related to respiratory disease [9].

Whilst demonstrating great promise in recovering parameters relevant to ventilatory phsyiology, two particular limitations of the current MFS-LNL technology must be solved to improve the overall fitting, allow the recovery of parameters relevant to the vascular physiology of the lungs and to ease its use in clinical settings. These limitations are: i) the air-breathing period of the protocol is fairly long for a clinical test because the pre-existing assumptions of the lung model require a settling time for the participant to reach a steady state before useful data can be acquired, and ii) the LNL has an unknown input in the rate and gas composition of blood flow into the lung (measuring these would necessitate a highly-invasive pulmonary arterial catheter). It is to solve those two limitations that the model of the circulation and body gas stores has been developed in this thesis [1].

3.2 Measurement of respiratory exchange

3.2.1 History and current commercial devices

Measurement of gas exchange at the mouth has attracted clinical and scientific interest both due its noninvasive nature and the physiological insights it provides [162]. Over 100 years ago respiratory exchange in humans was measured by collecting expired gas over a given time period using a Douglas bag and then measuring the final mixed gas composition and volume [163]. This technique is only capable of estimating exchange over periods of many breaths and cannot provide information on a breath-by-breath basis or probe dynamic gas flux during each breath. Significant technological advances have been made and commercial instruments for measuring respiratory flow of specific gases over shorter time scales are now available. These devices are capable of excellent accuracy when the gas content is stable. For example, side-stream sampling by a Datex-Ohmeda

Capnomac Ultima 'rapid gas-analyser' reportedly measures oxygen concentration with a standard deviation of 0.1% under steady state conditions [164]. Thus, for most purposes, modern side-stream analysers are capable of accurate estimates of gas composition under steady state conditions. However, there is an important distinction between the ability to accurately measure steady gas compositions and the ability to accurately track dynamic breath-related changes in both composition and rate of flow for estimates of gas exchange.

Side-stream analysers suffer from several issues that limit their accuracy when estimating the gas exchange profile both during a breath and on a breath-to-breath basis. Their greatest limitation is not the precision or the sensor response speed but the pure delay caused by the sampling catheter which removes samples of gas from the main flow stream to estimate composition whilst flow is simultaneously measured along the main flow stream. During breathing both gas composition and flow rate change dynamically so aligning the timing of these two measurements is problematic and limits the temporal accuracy of gas composition and flow matching.

Oxygen in particular requires a sampling catheter in modern commercial devices as the standard design uses paramagnetic sensors which cannot be placed in the main gas flow stream [165]. Therefore, when it comes to using oxygen monitors to measure breath exchange the measurements of oxygen exchange are particularly sensitive to delays. To further complicate matters, breath-by-breath oxygen exchange is especially sensitive to measurement error due to the large quantities inspired and expired with only a relatively small net exchange [166]. Assuming a typical oxygen consumption of 250 ml/min and a typical inhaled oxygen volume per minute of 1.4 L/min (= 7 L/min ventilation multiplied by a 0.2 fraction of inspired oxygen), the proportion of inspired oxygen exchanged is only around 0.18. For carbon dioxide this value will be closer to 1. A temporal error as small as 20 ms can result in a 5% error in pulmonary gas exchange measurements for a device that accurately measures stable oxygen tension. Indeed, most commercial instruments have a measurement accuracy around +/- 5% during dynamic breath-related changes in gas content [167]. In normal breathing at rest, the human lung turns over approximately twice its own volume in gas every minute. Therefore, if one attempted to track total lung volume using an instrument with a 5% error between inspiratory and expiratory flow, the lung would be observed to inflate or deflate by 10% of its own volume every minute.

Thus, to use measured data to drive lung models, the measurements have to be far more accurate than available with current commercial instruments.

A further issue is that the measurement environment is very dynamic, with temperatures, pressures, water vapour content, density and viscosity all varying continuously through the respiratory cycle. Clearly, total gas flow at a molecular level must be measured accurately in order for individual gas exchanges to be estimated accurately and all these variables must be known for an accurate and precise measure of total molecular flow. Most commercial methods ignore these considerations and to date no commercial device measures water vapour content as it varies rapidly during the respiratory cycle.

3.2.2 The molecular flow sensing device

The Molecular Flow Sensor (MFS) [8, 168] was developed specifically to solve the aforementioned issues. The MFS is a prototype in-airway device that allows high-resolution gas composition data acquisition at 10 ms intervals. The high resolution is achieved through improvements in both flow and composition estimates. The result is a major improvement to the readings available from current commercial side-stream gas analysers [8].

The most significant improvement in gas exchange measurements is achieved through being entirely spectroscopic, with an independent laser used to analyse each gas species within a single main gas stream. This allows gas composition measurements to be in precise temporal alignment with measures of respiratory flow. The MFS device can measure oxygen, water and carbon dioxide flux with the capability for additional tracer gases: acetylene and methane. Laser absorption spectroscopy is virtually instantaneous and is predicated on the Beer-Lambert law which relates attenuation (absorbance) of light to the medium through which it is travelling: $A = \epsilon lc$ where A, measured attenuation; ϵ, the absorptivity of the species in question (an intrinsic quality of a species at a given wavelength); l, path length of the laser light; c, the concentration of the absorbing species. Thus, one can estimate the concentration of the gas of interest (c) if the attenuation of the light (A) is measured, and the path length (l) of the laser and the coefficient of absorbance (ϵ) are known.

Carbon dioxide and water absorb relatively strongly, which means measurements can be made over short path lengths in the device airway. The lasers used to detect these two species are multiplexed through the same optic fibre. The lasers pass through the airway and are reflected off a mirror so that they pass back through the airway in a ~ 5 cm long 'V' path to the detector (see Fig. 3.1). Although not necessarily directly of interest, measuring water vapour spectroscopically allows the proportion of gas flowing out the mouth that is water to be correctly accounted for, and thus is very important for accurately estimating the exchange of other gases.

Oxygen is a much poorer light absorber so the path length has to be enhanced because a 'V' path in the small airway space would be insufficient. The oxygen laser exploits cavity-enhanced absorption spectroscopy (CEAS), in essence two mirrors bounce the laser light back and forth through the gas mixture many times to compensate for its longer path-length and allow more significant light absorbance to occur to increase the signal to noise ratio [169]. The mirrors used in the MFS are highly reflective with a probability of reflection being 0.9975 versus that of transmission of 0.0025. Light is not lost where it is not reflected but is transmitted. Therefore, CEAS increases the path-length to around 10 m (for every 1 in 400 reflections the light will be transmitted (=0.0025); the size of the cavity is approximately 2.5 cm; 400 multiplied by 2.5 cm = 10 metres). In practice, the path length is calculated through calibration using N5 (laboratory-grade 99.995%) oxygen.

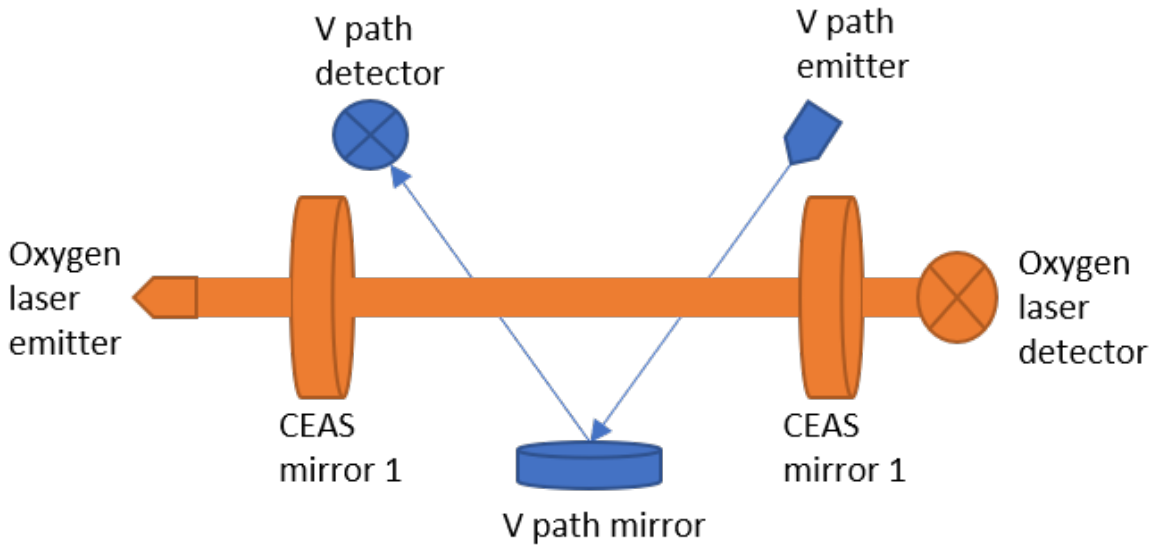

Figure 3.1. Schematic of the MFS from a cross section view through the airway showing laser path design. Orange: oxygen laser emitter, path, mirrors and detector (N.B. the oxygen is reflected many times between the two mirrors to increase the effective path length via cavity enhanced absorption spectroscopy - CEAS); Blue: V path laser emitter, path, mirror and detector (N.B. the V path consists of both carbon dioxide and water lasers multiplexed within the same optic fibre).

The flow is measured in the MFS via two inbuilt pneumotachography components (meshes and pressure sensors), one either side of the laser absorption space allowing temporal alignment with the spectroscopy-based gas composition measurements. Flow (V) is estimated using the recorded pressure drop (δP) across the two pneumatograph meshes. During breathing the flow in the measurement space may be non-steady and/or turbulent. Therefore, a simple linear relationship between δP and V that is found in true laminar flow will not be representative. Instead, the pressure drop was modelled through addition of 'major head loss', which is linearly proportional to the flow and viscosity of the gas mixture, and 'minor head loss', which is proportional to the square of flow and linearly proportional to the density. To allow this model to be solved, the MFS measures in-airway temperature and ambient pressure (with a time resolution of the same order as its spectroscopy measurements). Combining these measures with gas composition readings from spectroscopy allows viscosity and density to be estimated. The ambient pressure and temperature are also used to estimate the total gaseous molar concentration which is finally divided, based on composition, into estimates of flux of each molecular species.

Whilst oxygen, carbon dioxide and water are measured, the balance gas is assumed to

be nitrogen. This balance gas is given a value such that the total gas content is brought to the prevailing temperature and pressure. It is worth noting that in reality the balance gas will be a mixture of primarily nitrogen with other trace atmospheric gases such as argon (any argon present can be treated as if it were nitrogen). In most cases this thesis will refer to the balance gas simply as nitrogen.

These advances in accuracy and precision were necessary to enable the data to be used with a model of the lung to identify inhomogeneities within the lung [161].

3.3 Inhomogeneity in the lung

Lung inhomogeneity is a measure of a lack of uniformity or of a mismatch between any one or combination of: i) proportional ventilation to each unit of alveolar volume, ii) proportional blood flow to different alveolar regions of the lung, iii) the volumes of conducting zones supplying alveolar units (i.e. anatomical deadspace) and iv) the matching of ventilation and perfusion across the lung. Lung pathologies tend to target and/or progress more rapidly in small pockets of the lung with remaining areas being fairly healthy [170]. Therefore, large increases in inhomogeneity usually precede even small increases in mean global disease. For this reason, global measures of function usually can only detect late stage disease when the pathology has already progressed to large areas of the lung. Thus, a superior technique to detect early disease would be to assess the degree of heterogeneity rather than global change. For example, with COPD a technique that specifically detects alveolar compliance heterogeneity would diagnose disease earlier than global measures from spirometry.

3.3.1 Previous attempts to measure lung inhomogeneity

Several techniques for measuring lung inhomogeneity have been developed: multiple inert gas elimination technique (MIGET) [171, 172, 173], ventilation mismatch using CT or MRI [174] and single and multiple breath inert gas washout techniques to give lung clearance indices [175]. Unfortunately, these suffer from issues such as invasiveness and radiation, and as such no simple noninvasive test for inhomogeneity has achieved large scale clinical adoption.

3.3.2 Log-normal lung model

One approach developed recently to estimate lung inhomogeneity is based on a computational model of the pulmonary system and gas-exchange, the log normal lung (LNL), with the goal of recovering a set of clinically useful indices of lung function from noninvasive MFS experimental data [161, 9]. If successful, this would be beneficial in the clinical setting where there is currently no 'gold standard' for measuring lung inhomogeneity, which is thought to be one of the first signs of chronic obstructive pulmonary disease [176]. To achieve these goals, the model had to be sufficiently rich that it encompassed inhomogeneity, but also sufficiently parsimonious that the clinically relevant indices could be identified from the gas exchange measurements taken by the MFS at the mouth (which is separated by many branching airways from the information of interest).

The LNL model of the lung is strictly compartmentalised into 3 subtypes: a common dead space compartment (representing the dead space introduced by the device), completely mixed alveolar compartments and their coupled personal dead space compartments (Fig. 3.2). In this model it is assumed that gas exchange only occurs in the alveolar compartments, whose gas compositions remain entirely uniform at all times. This is similar enough to the physiology [177], which consists of millions of tiny alveoli where diffusion is very rapid, that it is not expected to be an issue for our purposes.

To allow sufficient inhomogeneity to be modelled, the LNL model consists of 125 independent functional lung units in parallel, each with their own share of the total perfusion, dead space and compliance. Despite the fairly large number of compartments the model lung is designed such that it can be constructed from only 5 parameters. This parsimony allows the model to be efficiently solved using a non-linear optimisation routine.

The reduction to 5 parameters is accomplished through assuming a continuous normal distribution for the deadspace and a bivariate log normal distribution for the compliance and perfusion. The model then only solves for the variance of these parameters rather than the individual values for each compartment. A bivariate log normal distribution was chosen to reproduce the ventilation/perfusion matching that occurs in the lung (see Chapter 2), and was given a correlation coefficient of 0.8. Actual human lungs are unlikely to follow these simple distributions perfectly but in most situations this should not be an

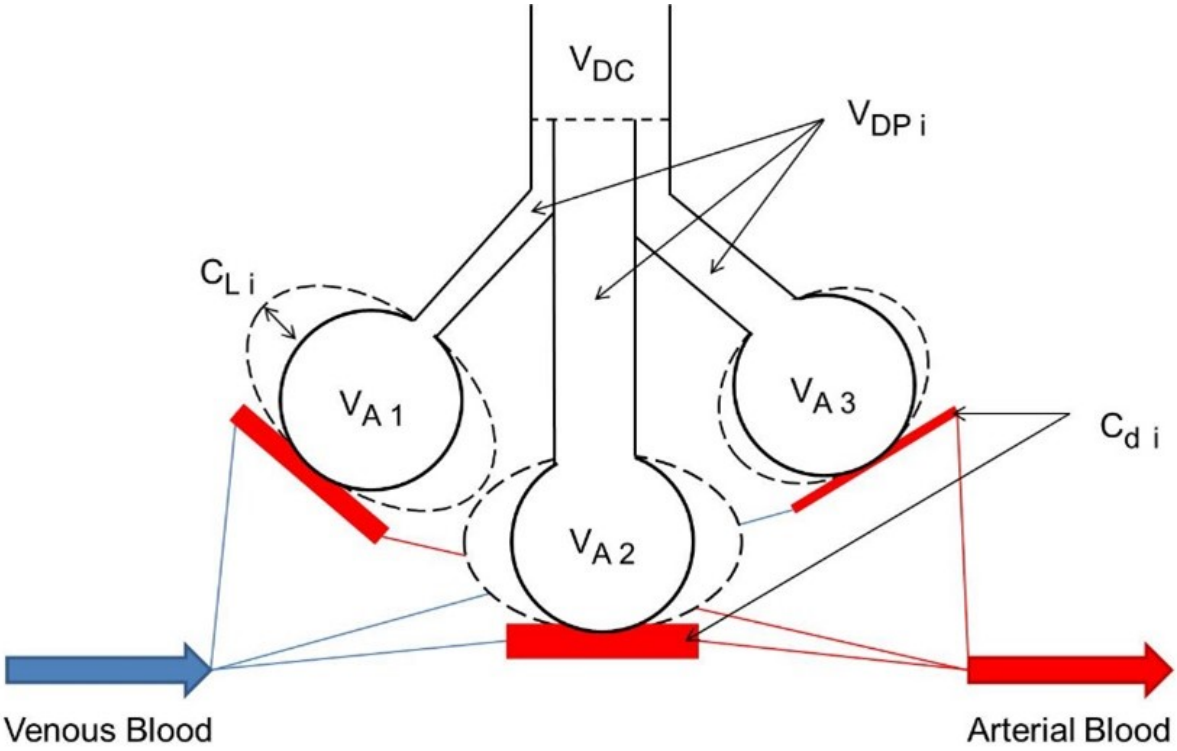

Figure 3.2. Schematic of the Log-Normal Lung model displaying 3 stylised lung compartments and their component share of the total perfusion (C_d), dead space (V_{DP}) and compliance (C_L) but with identical volume at functional residual capacity (V_A). Taken from [178]. The model is strictly compartmentalised into 3 subtypes: V_{DC}= a common dead space compartment (representing the dead space introduced by the device); V_A= completely mixed alveolar compartments and V_{DP}= their coupled personal dead space compartments. It is assumed that gas exchange only occurs in the alveolar compartments, whose gas compositions remain entirely uniform at all times.

issue. These distributions were found to be reasonable approximations of data taken from detailed biophysical studies [179, 180].

3.3.3 Parameter estimation from molecular flow sensor experimental data using the log-normal lung

When considering the LNL, it is useful to consider the principle of solving a model in the 'forward' and 'inverse' directions. The 'forward' problem involves evaluating a function with a given set of inputs to gain the outputs. In the case of the LNL this is using the intrinsic parameters of the lung and the inspired gas to estimate the composition of expired gas. The inverse problem is using known outputs to find the appropriate input/parameter set. For the LNL this is using the measured inspired gas and respired gas flow, and estimating the set of intrinsic lung parameters which would closely satisfy

the measured expired gas output.

Governing equations are based on the law of conservation of mass. As such it is trivial to solve the forward problem by inputting the MFS measured inspired gas content to a model lung constructed by setting a subset of parameters (see table 3.1) to reasonable physiological values and assigning values to the parameters determining lung physiology. However, these parameters are not measured directly by the MFS so to get representative lung parameter values solving the inverse problem is required.

In comparison with the forward problem, solving the inverse problem is computationally much more intensive. To estimate the parameter set from experimental data a recovery procedure is carried out (the inverse problem is solved). This involves minimising the squared differences between the model's simulated gas fractions being expired at the mouth and the experimentally measured data. More specifically, a non-linear least squares optimisation function is used to find the set of parameters that minimise the objective function. To calculate the simulated gas fractions being expired at the mouth a single iteration in the forward direction is solved using a given set of model lung parameters. The forward model consists of a single evaluation of the objective function. To solve the inverse problem this evaluation is repeated many times with different model lung parameter sets (initially a best guess) in order to find the minimum difference between simulated and experimental gas fractions. The parameter values that give this minimum are then assumed to be close to the true physiological value. In other words, the objective function is minimised when simulated expired gas fractions at the mouth are as close to those measured by the MFS as possible.

The profile of expired partial pressures of oxygen and carbon dioxide over a single breath provides physiological information on the distribution of anatomic dead space and the distribution of compliance (amongst other factors such as the ventilation perfusion matching). If all the personal dead space volumes supplying every alveolus were of identical length/volume and the compliances were identical for all compartments there would be a step change in the gas partial pressure at a certain expired volume and

*
†
‡

*Measured by the MFS.
†Measured by the MFS.
‡Must be inferred from MFS data using a multi-stage computation.

Table 3.1. *Log normal lung parameters*

Forward model input:	
$\dot{V}$ *	the total flow rate of gas at the mouth
F^x †	inspired composition/fractions of gas x
F_v^x ‡	venous gas concentrations
I_c	initial conditions for the differential equations
Set parameters:	
$V_{\mathrm{CO_2}}$	CO2 tissue volume
V_{DA}	MFS apparatus deadspace volume
$\dot{Q}$	Cardiac output
$\rho_{\dot{V}\dot{Q}}$	Correlation of compliance and perfusion
Parameters recovered by the inverse problem:	
V_A	Total alveolar volume when the lungs are at FRC
σ_{Cl}	Width of the compliance distribution
V_{DP}	Total personal dead space volume
σ_{DP}	Width of the deadspace distribution
σ_{Cd}	Width of the perfusion distribution

time when the gas fractions suddenly changed from a percentage close to air (from the conducting zones) to percentages equilibrated with the blood (from the alveolar zones). Physiological inhomogeneity in the lung changes these properties and causes smearing in this profile. The more smeared and sigmoidal the change in partial pressures the wider the distribution in alveolar compliance or dead space volumes that supply alveolar units.

Modelling of both these parameters together (deadspace and compliance distributions) is a major novel property of the LNL model. A further remaining question is whether the LNL can correctly distinguish the combination of these two properties that causes this smearing. Ensuring these two parameters reflect the underlying physiology is required to give accurate estimates of the gas content in the blood leaving the lungs in health. Accurately estimating the gas state of the blood leaving the lungs in health is a key assumption of the PE diagnostic technique presented here. This question is briefly explored in a validation study using enhanced gravity (see Chapter 8).

3.4 Experimental measurement protocol

To estimate these parameters of lung function, using the LNL model and experimental data from the MFS, a nitrogen washout protocol is followed. The original protocol described by Mountain at al. [9] involves a 10 minute air-breathing period followed by

a 5 minute nitrogen washout where the subject breathes pure oxygen. The subject is connected to the MFS by a mouthpiece with their nose sealed to ensure that all gas flux passes through the device. The nitrogen washout is used to estimate lung volume from the volume of nitrogen expired and a simple four compartment model of the body's dissolved nitrogen stores.

It is relatively trivial to see how lung volume information can be inferred from the nitrogen washout as from the start of the nitrogen washout no more nitrogen enters the lungs so all the expired nitrogen has exited from the alveolar volume. In addition, the profile of the nitrogen washout represents information on the distribution of ventilation and perfusion (due to body stores of nitrogen). For instance, if the decay is a perfect exponential decrease it implies perfect $\dot{V}/\dot{Q}$ matching and uniform alveolar ventilation distribution. However, if there are two different time constants for the nitrogen washout decay it implies two different populations of lung units: a well ventilated and a poorly ventilated group.

3.4.1 Success in detecting increases in lung inhomogeneity parameters associated with respiratory disease

Preliminary work using the MFS and LNL has been promising, showing highly significant and repeatable differences between healthy volunteers and patients suffering from chronic obstructive pulmonary disease (COPD) [161, 178, 9]. A representative example of the results is displayed in Fig. 3.3 which shows the distribution (inhomogeneity) of deadspace:volume ratios is both greater and has more spread in the COPD patient. This technique has also shown promise in asthma patients where the measure of compliance distribution predicted whether clinicians would decide to escalate therapy [181]. These results lend support to the hypothesis that disease can be diagnosed earlier using inhomogeneity as a metric. This unprecedented insight into lung function is made possible by the high-resolution MFS device, simple protocol and novel model of the lung.

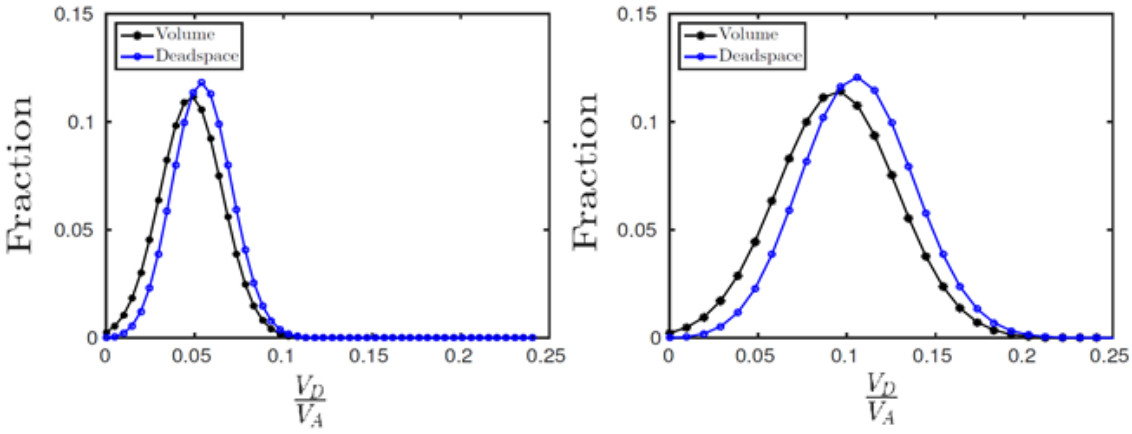

Figure 3.3. The results from the MFS-LNL model technique showing the distributions for deadspace:volume ratios (VD/VA) for a young and healthy participant (left) and a COPD patient (right). Taken from [178].

The ability of the LNL model to make effective use of the high-resolution data from the MFS to recover various useful parameters that describe lung function suggests it is a suitable model of the lung for our purposes.

3.5 Limitations of log-normal lung

The MFS-LNL technique has proved capable of recovering useful respiratory measurements of underlying cardiopulmonary function. However, there are two limitations in the current MFS-LNL technology that are especially problematic for model estimates of vascular features. First, the LNL has an unknown input in the rate of blood flowing into the lung and its composition. Second, the air breathing period of the test is fairly long for a clinical test and the shorter the test the more tolerable it is for patients who are elderly or unwell (and whose ability to co-operate to avoid leak from the mouthpiece may be somewhat limited). This is because the original LNL model required a 5 minute settling period on the mouth piece in an attempt to bring the participant closer to a steady state and thus reduce the influence of changes in the circulating gases. The primary work of this thesis aims to solve these two limitations simultaneously using a novel model of the circulation and body gas stores.

3.5.1 Importance of considering blood gas stores and recirculation

As outlined in the previous Chapter, significant quantities of gas are stored in the body tissues [65, 29] in dynamic equilibrium with the blood that supplies them. When there are changes in the composition of inspired gas or the rate of ventilation the arterial gas partial pressures change concomitantly. This recirculates and re-enters the lungs from the mixed venous pool. Whatever the change in arterial pressure, the body gas stores act to buffer and retard the change in the mixed venous blood. This is particularly important when changing the inspired gas, such as during a nitrogen washout. However, it is also relevant when there are changes in ventilation rate which frequently occur during respiratory experiments due to the tendency for human participants to hyperventilate when placed on a mouthpiece. In fact, when connected to the MFS, large changes in venous concentrations often occur because participants are prone to hyperventilation. This hyperventilation causes hypocapnia and a loss of CO_2 from bicarbonate stores in the body. This will necessarily cause a gradual drop in both the venous CO_2 and end-tidal CO_2 fraction. Due to this important influence of the tissue stores on gas exchange in the lungs, this aspect of the model must be considered carefully. The pre-existing LNL relied on a simple circulatory model to account for important changes in gas storage.

3.5.2 Modelling of the circulatory system within the log-normal lung

There are two main inputs to the LNL model: inspired gas and pulmonary arterial gas content. These equilibrate in the alveoli to generate the LNL output: expired gas and pulmonary venous gas content. The inspired gas composition and volume are measured to a high degree of accuracy by the MFS. Conversely, pulmonary arterial gas content cannot be measured non-invasively. Therefore, correctly approximating the mixed venous, which becomes the pulmonary arterial, input to the lungs is important when modelling the lung using the LNL. The LNL must model both normal air breathing, where nitrogen and oxygen blood compositions are fairly steady, and the nitrogen washout, where oxygen and nitrogen blood compositions change much more dramatically. Blood carbon dioxide

composition can change in either period depending upon alveolar ventilation.

Here, I discuss the recirculation modelling present in the pre-existing LNL and the approximations used where recirculation is ignored during air breathing.

3.5.2.1 Recirculation modelling during the washout

Physiologically, the gas composition of blood returning to the lungs is determined by the blood that leaves the lungs recirculating through the tissues before passing through the heart back to the lungs. In the course of this recirculation blood gases are influenced by both metabolism and exchange with the tissues. For the pre-existing LNL model, there is no recirculation model present for any gas during the air breathing phase of the nitrogen washout protocol. Thus, the composition of the blood leaving the lungs has no influence on the composition of the blood returning to the lungs. This simplifying assumption was made due to the lower expected variation in blood gas content during normal air breathing. Inspired carbon dioxide is not expected to change significantly during the washout phase of the protocol either, so no recirculation model is used for carbon dioxide at any point. Contrastingly, during the nitrogen washout phase the composition of nitrogen and oxygen in the blood leaving the lungs changes dramatically, so simple approximations of recirculation were used.

Nitrogen levels progressively drop during the washout in the alveoli, and consequently arterial and recirculating venous blood nitrogen also decrease. Nitrogen recirculation was modelled by the LNL during the washout using a basic compartmental storage model from the literature [65]. The Baker and Farmery nitrogen model is described in more detail in Chapter 2.

The rate of change of venous O_2 concentrations during the high O_2 breathing phase will be different to air breathing due to recirculating high arterial O_2 (itself caused by the high oxygen fraction inspired). If the same venous O_2 content as during air breathing is assumed (which would be lower than the true value caused by recirculation of the high O_2), this will lead to the model erroneously assigning more O_2 transit into the blood from the alveoli than actually occurs. What had been found previously was that if this process was omitted the oxygen uptake by the LNL model was too high, resulting in a reduction over time in the total model alveolar volume. To correct for this the venous concentration

of oxygen is allowed to rise to a value such that the oxygen flux into the blood is at a low enough value to ensure a stable alveolar volume. In practice this is achieved by adopting a simple, homogeneous model with only one compartment that has a single parameter for the volume of distribution of venous $O2(V_L(O2))$.

Therefore, oxygen recirculation was modelled using effectively a time constant given to the way the blood flow leaving the lungs could influence the amount of oxygen in the blood flow entering the lungs. This time constant was expressed as a stored volume of oxygen in the blood. This time constant or volume ($V_L(O2)$) was assessed for each participant in a sub-optimisation where the objective function was to keep the lung volume at FRC constant throughout the high oxygen breathing phase.

3.5.2.2 Estimating the pulmonary arterial gas content input during air breathing

In the pre-existing LNL method, recirculation and metabolism are not modelled for all gases during the air breathing period. However, the LNL still requires an input of blood gas contents from the pulmonary artery. So instead, a mean pulmonary arterial blood concentration and linear trend term are estimated to generate the required unmeasured input to the model [9]. Note that during air breathing this method is used for both oxygen and carbon dioxide but is extended into the washout only for carbon dioxide. Consequently, the blood flowing into the model lungs has either steady or linearly drifting CO_2 and O_2 gas concentrations during the air breathing period.

This simple linearly drifting concentration in the mixed venous/pulmonary arterial input to the model is first estimated by a simplified 'continuous model'. The continuous model is similar to the main LNL model but utilises a constant flow of air (rather than physiological breaths in and out) and only runs during the air breathing phase as it utilises the Haldane transformation [182]. This states that the volume of nitrogen inspired and expired from each unit on a single breath will be the same and this assumption is clearly violated during the nitrogen washout phase.

This was confirmed to be an important component of the pre-existing model as simulated venous concentrations rarely remained constant during the air breathing period in data sets collected with the MFS.

3.6 Shortcomings related to the circulatory system and thesis objectives

Currently, global circulatory parameters the LNL model recovers show insufficient intra-subject repeatability and little correlation with any subject groups [9]. In fact, this has led to the pre-existing LNL modelling using a set value for ventilation-perfusion correlation (ρ) and a set approximation for cardiac output. The primary reason for these deficiencies is hypothesised to be the oversimplified modelling of the circulation and body gas stores.

One of the major circulatory modelling issues is the assumption that the blood flowing into the lungs has either steady or linearly drifting CO_2 and O_2 gas concentrations during the air breathing period through forcing a linear concentration drift fit in the mixed venous/pulmonary arterial input. This does not allow the model to account for complex, non-linear changes during the air breathing period and the gas compositions in the blood leaving the lungs do not influence the blood entering the lungs (i.e. there is no recirculation during air breathing).

In an attempt to minimise changes in recirculating gas contents, and circumvent this modelling deficiency, the protocol included a settling period during the first five minutes of the 10 minute air breathing period. The model only began fitting data after this initial 5 minute period. The goal of this was to provide a physiological steady state after which the model starts fitting to the data. However, the significant trend terms fitted to the mixed venous oxygen and carbon dioxide concentrations demonstrated that this steady state was not truly occurring. Addressing this issue through improved modelling is preferable to extending the settling period because the protocol is already fairly long for a clinical test.

The second major issue is that the recirculation models used for nitrogen and oxygen during the nitrogen washout period are overly simple and no recirculation model is used for carbon dioxide. For the oxygen recirculation, the model includes several unphysiological assumptions with a crude single tissue compartment with no temporal delays that is scaled solely to maintain model lung volume. This is a pragmatic and entirely empirical fix but does not represent the underlying biology. The nitrogen recirculation, although more detailed, does not incorporate any circulatory delays and is based upon hypothetical

compartments.

Thirdly, metabolism is only proxied through the estimate of returning blood and metabolic rate is not truly represented by the LNL model.

The technical objectives of this thesis are to complete the model of the body gas stores by including not only gases in the lungs but also those dissolved in the rest of the body, along with the influence of tissues on circulating gases through metabolism. This will improve the model in two ways. Firstly, metabolism will be incorporated into the model so that the consumption of oxygen and production of carbon dioxide are parameters of the system estimated at the mouth (after buffering by all the stores). Secondly, recirculation of all model gases will be considered. This removes an unknown input to the model, instead using the output of the LNL model to directly influence its own input.

3.7 Summary

In summary, the pre-existing work to develop the MFS device and LNL model provides a strong platform to work from. However, as a consequence of gas storage within the body, information on gas exchange with the alveolar compartments alone is not sufficient to estimate venous concentrations. The current features of the LNL modelling prevents any chance of recovering values for use in PE diagnosis. The aim of this thesis is to write an improved model of the circulation and body gas stores that will remove some of the current limitations of the technology and may allow for better estimates of both the total perfusion and perfusion distribution, and therefore detection of malperfusion as occurs in PE.

Chapter 4

Circulatory and body gas stores modelling

4.1 Introduction

The gas stores of the lung exchange with the atmosphere via the pulmonary ventilation and with the rest of the body via the pulmonary blood flow. In terms of measurement, the ventilatory exchange is far more accessible than the exchange occurring via the blood. For this reason, both experimental and modelling studies of the lung often make simplifying assumptions in relation to the gas exchange with the blood, for example that the composition of the blood flowing into the lungs is constant and that there is no recirculation. Indeed, one of the most significant limitations of the pre-existing LNL (described in the previous Chapter) is that an unknown input to the model, mixed venous (essentially equivalent to pulmonary arterial) blood gas contents, must be estimated using a simple linear trend term.

A more complete approach to the problem would be to include a model of the circulation and systemic body gas stores which includes metabolic consumption of oxygen and production of carbon dioxide. With such an approach, gas concentrations in the blood flowing into the lung will be generated automatically from past blood-gas concentrations leaving the lungs. Regarding the LNL model specifically, modelling the circulation as a closed loop and allowing recirculation would remove the requirement to estimate the pulmonary arterial input; it would instead be generated automatically as a consequence of

previous lung inputs. This reduces the LNL model to a single input: the highly-accurately measured inspired gas (and total expired gas volume). My primary objective is to create a physiological model of this process, the circulation and body gas stores (CBGS) model [1].

There are already a considerable number of existing models of the body gas stores in the literature. These have all been generated for specific purposes. Some are concerned with carbon dioxide [32, 60] and others with inert gases [65], including anaesthetics [67, 66]. However, most do not provide a single integrated model for all gases. Furthermore, many tend to be built from hypothetical compartments whose parameters are set to values that allow a fit to measured data with little or no anatomical basis. In most cases, these models are only concerned with time scales sufficiently long that circulatory delays may be ignored [65, 29, 32, 60, 62], although there are some exceptions relating to the anaesthetic gases [67, 66].

My aim is to generate a model that has an anatomical/physiological basis to its compartments, that models both circulatory delays and gas stores, and that is applicable to both the respiratory gases and to other gases for which tissue gas solubilities can be obtained. Finally, individual humans differ substantially in size, and as a consequence in their physiology and gas storage capacity. Thus a further objective is to develop a model that can be scaled to the size and body composition of an individual. Thus in this Chapter, I seek to produce a more general purpose model that: i) is relevant for both respiratory (CO_2 and O_2) and inert gases; ii) is based firmly on anatomy and not arbitrary compartments; iii) can be scaled to individuals of different body sizes and compositions; and iv) incorporates arterial and venous circulatory delays as well as tissue volumes so that it can reflect rapid transients with greater precision. A previously published model was used for the blood gas chemistry of CO_2 and O_2 [39].

4.2 CBGS model construction and execution

4.2.1 CBGS model general description

The CBGS model consists of a set of independent body compartments, with each connected to the lung by independent parallel circulatory paths (Fig. 4.1). The

arrangement is identical for all tissues apart from the liver and gastrointestinal tract (GIT), which mimic the anatomy of the portal system (where the liver is supplied both directly by the heart and also by the blood exiting the gastrointestinal tract). The arterial and venous volumes of this circulatory system are based on reported tissue blood volumes together with data from a detailed anatomical model for the large arteries and veins. In this section I describe the model's construction, its initialisation and execution. My model must have a set of defined parameters. To do this I begin with a set of values for 'standard man'.

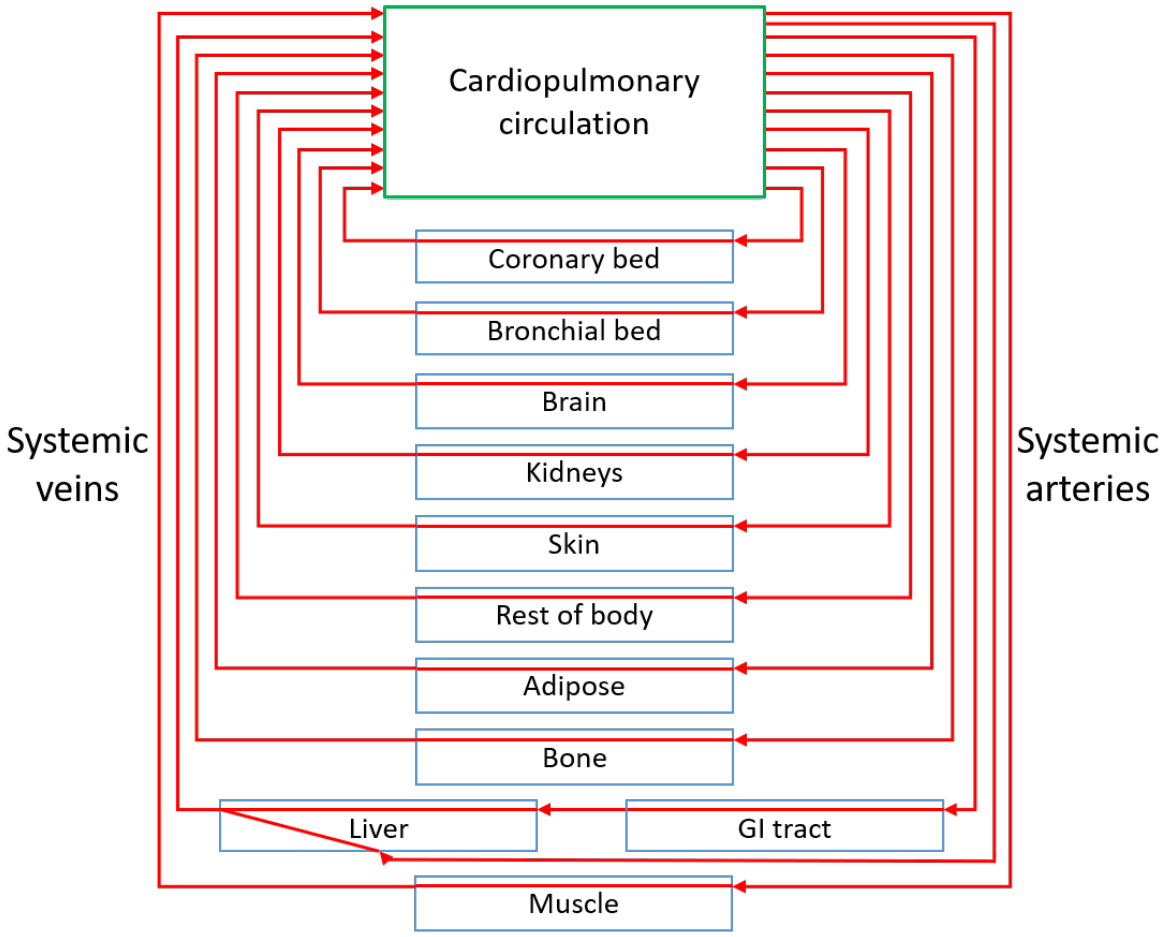

Figure 4.1. Schematic of the model of the circulatory and body gas stores. Vessels are arranged in parallel flow streams of differing lengths and perfusions. The connected tissues have differing volumes and partial-pressure to concentration storage relationships.

4.2.2 Construction of model for standard man

The compartments of my model for a standard man (male, 1.8 m tall, 70 kg mass and 25 years old) were based on data from the International Commission for Radiological Protection (ICRP) [183, 15]. Relative organ weights from [183] are as summarised in Table 7 of Brown *et al.*'s review [67]. In my model, I used a single compartment for the

gastrointestinal tract and spleen that feeds into the hepatic portal vein, and condensed the other smaller organs (adrenals, pancreas, and thyroid) into a single, rest of body, compartment. This resulted in a model with a total of 11 compartments, the details of which are given in Table 4.1. Note the model consists of 10 defined compartments with an additional 'rest of body' compartment that contains a miscellaneous mix of the remaining tissues. In order that gas concentrations could be expressed per unit volume, the volumes for each compartment were calculated by dividing the mass of each compartment by the relevant tissue density [67, 184, 183].

Table 4.1. *Circulation and body gas store (CBGS) parameter values for a standard man.*

Tissue	Mass $/kg$	Density $/kgL^{-1}$	Qf	V_c $/L$	V_a $/L$	V_v $/L$	t_D $/s$
Adipose	14.99	0.916	0.050	0.011	0.070	0.266	80.1
Bone	10.01	1.469	0.050	0.011	0.090	0.351	104.2
Brain	1.40	1.036	0.120	0.027	0.039	0.127	18.5
GI tract*	1.34	1.046	0.180	0.040	0.127	0.328	31.7
Heart	0.34	1.030	0.040	0.009	0.010	0.039	16.8
Kidneys	0.31	1.050	0.190	0.042	0.056	0.186	17.3
Liver†	1.80	1.051	0.065	0.054	0.105	0.573	130.0
Lungs‡	0.53	1.051	0.025	0.006	0.022	0.089	53.8
Muscle	28.00	1.041	0.170	0.038	0.207	0.780	69.5
Skin	2.60	1.183	0.050	0.011	0.050	0.182	56.0
Blood	5.53	1.060	NaN	NaN	NaN	NaN	NaN
ROB	3.16	1.050	0.060	0.013	0.052	0.189	49.0
Citation	[67, 183, 15]	[67, 183]	[185, 186, 187, 15]	[188, 189, 15]	[190, 191, 192]	[193, 194]	

Qf, fraction of total perfusion; V_c, capillary volume; V_a, arterial volume; V_v, venous volume; t_D, total transit time through systemic arteries, capillaries and veins for each compartment; GI, gastrointestinal; ROB, rest of body.

Reference values for the perfusion and blood volume of each tissue are as recommended by the ICRP [15] (see Section 7.7.2, p142). These were derived principally from [185, 186, 187]. The total systemic capillary volume was assumed to be 5% of the total blood volume [188, 189], and this was distributed between the compartments based on their relative perfusion. The capillary volume for each organ was subtracted from the total

*
†
‡

*The vein for the GI tract represents the portal vein supplying the liver.
†The values for the liver are for the hepatic artery and vein.
‡The perfusion and vessel values for the lungs are for the bronchial circulation only.

blood volume for that organ. This remaining volume was distributed between the arteries and veins for that compartment in a ratio of 1:3. The volumes for each compartment are summarised in Table 4.1.

In addition to the blood within the organs, there is also blood in the large arteries (6%) and veins (18%) outside of the organs [15]. This needs to be distributed across the parallel and entirely independent blood vessels of the CBGS model. Volumes for 128 segments of the major arteries were calculated from a detailed morphometric model of the arterial tree [190], as tabulated in Appendix table A.1 (details processed data used to calculate the arterial volumes). The vessel identification number provides its location in the condensed circulatory model illustrated in Fig. 4.1. These volumes were then rescaled to sum to 6% of total blood volume.

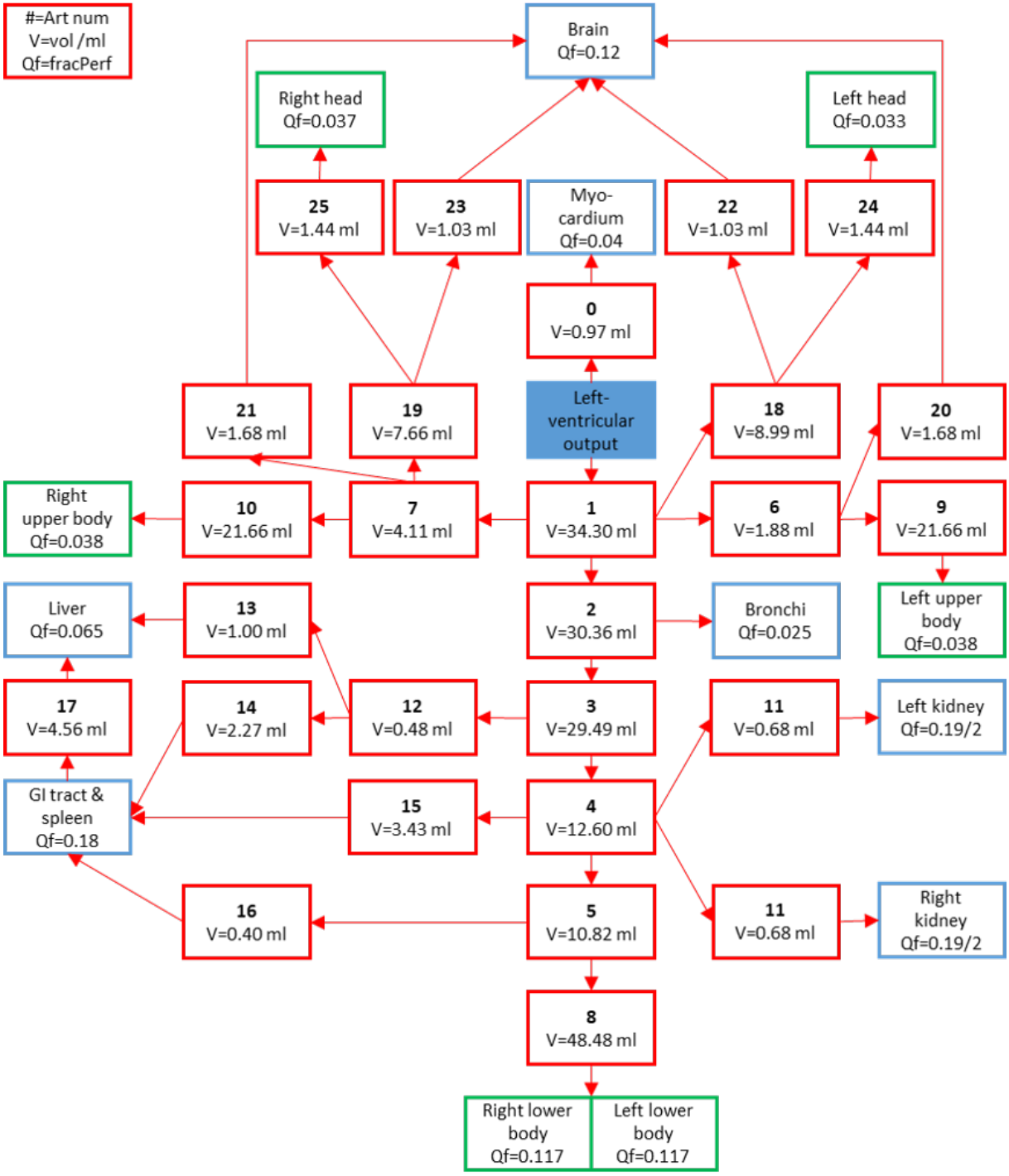

Figure 4.2. Schematic of the arterial tree used to calculate total vessel volumes for each compartment. Art num, artery number corresponding to the key used in table A.1 (Appendix); V, arterial segment volume /ml; Qf, fraction of the total perfusion supplied to the compartment. Red boxes, vessels; blue boxes, discrete tissues; green boxes, dispersed tissue sites; blue filled box, heart.

Following this, the 11 compartments were classified either as discrete tissues (heart, lungs, kidneys, liver, GI tract/spleen, brain), where their specific arteries could be identified within the arterial tree, or else as dispersed tissues (muscle, skin, adipose, bone, rest-of-body) where this was not the case. Conceptually, the discrete tissues were "attached" to their specific arteries. All other arteries were considered to supply the

dispersed tissues. The number of dispersed tissue sites was progressively reduced by merging distal arteries with their attendant dispersed tissue until it was not possible to go further without merging one of the discrete tissues (Fig. 4.2). This resulted in 5 blocks of dispersed tissue: left and right head and neck supplied by the left and right external carotid arteries; left and right arms/torso supplied by the left and right subclavian arteries (distal to origin of vertebral arteries); and lower body supplied by the left and right iliac arteries.

The blood flow for the GI tract & spleen compartment arises from multiple arteries, and therefore the compartment's total blood flow has to be apportioned between these. This apportioning was based on the blood flows to the large intestine (vessel 16, fraction of total perfusion, Qf, = 0.04), the small intestine (vessel 15, Qf = 0.1) and the stomach and spleen (vessel 14, Qf = 0.04) [15]. In a similar manner, values for the resting blood flow to the arteries supplying the dispersed tissues were taken from the literature [195]. Using these values, the following percentage distributions for perfusion of the dispersed tissue sites were calculated: right head and neck (excluding brain) 3.7%, left head and neck (excluding brain) 3.3%, left and right arms/trunk 7.6% and lower body 23.4%.

For all 128 segments of the arterial tree, the fraction of blood flow supplying each of the compartments of the CBGS model was calculated. This step allowed the blood volume for each segment of the arterial tree to be apportioned between the compartments of the CBGS model in proportion to blood flow. The total dispersed perfusion fraction that is split between these sites is equal to the sum of the dispersed tissues and the other tissues not specified in my model.

The ICRP data do not provide a break down for the different dispersed tissue types at the five sites of the model (left head, right head, left upper body, right upper body and lower body). Consequently, these five sites were condensed into one single site per dispersed tissue type.

A volume for the portal vein was calculated from its diameter [193] and length [194]. This was subtracted from blood volume in the large veins [15], and the remaining volume distributed to the compartments in proportion to arterial blood volume. The results of these calculations are given in Table 4.1. The pulmonary blood volume was treated as a single compartment with blood entering from all compartments.

Resting metabolic rates for each tissue were taken from [196]. The values in kcal/kg/d were converted to rates of oxygen consumption using a conversion factor of 4.825 kcal/L of oxygen consumed [197]. Wang *et al.* [196] gave a residual value for metabolism per unit mass for the tissues not included in their study, and this was distributed across the remaining tissues of my model.

4.2.3 Scaling the CBGS model to individuals

Individuals differ in size and body composition. To account for this, the model is scaled to a particular individual using their height, mass, sex and age. First, an estimate of fat percentage by mass, f_{fat}, is made using the following Eq. 4.2:

$$BMI = mass/height^2 \tag{4.1}$$

$$f_{fat} = \frac{1.2(BMI) + 0.23(age) - 10.8(isMale) - 5.4}{100}, \tag{4.2}$$

where BMI is body mass index, and $isMale$ is set to 0 for women and 1 for men [198]. This technique gives superior estimates of adiposity than BMI alone (Eq. 4.1 [199]).

An individual's lean body mass can then be calculated by subtracting the mass of their adipose tissue from their total body mass. This enables an individual's lean body mass and their adipose tissue mass each to be expressed as a fraction of that associated with the standard man. These fractions can then be used to produce an appropriately scaled model of the individual from the values associated with standard man and the standard man lean and fat fractions.

4.2.4 Solubilities and partition coefficients

The gases included in the model are CO_2, O_2 and N_2 together with capability for two exogenous gases, CH_4 and C_2H_2, for which rapid sensing technologies have been developed within the MFS (CH_4 and C_2H_2 measurement was not ready for testing within the time frame of this thesis). Both CO_2 and O_2 react reversibly with blood, where the total content of each gas (dissolved plus reversibly-reacted) depends upon the partial pressures of both gases. I used the model of O'Neill & Robbins to describe this

relationship which incorporates both the Bohr and Haldane effects [39].

As well as dissolving physically in the tissues, CO_2 also reversibly reacts with water to form H^+ and $HCO3^-$, and the extent to which this reaction occurs depends upon the intrinsic buffering of the cell type. I share the concerns of Cherniack and Longobardo [29] on literature reporting CO_2 tissue partition coefficients that take into account extrinsic buffering capacity through the movement of $HCO3^-$ ions across the cell membrane. Instead my solubility estimate uses $HCO3^-$ as a measure of CO_2 in the cell and assumes only intrinsic buffering (no movement of $HCO3^-$ in and out of the cell). Values for this buffering capacity are not reported for most cell types and so I adopted a value of 15 mmol/L/pH unit [200] with an intracellular water fraction of 70% as applicable for most tissues. For muscle, the value is higher, and I used the measured value of 25 mmol/L/pH unit reported for cardiac muscle [201]. The intrinsic buffer capacities were converted to apparent CO_2 solubilities using the Henderson Hasselbalch equation of the form:

$$pH = pK_a + log_{10}(\frac{[A^-]}{[AH]}) \tag{4.3}$$

here the conjugate acid term, $[AH]$, is molar equivalent to the CO_2 partial pressure, P_{CO_2}, multiplied by its solubility term a. $[A^-]$ is $[HCO3^-]$. Thus:

$$\frac{[HCO3^-]}{(aP_{CO_2})} = 10^{(pH-pK)} \tag{4.4}$$

$$[HCO3^-] = aP_{CO_2}10^{(pH-pK)} \tag{4.5}$$

With an assumed intracellular pH of 7.2 (pH of 7.04 for muscle), an initial CO_2 partial pressure, P_{CO_2}, of 40 mmHg, an acid dissociation constant, pK, of 6.1 for $H2CO3$ and a physical solubility of CO_2 in water, a, of 0.03 mmol/L/mmHg one can calculate the $HCO3^-$ concentration for muscle and other cells. Using the buffering capacities defined above, $[HCO3^-]$ will increase by 2.5 and 1.5 mmol/L for a change in pH of 0.1. One can then use eq. 4.5 to find the P_{CO_2} at this new pH point. Finally, one can then estimate the intrinsic solubility using the volume of one mole of gas at STPD (standard temperature

and pressure, dry) and the change in [$HCO3^-$] per unit of P_{CO_2}:

$$S_i = \frac{22.4}{1000}([\mathrm{HCO3^-}]^{t+1} - [\mathrm{HCO3^-}]^t)/(P^{t+1}_{\mathrm{CO2}} - P^t_{\mathrm{CO2}}) \tag{4.6}$$

where S_i is the intrinsic solubility; t indicates the value before buffering and $t+1$ the value after buffering; [$HCO3^-$] and $P_{\mathrm{CO_2}}$ are given at the first and second pH values. These apparent solubilities were added to a physical solubility for $CO2$ in the tissue that was taken as equal to the value for plasma for all tissues but fat [30]. For most tissues the fraction that is water is around 0.7 and the solubility must be scaled by this value to give an estimate of solubility in L_{STPD} gas per L of tissue.

For $O2$, its ability to react reversibly with myoglobin in muscle was ignored as the model is only concerned with P_{O_2} values where myoglobin is saturated with $O2$. For all tissues but fat, the intracellular solubility for oxygen was assumed to be equal to that in plasma.

Weathersey and Homer [30] have provided a review of inert gas solubilities in biological tissues and fluids. For setting the solubility of $N2$, $CH4$ and $C2H2$ in blood, I gave precedence to values for human blood, and to values where the investigators had also reported solubilities in water that were close to their well-established values. Most solubilities taken from this review were given as Ostwald values. The Bunsen values can be calculated by converting to standard temperature of 273.15 K by multiplying by 273.15/310. One can then convert to Henry's values by dividing by standard pressure to give values per unit pressure. For $N2$ there are some exceptions to this for fat, liver and brain where the Bunsen value is given.

For $N2$ and $CH4$, the tissue solubilities were assumed to equal the blood solubility for all tissues except brain and fat. The solubility in brain was taken as 6% higher than that for blood for $N2$ and 8% higher for $CH4$ [30]. For $C2H2$, tissue solubilities were assumed to equal the blood solubility for all tissues except fat.

The adipose compartment required special treatment for all gases. For $CO2$, a physical solubility in human fat of 1.67 times its value in water has been reported [202]. To obtain an overall solubility for adipose tissue, I assumed that the tissue was 80% fat and 20% aqueous [183], and that no proton buffering occurred in the fat element. For $N2$, the

solubility in pure body fat has been reported to be around 5 times that in water [203]. I also note that the partition coefficients between olive oil (a liquid plant fat) and water are very similar for N_2 and O_2 (at around 5). For this reason, to determine the O_2 solubility in adipose tissue (80% fat, 20% aqueous) from its solubility in water, I used the same multiplier of 4.2 (5 multiplied by 0.8) as I used for N_2. CH_4 is noticeably more soluble in blood than in water, and is around 10 times more soluble in olive oil than in water [30]. In the absence of better data, I assumed a solubility in adipose tissue 8-fold greater than in water. For C_2H_2 the oil:water partition coefficient is around 2 [30], and by the same logic, I assumed a solubility in adipose tissue of 1.6 times that in water. The overall tissue solubilities used are given in Table 4.2 in terms of L(STPD)/L(tissue)/Pa (the change in litres of gas stored per litre of tissue for a concomitant change in partial pressure of one pascal). These values are indifferent to the participant.

Table 4.2. *Gas specific values for a standard man used in the CBGS model.*

Tissue	m_{T,CO_2} $/L_{(STPD)}L^{-1}Pa^{-1}$	m_{T,O_2} $/L_{(STPD)}L^{-1}Pa^{-1}$	m_{T,N_2} $/L_{(STPD)}L^{-1}Pa^{-1}$	m_{T,CH_4} $/L_{(STPD)}L^{-1}Pa^{-1}$	m_{T,C_2H_2} $/L_{(STPD)}L^{-1}Pa^{-1}$	M_{O_2} $/L_{(STPD)}L^{-1}s^{-1}$
Adipose	$1.05x10^{-5}$	$10.78x10^{-7}$	$5.67x10^{-7}$	$2.15x10^{-6}$	$1.22x10^{-5}$	$1.08x10^{-5}$
Bone	$1.54x10^{-5}$	$2.27x10^{-7}$	$1.28x10^{-7}$	$3.48x10^{-7}$	$7.56x10^{-6}$	$2.88x10^{-5}$
Brain	$1.54x10^{-5}$	$2.27x10^{-7}$	$1.35x10^{-7}$	$3.76x10^{-7}$	$7.56x10^{-6}$	$57.57x10^{-5}$
GI tract	$1.54x10^{-5}$	$2.27x10^{-7}$	$1.28x10^{-7}$	$3.48x10^{-7}$	$7.56x10^{-6}$	$2.88x10^{-5}$
Heart	$1.70x10^{-5}$	$2.27x10^{-7}$	$1.28x10^{-7}$	$3.48x10^{-7}$	$7.56x10^{-6}$	$105.55x10^{-5}$
Kidneys	$1.54x10^{-5}$	$2.27x10^{-7}$	$1.28x10^{-7}$	$3.48x10^{-7}$	$7.56x10^{-6}$	$105.55x10^{-5}$
Liver	$1.54x10^{-5}$	$2.27x10^{-7}$	$1.28x10^{-7}$	$3.48x10^{-7}$	$7.56x10^{-6}$	$47.98x10^{-5}$
Lungs	$1.54x10^{-5}$	$2.27x10^{-7}$	$1.28x10^{-7}$	$3.48x10^{-7}$	$7.56x10^{-6}$	$2.88x10^{-5}$
Muscle	$1.70x10^{-5}$	$2.27x10^{-7}$	$1.28x10^{-7}$	$3.48x10^{-7}$	$7.56x10^{-6}$	$3.12x10^{-5}$
Skin	$1.54x10^{-5}$	$2.27x10^{-7}$	$1.35x10^{-7}$	$3.48x10^{-7}$	$7.56x10^{-6}$	$2.88x10^{-5}$
Blood	*	*	$1.44x10^{-7}$	$3.48x10^{-7}$	$7.56x10^{-6}$	-
ROB	$1.54x10^{-5}$	$2.27x10^{-7}$	$1.28x10^{-7}$	$3.48x10^{-7}$	$7.56x10^{-6}$	$2.88x10^{-5}$
Citation	[201, 200, 202, 30]	[204, 30]	[203, 30]	[30]	[30]	[197, 196]

$m_{T,X}$, tissue gas dissociation gradient for gas X; M_{O_2}, oxygen consumption; *, these are not constant and the values arise from the blood gas dissociation curves. At a standard mixed venous P_{CO_2} of 6.1 kPa and P_{O_2} of 5.3 kPa the values are approximately: 3.12 x 10^{-5} $L_{(STPD)}L^{-1}Pa^{-1}$ for CO_2 and 2.26 x 10^{-5} $L_{(STPD)}L^{-1}Pa^{-1}$ for O_2.

4.2.5 Gas exchange between circulation and body tissues

The tissue, its capillary blood and the new influx of blood are equilibrated through a set of governing equations that use the concentration to partial-pressure relationships for the

blood and tissues defined in the CBGS model setup.

4.2.5.1 Equilibration between tissue and blood for inert gases

For inert gases, the equation for conservation of matter for each gas, x, across each compartment, c, is as follows:

$$\left[V_T^c \beta_{T,x}^c + V_b^c \beta_{b,x}\right] \frac{dP_{v,x}^c}{dt} = \dot{Q}^c \beta_{b,x} (P_{a,x}^c - P_{v,x}^c) \tag{4.7}$$

where V_T^c is the tissue volume for compartment c; $\beta_{T,x}^c$ is the solubility for gas x in the tissue of compartment c; V_b^c is the volume of blood in the capillaries for compartment c; $\beta_{b,x}$ is the solubility for gas x in blood; $P_{v,x}^c$ is the partial pressure of gas x in the capillary/venous blood of compartment c; t is time; $\dot{Q}^c$ is the perfusion to compartment c; and $P_{a,x}^c$ is the partial pressure of gas x in the arterial blood supplying compartment c.

Inert gases, including nitrogen, have a simple linear partial-pressure to concentration relationship in the blood and between blood and tissue. Thus the partial pressure is solved using the simple governing equation (eq. 4.8) to find the partial-pressure that satisfies a full equilibration between the capillary blood and tissue.

$$P_{gas}^c = \frac{A_{\Delta b}^c + A_T^c + A_b^c}{(\beta_b (V_b^c + V_{\Delta b}^c) + \beta_T^c V_T^c)} \tag{4.8}$$

Where for compartment c: P_{gas}^c=equilibrium partial pressure for inert gas; $A_{\Delta b}^c$=quantity of gas in the inflowing blood; A_T^c=quantity of gas in the tissue store; A_b^c=quantity of gas in the capillary blood in the tissue; β_b=slope for the P_{gas}^c-concentration relationship for the blood; β_T^c=slope for the P_{gas}^c-concentration relationship for the given tissue; V_b^c=capillary blood volume; $V_{\Delta b}^c$=inflow blood volume; V_T^c=tissue volume.

The tissue and blood concentrations that satisfy the equilibrium partial pressure are then calculated using:

$$C_T^c = \beta_T^c P_{gas}^c (t+1) \tag{4.9}$$

4.2.5.2 Equilibration between tissue and blood using the blood model

The exchange for CO_2 and O_2 is coupled through the Bohr and Haldane effects. As a result, both the CO2 and O2 must be considered together when converting between their partial pressures and concentrations due to the complex interplay in their relationship, namely the Bohr and Haldane effect. The total content of *gas* in tissue c and its capillary supply (T^c_{gas}) at time $(t+1)$ is dependent upon the prior total content accounting for the influx ($\dot{Q}^c_a C^c_{a_{gas}}(t+1)$), outflux ($\dot{Q}^c_v C^c_{v_{gas}}(t)$) and metabolism ($\Delta t.m^c_{gas}$) that occurs over the timestep, see equation 4.10 (N.B. $\dot{Q}^c_a = \dot{Q}^c_v$ and is simplified to: $\dot{Q}^c$).

$$\begin{bmatrix} T^c_{CO_2}(t+1) \\ T^c_{O_2}(t+1) \end{bmatrix} = \begin{bmatrix} T^c_{CO_2}(t) + \dot{Q}^c C^c_{a_{CO_2}}(t+1) - \dot{Q}^c C^c_{v_{CO_2}}(t) + \Delta t.m^c_{CO_2} \\ T^c_{O_2}(t) + \dot{Q}^c C^c_{aO_2}(t+1) - \dot{Q}^c C^c_{vO_2}(t) + \Delta t.m^c_{O_2} \end{bmatrix} \tag{4.10}$$

where $C^c_{a,x}$ is the arterial concentration of gas x (here CO_2 or O_2) supplying compartment c; $C^c_{v,x}$ is the capillary/venous concentration of gas x leaving compartment c; and m^c_x is the metabolic production or consumption for gas x in compartment c.

So conservation of matter across each compartment can be given as follows:

$$\begin{aligned} &\begin{bmatrix} V^c_T \beta^c_{T,\mathrm{CO2}} + V^c_b \frac{\partial C^c_{v,\mathrm{CO2}}}{\partial P^c_{v,\mathrm{CO2}}}\Big|_{P^c_{v,\mathrm{CO_2}}, P^c_{v,\mathrm{O_2}}}, & V^c_b \frac{\partial C^c_{v,\mathrm{CO2}}}{\partial P^c_{v,\mathrm{O2}}}\Big|_{P^c_{v,\mathrm{CO_2}}, P^c_{v,\mathrm{O_2}}} \\ V^c_b \frac{\partial C^c_{v,\mathrm{O2}}}{\partial P^c_{v,\mathrm{CO2}}}\Big|_{P^c_{v,\mathrm{CO_2}}, P^c_{v,\mathrm{O_2}}}, & V^c_T \beta^c_{T,\mathrm{O_2}} + V^c_b \frac{\partial C^c_{v,\mathrm{O2}}}{\partial P^c_{v,\mathrm{O2}}}\Big|_{P^c_{v,\mathrm{CO_2}}, P^c_{v,\mathrm{O_2}}} \end{bmatrix} \begin{bmatrix} \frac{dP^c_{v,\mathrm{CO2}}}{dt} \\ \frac{dP^c_{v,\mathrm{O2}}}{dt} \end{bmatrix} \\ &= \begin{bmatrix} \dot{Q}^c C^c_{a,\mathrm{CO2}}(P^c_{a,\mathrm{CO2}}, P^c_{a,\mathrm{O2}}) - \dot{Q}^c C^c_{v,\mathrm{CO2}}(P^c_{v,\mathrm{CO2}}, P^c_{v,\mathrm{O2}}) + m^c_{\mathrm{CO2}} \\ \dot{Q}^c C^c_{a,\mathrm{O2}}(P^c_{a,\mathrm{CO2}}, P^c_{a,\mathrm{O2}}) - \dot{Q}^c C^c_{v,\mathrm{O2}}(P^c_{v,\mathrm{CO2}}, P^c_{v,\mathrm{O2}}) - m^c_{\mathrm{O2}} \end{bmatrix} \end{aligned} \tag{4.11}$$

The blood partial pressures are estimated using the blood model:

$$P^c_{v,\mathrm{CO2}} = f(C^c_{v,\mathrm{CO2}}, C^c_{v,\mathrm{O2}}) \tag{4.12}$$

$$P^c_{v,\mathrm{O_2}} = g(C^c_{v,\mathrm{CO_2}}, C^c_{v,\mathrm{O_2}}) \tag{4.13}$$

where f and g are blood gas lookup table functions.

Due to the complex nature of the concentration to partial pressure relationship of the blood and the linear relationship in the tissues it is not possible to easily calculate the equilibrium partial pressure when a bolus of differing concentration is added. One

could estimate it accurately using an optimisation routine but this would be too slow for my purposes. Instead I use a 2D Newton-Raphson approximation to estimate the new equilbrium partial pressure (4.14-4.17).

$$x_{n+1} = x_n - \frac{f(x)}{f'(x)} \tag{4.14}$$

$$f(x) = \begin{bmatrix} \frac{C^c_{CO_2}(P^c_{CO_2},P^c_{O_2}).V^c_b + \beta^c_{T,CO_2}.V^c_T.P^c_{CO_2}}{V^c_b} - \frac{T^c_{CO_2}(t+1)}{V^c_b} \\ \frac{C^c_{O_2}(P^c_{CO_2},P^c_{O_2}).V^c_b + \beta^c_{T,O_2}.V^c_T.P^c_{O_2}}{V^c_b} - \frac{T^c_{O_2}(t+1)}{V^c_b} \end{bmatrix} \tag{4.15}$$

$$f'(x) = \begin{bmatrix} \frac{\partial C^c_{CO_2}}{\partial P^c_{CO2}} + \beta^c_{T,CO_2}.\frac{V^c_T}{V^c_b}, & \frac{\partial C^c_{CO_2}}{\partial P^c_{O_2}} \\ \frac{\partial C^c_{O_2}}{\partial P^c_{CO_2}}, & \frac{\partial C^c_{O_2}}{\partial P^c_{O_2}} + \beta^c_{T,O_2}.\frac{V^c_T}{V^c_b} \end{bmatrix} \tag{4.16}$$

$$\begin{bmatrix} P^c_{CO_2}(t+1) \\ P^c_{O_2}(t+1) \end{bmatrix} = \begin{bmatrix} P^c_{CO_2} \\ P^c_{O_2} \end{bmatrix} - \Big[f'(x)\Big]^{-1} \Big[f(x)\Big] \tag{4.17}$$

Where all the partial pressures are at time (t) unless specified otherwise.

Again tissue and blood concentrations that satisfy the equilibrium partial pressure are calculated using:

$$\begin{bmatrix} C^c_{vCO_2}(t+1) \\ C^c_{vO_2}(t+1) \end{bmatrix} = \begin{bmatrix} \frac{T^c_{CO_2}(t+1) - \beta_{T,CO_2}.V^c_b.P^c_{CO_2}(t+1)}{V^c_b} \\ \frac{T^c_{O_2}(t+1) - \beta_{T,O_2}.V^c_b.P^c_{O_2}(t+1)}{V^c_b} \end{bmatrix} \tag{4.18}$$

$$C^c_T = \beta^c_T P^c_{gas}(t+1) \tag{4.19}$$

In this thesis the blood gas model of O'Neill and Robbins [39] is used to convert between: i) paired partial pressures of carbon dioxide and oxygen to their concentrations and ii) paired concentrations of carbon dioxide and oxygen to their partial pressures. However, it is possible to use the CBGS model with any other blood gas model with similar capabilities.

4.2.6 Setting initial conditions

To initialise the model under steady-state conditions, it is sufficient to know arterial blood gas contents for CO2, O2 and N2. The entire arterial tree is assumed to have a uniform concentration. This blood fills the arterial tree, and the metabolic exchange

and blood flow to the individual tissues determines the tissue stores and venous blood concentrations for each compartment. The connected tissue capillary blood is assumed to be in equilibrium with its venous outflow. If the mixed venous rather than the arterial concentration is known, the arterial concentration is easily calculated from the cardiac output and the total metabolic oxygen consumption and carbon dioxide production of the tissues:

$$C_a^c = \frac{\sum \dot{Q}^c C_v - \sum M_x^c}{\sum \dot{Q}^c} \tag{4.20}$$

where C_a^c is the arterial concentration for compartment c and gas x; C_v is the mixed venous gas concentration for gas x; $\dot{Q}^c$ is the perfusion to compartment c and M_x^c is the metabolism for compartment c and gas x.

Then working forwards in the direction of blood flow one can simply calculate each individual compartment's venous concentration using each individual tissue metabolism and perfusion.

The initialisation procedure for the tissue gas contents requires finding the venous blood partial pressure using the blood table lookup. I assume the compartments are in equilibrium with the venous blood exiting them so concentrations of $CO2$ and $O2$ ($C^c_{v,CO2}$, $C^c_{v,O2}$) in the compartment are calculated from these partial pressures according to the tissue solubility (eq. 4.19). The issue is that, when I start to run the model, the one step Newton-Raphson approximation begins to change the amounts of $CO2$ and $O2$ in the compartment very slightly. As a result, the compartmental venous concentrations for $CO2$ and $O2$ also start to change. This is typically much smaller than 1 percent and does not compromise conservation of mass (as it only changes the ratio of gas stored in tissue versus blood). Nevertheless, I sought to eliminate this.

When using the Newton-Raphson approximation there is a complication that one must account for as the approximation does not converge on the final value immediately. So a single calculation from arterial values through the tissue to give venous values will give a mixed venous and tissue value which will slowly shift towards the convergent value (N.B. the difference is very small). Multiple iterations, a 'burn-in', of the Newton-Raphson approximation could be used to converge closer to the model's equilibrium

concentrations. However, a better solution would be to find the starting concentration for CO_2 and O_2 in each compartment that generates the convergent end point for the compartmental venous blood values. To solve this problem the one-step Newton-Raphson approximation was embedded within a non-linear solver (I utilised the Matlab function fmincon) that minimises: $(C^c_{v,\mathrm{CO_2}}solver - C^c_{v,\mathrm{CO_2}}exact)^2$ and $(C^c_{v,\mathrm{O_2}}solver - C^c_{v,\mathrm{O_2}}exact)^2$, by varying the initial compartmental tissue concentrations for CO_2 and O_2 until the correct concentrations are found. The initial guesses for the starting tissue concentration for the non-linear solver are calculated as before using eq. 4.19. The objective function comprises a single 10 ms perfusion step for my Newton-Raphson solver. The model is executed with the blood flow in and out of the capillary. The update for the tissue concentrations for CO_2 and O_2 and for the $C^c_{v,\mathrm{CO_2}}$ and $C^c_{v,\mathrm{O_2}}$ is then calculated. The non-linear solver then progressively adjusts $C^c_{t,\mathrm{CO_2}}$ and $C^c_{t,\mathrm{O_2}}$ until the $C^c_{v,\mathrm{CO_2}}$ and $C^c_{v,\mathrm{O_2}}$ from the solver exactly match the values for the given tissue metabolism and blood flow.

If it is desirable to depart from either the standard metabolic rate or cardiac output specified by the model for an individual, it is necessary to apportion these variations across the tissues of the model. In the case of moderate exercise, it is reasonable to focus any increase in blood flow or metabolism on skeletal muscle (in heavy exercise, there will be some reductions in the perfusion of other organs). Variations in metabolic rate at rest are likely to arise predominately from fluctuations relating to the digestion, absorption and metabolism of food. Although somewhat arbitrary, I chose to ascribe 60% of any variation in metabolic rate to the GI tract, liver and skeletal muscle, and apportion the remaining 40% across all other tissues in relation to their existing metabolism. As blood flow tends to follow metabolism, I used the same approach for distributing variations in cardiac output.

4.2.7 CBGS execution

To run the model within a closed-loop circulation, some model of the lung is required to alter the composition of the mixed venous blood as it flows across the pulmonary circulation and back into the systemic arterial tree. Thus, for a given time step a small bolus of blood is drawn from the pulmonary blood volume, equilibrated as appropriate to provide the new blood gas contents, and then during execution, the blood is passed into

the segments of the arterial tree in proportion to their share of total blood flow. For each compartment an equivalent amount of blood is drawn from the distal end of the arterial tree, this enters the capillary bed for the compartment and displaces an equal volume of blood into the associated vein. The new capillary blood is mixed with the remaining capillary blood and then the gases are equilibrated between blood and tissue according to Eq. 4.7 & 4.11. Finally, the blood added to the veins in each compartment is used to displace equal volumes from the central ends of the veins, and is then mixed with the pulmonary blood volume. The ultimate result for that iteration being the same volume of blood exiting from the systemic venous side of the circulation with an estimate of mixed venous blood concentration (Fig. 4.3).

4.2.7.1 Modelling blood flow using plug flow

It is crucial that mass is conserved throughout this process. The movement of blood is modelled using plug flow, defined by an idealised uniform velocity of flow across the cross-section of the vessels. This simple flow profile is used in the airways of the LNL [9] and others [205]. To compute perfusion delays using this flow model I employed the method of characteristics [206].

In practice this is achieved by treating the vessels as a set of inelastic pipes split into separate blocks for each with their own blood volume and gas concentrations. The input bolus volume is dependent upon the chosen time period for each iteration, the cardiac output and the fractional perfusion to that compartment. For my work this is repeated every 10 ms time period (matching the measurement frequency of the MFS device) but could be solved for any given time period.

The main problems associated with modelling convection delays in this case are that the volume of gas or blood are not necessarily constant from one bolus/time-step to the next, and the volumes of the pipes themselves are not necessarily integral multiples of the volume of blood in each time step (even if this were constant).

The approach I adopt to modelling these phenomena is to split the vessels into varying segmental blocks (Fig. 4.3). These are represented by arrays of gas contents and blood volumes that ascend cumulatively in the opposite direction to the flow of blood. This allows the incoming bolus of blood's volume and content to be simply summed to the

existing cumulative volumes and contents via concatenation. The volume exiting the vessel will be the same as the input, as I assume no vessel compliance. To estimate the content that will exit the other end of the vessel I use the known transitory blood volume to undertake linear interpolation along the cumulative volume segment on the output end of the vessel and sum with any other segment gas contents that entirely exit the vessel to give the total gas content output. This interpolation will stop short at precisely the volume of the pipe, leaving a new array to drive the next simulation interval.

The next step is to supply the volume and content output from the arterial system to the tissue. During the first step a blood bolus of volume equivalent to the input volume and the starting, previously equilibrated, gas concentrations leave each tissue compartment into the veins. The volume input and output for each 10 ms timestep is adequately small compared to the overall tissue capillary volume that this is a reasonable assumption.

The tissue, its capillary blood and the new influx of blood are then equilibrated through the governing equations that use the concentration to partial-pressure relationships for the blood and tissues to compute the new equilibrium partial pressure as described in the previous section. Nitrogen has a simple linear partial-pressure to concentration relationship in both the blood and tissues so the equilibrium partial pressure can be solved analytically (Eq. 4.7). Conversely, both the CO_2 and O_2 must be considered together when converting between their partial pressures and concentrations due to the complex interplay in their relationship. This conversion is solved numerically using a model of CO_2 and O_2 gas carriage by the blood previously developed by our group [39]. Furthermore, due to the complex nature of the concentration to partial pressure relationship of the blood and the linear relationship in the tissues it is not possible to easily calculate the equilibrium partial pressure when a blood bolus of differing concentration is added and must equilibrate with blood and tissue. Instead a 2D Newton-Raphson approximation is used to estimate the new equilibrium partial pressure (Eq. 4.11).

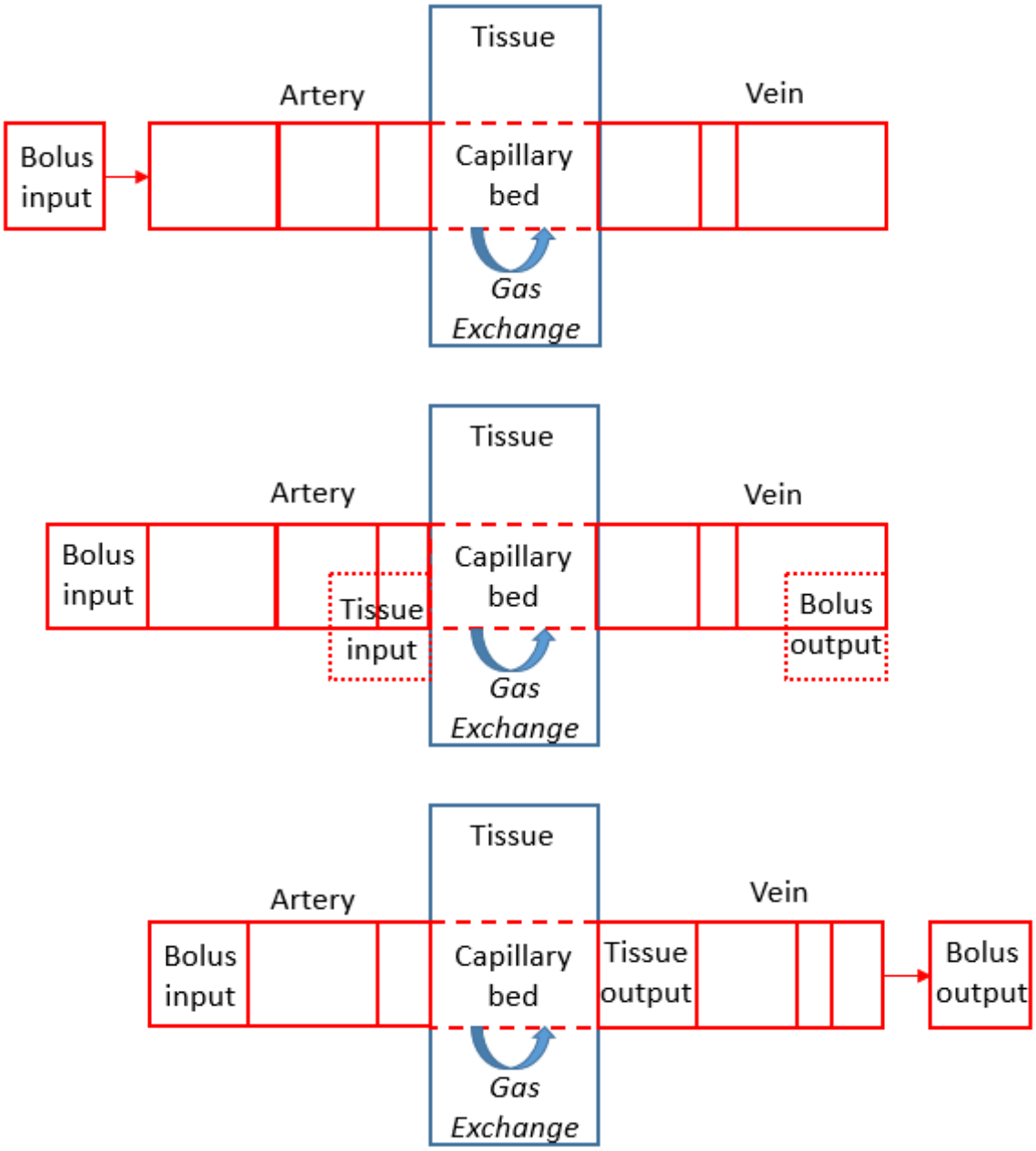

Figure 4.3. Schematic of the segmental flow for one tissue within the CBGS model. Red rectangles represent individual blocks of blood in the arteries and veins, each with their own volume and gas content. Shown here are three steps: i) a bolus of blood is added to the arterial circulation, ii) a volume of blood equivalent to the input bolus is moved from the arterial circulation into the tissue and equilibrated, iii) a bolus of blood (of equal volume to the input) is removed from the venous end of the circulation.

The new tissue and blood concentrations that satisfy the equilibrium partial pressure are then calculated. On the venous side, plug flow and the method of characteristics are again employed, giving the final blood concentration and volume output from the veins for that iteration of the run. The only peculiarity is the GIT-hepatic circulation. Blood is pumped through the GIT and equilibrated before being pumped into the liver through a portal vessel. In the liver the portal blood mixes with the blood pumped directly through

the hepatic artery before equilibrating. The summed volume from both inputs leaves via the hepatic vein (Fig. 4.1).

Using an array with 100 columns (equivalent to one second of blood flow), the model runs 20 times faster than real time. Thus it takes 3 minutes to simulate one hour of circulation.

4.2.8 CBGS implementation

The model was written in Matlab and will run on a standard Windows (or other) desktop. The circulation is first established as an object. The model input is an array, where the columns contain the cumulative blood volumes (based on the blood flow) and gas contents. Each row reflects an aliquot of blood and I chose to work with aliquots based on a fixed 10 ms step size for the simulation. However, the model can be given any time period. The output is an array of the same dimensions supplying the cumulative venous outflow volumes (which are the same as for the input) and the cumulative venous gas contents. If it is desired to run the model as a closed loop circulation, the model can be interfaced with any lung model that is capable of supplying the pulmonary venous outflow and receiving the pulmonary arterial inflow in the form described. The venous output can be mixed back into a pulmonary blood volume, if required.

4.3 CBGS discussion

The general purpose of developing the CBGS model was to provide a means to convert open system models for studies of gas exchange in the lung to closed system models, where the composition of blood leaving the lungs can subsequently determine the composition of blood returning to the lungs. In particular, I sought to develop a model that was related to anatomy and tissue type, that could be scaled to overall body size, that was relevant to both the respiratory gases and inert gases, and that included circulatory transit times as well as tissue storage capacities.

There is an immense amount of detail that relates to the circulation of blood through the body. It supplies many different organs via a complicated branching network for both the arterial and venous trees. The approach adopted in this work was pragmatic, and was

to focus on just the major organs and the anatomy of the major arteries and veins. A further limitation of the model is that, while it captures inhomogeneity between organs, it does not capture inhomogeneity within organs. For example, there is no distinction between cortical and medullary blood flow in the kidney, or between epicardial and endocardial blood flow in the myocardium. In addition, the dispersed organs are treated as having the same great vessel path length despite the fact that some of the tissue is close to the heart and other parts lie distally in the limbs. Overall, it is hard to determine how significant this missing inhomogeneity is to the overall results, although it is clear that this type of error will lead to the model predicting more rapid equilibration of gases than would be the case in practice. Ultimately, it rests with validation studies to determine whether the model is sufficiently realistic for its purpose, or whether additional detail or refinement is required.

The ICRP [15] provided a useful starting point for tissue masses, together with their blood contents and blood flows. Furthermore, the tissue solubilities for nitrogen and oxygen are fairly well characterised. The same is not true for carbon dioxide, where early attempts to measure tissue storage capacities gave rather variable results that depended on equilibration time [29]. Carbon dioxide reacts with water to form bicarbonate and protons. The latter can be buffered intracellularly, and this in turn is likely to give rise to transmembrane ion fluxes that may underlie the somewhat variable results. Indeed, in relation to intracellular buffering, Roos and Boron [207] wrote, "Thus estimates [of buffering power] that are contaminated by ion fluxes lack definition and have meaning only when the experimental conditions are carefully defined". For this reason, I chose to work from estimates of intrinsic buffering power where such potential shifts had been minimised. Of course, in-vivo such ion fluxes will begin even over relatively short timescales including over minutes such as in my investigations. However, these mostly exchange the buffer task from intracellular to extracellular or vice-versa. As such ignoring these should not affect the overall buffing capacity within my model. One possibility would have been to adopt or develop a detailed model of exchange between the intracellular and interstitial compartments, and between the interstitial compartments and blood, such as those by Rees and Andreassen [208] and Wolff [209]. However, many of the parameters required for such models are not well described, and over the relatively short timescales with which

my model is concerned (~ 10 minutes), these ion shifts tend more to redistribute the 'site' of CO_2 storage, rather than fundamentally change the overall carbon dioxide storage capacity. Over longer time scales (~ hours), slower processes like CO_2 storage within bone matrix or bicarbonate excretion by the kidney become more important and these will be affected by such transmembrane ion fluxes. However, these aspects of CO_2 storage are not very significant over the relatively short time courses with which I am concerned.

There are other methods of calculating solubility values from other pieces of literature. For CO_2 tissue compartment dissociation gradients there are previous experimental measurements [32]. These form the basis for some previous CO_2 storage models. Preliminary work with my model showed reasonable fitting to literature and experimental work only when these values were reduced by half. This is in line with recommendations by Cherniack & Longobardo who suggest these whole tissue literature values are too high [29]. The literature also reports values for nitrogen blood-tissue partition coefficients. As my model uses tissue volumes (derived from literature tissue masses and densities) I can covert partition coefficients to dissociation gradients by multiplying by the measured solubility of nitrogen in blood: 0.0146(L/L/atm) [65, 210]:

$$\frac{C^T_{N_2} : C^B_{N_2}}{C^B_{N_2}} : P_{N_2} = C^T_{N_2} : P_{N_2} \tag{4.21}$$

These give values similar to those assigned in my method section. I could not find other sources in the literature for oxygen dissociation gradients. Models that do use oxygen simply use the solubility of oxygen in blood serum: $2.285\text{x}10^{-7}$ (L/L/Pa) [204].

The model has been designed so that it can be used with inert gases other than nitrogen provided that the relevant solubilities are known. These have been collated for a number of the more common gases [30]. Where these are not known, one possible approach is to use a theoretical calculation of the tissue partition coefficients, such as that developed by Abraham *et al.* [211, 212]. However, for a few cases where the experimental values were known, I found that the theoretical calculation was not very precise, and indeed it could be better just to assume that the blood-tissue partition coefficient was unity. Thus a major limitation with introducing gases into the model lies with uncertainly around their solubility coefficients, especially in those cases where the solubility in different tissues has

never been measured.

Inert gas have frequently been used because of their greater solubilities, and it is interesting to note that they have been used in particular for estimating cardiac output on the basis of their uptake from the lung. Here, a particular problem with this method is the rapid appearance of tracer gas recirculating back to the lungs from the tissues. An examination of Table 4.1 shows that the blood flowing to the kidneys is 19% of total blood flow and has a systemic circulation time of just 11 s. Furthermore, the blood flow to the kidneys is ~ 3 times their total weight every min, which means that tissue gas concentrations will change extremely rapidly to follow any change of concentration in the arterial blood. This emphasises the importance of the cardiac output in the CBGS model, but also illustrates a potential use of the model to account for the recirculation of tracer gas in these techniques to measure cardiac output. This thesis will not utilise the model's CH_4 and C_2H_2 capability but it will form the basis of future work.

The model of [190] provided the starting point for the arterial tree. One of the tasks in developing my model was to find an appropriate way to convert this branching model into the simpler system of a set of independent, parallel circulations to the chosen tissue types of the model. One unavoidable inaccuracy of this approach is the loss of an interdependence in the blood flows, whereby an increase in blood flow to one tissue will also reduce the circulation times for other tissues which have large arteries and veins in common. In retrospect, it would have been possible to maintain a branching structure for the very largest arteries and veins. Fortunately, the blood volumes and therefore transit delays for these are not so very large, e.g. 3.5% for the aorta.

Another approximation of the model is the condensing of the distributed tissues into single compartments, where the reality is that the circulatory lag times will vary substantially with actual anatomic location. Indeed, even with the discrete tissues there will be inhomogeneity in blood flow within them, for example between the cortex and medulla of the kidney. Some of these approximations will matter more than others, and future studies could approach this by conducting sensitivity analyses to see how important they are for different scenarios and gases.

4.4 Combining the CBGS with the LNL

The CBGS can be connected to any model of the lung in order to convert the CBGS venous output into a CBGS arterial input and create a closed circulatory system. For much of my work I combine the CBGS with the LNL, replacing the prior simple open circulation [9] (described in the previous Chapter).

The LNL is already set up to take mixed venous values, equilibrate them with its lung units and output an arterial value. It previously did this through a simple open circulation loop process outlined in the previous Chapter. All previous LNL body gas storage modelling was replaced by the CBGS. Combining the two models is then trivial if a pulmonary blood volume 'bin' is included. For each defined breath, a bolus of blood is removed from this 'bin' and added to the LNL whilst the CBGS output is added to it and mixed. The value for this blood bin is 19.5% of the participants estimated blood volume taken from the ICRP report's [15] values for heart (0.09) and pulmonary (0.105) blood volumes. The LNL pulmonary venous output is then fed into the CBGS to complete the closed circulatory system.

Once the standard man values have been adjusted to the individual's characteristics the initial state of the CBGS can be set by the LNL. This is determined by MFS measurements and the estimated parameter set from the LNL for that iteration of the non-linear optimisation routine. The initial mixed venous content, gas metabolisms and cardiac output are part of the overall LNL optimisation routine so can be used as an input here.

4.5 CBGS summary

A model for the body gas stores has been generated that is applicable to both the respiratory gases (CO_2 and O_2) and inert gases. It is based on anatomical details for organ volumes and blood contents together with anatomical details of the large arteries. It can be scaled to the body size and composition of different individuals. The model enables mixed venous gas compositions to be predicted from the systemic arterial compositions.

Chapter 5

Circulatory and body gas stores model validation

5.1 Introduction

An ideal approach to validation of the CBGS model (described in the previous Chapter) would be to vary the alveolar gas composition in a set of volunteers, and then to measure sequentially the composition of the mixed venous blood as it returns to the lungs. These sequential measurements could then be compared with those predicted by the model. However, the measurement of mixed venous composition is an invasive procedure that requires a catheter in the pulmonary artery, and this is difficult to justify ethically in healthy volunteers. As a result, model validation has proceeded by simulating experiments from the literature to determine whether the model can predict their reported results and by undertaking experimental studies where the output variable is respired gas exchange rather than mixed venous content. Each gas was validated separately.

One of the most important questions to be addressed was whether the CBGS model, when combined with the LNL model, could reproduce our MFS experimentally measured changes in expired gas fractions. Reliable estimates of gas storage and circulation in healthy humans were crucial for my proposed PE diagnostic technique to work.

5.2 Methods

In this section the process for model validation using both literature and experimental methods for nitrogen, carbon dioxide and oxygen are described [1].

5.2.1 Simulation of previously reported studies

The CBGS was used to simulate literature experiments where body gas stores are in flux for either nitrogen or carbon dioxide. In the case of CO_2, apneic oxygenation with tracheal clamping was simulated and for N_2, a nitrogen washout in dogs was simulated.

5.2.1.1 Nitrogen literature measurements

In the case of N_2, Groom *et al.* [213] provide experimental data for the mixed venous concentration of nitrogen in dogs at two time points following the introduction of pure oxygen in the inspirate. These values could be compared with those obtained by simulating the introduction of pure oxygen into a lung using our model. This was approximated using a simple alveolar step change from normal air to pure oxygen. In addition, Baker and Farmery [65] provide a simple four compartment model for nitrogen stores in humans with which the CBGS model results may be compared.

5.2.1.2 Carbon dioxide literature measurements

With respect to CO_2 carriage and storage, there are a number of reports describing the rate of increase of arterial P_{CO_2} that occurs during anaesthesia under conditions of apneic oxygenation, with sequential values reported by Stock *et al.*[214]. This rise is predominantly determined by the storage of CO_2 in the tissues, and can be simulated by the CBGS model. In this case the values for cardiac output and metabolism in the CBGS model were adjusted to match those for an average human under anaesthesia [215, 216]. Initial gas concentrations were set by equilibrating the arterial blood with high oxygen, whilst keeping CO_2 at normal levels [214]. This was to reproduce the high oxygen ventilation prior to apnea [214]. A simplified homogeneous lung, with alveolar P_{CO_2} and P_{O_2} to match the arterial concentrations, was then sealed at a supine functional residual capacity (FRC) lung volume of 2.2 L [217]. The lung was sealed to reproduce the

tracheal clamping in this experiment [214]. The time course for the rise in the systemic arterial P_{CO_2} was computed from the model, and this could then be compared with the experimental results.

5.2.1.3 Oxygen literature measurements

I was unable to identify any suitable data from the literature with which to validate the oxygen stores of the model.

5.2.2 Experimental validation

All experimental work on human participants was carried out in accordance with the general principles of the declaration of Helsinki, with ethical approval obtained from the South Central Oxford A Research Ethics Committee (reference number 17/SC/0172). All participants provided written informed consent prior to the study. Body gas stores were experimentally manipulated through various interventions: hyperventilation and rebreathing for CO_2, and multiple nitrogen breaths for O_2.

5.2.2.1 Data collection

For each validation experiment, three participants were studied. In the case of the oxygen validation experiment, one of these participants was not available and another was therefore substituted. The physical characteristics of the participants are given in Table 5.1. Participants were asked to refrain from food two hours prior to study to avoid post-prandial changes in metabolic rate and acid-base balance. Experimental studies were conducted using a MFS device to provide highly accurate, highly precise measurements of gas exchange (see [8] and Chapter 3). Experiments were carried out with participants connected to the MFS via a mouthpiece and with a nose clip to ensure all respiratory gas passed through the measurement head.

Table 5.1. *Participant characteristics*

Participant	Sex	Height /m	Weight /kg	Age /yr	FRC $/L_{(BTPS)}$	A-a O_2 gradient /kPa
#1	M	1.85	80	25	4.63	1.23
#2	M	1.79	90	39	2.08	0.78
#3	M	1.84	71	34	4.49	1.00
#4	F	1.65	57.5	22	2.33	0.69

5.2.2.2 Nitrogen perturbations

The lung contains large amounts of nitrogen which constitute a large proportion of the total body gas store. Consequently, the tissue body gas stores cannot be easily investigated until the lung gas stores have been cleared. No experimental validation was attempted for N_2 because the contribution from the lung gas stores associated with any change in inspired N_2 would swamp the exchange with blood until a new steady state for lung gas stores was established, and after that period the magnitude of the N_2 exchange with the blood would be too close to the limits of precision for the molecular flow sensor (even for a complete washout of N_2 with pure O_2) [8].

5.2.2.3 Carbon dioxide perturbations

Two validation experiments were conducted for CO_2. The first of these involved increasing CO_2 to above normal by rebreathing gas contained within a 6 litre anaesthetic bag. The bag was filled to a volume of ~ 4 litres with a mix of O_2 and CO_2 such that the CO_2 partial pressure matched the mean end-tidal CO_2 measured during the air phase of the Mountain *et al.* [9] protocol. This was to ensure the bag's starting CO_2 partial pressure was close to the participants starting concentration of arterial carbon dioxide (around 5%) but otherwise fully oxygenated to barometric pressure. The participant end-tidal and arterial partial pressures are assumed to be close to equilibrium. The participant was connected via a mouthpiece and nose clip to the MFS, whose outlet connected to a two way tap and the anaesthatic bag. The experiment began with the participant breathing room air through the apparatus mouthpiece for 5 min, after which rebreathing was started at the end of expiration, at FRC, by switching the inspirate from air to rebreathing from

the bag. Rebreathing from a limited reservoir combined with the effect of metabolism causes a dynamic perturbation in gas concentrations inspired and thus retention of CO_2 in the body over time, providing a sound test for our CBGS model using the MFS. The initial air-breathing period allowed a measure of resting metabolism to be gathered.

The second validation experiment for CO_2 involved decreasing the CO_2 to below normal by asking the participant to undertake a period of voluntary hyperventilation. The participant breathed normally for 5 min and then was asked to increase their tidal volume and breathing frequency to target an end-tidal partial pressure for CO_2 of 3.33 kPa. The breathing rate was then adjusted to clamp the end-tidal partial pressure for CO_2 to this value for a further 10 minutes. In contrast to rebreathing, hyperventilation induces progressive loss of CO2 from the lungs by drawing CO_2 out of the pulmonary circulation and thus causing a drop in body gas stores.

5.2.2.4 Oxygen perturbations

A single validation experiment was performed for the oxygen stores. As the primary store of oxygen is that bound to haemoglobin in the circulating blood, and as the arterial blood is close to fully saturated with oxygen during air-breathing, the required experiment is one that reduces the oxygen saturation of haemoglobin in the blood. Therefore, the protocol involved reducing the oxygen in the lungs by washing it out with a hypoxic gas mixture. The most straightforward way of achieving this is with elevated nitrogen. The protocol started with the participant breathing room air for 5 min such that their metabolic oxygen consumption could be estimated. The inspired gas was then switched to pure nitrogen for 2-3 breaths prior to being changed to a mixture containing oxygen at ~ 10 kPa for ~ 3-4 min. The aim of this being to reduce arterial oxygen to around 7 kPa for this time. A pulse oximeter was used to check that arterial saturation remained above 80%. The participant was returned to breathing air for the final ~ 3-4 min of the protocol.

5.2.2.5 Data analysis

In order to compare the experimental results for gas exchange at the mouth with the model output, a model for the lung has to be incorporated between mixed venous outflow and systemic arterial inflow to the CBGS model. This lung model can be driven by the

experimentally-recorded inspiratory and expiratory flows together with the inspired gas composition. The outputs of the model are the N_2, CO_2 and O_2 concentrations within the total expiratory flow, and these enable the breath-by-breath gas exchange for the model to be calculated.

The particular model of the lung used was that of Mountain et al. [9] as described in the Chapter 'Starting technology' which when used in conjunction with the body gas stores model will be referred to as the combined CBGS-LNL model. The primary reason being this model allows for a number of inhomogeneities to be present. Importantly, participant-specific values for these lung parameters could be estimated in preliminary experiments according to the washout protocol of Mountain *et al.*, although here the fitting routine utilised the combined CBGS-LNL model rather than the original LNL [9]. The experimental validation data were collected soon after this nitrogen washout experiment was complete to ensure inhomogeneity parameter changes would be negligible. For each of the validation experiments performed, oxygen consumption and carbon dioxide production were estimated from the preliminary air-breathing phase of the validation experiments. These metabolic rates were incorporated into the CBGS model and were assumed to be fixed throughout each experiment. This left just the initial conditions to be estimated from the validation experiments, which were the starting concentrations for the gases in the systemic venous blood and tissues together with the starting gas concentrations and volumes in the lung. These values were estimated by fitting the combined CBGS-LNL model to the validation measurements using a non-linear optimisation routine with the previously recovered participant lung inhomogeneity parameters fixed whilst allowing just the initial mixed venous values and the alveolar lung volume to be varied.

The A-a gradient for O_2 from the model over the air-breathing period is shown in Table 5.1 for each participant. The values are all within reasonable bounds and suggests the LNL is performing well at estimating ventilation-perfusion values.

In order to explore the performance of the CBGS specifically, exactly the same process as that outlined above was followed but with a dummy CBGS model in place which contained no dissolved or reacted gas stores. The fit between the MFS measured data and LNL-CBGS simulation and the dummy simulation without the CBGS (LNL alone) were then compared.

5.3 Results

5.3.1 General model properties

The overall properties of the model (for a standard man at rest) were first explored by imposing a 1 kPa step increase in partial pressure at the arterial inflow for each of three gases in turn and plotting the subsequent changes in venous blood composition (Fig. 5.1). Panels A, B and C illustrate the change in concentration (as a fractional change towards the new steady-state value) at the venous outflow for the individual compartments of the model for N_2, CO_2 and O_2, respectively. The different delays before the onset of the response are apparent on the x-axis and these reflect the different circulatory times for the different compartments. It is clear that, once any given transient perturbation has begun, the subsequent speed of equilibration differs substantially between the tissues. Of the tissues considered here, the fastest compartment is renal, which is unsurprising since the kidneys receive $\sim 20\%$ of the total cardiac output, but have a combined mass of only ~ 300 gm.

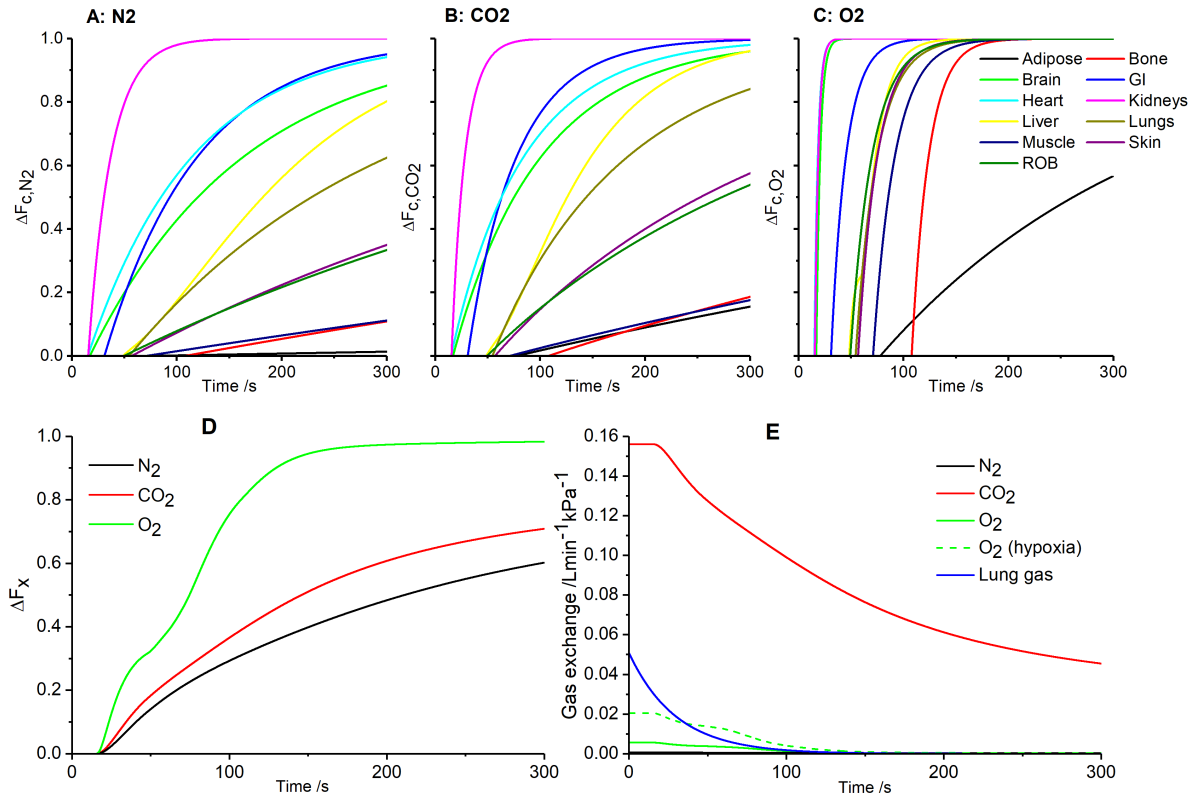

Figure 5.1. The responses of the circulatory model (for a standard man at rest) to a step change in 1 kPa for N_2, CO_2 and O_2. A,B,C: Fractional change from old to new steady-state venous concentrations for each of the 11 compartments after a 1kPa rise in (A) N_2, $\Delta F_{c,N_2}$; (B) CO_2, $\Delta F_{c,CO_2}$; and (C) O_2, $\Delta F_{c,O_2}$. D: Fractional change from old to new steady state concentration in the pulmonary vascular blood volume after a 1 kPa rise for each of the gases, ΔF_x. E: Variation in gas exchange at the level of the pulmonary capillaries for each of the three gases following a 1 kPa step increase in alveolar/arterial gas tension. Also shown are: i) the variation in gas exchange for a change in alveolar/arterial O_2 from 6.66 to 13.3 kPa, and ii) the variation in gas exchange at the mouth for a 1 kPa change in alveolar concentration. Parameters used for generating plots are those for standard man.

From panels A, B and C of Fig. 5.1, it is also apparent that the speed of response between the different tissues is both faster and far less varied for O_2 than it is for CO_2 or N_2. This arises because, even in euoxia, the ability of haemoglobin to reversibly bind O_2 dominates the solubility of O_2 in the body. The speeds of response appear somewhat slower for N_2 than for CO_2, and this arises because, unlike N_2, the apparent solubility of CO_2 in the blood is somewhat greater than the apparent solubility of CO_2 in the tissues (Table 4.2). The slowest response is for N_2 for the adipose tissue compartment, where equilibration has hardly begun at the 5 min point. This arises because N_2 is substantially more soluble in fat than it is in an aqueous environment.

Panel D of Fig. 5.1 illustrates the fractional change towards the new steady-state concentrations in the mixed venous blood for N_2, CO_2 and O_2. Unsurprisingly, the

fastest change is for O_2. At the 5 min time point, the concentrations for N_2 and CO_2 are both more than 50% towards their new equilibrium values. These fractional changes in venous concentration can be very different from the fractional completion for the change in the amount of gas stored. Indeed, in the case of N_2, more than half of the gas store is predicted to be in the adipose tissue compartment, and that has barely begun to change at the 5 min time point.

Panel E of Fig. 5.1 illustrates the rate at which N_2, CO_2 and O_2 are being loaded into the body stores via the circulation (these values would be zero for each gas under equilibrium conditions) for the 1 kPa increment in partial pressure in the arterial inflow. The rate of loading of CO_2 vastly exceeds the rate of loading of the other two gases while the rate of loading for N_2 is scarcely visible above the x-axis. For N_2, the comparison of exchange rates between the lung gas stores and the tissue gas stores illustrates why it was not possible to undertake validation experiments through measuring N_2 exchange at the mouth. For O_2, the exchange can be enhanced by incorporating a degree of hypoxia so that the storage is operating over the steep part of the oxygen dissociation curve for blood haemoglobin. The figure illustrates this as a mean rate of oxygen storage per kPa over a range of 6.66 kPa to 13.33 kPa of P_{O_2}, approximately the range employed in our validation experiments.

For purposes of comparison, Panel E of Fig. 5.1 also illustrates the rate at which a gas would be loaded into the gas stores of the lung for a 1 kPa increment in partial pressure in the inspired gas. This line for the washout profile was generated using an equation for washout speed from a given volume eq. 5.1 derived as such:

The standard solution for a lung washout is:

$$C(t) = C_{init} e^{\frac{-t}{T}} \tag{5.1}$$

where $C(t)$ is the concentration in the lung at time t, C_{init} is the starting concentration and T is the time constant. We differentiate to yield:

$$\frac{dC}{dt} = \frac{-1}{T} C_{init} e^{\frac{-t}{T}} \tag{5.2}$$

multiplying by the lung volume at FRC, V_{FRC}, (at STPD) gives:

$$V_{FRC}\frac{dC}{dt} = \dot{V}_{Lung} = V_{FRC}\frac{-1}{T}C_{init}e^{\frac{-t}{T}} \tag{5.3}$$

For a 1kPa step, C_{init} =$1/P_B$ as the volume of gas in in the lung corresponding to 1kPa is V_{FRC}/P_B. Standard P_B is 101.3 kPa. If we assume the lung manages two turnovers per min, then T=0.5 min.

Finally we must provide a lung volume. The lung volume chosen was 3.35 L, an appropriate lung volume for a 25 year old standard man 1.80 m tall according to equation 5.4 [218].

$$V_{BTPS} = 2.34H + 0.009A - 1.09 \tag{5.4}$$

where V_{BTPS} is functional residual capacity at BTPS (body temperature, ambient pressure and gas saturated with water vapour) in L; H is height in m and A is age in years.

This FRC value must be converted from BTPS to STPD, V_{STPD} using eq. 5.5 and the standard barometric pressure P_B:

$$V_{STPD} = V_{BTPS}\frac{273}{273+37}\frac{P_B - 47}{760} \tag{5.5}$$

By comparing the rate of gas storage in the lung against the body gas stores for each gas we can estimate the likelihood of successful validation for each gas when measured at the mouth. If the moment by moment gas exchange from the CBGS model is totally dwarfed by the moment by moment total gas exchange (body gas and lung storage) then the fraction of the gas exchange arising from the blood at any moment in time will also be very low. This then indicates validating the CBGS model with respiratory measurements at the mouth will not be feasible. It is clear from this that nitrogen has a much smaller rate of storage in the tissue than in the lungs.

5.3.2 Nitrogen validation

As previously indicated, it was not possible to undertake experimental validation of the model for nitrogen exchange using the MFS. A comparison between a simulated nitrogen

washout using the CBGS model could be drawn with both experimental data from the dog [213] and with a prior model of nitrogen stores given by Baker and Farmery [65]. As the data were provided as fractions of initial nitrogen over time the comparison to the decay in our simulation did not need to take into account differences in total mass between human and dog. Furthermore, metabolism is not applicable to nitrogen so differences between humans and dogs in this regard can be ignored. We note that the composition of tissues and perfusions will not be identical. This comparison is shown in Fig. 5.2. The model predicted the experimental data points for the concentration of nitrogen in the mixed venous blood extremely well. The CBGS model was also consistent with the Baker and Farmery model at the later time points, but it gave concentrations for nitrogen that were significantly higher at earlier time points. In relation to this, it should be noted that the Baker and Farmery model is a simple four compartment model with no circulatory lags.

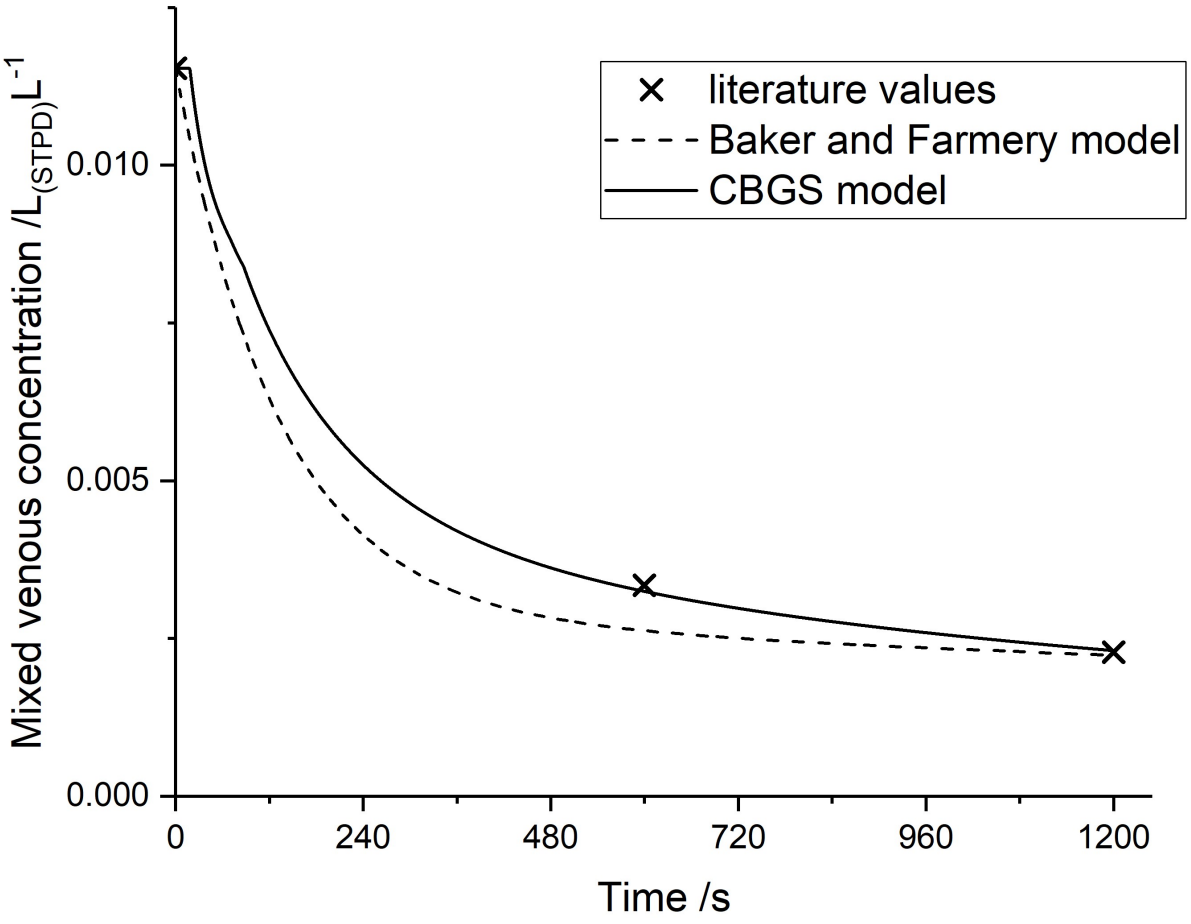

Figure 5.2. Mixed venous N_2 concentration following a switch to breathing pure oxygen. Full line, CBGS simulation (parameters are as for standard man); broken line, model of Baker and Farmery [65]; symbols, mean measured values for dog [213].

5.3.3 Carbon dioxide validation

The literature provides data for the change in arterial partial pressure for CO_2 over time in anaesthetized patients who have first been given pure oxygen to breathe and then had their trachea occluded [214]. Typically, the arterial partial pressure for CO_2 rises by ~ 1.6 kPa in the first minute and this is followed by an increase of ~ 0.45 kPa/min for the next ~ 4 minutes [214]. The profile of the model's systemic arterial CO_2 partial pressure ($PaCO_2$) can be directly compared to the experimental results. Figure 5.3 illustrates these values together with a simulation of the experiment using the CBGS model. While there is some difference in the absolute values between data and model, the agreement between model and data for the overall form of the response is extremely good. The model gradient is 1.8 kPa/min in the first minute followed by 0.44 kPa/min for the next 4 minutes. It is of note that 92% of the CO_2 produced in this experiment is stored in the tissues and only some 8% in gaseous form in the lung.

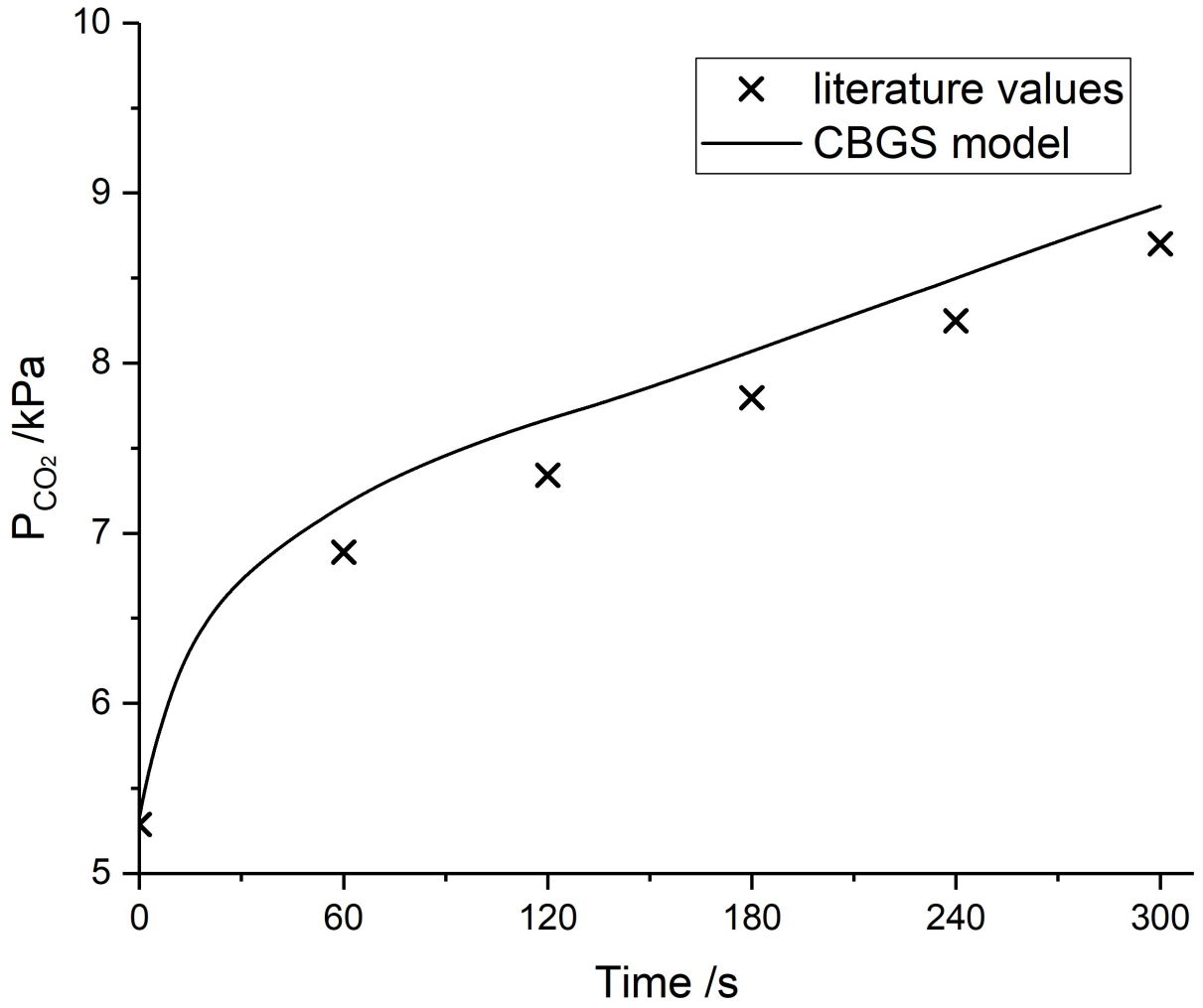

Figure 5.3. Increase in arterial P_{CO_2} during a period of tracheal clamping under conditions of pure oxygen. Full line, CBGS simulation; symbols, data from 14 anaesthetized humans (piecewise linear approximation gave an initial rise of 1.6 kPa in the first minute followed by a rise of 0.45 kPa each minute thereafter) [214]. CBGS parameters were for standard man, but with a metabolic rate appropriate for anaesthesia.

The graphs for gas volumes in the lung, the tissue and the blood gas concentrations demonstrate the substantial role body gas stores have in buffering changes in blood concentrations. Figures 5.4 & 5.5 show the volume of CO_2 in the lungs remains very stable relative to the rate of oxygen volume depletion whilst the CO_2 concentrations in the tissues rise. This demonstrates the substantial role body gas stores have in buffering changes in blood concentrations.

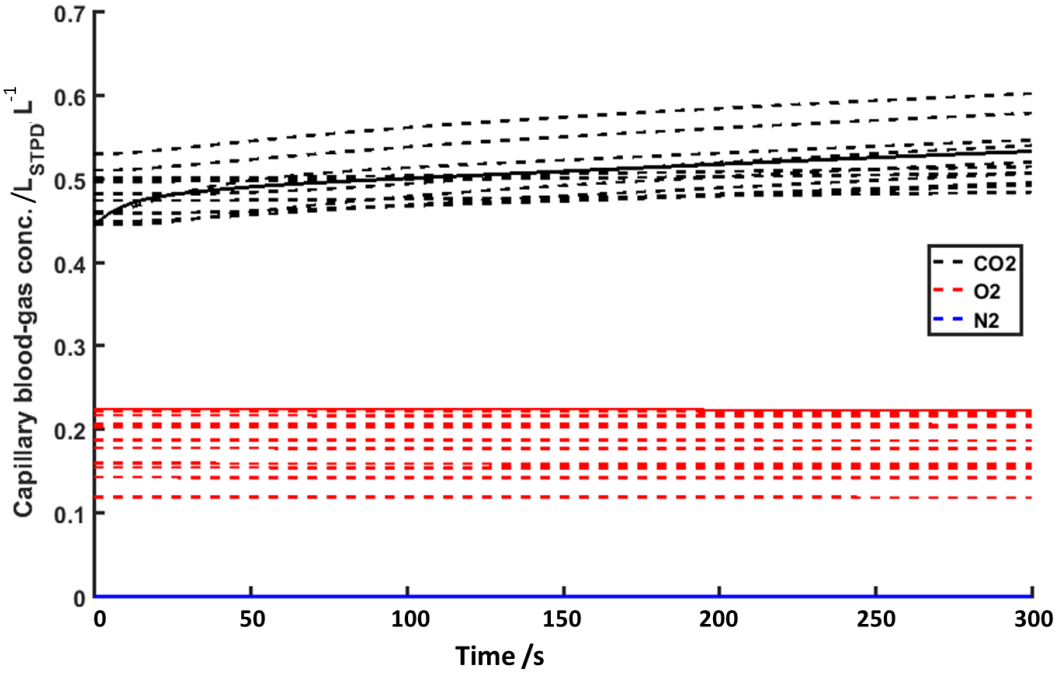

Figure 5.4. Results for CO_2, N_2 and O_2 levels from the CBGS model simulation of apneic oxygenation in a standard man. The gas concentrations in each of the 11 capillary beds are shown with the hatched lines, solid lines represent the arterial gas concentrations.

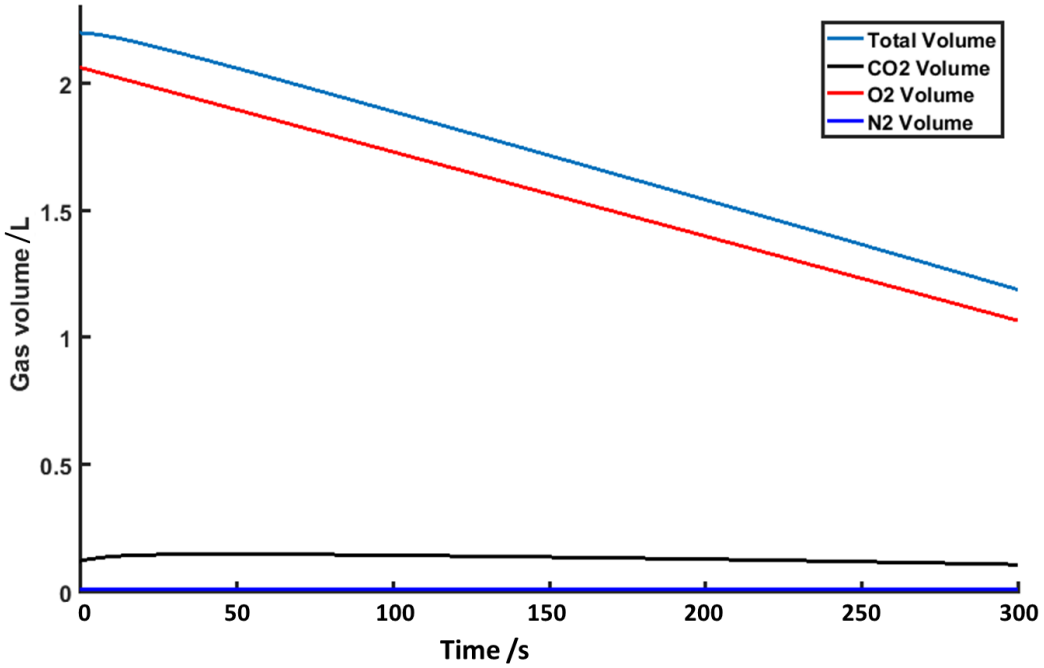

Figure 5.5. Simulated gas volumes in the simple single compartment lung during apneic oxygenation in a standard man.

Experimentally, rebreathing was studied in three subjects using an anaesthetic bag prefilled with a mixture of carbon dioxide, at a partial pressure designed to match the alveolar P_{CO_2} ($\sim$ 5.5 kPa), and pure oxygen. The comparison between the experimental

results and model simulations is shown in Fig. 5.6. Both the CO_2 profiles in the airway and the records for the cumulative production of CO_2 are very similar between model and data. The cumulative error is always less than 5% of the total exchange. For comparison, the error for the cumulative CO_2 exchange is also shown in the case where the CBGS model has been replaced with a dummy model which does not contain any gas stores. Here, the cumulative errors in exchange are far greater, and Table 5.2 demonstrates that the mean squared error for the breath-by-breath CO_2 exchange is between 16 and 56 fold greater for the dummy model as compared with the CBGS model.

Table 5.2. *Quality of fit with and without circulatory model*

Hyperventilation		
Participant	$\epsilon_{\mathrm{CO_2}}\ /(Lmin^{-1})^2$	$\epsilon_{\mathrm{CO_2}}^{CBGS}\ /(Lmin^{-1})^2$
#2	0.0068	0.0019
#3	0.0129	0.0007
#4	0.0081	0.0004
Rebreathing		
Participant	$\epsilon_{CO2}\ /(Lmin^{-1})^2$	$\epsilon_{\mathrm{CO_2}}^{CBGS}\ /(Lmin^{-1})^2$
#2	0.0059	0.0004
#3	0.0232	0.0004
#4	0.0126	0.0005
Oxygen washout		
Participant	$\epsilon_{O2}\ /(Lmin^{-1})^2$	$\epsilon_{\mathrm{O_2}}^{CBGS}\ /(Lmin^{-1})^2$
#1	0.0083	0.0053
#2	0.0031	0.0020
#3	0.0018	0.0008

ϵ_{x}, mean squared error between the measured and simulated rate of exchange of gas x at the mouth without the model for the circulatory and body gas stores; $\epsilon_{\mathrm{x}}^{CBGS}$, mean squared error between the measured and simulated rate of exchange of gas x at the mouth with the model for the circulatory and body gas stores.

To study unloading the body stores of CO_2, a further set of experiments were conducted during which the participants undertook a period of voluntary hyperventilation. The comparisons between the experimental results and model simulations are shown in

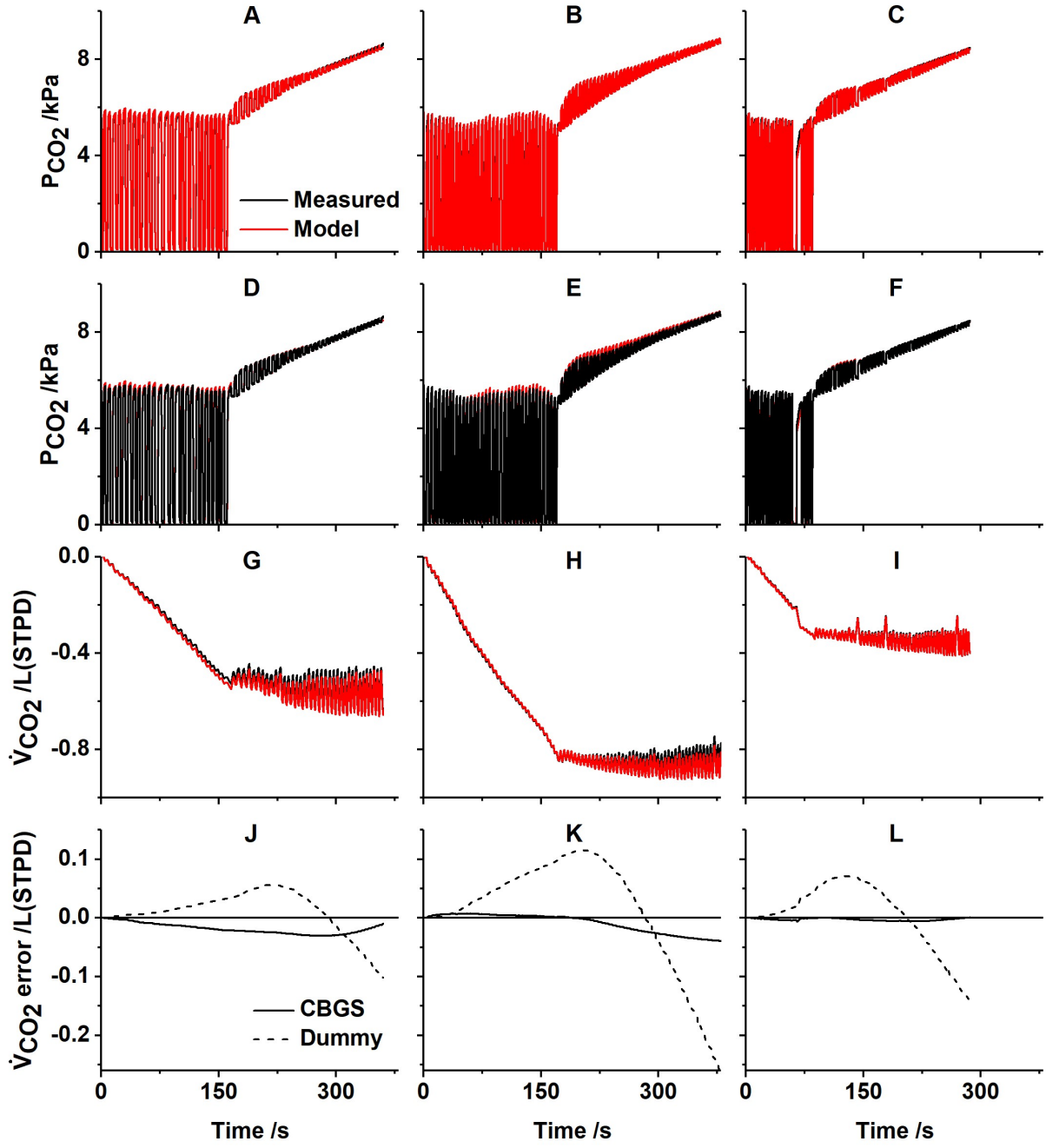

Figure 5.6. Experimental and model responses to rebreathing from a 6 litre bag for three participants. A,B,C: Airway P_{CO_2}, model superimposed on data. D,E,F: Airway P_{CO_2}, data superimposed on model. G,H,I: Cumulative CO_2 production ($\dot{V}_{CO_2}$), model superimposed on data. J,K,L: Cumulative error in CO_2 production (model - measured) when the CBGS model is included (full line) and when a dummy circulation is used (broken line). A,D,G,J: Participant 2. B,E,H,K: Participant 3. C,F,I,L: Participant 4. To derive the model output, participant specific inhomogeneity parameters were taken from a prior experiment; O_2 consumption and CO_2 production were estimated from the air-breathing phase of the experiment; and the initial mixed venous values together with the alveolar lung volume were estimated from the data.

Fig. 5.7. As for the rebreathing experiments, both the airway partial pressures and cumulative gas exchange records for CO_2 were very similar between model and data. The error in the cumulative CO_2 production between data and model is shown for both the CBGS model and the dummy model, and this illustrates clearly the importance of the

body gas stores. This is confirmed in Table 5.2, where the mean squared error for the breath-by-breath CO_2 exchange is between 4 and 22 fold greater for the dummy model compared with the CBGS model.

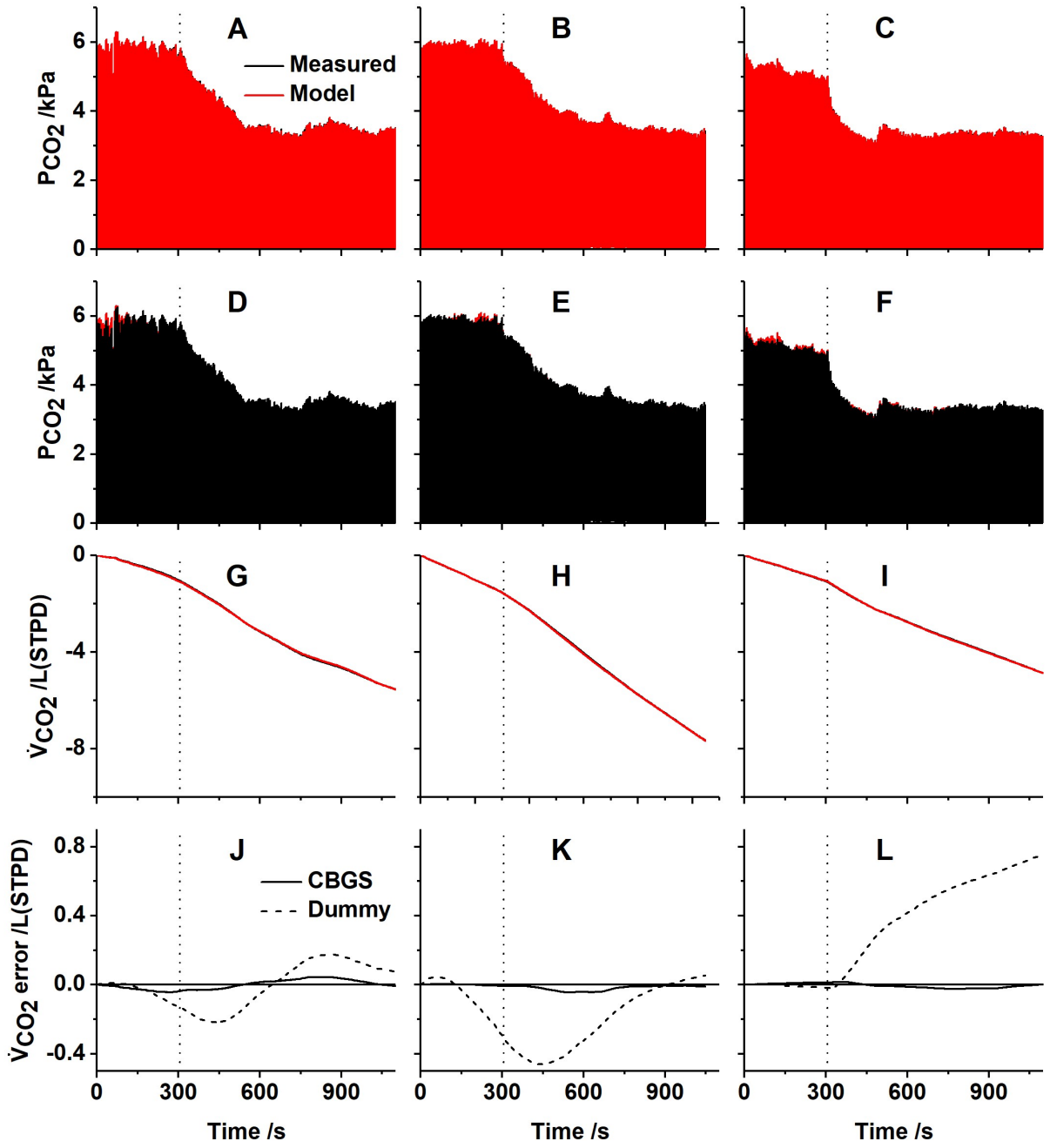

Figure 5.7. Experimental and model responses to voluntary, paced hyperventilation for three participants. A,B,C: Airway P_{CO_2}, model superimposed on data. D,E,F: Airway P_{CO_2}, data superimposed on model. G,H,I: Cumulative CO_2 production ($\dot{V}_{CO_2}$), model superimposed on data. J,K,L: Cumulative error in CO_2 production (model - measured) when the CBGS model is included (full line) and when a dummy circulation is used (broken line). A,D,G,J: Participant 2. B,E,H,K: Participant 3. C,F,I,L: Participant 4. To derive the model output, participant specific inhomogeneity parameters were taken from a prior experiment; O_2 consumption and CO_2 production were estimated from the air-breathing phase of the experiment; and the initial mixed venous values together with the alveolar lung volume were estimated from the data.

5.3.4 Oxygen validation

For oxygen, there were no data in the literature with which the model simulations could be compared. However, it was possible to reduce the oxygen stores somewhat by lowering

the inspired oxygen to generate an element of desaturation in the arterial blood. In the case of oxygen, the primary store is in the circulating blood. Therefore, the profile of its response to alveolar changes is expected to be far more rapid. The results are shown in Fig. 5.8. The profiles for the experimental and model airway P_{O_2} values were very similar for all participants, as were the cumulative records for the O_2 uptake. The cumulative error between data and model is shown for both the CBGS and the dummy models. Again, these errors were clearly smaller for the CBGS model. In this case, the mean squared error for the breath-by-breath O_2 exchange is at least 50% greater for the dummy model compared with the CBGS model for all participants (Table 5.2).

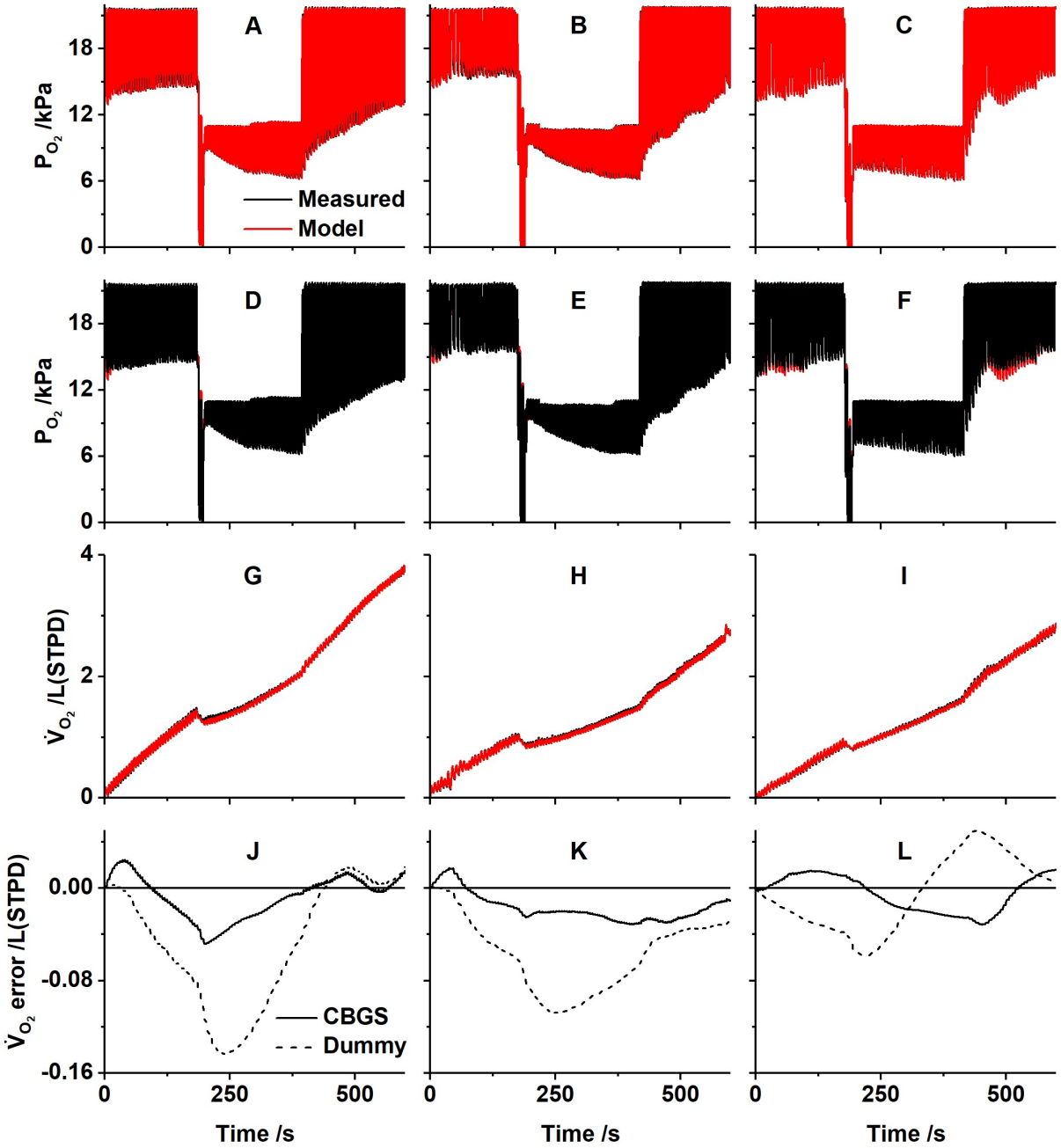

Figure 5.8. Experimental and model responses to the nitrogen washin protocol for three participants. A,B,C: Airway P_{O_2}, model superimposed on data. D,E,F: Airway P_{O_2}, data superimposed on model. G,H,I: Cumulative O_2 production ($\dot{V}_{CO_2}$), model superimposed on data. J,K,L: Cumulative error in O_2 consumption (model - measured) when the CBGS model is included (full line) and when a dummy circulation is used (broken line). A,D,G,J: Participant 1. B,E,H,K: Participant 2. C,F,I,L: Participant 3. To derive the model output, participant specific inhomogeneity parameters were taken from a prior experiment; O_2 consumption and CO_2 production were estimated from the air-breathing phase of the experiment; and the initial mixed venous values together with the alveolar lung volume were estimated from the data.

5.3.5 Experimental validation results summary

Inspired gas is an input to the model. Therefore, the inspired partial pressure in all graphs will necessarily be equivalent for both measured and model values. However,

the expired gas pressures are derived by the model. Thus the degree to which the model and measured expired partial pressures match indicates how well the LNL-CBGS is reproducing physiology. For the hyperventilation, rebreathing and nitrogen washin experiments, good agreement is shown between model and measured values with the maximum error between measured and model cumulative volume never exceeding 0.1 litres. More importantly, the model reproduces the profile of the dynamic changes seen in each experimental perturbation of body gas storage.

5.4 Discussion

An ideal route to validation of the present model would have been to introduce, via the gases in the lung, known systemic arterial concentrations and then follow the changes in mixed venous concentrations over time. However, this would have required the insertion of a pulmonary arterial catheter and this could not be justified in healthy volunteers. Instead, the validation had to proceed either by attempting to predict existing findings within the literature, or by conducting experiments and measuring instead the gas exchange at the mouth. Measurement of gas exchange at the mouth is far less satisfactory than measurement of mixed venous concentrations because changes in the lung stores for the gases have the potential to substantially affect the results obtained. Furthermore, it becomes necessary to incorporate a computational model of the lung between the venous and arterial ends of the CBGS model to allow for the changes in lung gas stores. In order to demonstrate that the CBGS model was necessary to model the gas exchange accurately, the process was also followed using a dummy CBGS model that had no body gas storage capacity. For both CO_2 and O_2, for all participants, the fit to the gas exchange data were very substantially worse with the dummy CBGS model in place.

The challenge of conducting the validation through measurements of gas exchange at the mouth is at its greatest for the least soluble gases. These have the smallest storage capacities in the compartments of the CBGS model, and gas exchange at the mouth is completely dominated by the lung gas stores. In this sense, the validation will have been more reliable for CO_2 than for O_2. In the case of N_2, experimental validation through measurements of gas exchange at the mouth was not feasible for this reason. Thus, at the

current time the validation of the model for inert gases is distinctly limited. One potential way forward for validating the model further for inert gases is to use tracer gases that have far greater solubilities than N_2, such as acetylene and nitrous oxide. Indeed, these gases have been used for estimating cardiac output from the rate of their uptake from the lung. During such experiments, it would also be valuable to explore the influence of different body builds in greater detail.

As far as the author is aware, this is the most complete model of the circulation and body gas stores as of writing. The CBGS model can be compared with previous models for the body's gas stores, and for N_2 we have illustrated the comparison with that of [65] in Fig. 5.2. Here, the only experimental data are for the dog, and therefore it is only possible to note that the models differ somewhat during the initial, more rapid transient, but converge at later time points.

Several models of body CO_2 storage have been reported in the literature. Single compartment models reproduce experimental data very poorly [29]. Some multi-compartment models perform better, and over time periods longer than $\sim$ 30 min can closely reproduce experimental data [32, 60]. However, they reproduce poorly the effect of CO_2 storage in shorter experiments. Their fit to the data is only improved with post hoc manipulations such as unrealistic redistributions in perfusion, unrealistic changes in metabolism or arbitrary changes in the tissue CO_2 solubility in a subset of tissues to match that of water [63]. In contrast, our model reproduces experimental perturbations in CO_2 very well across these shorter time frames without any physiologically unrealistic manipulations. The success of the CBGS in modelling changes in body CO2 over periods of 5-10 minutes is likely due to its large set of physiologically accurate compartments combined with anatomically correct temporal delays. The segmental modelling of the blood vessels also allows them to act as a rapid and dynamic store. However, it should be noted the CBGS does not include the comparatively slow renal and bone buffering of CO_2 changes. This is not a significant limitation for our purposes over experiments less than 15 minutes.

For whole body O_2 stores, the only dynamic model of which we are aware is that of Cherniack and Longobardo [64]. They incorporated O_2 solubilities into the CO_2 model of Farhi and Rahn [32]. This model reproduced experimental perturbations in body O_2

stores over a 3-min period poorly unless O_2 consumption was reduced at a specific time point. While such a model summarises the specific experiment, it clearly cannot be used to predict responses more generally for other scenarios. In contrast, our model tracked the dynamic fall and rise in O_2 stores over a ~ 10-min protocol without the need to postulate adaptive changes in metabolism.

To conclude, the work in this Chapter indicates the CBGS model can accurately estimate the storage and recirculation of gases using only an arterial input of blood flow and gas concentration. Coupling this model to models of lung physiology should allow a more integrated approach to cardiopulmonary gas transport, and this offers opportunities to improve physiological assessment of cardiopulmonary function in health and the potential for detection of dysfunction as in PE.

Chapter 6

Detection of pulmonary malperfusion

6.1 Introduction

Ventilation ($\dot{V}_A$) and perfusion ($\dot{Q}$) are closely matched within healthy human lungs to promote efficient gas exchange. Due to gravitational and anatomical factors this matching is imperfect (see Chapter 2) and the lungs display a distribution of ventilation to perfusion ($\dot{V}_A/\dot{Q}$) ratios. Pulmonary embolism (PE) is a blockage of the pulmonary arteries or arterioles that supply the lung with blood for gas exchange (see Chapter 2). Consequently, PEs result in regions of the lung that are ventilated but not perfused (without blood supply). Intuitively, this corresponds to regions of the lung having very large (or infinite if there is no flow whatsoever) $\dot{V}_A/\dot{Q}$ ratios. Thus PEs result in a bimodal distribution of $\dot{V}_A/\dot{Q}$ in such lungs, with one peak around a normal $\dot{V}_A/\dot{Q}$ and other around a much higher $\dot{V}_A/\dot{Q}$.

The 'physiological deadspace' is the sum of the 'anatomical deadspace' and the 'alveolar deadspace', the latter being an apparent deadspace arising through $\dot{V}_A/\dot{Q}$ mismatch (this is a small but non-zero value in health). In disease, the very large $\dot{V}_A/\dot{Q}$ ratios associated with PE increase the 'alveolar deadspace' and make gas exchange less efficient as a result. The anatomical deadspace is expected to be normal in patients with PE.

The LNL model (described in Chapter 3) identifies the anatomical deadspace through the shape of the expired gas profile (expirogram). However, for $\dot{V}_A/\dot{Q}$ mismatch (which generates the alveolar deadspace) the LNL model assumes a unimodal $\dot{V}_A/\dot{Q}$ distribution.

Gas exchange with a unimodal distribution cannot be as inefficient as with a bimodal distribution where a significant component of the ventilation is wasted in compartments with no perfusion, and for that reason one would expect a measured arterial P_{CO_2} to be higher than that predicted by the LNL model in patients with PE.

The diagnostic proposed here is to compare measured blood P_{CO_2} values with those predicted from the combined LNL-CBGS model to probe if this difference is raised in PE. The proposed experimental design involves collecting data using the MFS whilst participants undergo the nitrogen washout protocol (see Chapter 3) and blood gas values are sampled. The MFS data will be modelled using the combined LNL-CBGS model. The specific hypotheses are: i) the combined LNL-CBGS modelling can accurately simulate measured gas content in the blood from breath exchange data in healthy participants and ii) a departure of the modelling from the measured blood sample indicates very high $\dot{V}/\dot{Q}$ lung units present in PE.

Whilst an arterial blood gas measurement may be optimal, it generally requires an experienced physician to draw the sample, and this is not ideal for a diagnostic that should be less demanding on hospital resources than existing alternatives. Arterialised blood samples can be approximated to some degree by blood drawn from a warmed hand vein, and this may reasonably be undertaken by non-medical personnel. Blood R-lines describe the locus for the P_{CO_2} and P_{O_2} change in the blood as O_2 is taken up and CO_2 released by metabolism (see 6.2.2). The LNL-CBGS model allows us to calculate blood-R lines; thus, as long as the respiratory quotient is accurate, allowance can be made for any gas exchange that has occurred in the warmed hand vein sample by comparing the blood P_{CO_2} and P_{O_2} with this line rather than with the predicted arterial value.

This work differs from the AVDSf technique described in Chapter 2 for several reasons: i) it does not estimate alveolar gas from end-tidal gas directly but instead uses a detailed model of the lung with many alveolar units (fitted to respiratory measurements) which includes the effects of ventilation and perfusion inhomogeneity (these have an important influence on alveolar state), ii) this model lung uses a more detailed method to estimate the anatomic dead space created by the conducting airways iii) both oxygen and carbon dioxide partial pressures are used in the comparison rather than just one of these gases, iv) modelling of the circulation allows construction of R lines and the potential for venous

rather than arterial samples to be used for comparison.

The work of this chapter began by refining the protocol in the laboratory on healthy volunteers and then exporting the technique to the local hospital. Ideally, a large number of patients suspected of having a PE would have been recruited from the John Radcliffe hospital and studied using hand warmed venous blood data. Unfortunately before many patients could be studied, the work was halted because of the COVID pandemic. The few results that were obtained are presented here.

6.2 Methods

6.2.1 Blood sampling site selection

This protocol relies on the recovery of the error between modelled and measured blood. This demands a blood sample be taken and its gas partial-pressures measured so that the state can be compared to that of the model simulation.

The site of blood sampling should consider both expected modelling accuracy and practical limitations. Using the LNL output, the CBGS model generates information on the gas contents of arterial, tissue and mixed venous blood. The most accurate model estimates of blood gas partial pressures are expected to be arterial as these are most closely related to the MFS gas exchange measures (and are directly output from the LNL). Peripheral venous blood is not representative of the mixed venous circulation. Simulations of mixed venous gas are expected to be superior to individual tissue venous blood simulations because each individual tissue's venous blood will have differing respiratory quotients (RQ) which involve further assumptions by the CBGS whilst the overall respiratory quotient represented by the arterial and mixed venous blood is more directly accessible from the MFS data and the LNL. A further issue with using individual venous outputs is estimates of individual tissue gas partial pressures (and their attendant venous outputs) will also depend upon CBGS model assumptions of perfusion distribution.

Although arterial puncture is ideal from a modelling perspective, it requires a trained and skilled clinician. Likewise, measuring mixed venous blood samples would require a right heart catheter which is not ethically justifiable. To be feasible as a routine technique

for diagnosis of PE the required blood sample would ideally be peripheral venous blood to avoid these practical challenges. However, as explained previously venous simulations are subject to further, somewhat arbitrary, assumptions by the CBGS model.

Therefore, a compromise of using 'arterialised' venous samples was selected. This allows easy access for blood sampling whilst minimising the influence of model assumptions. 'Arterialising' a venous sample is achieved through warming the forearm and hand. Homeostatic thermoregulation by the body results in vasodilation of the hand arterioles and recruitment of additional capillaries. Metabolism in the hand will remain essentially equivalent but with a far greater blood supply. This then causes the blood leaving the hand in the veins to be more similar to arterial blood in its blood gas content as metabolism is swamped by the increased supply of fresh blood.

6.2.2 R-line construction and blood sample comparison

Following on from the introduction, the test metric is defined as the difference between the simulated model blood gas partial-pressures and those of a measured sample. In summary, the proposed technique uses MFS breath exchange data to model the lungs and circulating blood gas contents. The simulation is then temporally aligned and compared with a measured blood gas sample. To allow simulation comparison to blood samples ranging from arterial to mixed venous the LNL-CBGS model outputs R-lines.

R-lines are diagrams of blood and air CO_2 and O_2 partial pressures constructed using inspired and alveolar gas partial pressures, arterial and venous CO_2 and O_2 concentrations, and the respiratory quotient (RQ) for gas exchange [219, 106, 220]. The R-line itself is the locus of pairs of values of P_{CO_2} and P_{O_2} (or their associated concentrations: C_{CO_2} and C_{O_2}) for gas or blood that are consistent with one particular value of RQ, given a particular reference starting pair ($P_{CO2,ref}$, $P_{O2,ref}$, or $C_{CO2,ref}$, $C_{O2,ref}$). The RQ specifies for every mole of O_2 added to or removed from the gas or blood, how many moles of CO_2 have to be added or removed (RQ=V_{CO_2}/V_{O_2}). Typically, the reference values for the lung are the pair of values for P_{CO_2} and P_{O_2} associated with the inspired gas, or for the blood, the pair of values associated with the systemic mixed venous blood. Although referred to as R-lines, when plotted on a P_{CO_2}/P_{O_2} diagram, these are actually curves - for blood because of the curvilinear nature of the blood gas dissociation curves and for gas because

of the expansion or contraction of the gas that occurs for any value for R other than 1.

Examples of blood R-lines are displayed in 6.1. The respiratory quotient gives the linear gradient of the line between the arterial and venous points when graphed as concentrations. When the arteriovenous blood gas concentrations are converted to partial pressures the linear relationship becomes a curved line due to the non-linear relationship between CO_2/O_2 partial pressures and concentrations in the blood. Given the same respiratory quotient, blood will change from arterial to venous by following the path of partial pressure co-ordinates determined by this line.

The simulated R-line output for each data set is constructed by averaging arterial and venous gas values over a given time period with a set delay to account for the transit time from the pulmonary vein/systemic artery to the hand vein as well as the minor delays involved in extracting the sample. The respiratory quotient used is estimated by the LNL-CBGS. Based on these considerations, a somewhat arbitrary lag time of 30 seconds and an averaging time of 45 seconds was selected.

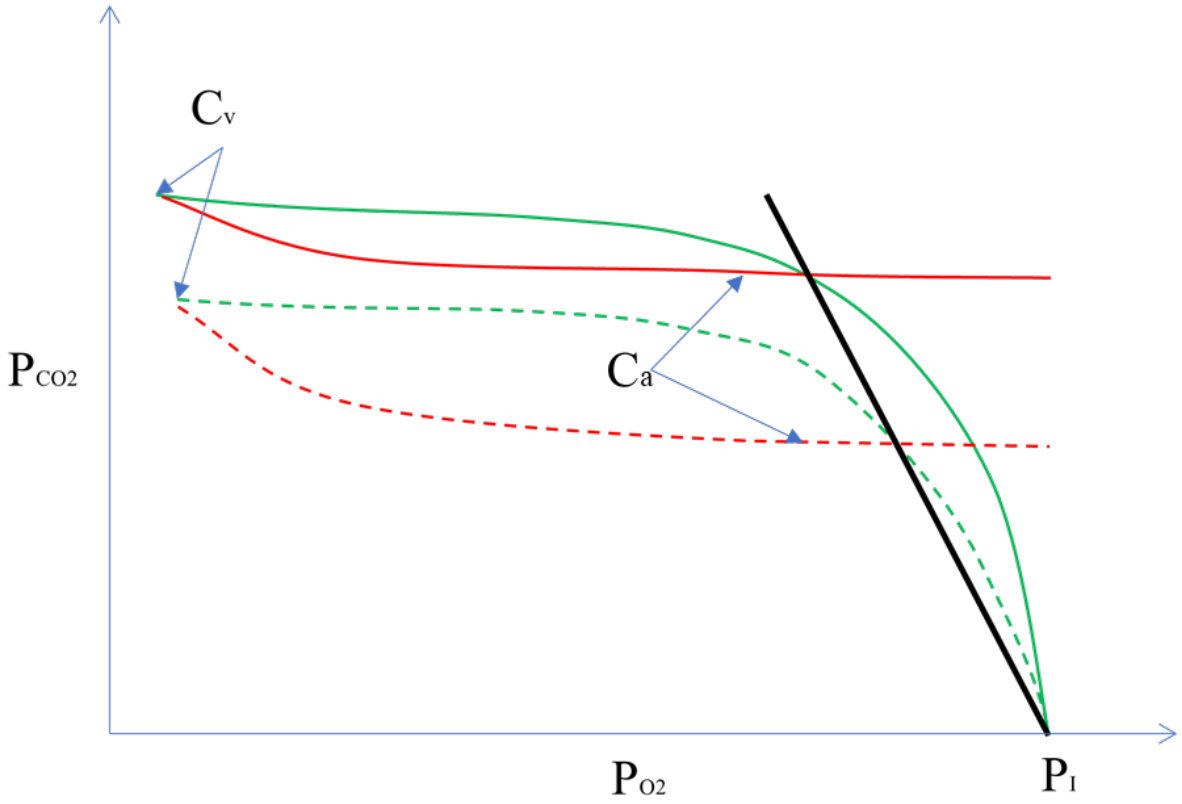

Figure 6.1. Expected R-lines described by data from the LNL (checked lines) and from blood samples (solid lines) in patients with PE. Where PI represents the composition of inspired gas, Cv the composition of mixed venous blood, Ca the composition of systemic arterial blood, the black line the gas R-line, the green the V/Q line or pareto frontier that an ideal lung could take and the red lines the blood R-lines. The gas R-line is the same in both as the LNL can accurately determine the R-value and inspired gas concentrations. Although the shape of the blood lines is set at a given R-value (respiratory exchange ratio) their translational position depends upon the 'starting' composition of mixed venous blood for the blood R-lines and the inspired air for the gas R-lines. It is expected that the R-lines from the LNL and blood samples will be almost identical in healthy participants.

This simulated R-line (which contains all possible blood partial pressure CO_2 and O_2 pairings from arterial to venous for a given RQ) can then be compared to an accompanying measured blood sample. To quantify the difference, the minimum distance of the measured point from the R-line that connects the arteriovenous points is calculated to give the blood error: ϵ_B. The R-line and error are calculated in the same way regardless of whether the sample is arterial or arterialised venous blood.

The model is expected to incorrectly estimate $P_{\mathrm{CO_2}}$ and $P_{\mathrm{O_2}}$ in PE (Fig. 6.1). This is a result of the LNL's non-linear optimisation routine assuming a set $\dot{V}/\dot{Q}$ correlation and a bivariate lognormal distribution for the compliance and perfusion. As described in the introduction, this does not allow for the contingency of lung units with a high disparity of $\dot{V}/\dot{Q}$ or no perfusion as in PE.

6.2.3 Blood sampling testing

Having selected the blood sampling site and the calculation of the metric of interest I move onto exploring the practicality, number and timing of blood measurements. As this was a novel area, the most appropriate timing for the blood samples and their frequency was unknown. In this section refinement of the blood gas collection is carried out in healthy participants.

Previous group work showed gas stores were often perturbed by breathing through the MFS. If a steady state is assumed prior to breathing through the mouthpiece the LNL-CBGS estimate for an initial blood R line could be compared to a venous blood sample taken immediately prior to breathing. Venous blood samples taken during the air-breathing phase can also be used with the temporal alignment technique described in the previous section. Blood samples during the high-oxygen phase were not tested as the dramatic changes in oxygen and nitrogen body gas stores was certain to make modelling and temporal alignment with the blood sample more challenging.

A hand warming box device was purchased from the University of Vermont Medical Centre. The box consisted of a heating element and a fan that warmed a space large enough to place the hand and forearm within. The accompanying instructions recommended 10 to 15 minutes of hand warming using air heated to 55 degrees Celsius to obtain 'arterialised' venous blood.

To explore an appropriate experimental design, two healthy volunteers were recruited. The hand warming box was pre-heated to 55 degrees Celsius. A venous cannula was placed into a vein on the back of the hand and a blood sample extracted prior to heating. The cannulated arm was then placed in the hand warming box. Further blood samples were taken every 5 minutes for a further 20 minutes. The volunteers were then connected to the MFS with simultaneous pulse oximetry measurements from a finger whilst further samples were taken every 2 minutes during the air-breathing procedure.

This laboratory testing showed highly effective 'arterialisation' of the sample in both volunteers with significant rises in blood gas oxygen saturation to values close to those simultaneously measured with a pulse oximeter. The testing revealed that collecting blood samples every 2 minutes was unwieldy. In addition, blood oxygen saturations peaked after around 10 minutes of hand warming so the warming period could be reduced

to 10 minutes. The protocol was modified to include only 1 blood sample immediately prior to commencing breathing and another approximately 3 minutes into the 7 minute air-breathing period. This preliminary work suggested in healthy subjects the model can accurately match the R-line to blood partial pressures for carbon dioxide and oxygen in arterialised venous samples.

Exporting the hand warming box to the John Radcliffe hospital proved impossible due to a lack of certification and electrical safety testing. Instead, a similar commercial device was used (the GreenCross Medico Airglove). This gave the same 'arterialisation' results but used a disposable inflatable plastic glove to warm the arm and hand.

6.2.4 Pulmonary embolism diagnosis experimental method

Having refined the methodology in previous sections, the finalised procedure used in clinic was as follows:

1. Sit participant comfortably by MFS prior to starting breathing through the device.
2. Place tourniquet on upper arm and insert catheter into hand vein.
3. Place arm with catheter in arm warming Airglove and begin heating.
4. Heat for 10 minutes.
5. Start the MFS software.
6. Take a blood sample by:
    (a) Set the three-way tap (3WT) to connect between catheter and flush syringe and draw back around 1 ml blood (ignore the flush solution becoming progressively more bloody).
    (b) Set 3WT to connect between catheter and sample syringe and take sample
    (c) Set 3WT to connect between catheter and flush syringe and inject around 1 ml of flush down catheter.
    (d) Cap sample syringe and store on ice.

7. Immediately, but with minimal disturbance, place the noseclip on the participant and start them breathing through the apparatus via the mouthpiece with the inspirate set to air. Ensure there are no leaks.

8. After around 3 minutes of breathing air take another blood sample using the same technique.

9. After 7 minutes of breathing air switch the inspirate to medical grade oxygen to carry out the nitrogen washout period for 5 minutes.

10. Remove the participants noseclip and take them off the mouthpiece whilst catching saliva build-up in tissue. Remove venous cannula.

11. Immediately analyse the blood samples in the blood gas analyser (here a Radiometer ABL90 FLEX PLUS was used).

12. Submit data for analysis by computer server.

The requirements for the protocol are:

1. MFS system with gas supplies.

2. Airglove for hand and arm warming.

3. Mouthpiece and nose clip.

4. Immediate access to laboratory-grade blood gas analyser.

5. Heparinised syringes for taking blood gas samples, labelled in numerical order.

6. One 10 ml syringe filled with saline.

7. Medium gauge intravenous cannula (20G or 22G) for hand vein cannulation with associated sterile dressing.

8. Sampling catheter to attach to intravenous cannula with three-way tap at end distal to cannula.

9. Caps for blood gas syringes and ice to keep blood samples.

10. Tourniquet and hand-warming device.

11. LNL-CBGS model.

The nitrogen washout protocol described in Chapter 3 is modified from a 10 minute air breathing period to 7 minutes. This change was made due to findings that the initial 5 minutes of air breathing used to settle the participant into a steady state were in fact insufficient to generate equilibrium and the addition of the CBGS model allowing improved tracking of departures from a steady state. Reducing the total time of the protocol is favourable as it improves participant adherence and reduces the probability of boredom or other factors creating leaks through release of the mouthpiece.

21 participants were recruited from ambulatory care at the John Radcliffe Hospital. All participants were suffering from breathlessness and chest pain where PE was queried. MFS washout measurements were recorded whilst patients were kept in hospital awaiting clinical scans for PE (either CTPA or V/Q scintigraphy). The outcome of these imaging techniques was used for comparison to our technique. Sophisticated statistics are not necessary or appropriate because the sample is so small. Welch two sample t-tests comparing PE positive and PE negative groups were carried out for both blood samples taken before and during breathing.

Ethical approval and a trained clinician was provided for placement of the venous cannula in the hand and to take blood samples. The experiment proceeded if the attempt to take a blood sample at rest failed. Attempts to get a sample during breathing through the MFS continued until the final minute of the air breathing period at which point the experiment continued without an accompanying blood sample during air breathing (if no blood sample was taken either before or during air breathing, then this PE diagnostic approach would not be possible - although this was not the case for any of these data sets).

6.3 Results

Of the 21 participants who completed the protocol, 12 resulted in the LNL-CBGS failing to fit. The reasons for this included large leaks due to patient age and/or mental state making it challenging to keep their mouth securely on the mouthpiece. Four participants had nitrogen consumptions of over 200 ml/min indicating extreme leaking that would be

expected to cause model fitting failure. In three participants the clinician was unable to extract a blood sample after placing the venous cannula.

Characteristics of the 9 patients (6 males and 3 females) for whom the LNL-CBGS successfully recovered model lung parameters are shown in Fig. 6.2. Of these 9 participants 5 were confirmed to have PEs using standard clinical imaging. All 5 PEs were bilateral and classified as moderate to severe.

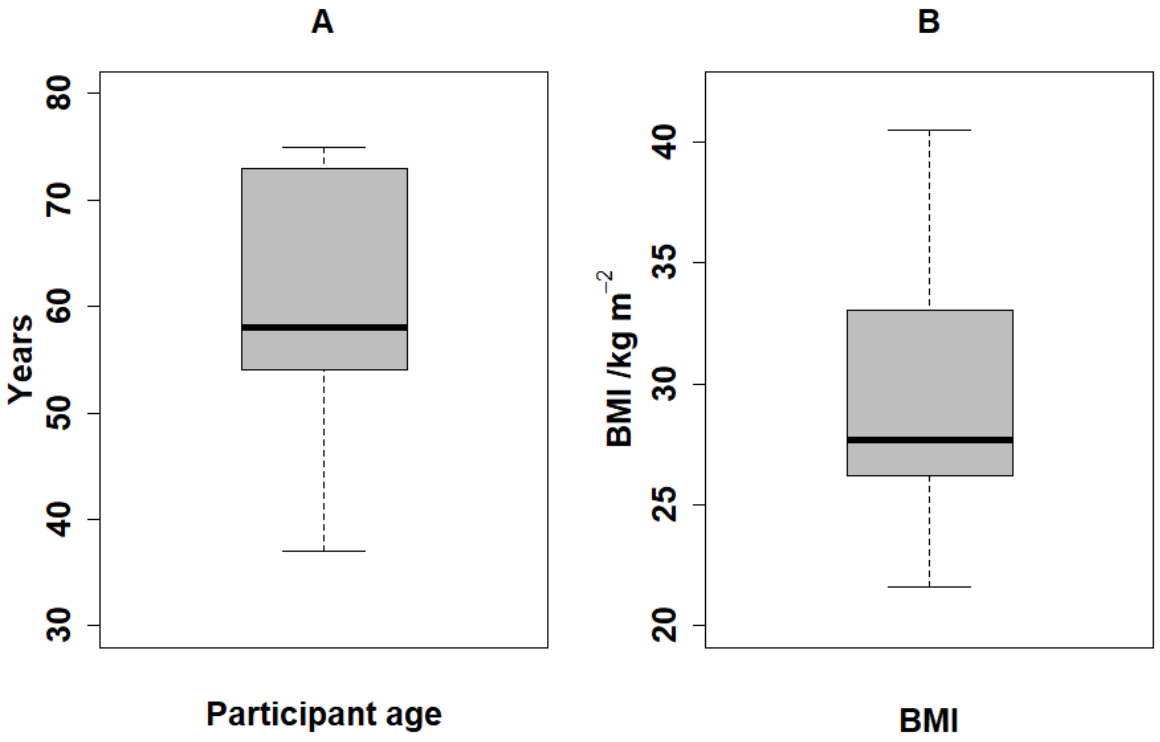

Figure 6.2. Box and whisker plots displaying PE study patient characteristics. A: patient age /years, B: patient BMI $/kgm^{-2}$.

6.3.1 Log-normal lung parameters recovered

The fitted LNL parameters recovered by the model are displayed as box and whisker plots against PE status in Fig. 6.3 and 6.4. In the case of the inhomogeneity parameters shown in Fig. 6.3 there appears to be no correlation with PE status. Fig. 6.4 shows a slight increase in deadspace (as a fraction of predicted FRC) and a slight decrease in FRC (as a fraction of predicted) with presence of PE. However, the sample is very small and thus the slight differences could easily be due to chance. Indeed, a Welch two sample t-test found no statistically significant difference between the means for PE positive and PE negative groups for deadspace (p=0.12) and FRC (p=0.24).

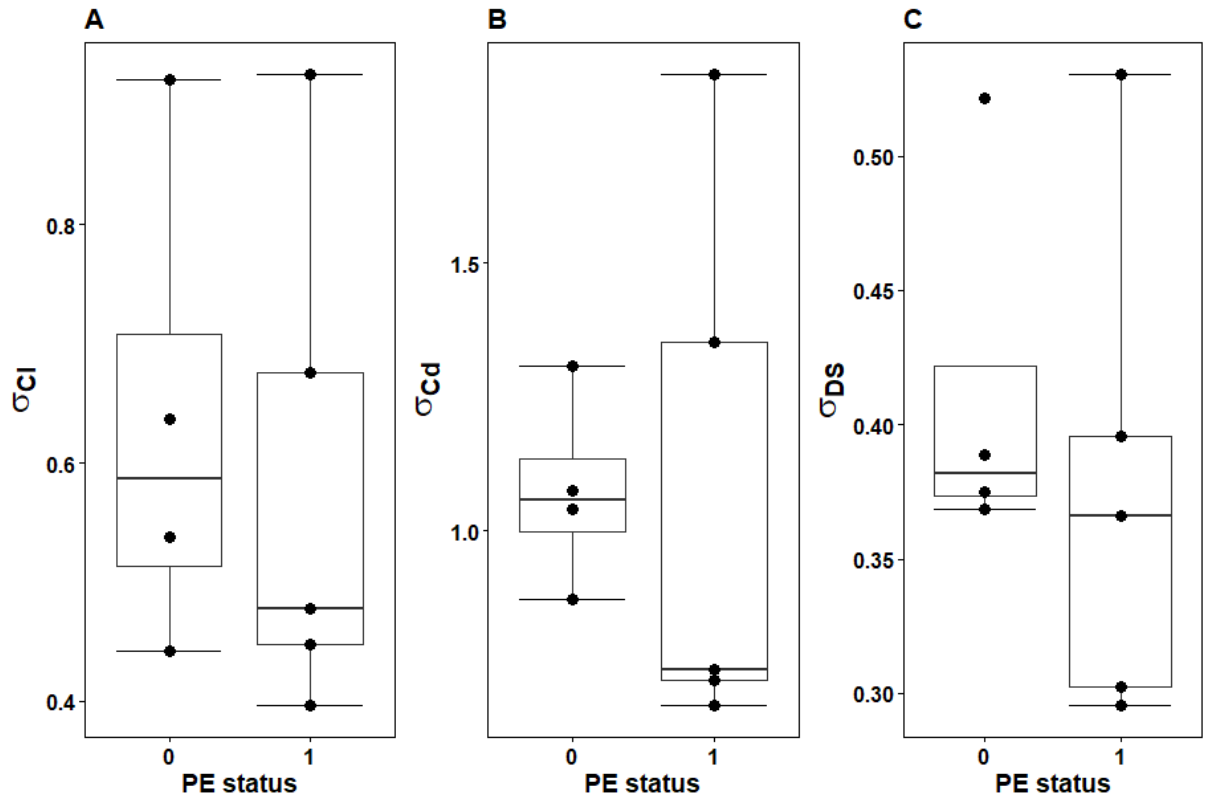

Figure 6.3. Box and whisker plots displaying LNL-CBGS inhomogeneity parameters against PE status. A: the width of the ventilation distribution (σ_{Cl}), B: the width of the perfusion distribution (σ_{Cd}), C: the width of the deadspace distribution (σ_{DS}). PE status: 0 = negative and 1 = positive.

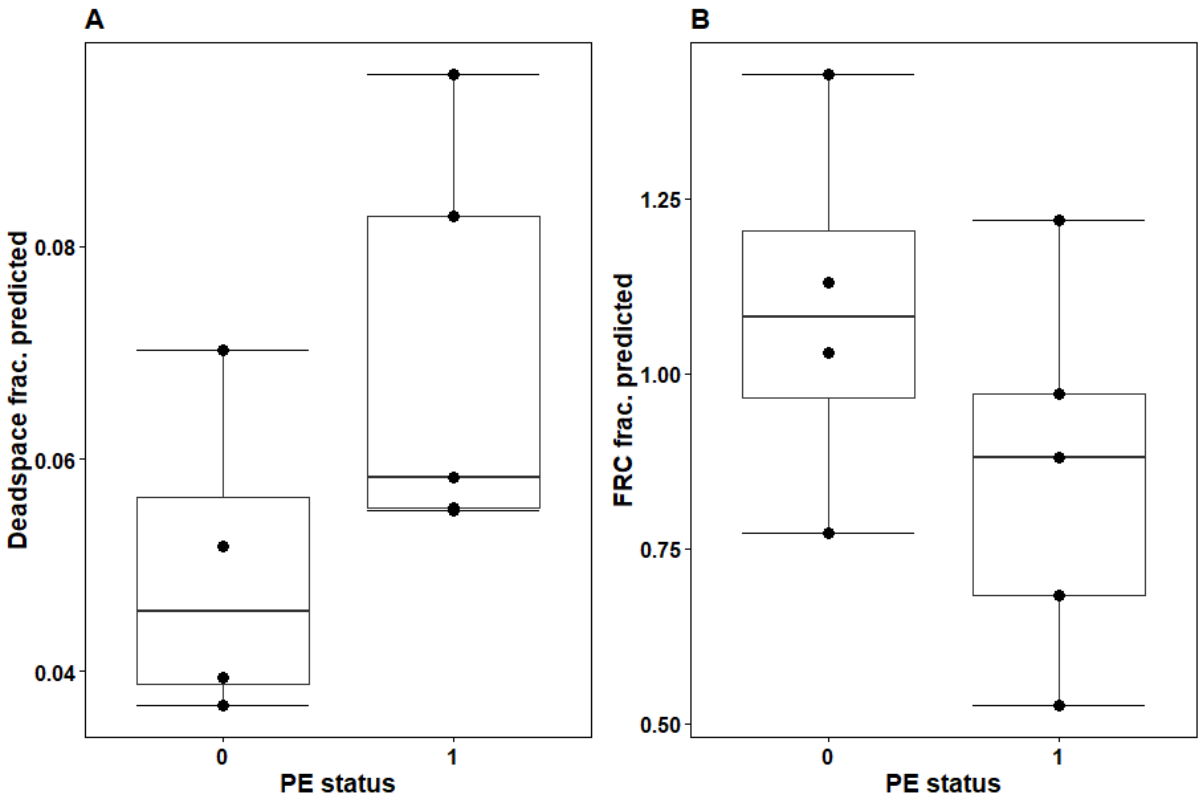

Figure 6.4. Box and whisker plots displaying LNL-CBGS volume parameters against PE status. A: model deadspace volume as a fraction of predicted FRC volume (based on participant height and sex), B: model FRC volume as a fraction of predicted FRC volume (based on participant height and sex). PE status: 0 = negative and 1 = positive.

6.3.2 Pulmonary embolism diagnosis using the blood R-line error

The LNL-CBGS model simulated R-lines were compared to measured arterialised-venous gas partial-pressures taken before and during air-breathing through the MFS to give ϵ_B (see Fig. 6.5). ϵ_B for the blood samples taken before breathing on the MFS appears to be unrelated to PE status. Contrastingly, in the sample taken while the patient was breathing on the apparatus ϵ_B appears strongly correlated with PE status, with ϵ_B close to zero in PE negative patients and close to 1 kPa in PE positive patients.

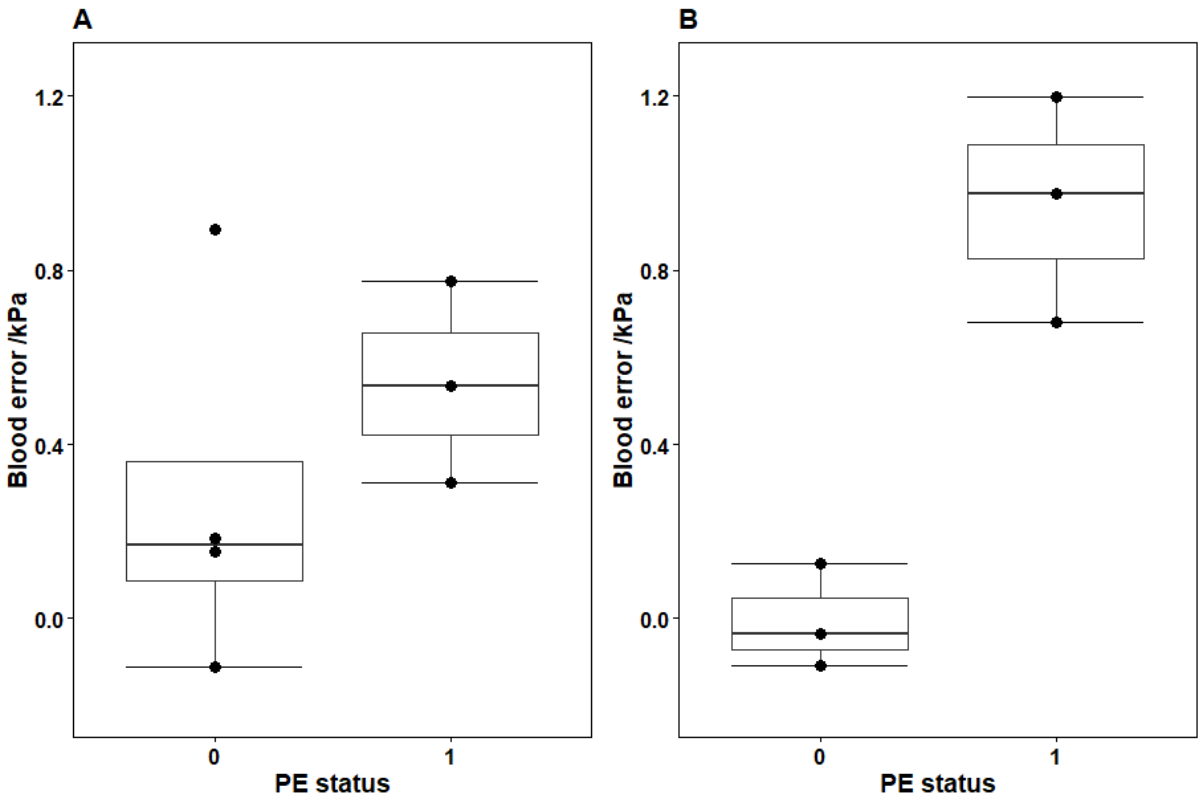

Figure 6.5. Box and whisker plots displaying the measured versus model blood error metric against PE status. A= blood error calculated using samples taken from the venous cannula immediately prior to breathing commencing and model simulations of blood R lines using initial conditions; B= blood error calculated using samples taken from the venous cannula during the air breathing phase of the washout and model simulations of R lines corresponding to the sample time but delayed by 45 seconds and averaged over 30 seconds to account for circulatory delays. The blood sample collection was not successful in all cases. There were 9 participants but due to unsuccessful blood sampling there are only 7 data points in A and 6 in B.

For the blood samples taken before breathing, a Welch two sample t-test found no statistically significant difference in the mean ϵ_B of PE positive and negative groups (p=0.35). However, a statistically significant difference between the ϵ_B means of PE positive and PE negative groups was found for the blood samples taken during air-breathing (p=0.017).

Example R lines compared to the blood sample taken during the blood test are shown in Fig. 6.6 for both PE positive and PE negative patients.

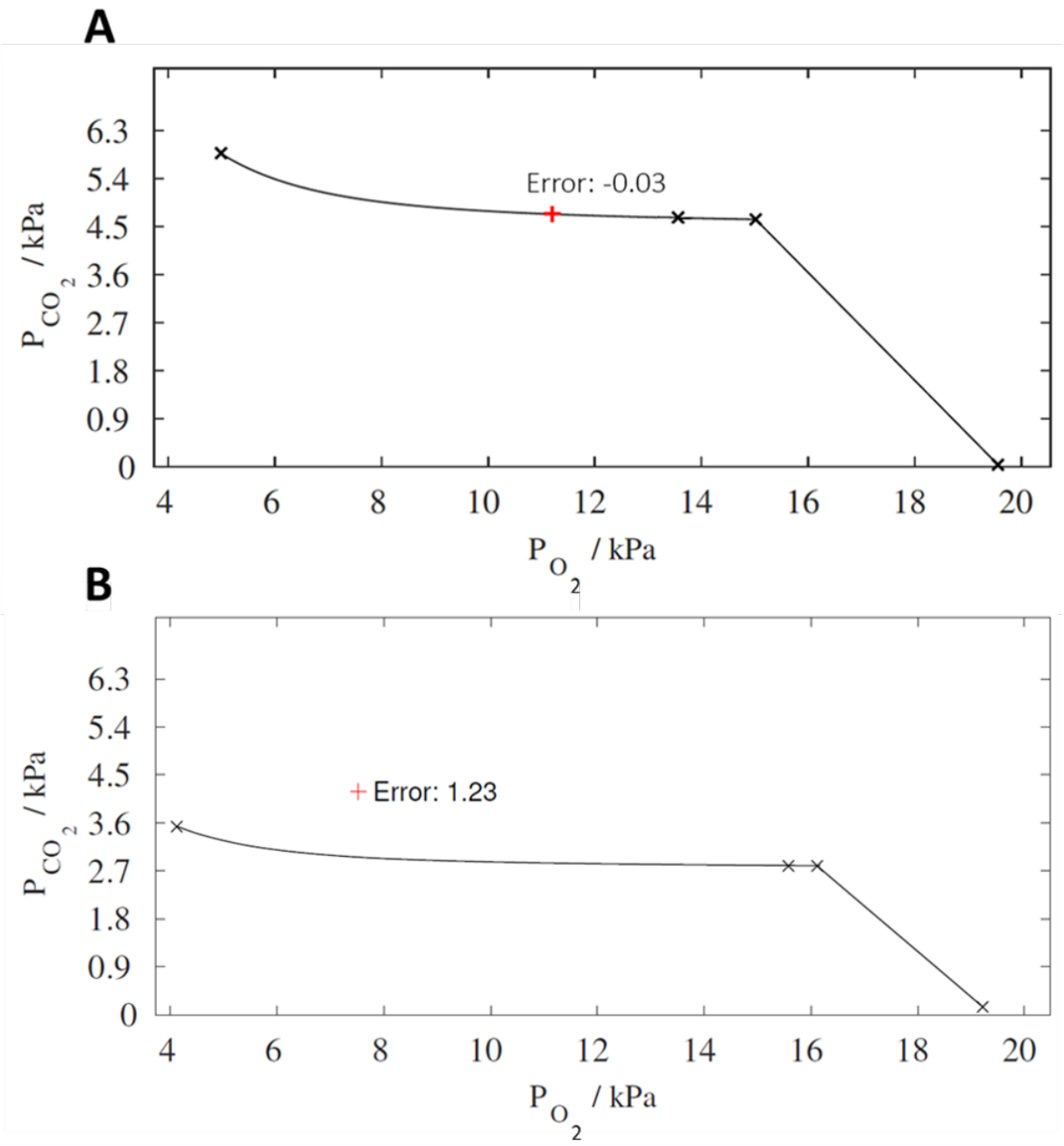

Figure 6.6. Examples of the LNL-CBGS model R line output plotted against the measured blood point taken during air breathing. A: PE negative, B: PE positive. Black lines= model simulated blood R lines; red cross= measured blood sample; Error= error between measured and model simulations of blood composition; black crosses= mixed venous, arterial, ideal and inspired gas partial pressure values.

6.4 Discussion

In this Chapter the potential of the combined LNL-CBGS model as a PE diagnostic tool was investigated using a cohort of individuals with suspected PE. The small data sample necessitates any conclusions be tentative. However, the data collected suggest PE positive

participants generate LNL-CBGS R-lines that are lower than concurrently collected blood samples during air breathing. PE negative participants do not show this effect. Both PE positive and negative groups display larger errors with the blood sample taken prior to breathing and no significant difference between groups.

Although a small sample, the data collected is very encouraging as there is no overlap between PE positive and negative participants for the samples taken during breathing and the means are different with statistical significance. This supports the hypothesis that when simulating MFS data from PE positive participants the LNL model does not correctly construct entirely un-perfused alveolar compartments and therefore estimates arterial and mixed venous blood contents less hypoxic and hypercapnic than measured. Further work with a larger sample and taking only samples during the air-breathing period (and not before breathing commences) is worth exploring.

A general limitation of this technique is that other causes for regions of the lung to be ventilated but not perfused (for example lung bullae) cannot be distinguished from pulmonary embolism, and therefore the test is likely to be most reliable in patients with otherwise reasonably normal lungs.

It should be noted that all the PEs in this sample are moderate to severe. Single segment and sub-segmental PEs were not studied and these will have smaller effects on gas exchange and therefore will be more difficult to resolve. Furthermore, without a larger sample to fully investigate false positive and negative incidence it is difficult to draw comparisons to existing diagnostic techniques (CTPA and V/Q scintigraphy).

In addition to providing excellent sensitivity and specificity, clinical imaging techniques (CTPA and V/Q scintigraphy) also give information on the location of PE within the lung. The LNL model consists of many compartments but provides no information on the location of these within the lung. Consequently, the location of a PE cannot be provided by the technique developed herein. Furthermore, the existing technique cannot provide information on the number of PEs. The same total volume of ventilated but unperfused lung can be caused by a single large PE or multiple PEs in smaller-calibre blood vessels. Although fitted results for these scenarios may vary slightly (because multiple smaller PE affected regions may vary in the deadspace volume supplying them and their proportional ventilation), this technique would not be able to determine the number of PEs present.

There are approximately 20 segments in the human lung. If it is assumed that each segment constitutes a similar volume, a pulmonary embolism obstructing the vasculature to a single segment will result in $\sim 5\%$ of the lung being ventilated but not perfused (ignoring any adaptive redistribution of ventilation from the PE segment to perfused regions). In future work, to estimate the extent of a patient's PE, an artificial 2-lung model could be created whose second lung would possesses an identical parameter set to the first with the exception of being entirely unperfused. Ventilation would then be titrated between the two lungs by arbitrary amounts until the experimental and model P_{CO_2} matched. Hence, by estimating P_{CO_2} from the combined model and then comparing these to measured arterialised blood samples a proxy measure of 'perfusion block' in the lungs could be made. Follow-up data on the diagnostic outcome of the suspected PE patients could be used to quantify the fraction of ventilation to the unperfused lung that indicates treatment is required. The goal of this procedure is to determine the percentage of lung tissue that is ventilated but unperfused.

Chapter 7

Validation of model prediction of blood R lines in health

7.1 Introduction

Ideally, a large number of patients suspected of having a PE would have been recruited from the John Radcliffe hospital and studied using blood data from a warmed hand vein. A small sample was obtained in this way (see previous Chapter). However, as a result of the pandemic restrictions I was unable to study this further. This left an incomplete investigation of the hypothesis that the model blood gas would closely match measured values for PE-negative participants. To further test this hypothesis and validate the technique a large sample of PE negative participants was required.

In place of the incomplete PE study, I instead leveraged data from work I was able to conduct on post-COVID patients where there was the opportunity to use the MFS device with concomitant blood gas samples. The aspects relating to COVID-19 are covered in the next Chapter but because patients were studied with the MFS whilst an arterial blood gas sample was collected (during the air-breathing phase of the washout procedure) it allowed calculation of the blood error measure described in the previous Chapter (albeit with arterial blood in place of warmed hand vein samples). Healthy controls and participants who contracted mild-COVID were extracted to allow investigation of the variance of this measure.

All participants had been documented not to have a pulmonary embolism through

CTPA taken on the same day. As these participants are PE-negative the hypothesis is that the LNL-CBGS model can accurately simulate measured blood gases in the absence of a PE.

7.2 Methods

For this validation work, MFS breathing measurements from 118 healthy control and non-hospitalised COVID-19 participants were extracted from the full data set (see the next Chapter for more details). Seated participants breathed air for 7 minutes followed by medical grade oxygen for 5 minutes. Mild COVID-19 participants were included as they only suffered from mild disease symptoms treated at home, similar to other common ailments, and it was not expected that this would effect measures of pulmonary malperfusion. In addition, all participants were scanned using CTPA on the same day and were confirmed to be PE negative.

Ethical approval and a trained clinician was provided for a single arterial blood gas sample from the radial artery in the wrist taken during breathing. Local anaesthetic (lidocaine) was administered to the wrist prior to commencing breathing through the device. This was to minimise discomfort and allow more normal breathing through the device. The first attempt at arterial puncture occurred at around 90 seconds into the air breathing period. Attempts to get a sample continued until the final minute of the air breathing period at which point the experiment continued without an accompanying blood sample.

7.3 Results

Of the 118 data sets from healthy controls and mild COVID-19 patients, 38 arterial blood samples were unsuccessful despite multiple attempts by the clinician in the allotted time period during air breathing. Of the remaining 80 data sets with blood samples all were successfully fitted by the LNL-CBGS model to give results.

For each of the 80 fitted lung and circulatory systems several different lag and averaging times were chosen for comparison to the measured blood sample (see table 7.1). The lag times chosen were 5, 10, 15, 20 and 30 seconds, and the averaging times chosen were 15,

30 and 45 seconds. The lag times were shorter than those chosen for the PE study as the blood samples in this study were arterial as opposed to venous.

Table 7.1. *Blood error statistics at different lag and averaging times.*

Time group	Lag time /s	Averaging time /s	Mean ϵ_B	Stand. dev. ϵ_B
L5A15	5	15	0.10	0.35
L5A30	5	30	0.11	0.32
L5A45	5	45	0.11	0.32
L10A15	10	15	0.12	0.33
L10A30	10	30	0.11	0.32
L10A45	10	45	0.11	0.32
L15A15	15	15	0.11	0.32
L15A30	15	30	0.10	0.33
L15A45	15	45	0.11	0.32
L20A15	20	15	0.11	0.32
L20A30	20	30	0.11	0.32
L20A45	20	45	0.10	0.32
L30A15	30	15	0.09	0.36
L30A30	30	30	0.09	0.33
L30A45	30	45	0.10	0.33
Overall			0.11	0.33

Mean and standard deviation of the blood gas error (measured minus model) for a variety of chosen delay and averaging times.

The lag and averaging times were used to determine the period of time relative to the measured sample that the circulation of the LNL-CBGS model would be used to construct the R lines (see previous Chapter). The closest point on the model R line was then subtracted from the measured gas point to give the blood error (ϵ_B) in kPa. The mean blood error for all the data sets and their corresponding standard deviations are displayed in table 7.1. The combined violin and box and whisker plots in Fig. 7.1 displays this in greater detail. As the boxes are the interquartile range half the observations are located between the boxes.

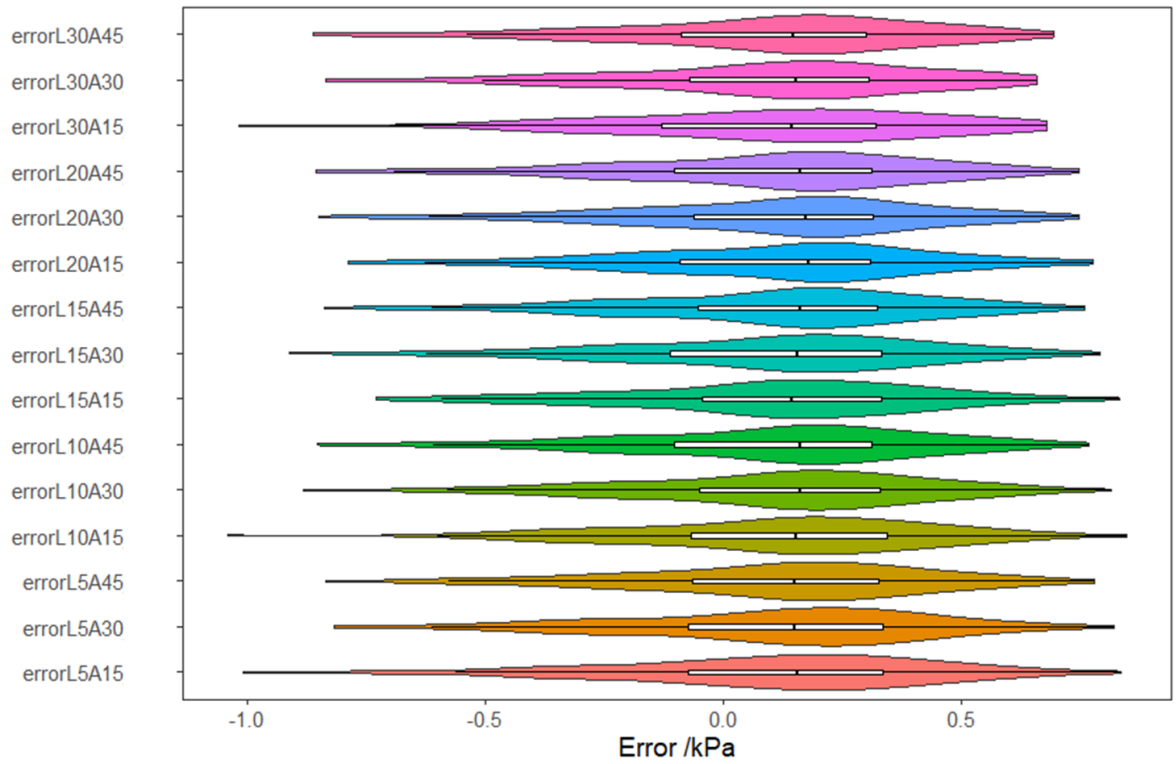

Figure 7.1. Combined violin and box and whisker plots displaying the error between the measured blood sample and the LNL-CBGS simulated blood R-line. The results are shown with varying lag times from the sample measurement to the simulation comparison in seconds (L) and the time in seconds over which the simulation was averaged (A).

7.4 Discussion

The results table and visualisation of the distribution of the data demonstrate that the chosen lag and averaging time have a minimal effect on the ϵ_B results. In all cases there is a slight positive bias of around 0.11 kPa, meaning the measured sample is slightly above the modelled R line. The results of this work are encouraging as there is only a small bias for the model to underestimate the P_{CO_2} in the blood relative to the measured value. As long as the bias is small it is unimportant for the purposes of using this as a diagnostic technique for PE.

An important factor to consider when assessing the feasibility of this method as a diagnostic technique is the variance of the blood error statistic. The variance (in conjunction with the difference in means between PE positive and negative participants) will determine the incidence of false tests. For diagnostic techniques to be adopted clinically these must be sufficiently small.

Fig. 7.1 indicates the distribution could be approximated as normal despite the

presence of some negative skew. The data collected in the previous Chapter has insufficient information to assess whether the PE positive state will also result in a distribution with a mild negative skew. To allow estimates using the available data I will assume both population distributions of ϵ_B can be approximated with normal distributions. The standard deviation of ϵ_B in this sample is approximately 0.33 kPa (all selected timings together). The difference between the means for the PE positive and PE negative groups in the previous Chapter is 0.96 kPa (0.95 - -0.01). It should be noted that the means of each group from the previous Chapter are calculated from a small sample and thus may not be representative of the population means. The sample size (n=3) for the PE positive sample from the previous Chapter is also small to estimate the variance so for these purposes it will be assumed that the variance for PE positive ϵ_B values is the same as for PE negative. Using the variance of ϵ_B from the larger sample of this Chapter (standard deviation=0.33kPa) this would make the two means approximately 3 standard deviations apart (0.956/0.33=2.90). This will result in significant overlap between ϵ_B values for PE positive and negative patients and a high degree of false test results (see Fig. 7.2). However, this may not necessarily mean the test is not of use depending on the cutoff value chosen.

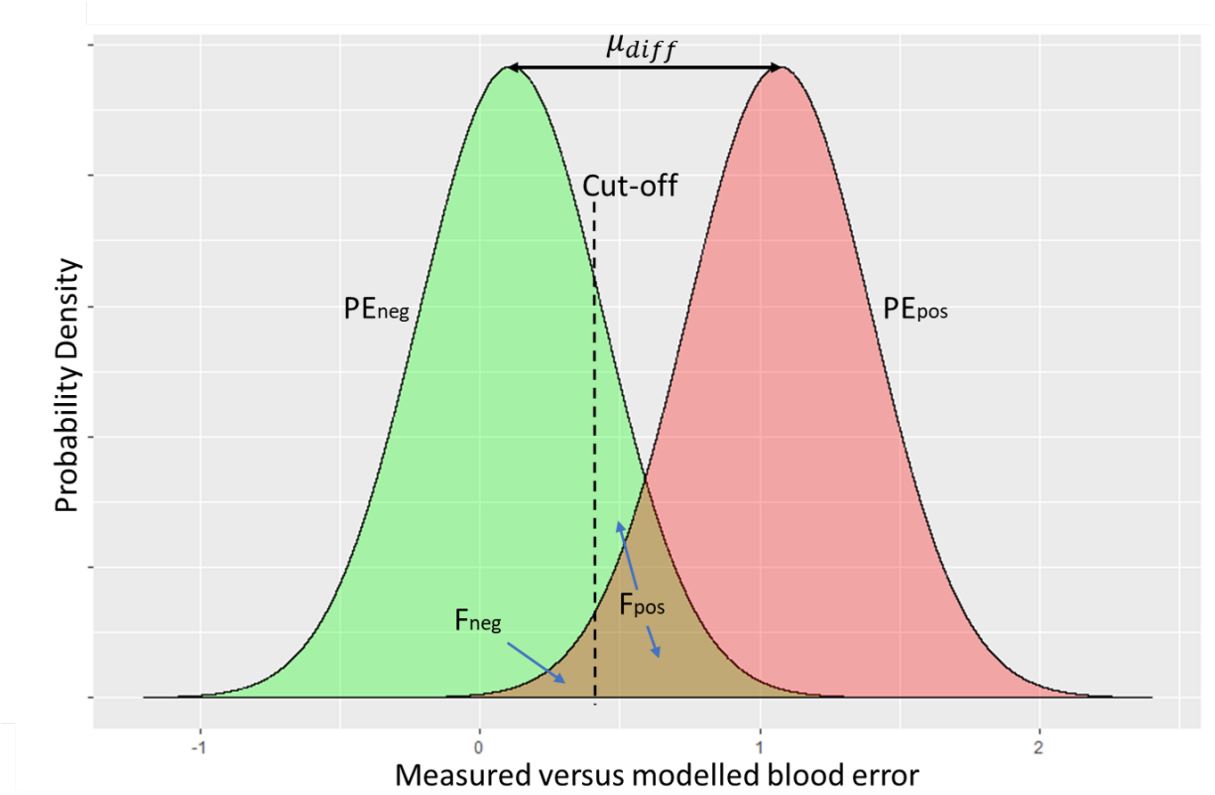

Figure 7.2. Theoretical probability density plot (PDF) of PE positive and PE negative ϵ_B distributions. PE_{neg} = PE negative distribution of ϵ_B values; PE_{pos} = PE positive distribution of ϵ_B values; Green fill = PE negative participants correctly identified; red fill = PE positive participants correctly identified; yellow-brown fill = overlap where PE positive and negative participants are predicted to give the same ϵ_B value; Cutoff = the chosen value for the screening technique to give a negative result; F_{neg} = false negative area; F_{pos} = false positive area; μ_{diff} = the expected difference between the mean ϵ_B for PE positive and negative participants (taken from the previous Chapter). The mean for PE negative participants (0.11 kPa) is based upon the sample mean from this study using mild-COVID and healthy participants. The PE positive mean (1.07 kPa) is estimated by using the range between PE positive and negative sample means from the PE study in the previous Chapter and adding this to the estimated PE negative mean. The variance of both PE positive and negative populations is based on the variance found in this Chapter for PE negative participants (using a measured arterial sample to calculate the blood error term).

The split between false negatives and positives will depend upon the chosen cut-off point for a 'positive' screening result. This technique is intended as a screening tool to reduce the number of patients being exposed to ionising radiation. As such, the false positive rate is much less important because patients falsely identified as positive for PE (along with all others positively screened) would be sent off for CTPA or V/Q scintigraphy scans for confirmation. Therefore, in this case a high false positive rate will not result in overtreatment. However, a high false negative rate would render this useless as a screening technique because these patients would have a PE but be left untreated. Therefore, for the test to be used in clinic, the false negative rate for a given cut-off point must be

considered in detail.

To estimate the sensitivity and specificity I assume i) a mean of 0.11 kPa for PE negative patients (from the findings of this Chapter) ii) a mean 0.96 kPa above this for PE positive patients (0.11+0.96=1.07 kPa) (from the difference between the means from the previous Chapter) and iii) a variance of 0.33 kPa for both. Two standard deviations below the mean of the PE positive group gives a ϵ_B value of 0.41 (=1.07-2(0.33)). Choosing this minimum cut-off point to exclude patients from the PE pathway would result in a false negative rate of 2.3% (assuming a normal probability distribution function). As the means are 2.9 standard deviations apart, this cut-off would result in PE negative patients with values 0.9 standard deviations above the mean being falsely assigned PE positive status. Therefore, the false positive rate would be 18.4%.

In conclusion, the findings here suggest this technique could show success as a supplementary screening test but would still rely on current gold standard techniques. Even with such a high false positive rate the screening test could still be of clinical use as it would remove a large proportion of the patients who do not have a PE from the clinical pathway. This would limit irradiation with a quick and cheap alternative. Further investigation with a larger sample of PE positive patients is indicated.

Chapter 8

Effect of COVID-19 on the cardiopulmonary system

8.1 Introduction

The work in Chapter 6 on PE was prematurely halted due to pandemic restrictions. This Chapter is a result of a change in direction where I was allowed to collect data using the MFS device on a cohort of participants recruited to investigate the physiological effects of COVID-19 after recovery from acute infection. This offered another interesting avenue of research using our developing technique.

When this work commenced, COVID-19 was a new disease and its full effects on physiology were not well characterised. Emerging research from the pandemic suggested COVID-19 infection could result in lingering, long term morbidity (see Chapter 2).

The work in this Chapter aims to test whether the MFS device combined with LNL-CBGS modelling can recover parameters related to the severity of acute COVID-19 disease even after recovery from the acute disease phase. Repeat measures after 6 months allow investigation of recovery from COVID-19 infection in the longer-term.

The primary hypothesis is that COVID-19 will cause pathological changes in LNL-CBGS parameters (for example reduction in effective lung volumes and a more inhomogeneous compliance distribution) although when this work began judgements on which would be affected were purely speculative. Any effects seen were expected to be greater the more severe the acute disease phase. The secondary hypothesis is that any

COVID based effects on the LNL-CBGS parameters will return towards normal baseline values with time as a result of the cardiopulmonary physiology recovering.

This work does not aim to help guide treatment or diagnosis but instead may provide insights into the pathophysiology of the disease and perhaps provide greater information into the underlying causes of post-infection COVID-19 symptoms.

8.2 Methods

8.2.1 Data collection

This study was carried out on a cohort of human participants recruited from British military personnel for the mCOVID (military COVID-19) study. The participants selected were affected by COVID-19 to varying degrees from severe infection and ventilation to mild symptoms that were treated at home. The cohort also included participants who had not recorded COVID-19 symptoms and gave negative antibody tests for COVID-19 to confirm absence of prior infection.

For my work data were collected from 117 participants (25 healthy controls and 92 with confirmed or suspected COVID-19). 66 returned for six month follow-up recordings (for a total of 183 data sets). Of these 115 baseline and 61 follow-up recordings were complete (for a total of 176 data sets). Several tests were aborted due to fainting and anxiety during the protocol (primarily related to the arterial sampling).

Measurements of gas exchange were collected using the molecular flow sensing device (see [8] and Chapter 3). Experiments were carried out with participants connected to the MFS via a mouthpiece and a nose clip to ensure all respiratory gases passed through the measurement head with minimal leakage. The protocol used was the standard nitrogen washout described by Mountain *et al.* [9]) but with a reduced 7 minute air breathing phase followed by the standard 5 minutes of medical oxygen (to washout nitrogen).

Together with MFS breathing data, detailed information was collected from each participant's acute disease period including but not limited to: presence of COVID-19 symptoms, confirmation of COVID-19 infection with PCR and antibody tests, admittance to hospital, admittance to intensive care unit (ICU), ventilation, days of ventilation, use of extracorporeal membrane oxygenation (ECMO) and symptoms.

When grouping COVID-19 severity for analysis we considered 4 groups: 0=healthy controls, 1=symptomatic COVID-19 patients who were not hospitalised, 2=COVID-19 patients who were admitted to hospital and 3=COVID-19 patients who were either admitted to ICU, admitted to ICU and ventilated, and admitted to ICU and given ECMO. Only a handful of participants studied were given ECMO or admitted to ICU without ventilation so they were included in a single 'severe COVID-19' group along with participants who were ventilated (see Fig. 8.1).

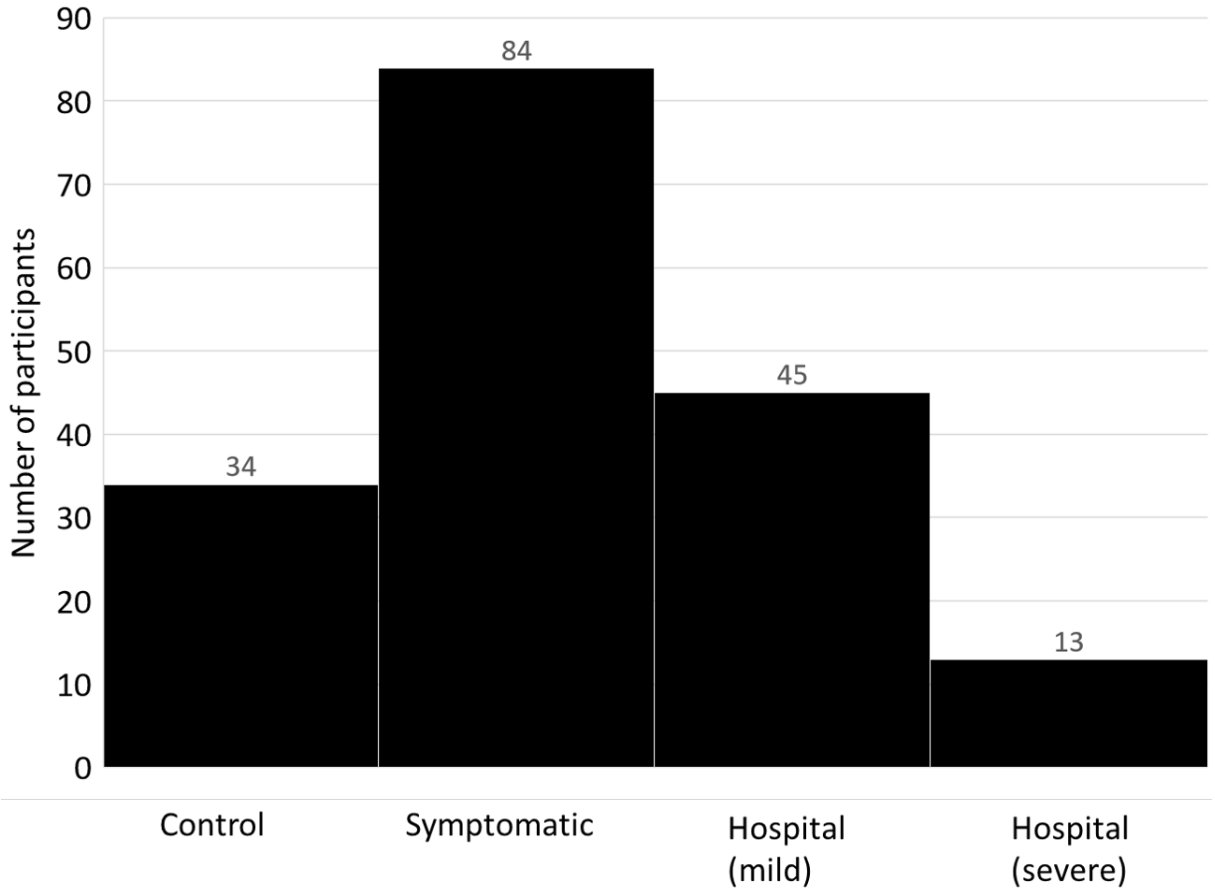

Figure 8.1. Histogram showing the numbers of participants within each COVID severity grouping. Control: the healthy controls who have not had COVID-19, Symptomatic: participants who contracted COVID-19 or had COVID-19 symptoms but were treated in the community, Hospital (mild): participants who were admitted to hospital during acute infection with COVID-19 but were not admitted to ICU, ventilated or given ECMO, Hospital (severe): participants who were admitted to ICU, ventilated or given ECMO as part of their treatment for COVID-19.

All participants were actively employed in the British military and therefore there was some bias on the age and sex of participants relative to the general population. Participant characteristics such as age, weight, height and sex were also collected for use within the CBGS and to estimate BMI (see 8.2). Within our data set sample there were 149 male and 27 female participants.

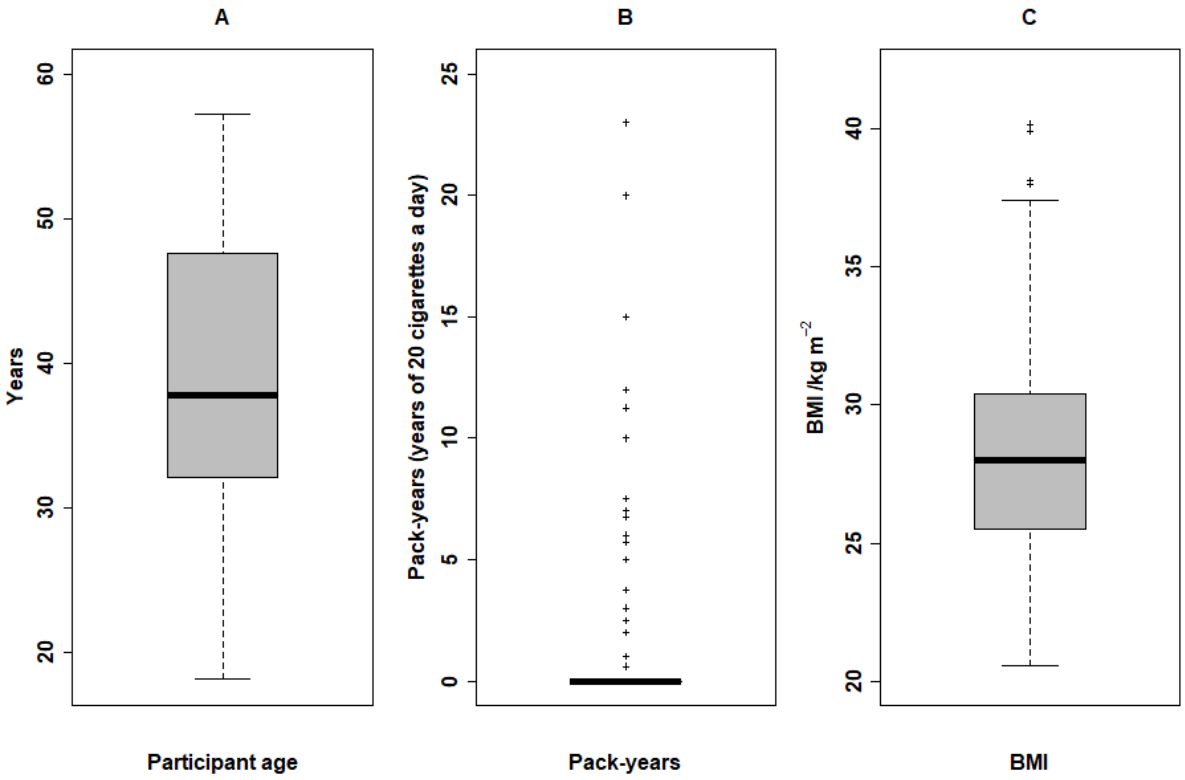

Figure 8.2. Box and whisker plots displaying mCOVID study participant characteristics. A: box and whisker plot showing the participant age in years. B: box and whisker plot showing the participant cigarette smoking pack-years. C: box and whisker plot showing the participant BMI in kgm^{-2}. Central lines indicate the median, boxes display the interquartile range whilst whiskers show the greatest value within 1.5 multiplied by the interquartile range, individual points beyond this display outliers.

8.2.2 Modelling

All MFS breathing data were analysed using the combined LNL-CBGS model. For each data set four optimisation routines with randomised starts were run. This was used to check that the recovered parameters had reached a stable solution. In all cases the optimisation recovered very similar outputs for all 4 runs suggesting that the routine was finding the minima in the space. However, 25 data sets failed to run leaving a total of 151 LNL-CBGS data points.

8.2.3 Statistical analysis

Linear mixed effects (LME) modelling of COVID severity and its relation to LNL lung parameters was undertaken in R [221]. Mixed linear models are flexible, take into account all the data and discard sources of variation in which one is not interested, all in a single model [222]. Mixed linear models are a more powerful test than an ANOVA. They reduce

the probability of a false significant result by incorporating the variance of replicates as well as repeats and can assign variance to several independent factors simultaneously.

The parameters chosen for LME modelling are shown in Table 8.1. The principles used to construct the LME models used here were: A) dependent parameters were outputs of the LNL-CBGS model thought to potentially be influenced by post-infection COVID-19, B) independent factors were either i) factors hypothesised to influence the dependent variables (COVID severity and time from infection depending on COVID status) ii) other participant characteristics believed to be major determinants of the dependent variable in question, and C) random effects factors for which the sample does not exhaust all possible outcomes and for which we expect there to be a random influence upon the data (in this case participant number).

Most LNL-CBGS parameters are as defined previously in Chapter 3 (for the distributions of ventilation, perfusion and dead space) and Chapter 6 (for the blood error calculation). However, FRC and deadspace volume must be standardised through scaling to participant size to allow meaningful comparisons. FRC is investigated as a fraction of the predicted FRC for a participant of that height (f_{FRC}^{pred}) whilst deadspace volume is investigated as a fraction of the same predicted FRC (f_{DS}^{pred}). The measured versus modelled blood partial pressures, ϵ_B, are also considered.

In addition, two values solely from the measured arterial sample (i.e. without any breath data or modelling) are used: i) the measured arterial partial pressure of CO_2, Pa_{CO_2} and ii) the alveolar-arterial gradient for O_2, Aa_{grad}, that is estimated using:

$$Aa_{grad} = (Patm - P_{H_2O})F_{O_2}^I - (Pa_{CO_2}/RQ) - PaO_2 \tag{8.1}$$

where $Patm$ is the atmospheric pressure, P_{H_2O} is the water vapour pressure, $F_{O_2}^I$ is the inspired oxygen fraction, Pa_{CO_2} is the partial pressure of CO_2 in the measured arterial sample, RQ is the respiratory quotient (assumed to be 0.8) and Pa_{O_2} is the partial pressure of O_2 in the measured arterial sample. These measures are commonly used in respiratory medicine and allow us to assess the chronic affect of COVID-19 on gas exchange independently of our modelling.

Table 8.1. *Linear mixed effects modelling parameters.*

Dependent	Independent					Random
σ_{Cl}	$COVIDseverity$	age	$packyears$	R_{6m}	R_{6m}*$COVID_{pos}$	$participant$
σ_{Cd}	$COVIDseverity$	age	$packyears$	R_{6m}	R_{6m}*$COVID_{pos}$	$participant$
σ_{DS}	$COVIDseverity$	age	$packyears$	R_{6m}	R_{6m}*$COVID_{pos}$	$participant$
ϵ_B	$COVIDseverity$	age	$packyears$	R_{6m}	R_{6m}*$COVID_{pos}$	$participant$
f_{DS}^{pred}	$COVIDseverity$	age	$packyears$	R_{6m}	R_{6m}*$COVID_{pos}$	$participant$
f_{FRC}^{pred}	$COVIDseverity$	age	BMI	R_{6m}	R_{6m}*$COVID_{pos}$	$participant$
Pa_{CO2}	$COVIDseverity$	age	$packyears$	R_{6m}	R_{6m}*$COVID_{pos}$	$participant$
Aa_{grad}	$COVIDseverity$	age	$packyears$	R_{6m}	R_{6m}*$COVID_{pos}$	$participant$

Table of dependent, independent and random factors used in linear mixed effects modelling of COVID-19 infection on LNL-CBGS results. The LNL model parameters used as dependent parameters are those listed in Chapter 3, 3.1 in addition to: ϵ_B= minimum error between the measured blood sample and the simulated R-line, f_{FRC}^{pred}=the fitted LNL model FRC divided by the predicted FRC (based upon participant physical characteristics) and f_{DS}^{pred}= the fitted LNL model anatomical deadspace (V_{DP}) divided by the predicted FRC, Pa_{CO2}= the measured arterial partial pressure of CO_2, Aa_{grad}= alveolar-arterial gradient for the partial pressure of O_2. The independent parameters considered in the mixed linear models are: $COVIDseverity$=COVID severity group, age=participant age /$years$, $packyears$=smoking pack-years (1 pack-year=7305 cigarettes), BMI=body mass index /kgm^{-2}, R_{6m}=the baseline and 6 month follow-up readings and the R_{6m} interaction with $COVID_{pos}$= presence of COVID-19 infection. $participant$=participant number and is a random effects factor in all cases which must be included due to the use of repeat measurements in the same participants. $COVIDseverity$, R_{6m}, $COVID_{pos}$ and $participant$ were specified as categorical rather than numerical parameters.

For most LNL model parameters assessed as dependent variables (x=σ_{Cl}, σ_{Cd}, σ_{DS}, f_{DS}^{pred}, ϵ_B, Pa_{CO2} and Aa_{grad}) the structure of the mixed linear model is as follows:

$$x \sim COVIDseverity + age + packyears + R_{6m} * COVID_{pos} + (1|participant) \qquad (8.2)$$

where x is the test variable, the $COVIDseverity$, age, $packyears$ and R_{6m}*$COVID_{pos}$ are fixed effect factors where R_{6m} is modelled as interacting with $COVID_{pos}$. $participant$ is a random effect factor. $COVIDseverity$, R_{6m} and $participant$ were specified as categorical rather than numerical parameters.

The structure of the mixed linear model used to assess LNL model FRC fraction of predicted value (f_{FRC}^{pred}) is structured similarly but includes BMI as an independent factor

due to its known influence on FRC [223]:

$$f_{FRC}^{pred} \sim COVIDseverity + BMI + R_{6m} * COVID_{pos} + (1|participant) \quad (8.3)$$

where f_{FRC}^{pred} is the test variable, $COVIDseverity$, BMI and R_{6m}*$COVID_{pos}$ are fixed effect factors where R_{6m} is modelled as interacting with $COVID_{pos}$. *participant* is a random effect factor. $COVIDseverity$, R_{6m} and *participant* were specified as categorical rather than numerical parameters.

8.3 Results

The effect of COVID-19 severity and other measured parameters on each of the LNL parameters of interest for all 151 successfully modelled data sets are displayed in scatter and box and whisker plots and then analysed using linear mixed effects modelling.

For all box plots in Fig. 8.3, 8.5, 8.7, 8.9, 8.11, 8.13, 8.15 and 8.17 the central line indicates the median, boxes display the interquartile range whilst whiskers show the greatest value within 1.5 multiplied by the interquartile range. Outliers are indicated with points outside the whiskers. In all plots the COVID-19 severity groups are defined as: 0=healthy controls, 1=symptomatic COVID-19 patients who were not hospitalised, 2=COVID-19 patients who were admitted to hospital, 3=COVID-19 patients who were admitted to ICU, ventilated and/or given ECMO.

For all linear mixed effects modelling results shown in Fig. 8.4, 8.6, 8.8, 8.10, 8.12, 8.14, 8.16 and 8.18: *Predictors*=the independent factors whose effect on the dependent variable is accounted for, *Intercept*=the estimate value of the dependent variable at the baseline or zero value for all independent variables (this is always for healthy controls who did not contract COVID-19 and other factors also at baseline/zero), *Estimates*: the estimated change in the dependent variable for a unit change in the independent variable, *CI*: 95% confidence interval of the *Estimates*, *df*: degrees of freedom, p=probability of null hypothesis (shown in bold if the significance is less than 0.05).

Fig. 8.3 suggests an increase in the distribution of lung compliance (σ_{Cl}) with increasing *age* and $COVIDseverity$ and no clear relationship with time after infection (R_{6m}). LME modelling, Fig. 8.4, shows those who suffered from COVID-19 symptoms

and those admitted to hospital but not ICU had significantly higher σ_{Cl} values than healthy controls when accounting for the effects of age, pack-years and recording number with its interaction with presence of COVID-19 infection. However, the patient group who were admitted to ICU with the most severe COVID-19 did not have significantly different σ_{Cl} values to healthy controls. Patient age ($p<0.001$) and pack-years ($p<0.001$) both also had a significant positive effect on σ_{Cl}. The effect size for both is small but a patient who was 50 years old and had been smoking a pack a day for 30 years would have a σ_{Cl} value over double (0.316+0.003x50+0.007x30=0.676) the value extrapolated for a newborn (0.316 the value of the 'Intercept'). The random variation caused by differences between participants for one standard deviation is similar to the estimated change caused by a single year of aging.

Fig. 8.5 suggests no relationships between σ_{Cd} and $COVIDseverity$, R_{6m} or age. This is confirmed by the LME modelling (see Fig. 8.6). As with σ_{Cl}, $packyears$ increase σ_{Cd} statistically significantly ($p=0.001$).

Fig. 8.7 suggests no clear relationships between σ_{DS} and $COVIDseverity$, R_{6m} or age. However, LME modelling (see Fig. 8.8) finds a statistically significant ($p<0.001$) relationship between age and σ_{DS}.

Both plots (Fig. 8.9) and LME modelling (Fig.8.10) indicate no statistically significant relationships between any tested parameters and the error between measured and simulated blood ϵ_B.

Fig. 8.11 indicates that $COVIDseverity$ and age significantly increase the anatomical deadspace volume (when expressed as a fraction of the predicted FRC; f_{DS}^{pred}). This is supported by LME modelling (Fig. 8.12) where both hospitalised groups of participants (but not mild symptomatic participants treated in the community) gave significantly ($p=0.012$ and $p<0.001$) higher values of f_{DS}^{pred} than healthy controls when accounting for the effects of age, $packyears$ and R_{6m}. The effect size was greater in the participant group admitted to ICU than the group admitted only to the general hospital. Increasing patient age also increased f_{DS}^{pred} with statistical significance ($p<0.001$).

FRC as a fraction of the predicted value (f_{FRC}^{pred}) appears to decrease with $COVIDseverity$ and BMI (Fig. 8.13). As the predicted FRC is based upon simple participant physical characteristics of height and sex, departure from this value either

represents random biological variation or environmental factors. LME analysis shown in Fig. 8.14 reveals a significantly lower f_{FRC}^{pred} for both hospitalised groups of participants relative to healthy controls (p=0.005 and p=0.018) when accounting for the effects of age, BMI, R_{6m} and R_{6m} with an interaction with COVID-19 disease presence. In addition, the effect on FRC is greater in the group that was admitted to ICU and was afflicted with more severe disease.

Plots for Pa_{CO2} (Fig. 8.15), imply a potential weak correlation with patient age. This is confirmed by LME modelling (Fig. 8.16) which finds a significant (p=0.016) negative influence of age on Pa_{CO2} but no significant effect of COVID-19 infection at any severity level or recording number.

Plots for Aa_{grad} (Fig. 8.17), suggest a potential increase in the width of the alveolar-arterial difference with more severe acute COVID-19. However, LME modelling (Fig. 8.18), finds no significant effect of COVID-19 disease at any severity level. Interestingly, there is a significant effect of COVID-19 interacting with the recording number on the Aa_{grad} value.

8.3.1 σ_{Cl} results

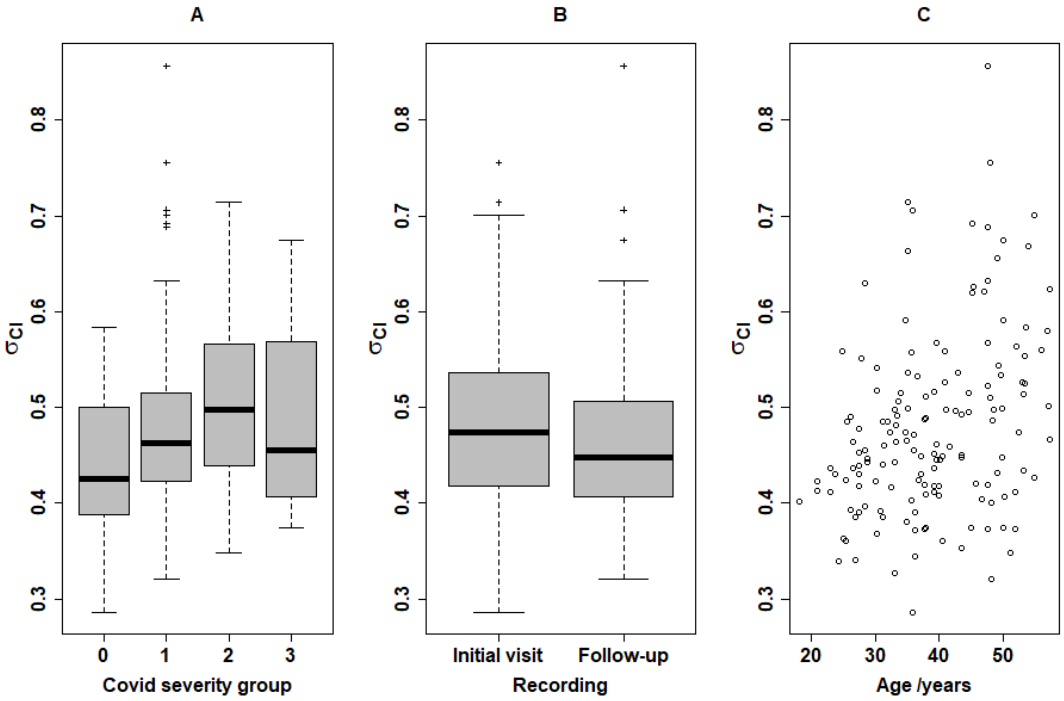

Figure 8.3. Results of the LNL-CBGS modelling with σ_{Cl} as the dependent variable plotted against A: each COVID severity group, B: the initial visit and the 6 month follow-up reading, and C: participant age in years.

	σ_{Cl}			
Predictors	*Estimates*	*CI*	*df*	*p*
Intercept	0.316	0.243 – 0.388	107.310	**<0.001**
Symptomatic	0.057	0.015 – 0.099	129.882	**0.009**
Hospitalised (mild)	0.060	0.012 – 0.109	125.104	**0.016**
Hospitalised (severe)	-0.013	-0.085 – 0.059	97.386	0.717
Patient age /years	0.003	0.001 – 0.005	96.810	**<0.001**
Pack-years	0.007	0.003 – 0.011	84.689	**<0.001**
Follow-up	-0.015	-0.072 – 0.042	82.306	0.601
Follow-up with COVID-19 interaction	-0.015	-0.078 – 0.047	79.592	0.630
Random Effects				
σ^2	0.004			
$\tau_{00\ Participant}$	0.003			
ICC	0.432			
$N_{Participant}$	106			
Observations	151			
Marginal R^2 / Conditional R^2	0.248 / 0.573			

Figure 8.4. Results of the mixed linear model with σ_{Cl} as the dependent variable. Produced using the software R.

8.3.2 σ_{Cd} results

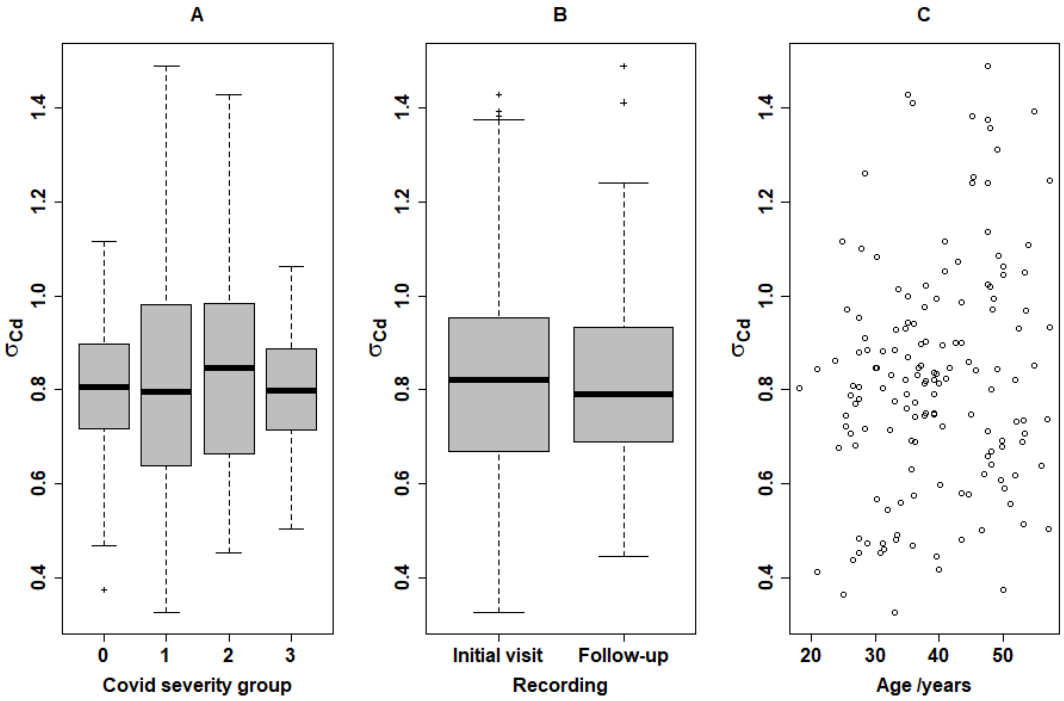

Figure 8.5. Results of the LNL-CBGS modelling with σ_{Cd} as the dependent variable plotted against A: each COVID severity group, B: the initial visit and the 6 month follow-up reading, and C: participant age in years.

	σ_{Cd}			
Predictors	*Estimates*	*CI*	*df*	*p*
Intercept	0.629	0.429 – 0.829	106.953	**<0.001**
Symptomatic	0.029	-0.086 – 0.144	127.229	0.616
Hospitalised (mild)	0.026	-0.107 – 0.159	122.651	0.702
Hospitalised (severe)	-0.131	-0.329 – 0.067	97.690	0.193
Patient age /years	0.004	-0.001 – 0.008	97.928	0.099
Pack-years	0.020	0.008 – 0.031	86.930	**0.001**
Follow-up	0.007	-0.142 – 0.156	77.518	0.926
Follow-up with COVID-19 interaction	-0.032	-0.196 – 0.132	75.134	0.699
Random Effects				
σ^2	0.027			
$\tau_{00\ Participant}$	0.026			
ICC	0.499			
$N_{Participant}$	106			
Observations	151			
Marginal R^2 / Conditional R^2	0.128 / 0.563			

Figure 8.6. Results of the mixed linear model with σ_{Cd} as the dependent variable.

8.3.3 σ_{DS} results

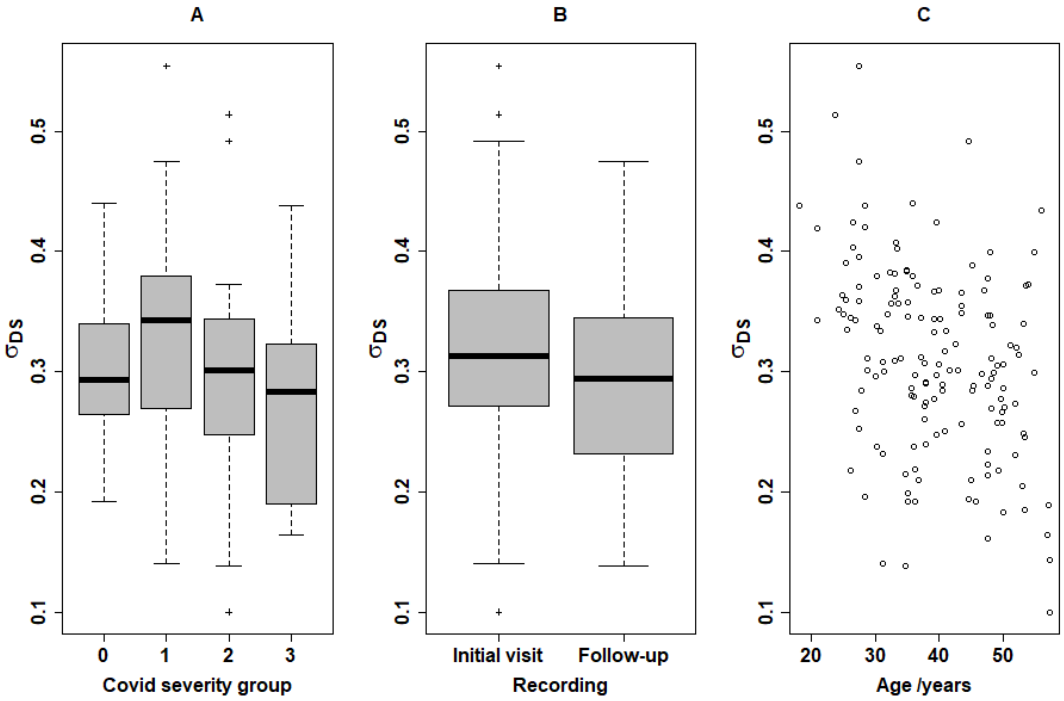

Figure 8.7. Results of the LNL-CBGS modelling with σ_{DS} as the dependent variable plotted against A: each COVID severity group, B: the initial visit and the 6 month follow-up reading, and C: participant age in years.

	σ_{DS}			
Predictors	*Estimates*	*CI*	*df*	*p*
Intercept	0.415	0.353 – 0.477	107.428	**<0.001**
Symptomatic	0.014	-0.022 – 0.050	130.718	0.433
Hospitalised (mild)	-0.001	-0.042 – 0.041	125.890	0.969
Hospitalised (severe)	-0.034	-0.095 – 0.027	97.296	0.267
Patient age /years	-0.003	-0.004 – -0.001	96.427	**<0.001**
Pack-years	0.002	-0.001 – 0.006	83.930	0.199
Follow-up	-0.033	-0.082 – 0.016	83.875	0.188
Follow-up with COVID-19 interaction	0.013	-0.041 – 0.067	81.056	0.630
Random Effects				
σ^2	0.003			
$\tau_{00\ Participant}$	0.002			
ICC	0.409			
$N_{\ Participant}$	106			
Observations	151			
Marginal R^2 / Conditional R^2	0.164 / 0.506			

Figure 8.8. Results of the mixed linear model with σ_{DS} as the dependent variable.

8.3.4 ϵ_B results

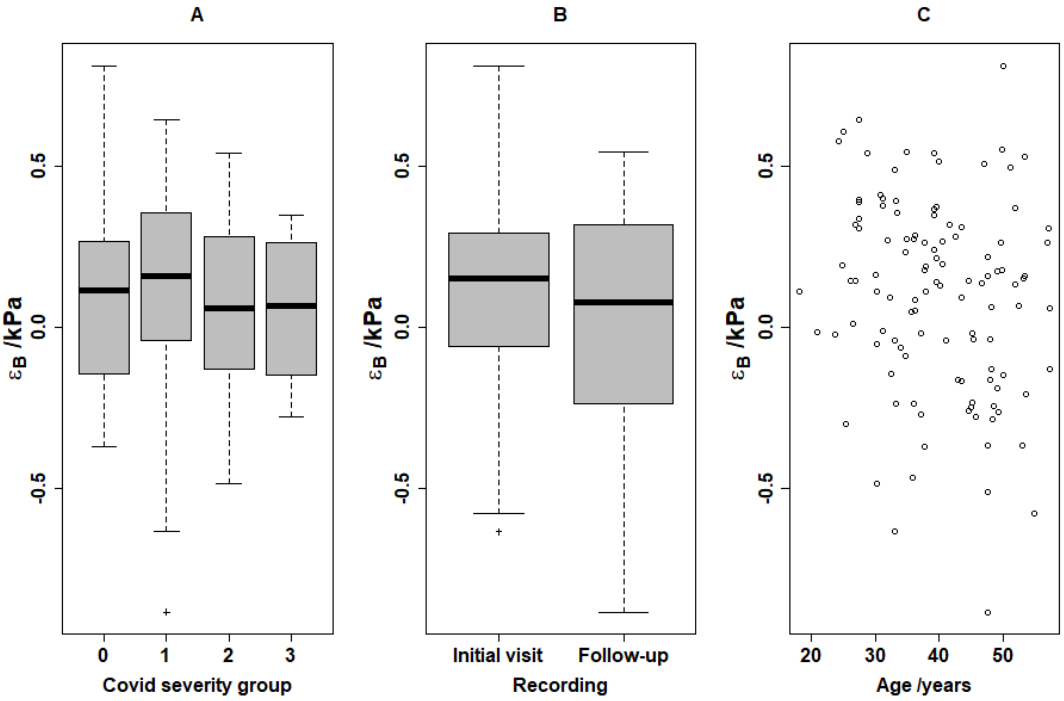

Figure 8.9. Results of the LNL-CBGS modelling with ϵ_B as the dependent variable plotted against A: each COVID severity group, B: the initial visit and the 6 month follow-up reading, and C: participant age in years.

	ε_B /kPa			
Predictors	*Estimates*	*CI*	*df*	*p*
Intercept	0.30	-0.03 – 0.62	87.20	0.070
Symptomatic	0.05	-0.14 – 0.23	102.08	0.621
Hospitalised (mild)	0.07	-0.13 – 0.27	99.71	0.495
Hospitalised (severe)	0.08	-0.19 – 0.36	83.45	0.540
Patient age /years	-0.01	-0.01 – 0.00	76.63	0.144
Pack-years	-0.01	-0.03 – 0.00	71.42	0.105
Follow-up	0.04	-0.22 – 0.30	59.92	0.755
Follow-up with COVID-19 interaction	-0.14	-0.43 – 0.15	59.42	0.326
Random Effects				
σ^2	0.07			
$\tau_{00\ Participant}$	0.02			
ICC	0.26			
$N_{\ Participant}$	87			
Observations	113			
Marginal R^2 / Conditional R^2	0.085 / 0.323			

Figure 8.10. Results of the mixed linear model with ϵ_B as the dependent variable.

8.3.5 f_{DS}^{pred} results

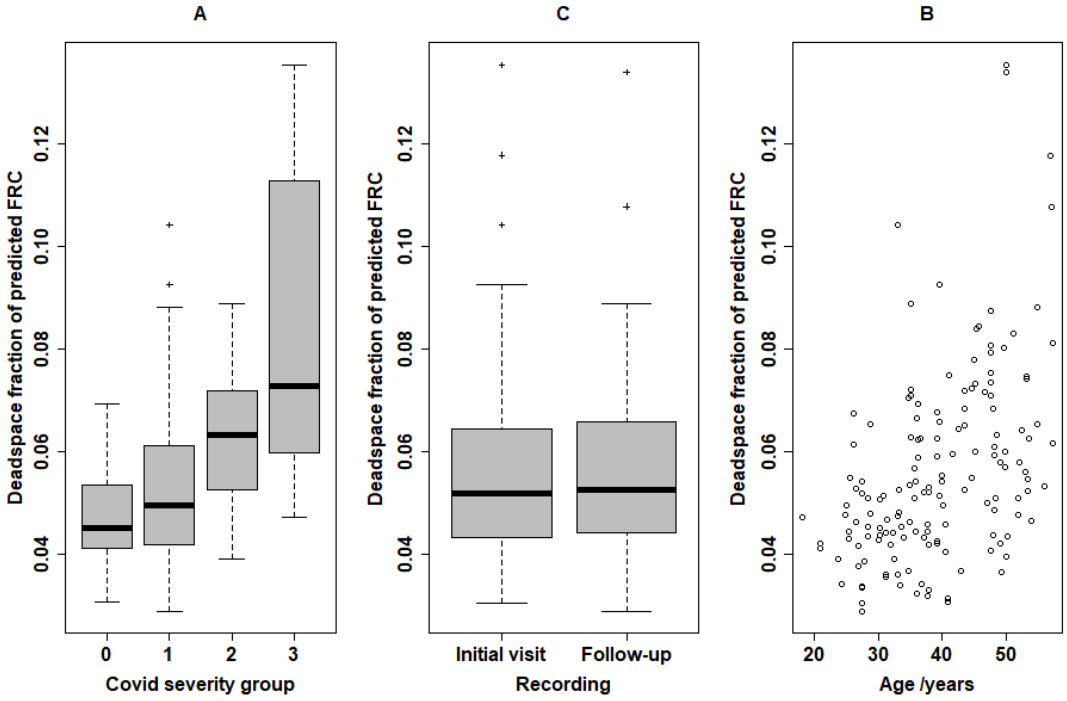

Figure 8.11. Results of the LNL-CBGS modelling with f_{DS}^{pred} as the dependent variable plotted against A: each COVID severity group, B: the initial visit and the 6 month follow-up reading, and C: participant age in years.

	Deadspace fraction of predicted FRC			
Predictors	*Estimates*	*CI*	*df*	*p*
Intercept	0.02210	0.00949 – 0.03472	106.28115	**0.001**
Symptomatic	0.00699	-0.00002 – 0.01400	113.53983	0.050
Hospitalised (mild)	0.01485	0.00667 – 0.02303	110.78464	**<0.001**
Hospitalised (severe)	0.02765	0.01493 – 0.04036	99.19940	**<0.001**
Patient age /years	0.00065	0.00036 – 0.00095	103.31792	**<0.001**
Pack-years	0.00053	-0.00020 – 0.00127	95.36080	0.152
Follow-up	-0.00097	-0.00755 – 0.00560	57.03393	0.768
Follow-up with COVID-19 interaction	-0.00205	-0.00923 – 0.00513	56.11709	0.570
Random Effects				
σ^2	0.00004			
$\tau_{00\ Participant}$	0.00016			
ICC	0.78636			
$N_{Participant}$	106			
Observations	151			
Marginal R^2 / Conditional R^2	0.384 / 0.868			

Figure 8.12. Results of the mixed linear model with f_{DS}^{pred} as the dependent variable.

8.3.6 f_{FRC}^{pred} results

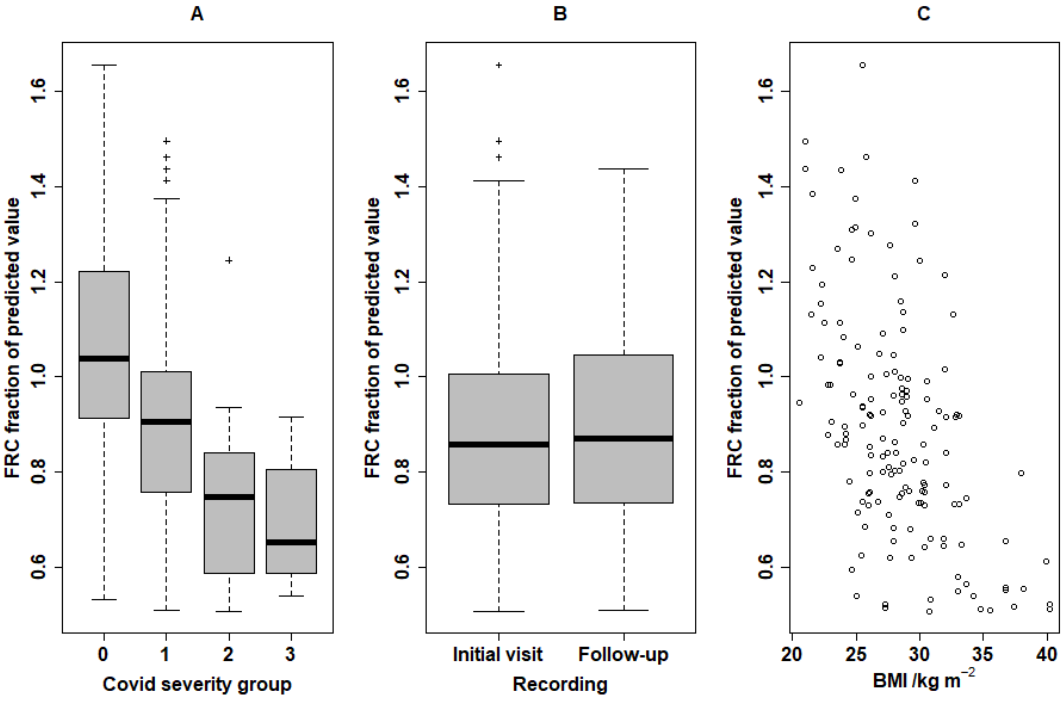

Figure 8.13. Results of the LNL-CBGS modelling with f_{FRC}^{pred} as the dependent variable plotted against A: each COVID severity group, B: the initial visit and the 6 month follow-up reading, and C: participant body mass index in kgm^{-2}.

	FRC fraction of predicted value			
Predictors	*Estimates*	*CI*	*df*	*p*
Intercept	1.622	1.318 – 1.926	103.085	**<0.001**
Symptomatic	-0.075	-0.179 – 0.029	107.409	0.154
Hospitalised (mild)	-0.188	-0.319 – -0.058	105.371	**0.005**
Hospitalised (severe)	-0.218	-0.397 – -0.038	99.904	**0.018**
Patient age /years	-0.000	-0.004 – 0.004	107.573	0.889
Patient BMI	-0.023	-0.033 – -0.012	101.207	**<0.001**
Follow-up	0.060	-0.012 – 0.131	50.528	0.101
Follow-up with COVID-19 interaction	-0.029	-0.107 – 0.049	50.120	0.459
Random Effects				
σ^2	0.005			
$\tau_{00\ Participant}$	0.035			
ICC	0.881			
$N_{Participant}$	106			
Observations	151			
Marginal R^2 / Conditional R^2	0.339 / 0.922			

Figure 8.14. Results of the mixed linear model with f_{FRC}^{pred} as the dependent variable.

8.3.7 Pa_{CO2} results

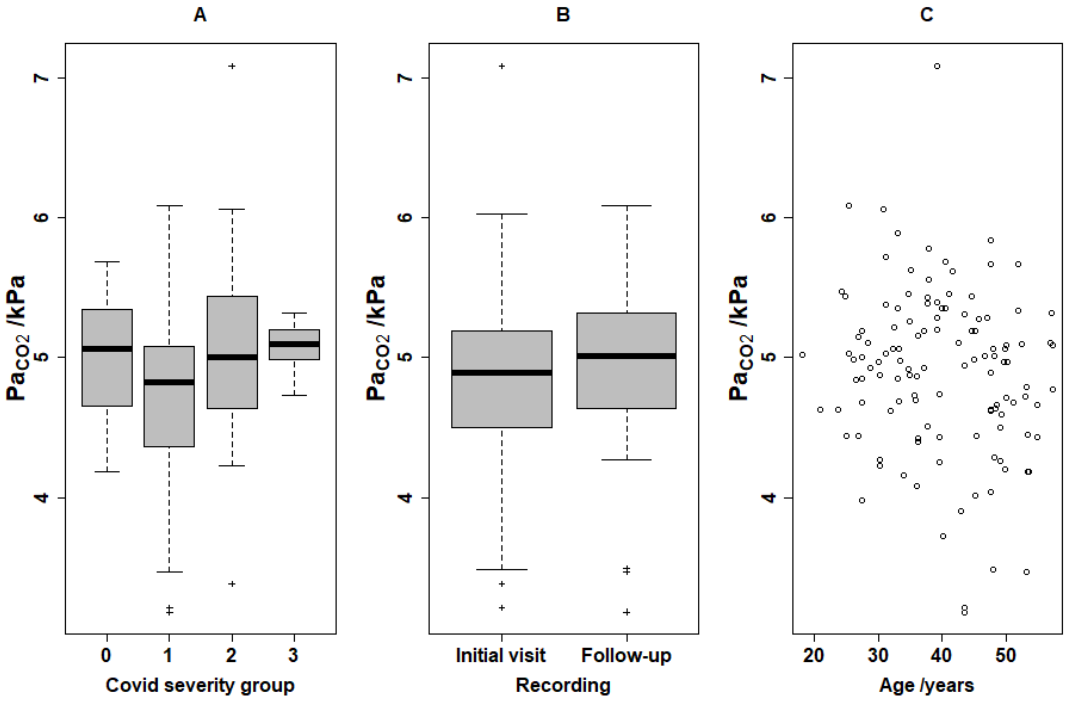

Figure 8.15. Results of measured arterial Pa_{CO2} as the dependent variable plotted against A: each COVID severity group, B: the initial visit and the 6 month follow-up reading, and C: participant age in years.

	Pa_{CO2} /kPa			
Predictors	*Estimates*	*CI*	*df*	*p*
Intercept	5.58	4.97 – 6.18	87.29	**<0.001**
Symptomatic	-0.27	-0.61 – 0.07	104.18	0.122
Hospitalised (mild)	0.16	-0.22 – 0.54	103.61	0.402
Hospitalised (severe)	0.20	-0.32 – 0.73	88.95	0.447
Patient age /years	-0.02	-0.03 – -0.00	77.08	**0.016**
Pack-years	-0.01	-0.04 – 0.02	80.37	0.667
Follow-up	0.19	-0.22 – 0.60	53.72	0.357
Follow-up with COVID-19 interaction	-0.05	-0.51 – 0.41	53.17	0.836
Random Effects				
σ^2	0.17			
$\tau_{00\ Participant}$	0.15			
ICC	0.48			
$N_{Participant}$	89			
Observations	121			
Marginal R^2 / Conditional R^2	0.134 / 0.546			

Figure 8.16. Results of the mixed linear model with Pa_{CO2} as the dependent variable.

8.3.8 Aa_{grad} results

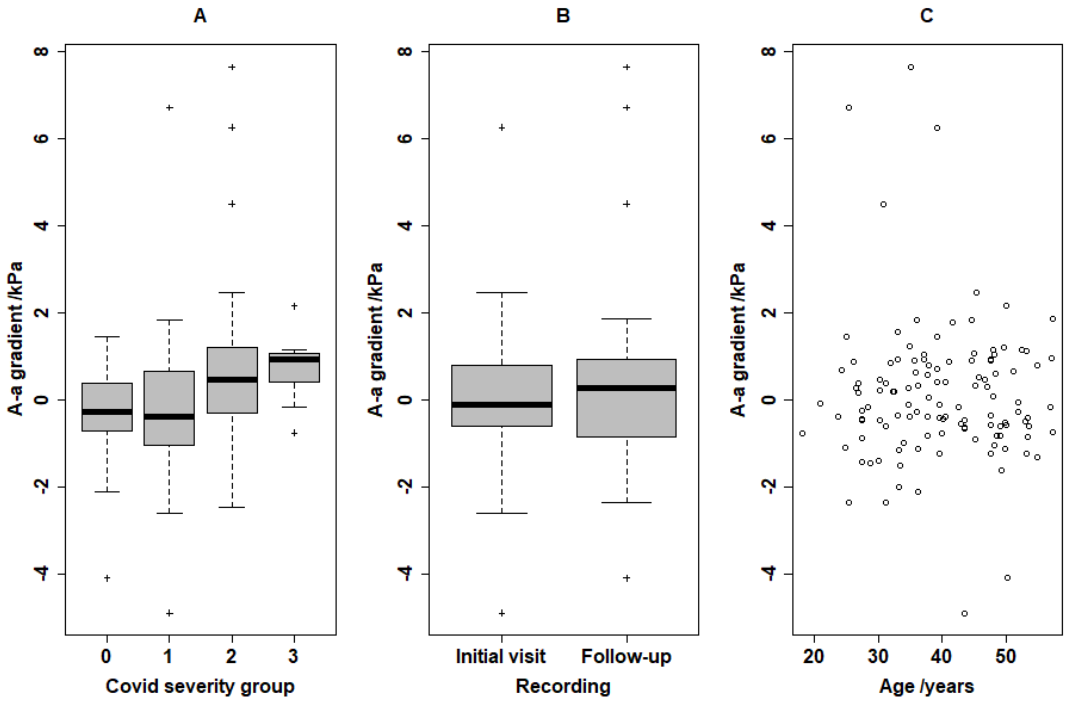

Figure 8.17. Results of the arterial gas based estimate of Aa_{grad} as the dependent variable plotted against A: each COVID severity group, B: the initial visit and the 6 month follow-up reading, and C: participant age in years.

	A-a gradient /kPa			
Predictors	*Estimates*	*CI*	*df*	*p*
Intercept	0.98	-0.53 – 2.49	86.78	0.201
Symptomatic	-0.55	-1.46 – 0.36	111.79	0.231
Hospitalised (mild)	0.79	-0.22 – 1.81	110.72	0.124
Hospitalised (severe)	0.53	-0.81 – 1.86	92.07	0.434
Patient age /years	-0.02	-0.05 – 0.01	67.91	0.139
Pack-years	0.01	-0.06 – 0.08	72.07	0.773
Follow-up	-0.98	-2.31 – 0.35	75.32	0.145
Follow-up with COVID-19 interaction	1.63	0.15 – 3.12	75.02	**0.032**
Random Effects				
σ^2	2.27			
$\tau_{00\ Participant}$	0.00			
$N_{Participant}$	89			
Observations	121			
Marginal R^2 / Conditional R^2	0.174 / NA			

Figure 8.18. Results of the mixed linear model with Aa_{grad} as the dependent variable.

8.4 Discussion

LME modelling uncovers several statistically significant relationships between LNL-CBGS parameters and both disease severity and patient characteristics. In several cases, when viewed as simple scatter and box plots the relationships are less clear. Presumably, this is because the LNL parameters are influenced by multiple independent factors in addition to COVID-19 severity such as age, pack-years and BMI. This makes it difficult to observe a relationship in isolation whilst LME modelling allows disentangling of the relationship between these parameters and the COVID-19 severity. It is worth noting that pre-existing conditions are not controlled for in this analysis. These (potentially confounding) conditions could also predispose patients to more severe COVID-19 and thus underlie or contribute to the observations attributed to COVID-19 disease.

COVID-19 had a statistically significant effect on σ_{Cl}, f_{DS}^{pred} and f_{FRC}^{pred}. For the LNL-CBGS parameters describing volumes (f_{DS}^{pred} and f_{FRC}^{pred}), only COVID-19 sufficiently severe to cause hospitalisation resulted in a significant change in their values. For both parameters the effect size was larger in the more severely diseased group admitted to ICU suggesting an increase in pathological pulmonary volume changes with disease severity. In both cases the observed change reduces effective lung function with increasing disease severity; f_{DS}^{pred} increases meaning there is a greater percentage of the lung air which is deadspace and thus unavailable for gas exchange whilst the f_{FRC}^{pred} decreases resulting in a smaller total volume for gas exchange. These effects will compound each other. Surprisingly, the most severe COVID-19 group did not have significantly different σ_{Cl} values from healthy controls unlike the symptomatic(mild) and less severely hospitalised groups. The reasons for this are unclear but may be related to the small sample size in the severely hospitalised group. Additionally, although statistically significant, the effect size of both symptomatic and mild hospitalisation with COVID-19 is small. The increase in σ_{Cl} in both COVID-19 groups of around 0.06 is the same as the difference the LME modelling attributes to only 20 years of healthy ageing.

The statistically significant relationship between age and the width of the pulmonary compliance distribution (σ_{Cl}) reproduces the findings of a previous smaller (N=12) study using the MFS and LNL [9]. In my work, participant age also had a significant affect on the width of the distribution of anatomical deadspace (σ_{DS}) and the volume of deadspace

as a fraction of predicted FRC (f_{DS}^{pred}). These results are not unexpected. Ageing causes a loss of alveoli and stiffening of the lungs due to increased collagen production by fibroblasts at the expense of elastin production [224]. The LNL-CBGS model's ability to detect these changes is encouraging and serves to validate the accuracy of the model lung recovered for each participant.

Cigarette smoking was found to affect both σ_{Cl} and σ_{Cd}. Indeed, a single pack-year resulted in over twice the increase in σ_{Cl} than that caused by one year of ageing. Furthermore, cigarette smoking was found to have a significant detrimental effect on the width of the distribution of blood flow to the lungs (σ_{Cd}). The underlying cause of this change in σ_{Cd} with pack-years could be due to the pathological remodelling of pulmonary arterioles and arteries in response to cigarette smoke as shown in animal models [225].

The observed reduction of f_{FRC}^{pred} with increasing BMI is supported by previous work in the literature [223]. Forno *et al.*, using fraction of predicted FRC, found a decrease in 0.17 for overweight/obese and 0.21 for obese participants. The findings in this Chapter are remarkably similar. For an increase in BMI from a normal 22 kgm^{-2} to an overweight 27 kgm^{-2}, FRC decreases by 0.165=(-0.023x5). For an increase in BMI from a normal 22 kgm^{-2} to an obese 32 kgm^{-2}, FRC decreases by 0.23=(-0.023x10). The LNL-CBGS model lung volume is reproducing behaviour observed using a different device and technique to measure FRC.

Neither, age, COVID-19 severity, recording number nor pack-years had an effect on the error between modelled and measured blood gas values (ϵ_B). This is an encouraging finding for its hypothesised use as a metric for diagnosis of PE as indifference to other disease and participant characteristics could allow greater specificity for PE. Due to COVID-19's known pathological effects on pulmonary vessels [226], one might expect specific increases in ϵ_B analogous to those seen in PE (see Chapter 6). COVID-19 virus infects human hosts via the angiotensin-converting enzyme 2 receptor which is expressed in vascular endothelial cells [227]. As these line the entire pulmonary vasculature, viral infection results in widespread pathology including thrombosis, endothelial inflammation and dysfunction [228, 229]. Indeed pulmonary vessel dysfunction underlies the hypoxemia observed in severe COVID-19 cases where lung ventilation is maintained but the lung still fails to appropriately oxygenate the blood. Uniform pathological changes in perfusion

would not be expected to cause changes in ϵ_B. Diseases are rarely uniform but even increases in perfusion inhomogeneity that retain a unimodal distribution should be detected by an increase in σ_{Cd} and not ϵ_B. Only a bimodal distribution of $\dot{V}_A/\dot{Q}$ ratio is expected to be detected as an increase in the error between modelled and measured blood gas. Hence, although COVID-19 causes blood vessel pathology, it presumably affects the entire lung vasculature in a unimodal (but heterogeneous) manner rather than as a specific diseased region as in PE (which creates a bimodal distribution). Furthermore, although COVID-19 can result in PE [229] (and some of the patients suffered from this during the acute disease phase) none had detectable PEs on the day of study. As such the lack or relationship between COVID-19 and ϵ_B is congruent.

Perhaps surprisingly, the follow-up recording did not significantly modulate any of the LNL-CBGS parameters. This implies that pathophysiological changes in anatomical deadspace and FRC caused by a COVID-19 infection severe enough to warrant hospitalisation remain for at least 6 months. Other work using CT scans, six months after infection, showed apparent fibrosis in the lungs of over 30% of patients who had recovered from severe COVID-19 [230]. Similarly to the results presented here, this effect was correlated with disease severity. In a sample of patients who were mechanically ventilated, high resolution CT scans three months after recovery showed residual complications such as fibrosis, reduced lung capacity and diffusion capacity in almost all cases [231]. This suggests the mechanism underlying our observation of reduced alveolar and increased deadspace volume could be alveolar destruction and/or damage to the alveolar-capillary membrane. The former would reduce total lung volume whilst the latter would increase the proportion of apparent deadspace volume by making affected regions unable to partake in gas exchange. Both of these effects are likely permanent. Furthermore, since loss of alveoli would result in smaller lungs, the chest wall space would be reduced at FRC and its outward traction force increased. This in turn would also expand the dead space. Altogether, this has concerning implications for the recovery of those with severe disease. However, other compensatory mechanisms may nullify most or all of these effects in the long term. There is a marked reduction in observed exercise tolerance in COVID-19 survivors [232]. However, this was not related to respiratory or cardiac limitations, at least after mild COVID-19 disease, but a result of anaemia, reduced extraction by the muscles

and other peripheral factors. Therefore, good functional recovery could be expected from most survivors of COVID-19 following a graded exercise regime.

Both parameters exclusively defined by the blood test, Pa_{CO2} and Aa_{grad}, do not use MFS breathing measurements or LNL-CBGS modelling. Physiologically, Pa_{CO2} is primarily determined by the homeostatic mechanism controlling body CO_2 storage and acidity. The lack of a relationship between measured Pa_{CO2} and disease severity suggests that the mechanisms regulating the ventilatory set point are not affected by COVID-19. Medical use of arterial blood gas testing to probe respiratory health is not uncommon. Alveolar-arterial oxygen differences (Aa_{grad}) increase in states of $\dot{V}/\dot{Q}$ mismatch and shunt. Perfect matching would result in perfect equilibration between air and blood, and therefore no difference between alveolar and arterial partial pressures. Since no COVID-19 severity group is associated with an increase in Aa_{grad}, this implies the lungs have not lost efficiency due to either shunt or increased $\dot{V}/\dot{Q}$ mismatch. Without more accurate estimates of alveolar oxygen partial pressure, this alone cannot be used to rule out any loss of lung efficiency post-COVID-19 (see next paragraph). However, this finding is in keeping with LNL-CBGS parameter findings. Regarding lung inhomogeneity, COVID-19 had a significant, but clinically negligible, effect on σ_{Cl} and no significant effect on σ_{Cd} and σ_{DS}. Significant and major changes in deadspace and alveolar volume with COVID-19, as estimated by the LNL-CBGS, would not be expected to generate a change in Aa_{grad} because they do not influence the partial pressures found in alveolar gas.

The Aa_{grad} is expected to have a mean value of 1 kPa in healthy young controls and increase as the lung becomes less efficient at exchanging gas with age [233]. However, the mean value found here is around 0.1 kPa and the coefficient of the effect of age is negative (although not statistically significant). The most likely explanation for these unexpected values is the assumption of a normal respiratory quotient of 0.8 is incorrect. The arterial samples were collected whilst the participant breathed through the MFS device. Hyperventilation, as is commonly found when humans are placed on breathing apparatus, results in a reduction in alveolar CO_2 and an increase in alveolar O_2. The apparent respiratory quotient measured at the mouth also rises, even to values well above one (thus moving away from the true metabolic respiratory quotient). The assumed respiratory quotient of 0.8 is used to estimate alveolar P_{CO_2}, which is used to calculate

the Aa_{grad}. This is a good example of why detailed and holistic modelling of the lung and circulation is superior to simple analyses. The modelling described in this thesis allows one to successfully recover measures of underlying physiology through accounting for the influence of experimental perturbations and controlling for other sources of variation.

Chapter 9

The lung under enhanced gravity

9.1 Introduction

This Chapter describes work conducted early in my doctoral studies to validate a central part of the LNL model. The LNL fits a set of parameters to measured expired gas compositions (see Chapter 3). Qualitatively, the expired gas compositions exiting a perfectly homogeneous lung would resemble a square wave (with some smearing due to longitudinal mixing between the dead space and alveoli). In healthy lungs this is never the case and the wave is smeared due to i) natural anatomical variation, ii) normal inhomogeneity in the dead space and iii) normal inhomogeneity in the compliance. The more smeared the expired gas composition profiles the greater the inhomogeneity in the distribution of ventilation (σ_{Cl}) and/or the greater the inhomogeneity in the distribution of the deadspace (σ_{DP}) (see Chapter 3). However, the degree to which the LNL is capable of separating these two physiological properties and distinguishing the underlying contributions to the smearing of the expired profile was unknown.

Gravity has a pronounced effect on lung physiology and function (see Chapter 2). Indeed, gravitational forces experienced at rest on Earth cause the lung to deform, affecting the distribution of ventilation and perfusion across the lung and also the degree of $\dot{V}/\dot{Q}$ matching. Acceleration can increase or decrease the magnitude of these effects depending on how the force vector aligns with the Earth's gravitational pull.

I took the opportunity to take measurements in seated and supine human participants under varying gravity levels [234]. Previous experiments utilising functional electrical

impedance tomography (EIT) [235] and radiology [236, 237, 238] have shown varying gravity causes perturbations in the perfusion and ventilation distributions across the lung, and the ventilation-perfusion correlation whilst not affecting the distribution of anatomical deadspace. These are parameters fitted by the LNL model.

Thus, this final chapter is a validation of the assessment of anatomical deadspace and its variance within the model. The primary aim is to test whether the current LNL modelling is capable of correctly distinguishing between the effects of ventilation and deadspace distributions on expired gas profiles. Under enhanced gravity the model should identify an increase in compliance distribution with no concurrent increase in the deadspace distribution. The ability for the model to correctly achieve this is important as a basis for the work undertaken in this thesis (because correctly estimating dead space is essential to the positioning of the blood R-line used to rule out PE).

9.2 Methods

9.2.1 Experimental methods

To investigate the effect of gravity on the cardiopulmonary system, participants were exposed to acceleration forces three times the acceleration experienced due to gravity on Earth ($9.81 m/s^2$) whilst breathing data were collected using the MFS. Other concurrent measurements were taken including pulse oximetry [234].

All participants had their fitness to undergo centrifuge exposure assessed by a medical officer prior to the study. The study was approved by the King's College London and QinetiQ Research Ethics Committees and was conducted in accordance with the Declaration of Helsinki. All subjects provided written informed consent.

Acceleration was achieved by spinning participants on a human centrifuge used for Airforce jet fighter training at Farnborough (credit Qinetiq 9.1). When the gondola on the end of the centrifuge arm spins, centripetal acceleration acting inwards causes a resultant inertial force away from the spin centre as per Newton's third law.

The protocol was undertaken under two conditions following the convention used in previous work with the gravitational force: (i) anteroposterior acting towards the spine ($+Gx$) and (ii) longitudinal to the axis of the body acting towards the feet ($+Gz$). For



Figure 9.1. The Qinetiq human centrifuge in Farnborough. Experimental team pictured.

$+Gx$, 11 participants were studied. For $+Gz$, 8 participants were studied.

Participants were placed in the centrifuge gondola (Fig. 9.2) in either the seated (x) or supine (z) position and underwent a nitrogen washout before, during and after being exposed to either $3Gx$ or $3Gz$. Washouts consisted of collecting gas flow data using the MFS during 10 minutes of normal air breathing followed by 5 minutes of medical grade oxygen (the longer technique originally used by Mountain *et al.* [9]). Medical oxygen contains around 99% oxygen which washes nitrogen out the lungs. In between each of the three measurements, ten minutes were given for the participant to rest in the gondola and wash back in atmospheric levels of nitrogen to their lungs.

Unlike other experimental work in this thesis, constant through-flow of oxygen during the washout was not permissible as gondola oxygen levels could not be allowed to rise for fire safety reasons. Instead, inspiratory gases were supplied to the centrifuge gondola via inflatable balloons with a one way demand regulator connected to the mouth piece to ensure inspiratory gas was uniform and rebreathing was negligible. The mouthpiece and nose clip were fixed in place using a face mask.

In addition to these data, three of the subjects had their systemic arterial blood sampled during every condition in both arms of the experiment.

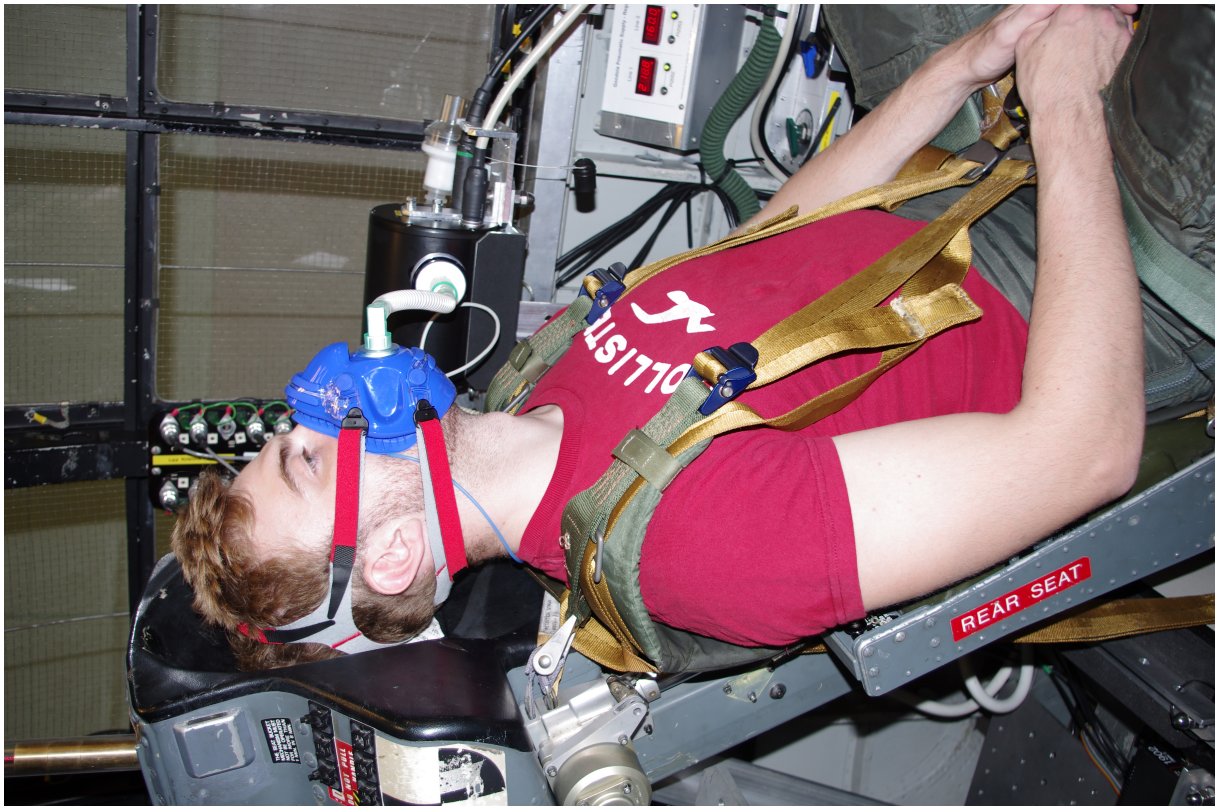

Figure 9.2. The centrifuge gondola equipment setup. The MFS can be seen connected to the mouth piece and supporting face mask via a connecting tube.

9.2.2 Statistical methods

Linear mixed effects (LME) modelling was used to assess the effect of enhanced gravity on LNL model parameters. The structure of the LME model *parameter.mdl* used was:

$$parameter \sim gravity + age + height + weight + (1|subject) \tag{9.1}$$

shown using R statistical programme notation where *parameter* is the test variable (either σ_{Cl} or the standardised deadspace distribution), the *gravity*, *age*, *height* and *weight* are fixed effect factors and *subject* is a random effect factor.

9.3 Results

The LNL non-linear optimisation routine successfully recovered parameter values for all 11 participant nitrogen washouts in the Gx protocol and 7 out of 8 participants who undertook the Gz protocol (the excluded participant having removed his mouthpiece during the procedure).

The parameter describing the width of the standard deviation in dead space (σ_{DP}) was standardised between subjects by multiplying it by the ratio of dead space volume divided by alveolar volume. This compound parameter appears to be indifferent to effects of Gx and Gz (Fig. 9.3).

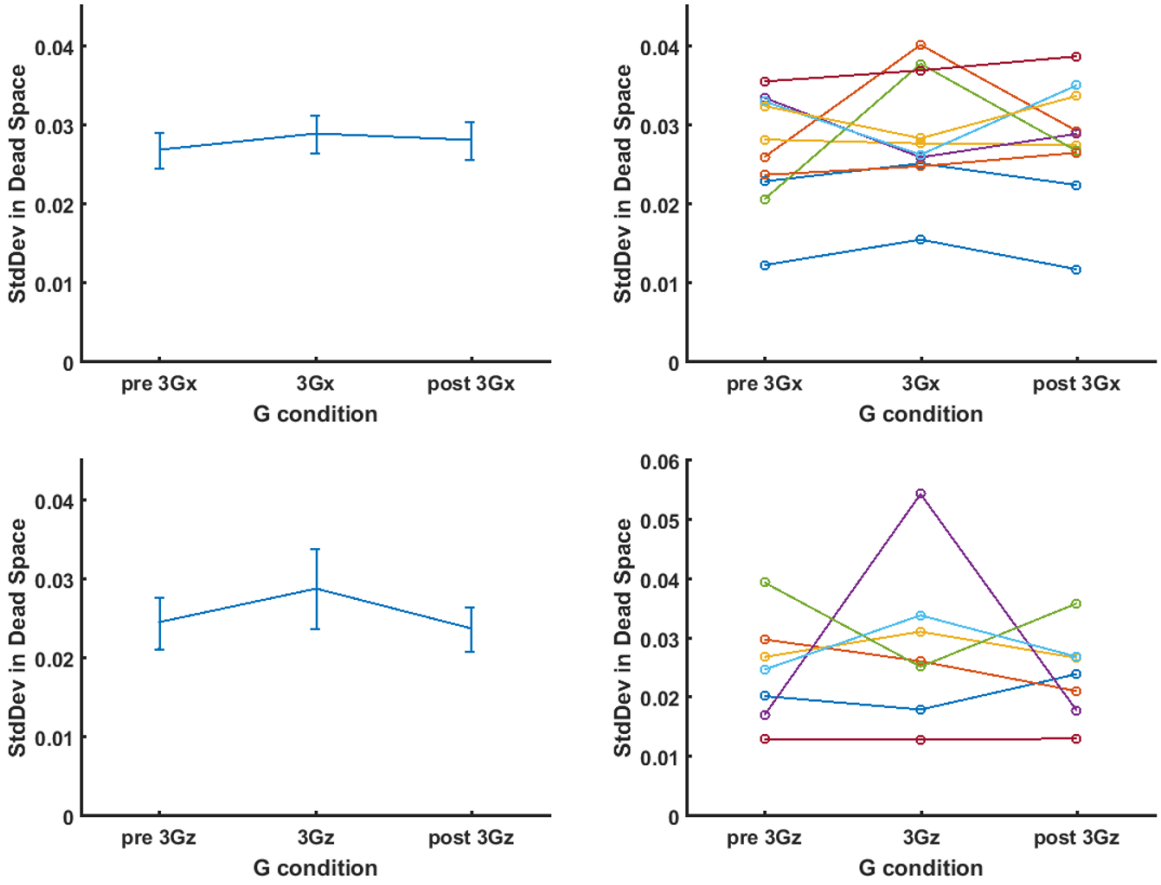

Figure 9.3. The width of distribution in the standardised deadspace recovered from the LNL model simulation of the nitrogen washouts before, during and after exposure to 15 minutes of enhanced gravity. Standardised dead space distribution is equal to the width of the standard deviation of the deadspace multiplied by the ratio of deadspace and alveolar volume. The left hand panels display the standard error of the mean of the data whilst the right hand panels display the results for each individual participant. The upper panels show the response to the Gx orientation whilst the lower panels are Gz orientation.

Contrastingly, the width of the standard deviation in lung compliance (σ_{Cl}) showed an increase with gravity exposure from baseline values for all subjects under both Gx and Gz and a marked aggregate increase in the mean compliance distribution and the standard deviation of this distribution width with Gx (Fig. 9.4). The compliance distribution rapidly returned to a lower value after 3G exposure (similar to the pre-exposure value) for all participants bar two in the Gx and one in the Gz protocol.

Mixed linear modelling of the lung compliance in R [221] (see eq. 9.1) showed that the $3Gx$ and $3Gz$ treatments gave significantly different ($p<0.05$) σ_{Cl} values to both baseline

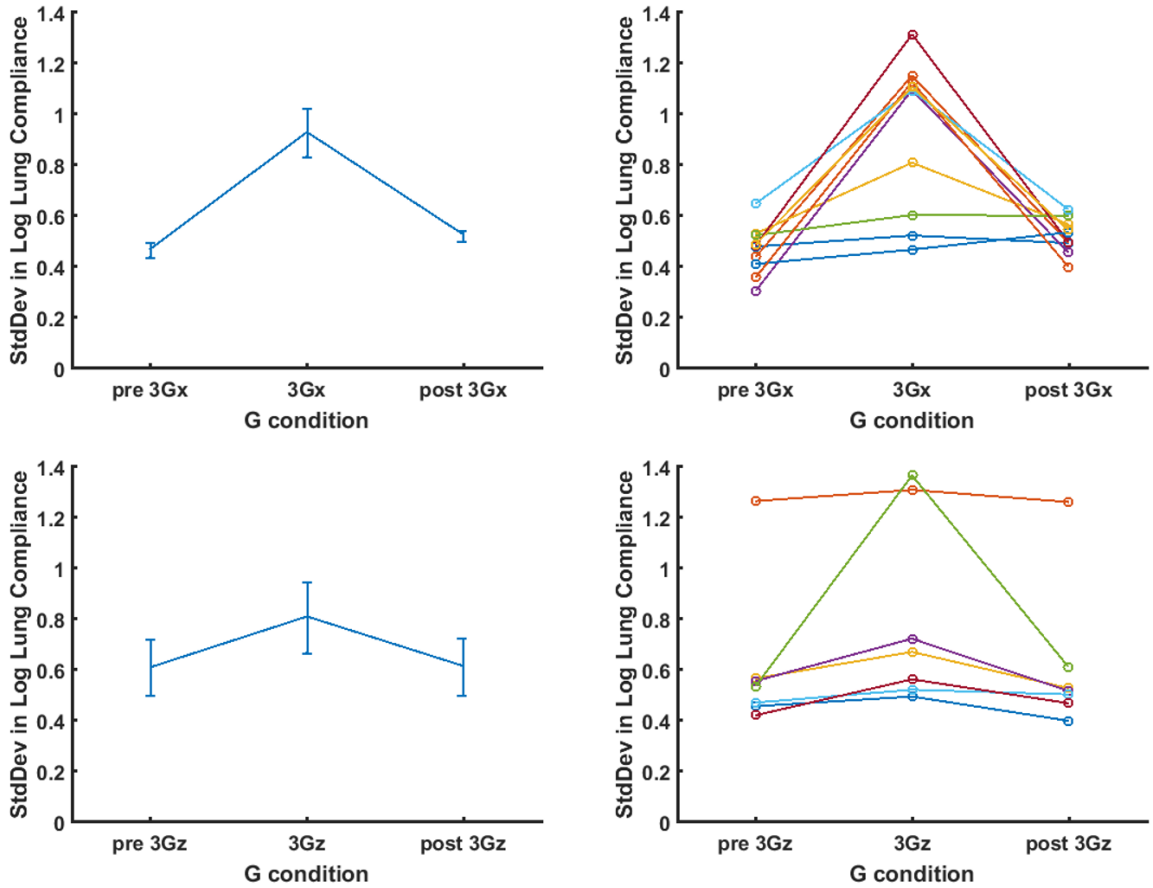

Figure 9.4. The width of the standard deviation in log-lung compliance recovered from a LNL model simulation of the nitrogen washouts before, during and after exposure to 15 minutes of enhanced gravity. The left-hand panels display the standard error of the mean of the data whilst the right-hand panels display the results for each individual participant (N.B. colour coding does not correspond to the same participants as those in Fig. 9.3). Upper panels show the response to the Gx orientation whilst the lower panels are Gz orientation.

(Gx p=2.7x10-5; Gz p=0.037) and the post procedure measurement (Gx p=4.7x10-6, Gz p=0.039) when accounting for the effects of age, height, weight and subject variation. For Gx (but not Gz) the height (p=0.019) and weight (p=0.042) of a participant also had a significant (p<0.05) effect on the compliance distribution value. In contrast, there was no significant effect from age (p=0.76).

The mixed linear modelling also suggests that after either the $3Gx$ or $3Gz$ exposure there is a rapid return of the distribution in lung compliance to a lower value that is not significantly (p>0.05) different from baseline for Gx (p=0.49) and Gz (p=0.97).

9.4 Discussion

Despite the challenging environment and the abnormal physiology under high gravity the pre-existing MFS-LNL model protocol was capable of non-invasively recovering responses of airway parameters to gravity that agree with existing literature [238].

The LNL parameter describing the distribution of lung compliance, σ_{Cl}, represents the distribution of fractional volume change from simulated FRC. As such, it is a direct representative of the distribution of local lung volumes. The increase in the compliance distribution under enhanced gravity seen in the results is indicative of the changes in the ventilation distributions in response to the greater gravity (rather than regional changes in alveolar elastic properties or compliance) increasing the existing gradient of pleural pressure and thus alveolar size in the direction of the gravity vector. This reproduces previous work using functional EIT on horizontal participants experiencing parabolic flight, which demonstrated that the distribution of local lung volumes during spontaneous and deep breathing was significantly determined by the presence (1G), absence (0G) or enhancement (2G) of gravity [235]. These experiments showed a positive correlation between increasing gravity and volume inhomogeneity.

Interestingly, in my work there appears to be a bimodal participant response of σ_{Cl} to gravity whereby three participants had a minimal response to $3Gx$ exposure, whilst one participant had a much greater response to $3Gz$. One participant in the Gz arm of the study had very high baseline compliance distribution which may indicate they have substantial lung pathology [9]. The repeatability of this effect could be explored in future work.

The LNL parameter describing the distribution of the anatomical deadspace, σ_{DP}, also behaves as expected by not changing significantly with increased gravity. The σ_{DP} represents serial dead space (conducting airways) connected to functioning alveoli and so will not be affected by the terminal airway closure experienced at 3G shown in Xe-133 experiments [237].

My experiments used enhanced gravitational force both rostral-caudal/longitudinal to the axis of the body acting towards the feet ($+Gz$) and anteroposterior/transverse to the body acting towards the spine ($+Gx$). Different results for the two orientations were expected for two reasons. Firstly, the positions expose the lung to a different height over

which gravity can act. In addition, the anatomical structure of the lung vasculature and bronchial tree is likely to interact with postural changes. These results showed a slightly greater response of σ_{Cl} to Gx than to Gz.

Enhanced gravity increases heterogeneity in ventilation-perfusion matching across the entire lung volume as well as increasing the heterogeneity of both ventilation and perfusion independently. As such, the nature of the increase in heterogeneity is slightly different to the increases in heterogeneity observed in PE, where specific regions are ventilated but not perfused (resulting in a bimodal distribution for perfusion and ventilation-perfusion matching) whilst the inhomogeneity of ventilation across the lung remains relatively unchanged.

To conclude, this experimental work confirmed that the LNL is capable of distinguishing between σ_{DP} and σ_{Cl} under enhanced gravity. The implication being that the model is also capable of separating out the contribution of the inhomogeneity in these two parameters under normal conditions in health and disease.

Chapter 10

Conclusions

In this Chapter the findings of this thesis are summarised and avenues for future work are discussed.

10.1 Summary of findings

Gas in the lung exchanges with the atmosphere through the pulmonary ventilation and with the rest of the body via the pulmonary blood flow. Ventilatory exchange is far more accessible to measurement than exchange occurring via the blood. For this reason, both experimental and modelling studies of the lung often make simplifying assumptions in relation to the gas exchange with the blood, for example that the composition of the blood flowing into the lungs is constant and that there is no recirculation present. This thesis presents a more complete approach to the problem which includes a model of the circulation and systemic body-gas stores, including the metabolic consumption of oxygen and production of carbon dioxide. With such an approach, the gas concentrations in the blood flowing into the lung are generated automatically from past blood-gas concentrations leaving the lungs.

First, the objective of creating a physiological model of this process, the CBGS model, was completed [1]. This model was then validated through tests that involved experimental perturbation of body gas stores through hyperventilation, rebreathing and low oxygen breathing. For these experiments the model approximated the profile of measured oxygen and carbon dioxide changes at the mouth closely. In the case of nitrogen, due to the nature of its physiological storage and the limitations of the resolution of the

MFS device I could not validate changes at the mouth in the same way. However, the model faithfully reproduced findings from a literature experiment [213].

Having developed and validated the model it was used to test the primary hypothesis of this thesis: that respiratory measurements combined with detailed cardiopulmonary modelling and a blood test could be used to diagnose PE. When using blood samples taken during the protocol, results were encouraging with our disease metric showing statistically significant differences between PE positive and negative patients. It is not yet possible to assess whether this technique could replace or supplement the existing D-dimer screening. However, if further work confirms its promise it could help screen populations for which D-dimer is ineffective (e.g. pregnant women and those with inflammation).

In the absence of a larger sample from the PE clinical study, validation work collected from 118 PE negative participants comparing LNL-CBGS estimates of blood gas state to measured values showed good agreement and suggested the technique could have utility as a PE screening technique. Estimates of false positive and negative rates using the variance found here indicates the technique would not have very high specificity. However, even if only a small proportion of the patient population can be removed from the pathway requiring radiological scans this would result in significant monetary savings and prevent large numbers of patients being exposed to radiation [111].

Testing the MFS device and LNL-CBGS model on a cohort of COVID-19 survivors showed that COVID-19 caused pathological changes in some lung model parameters, especially those related to volumes. Previous infection increased dead space and reduced effective alveolar volume with a more marked effect in more severe disease. Interestingly, this effect did not appear to improve with time. No correlation between COVID-19 severity and the PE disease metric (measured versus model blood error) was found. Despite COVID-19 having been found to often cause pathological changes in pulmonary vasculature these changes are different from those found in PE so this finding is not unexpected.

Finally, a study from early in my doctoral studies exposing participants to hypergravity showed increased model ventilation inhomogeneity but not anatomical deadspace inhomogeneity with increased gravity. This finding suggests the LNL model is capable of successfully distinguishing between these two sources of variation. This finding was

an important basis for this work because the model's estimate of deadspace affects the position of the simulated R line and thus the metric for PE diagnosis.

10.2 Future work

10.2.1 Further work on pulmonary embolism

The results of the study on PE were encouraging but ultimately limited by the small sample size. I believe further work with a larger sample size is justified by the data. The experimental protocol would be unchanged other than removing the blood sample taken before breathing through the device (as this was not significantly related to PE status). If this larger sample confirmed significant differences between PE positive and negative patients then more detailed defining of the cutoff limits for screening could be chosen.

In addition, this technique could be further developed to make quantitative estimates of the percentage of the lung that is ventilated but unperfused. This could be achieved by artificially creating unperfused lung units in the LNL-CBGS model and thus forcing a bimodal distribution into the model. The most straightforward way of achieving this would be to run and fit the model as usual and then duplicate the recovered model lung described by the fitted parameters. This second model lung would be entirely unperfused whilst the entirety of the blood flow is supplied to the first lung. The ventilation would then be split by some arbitrary amount between the two lungs and titrated until the model blood R line matched the measured blood sample. At this value it is assumed the model's bimodal distribution is representative of the pathophysiology. Therefore, at this value the fraction of ventilation to the second lung is the fraction of the lung affected by the PE. This process could be automated by using an optimisation procedure where the output of the objective function to be minimised is measured versus modelled blood error and the only parameter that is adjusted is the fraction of ventilation to each lung.

The human lung consists of 20 segments, so a PE affecting one segment will result in 5% of the lung being ventilated but not perfused. Ideally, a screening technique should be able to detect down to segmental PEs. Any higher resolution has debatable value. Indeed, whether sub-segmental PEs should be treated with anticoagulant drugs or left untreated is unclear and the detection of sub-segmental PEs has been implicated in

'overdiagnosis' and overtreatment [239]. The technique developed in this thesis displayed good sensitivity, with the test metric showing a large difference between PE negative and positive patients. However, all the PE positive patients in this study had multi-segmental PEs. The difference between health and disease with this metric is expected to shrink with PEs affecting smaller proportions of the lung. If the technique loses resolution below the segmental level this may not be an issue since these PEs may not require treatment.

10.2.2 Further work on COVID-19

In humans who had recovered from acute COVID-19 infection, the LNL-CBGS detected pathological changes in lung parameters related to volumes whilst those related to lung efficiency remained relatively normal. The hypothesised mechanism is loss of alveoli and destruction of alveolar-capillary membrane in restricted areas whilst remaining areas of the lung are left relatively untouched and function as normal. This effect was enhanced with more severe acute COVID-19 disease. However, the clinical meaningfulness of these findings is unclear. Future work could investigate whether these parameters correlated with or predicted participant symptoms and morbidity. For instance, cardiopulmonary exercise testing and perceived breathlessness changes over time could be compared with the LNL-CBGS output. Current results have not demonstrated recovery of pathological changes in lung parameters with the six month follow up recording. However, many participants did report feeling partially recovered. Investigations into whether this was due to other compensatory mechanisms could be carried out.

10.2.3 Other potential applications of the CBGS model

The CBGS model developed in Chapter 4 has a number of potential applications, especially when coupled with a model of the lung such as that provided by Mountain *et al.* [9]. Importantly for these applications, both the CBGS and LNL models can be tailored to a particular body size and makeup so that it is possible to accommodate variations between individuals.

One application relates to the study of stability of respiratory control, a topic of interest to high altitude physiology and to medical conditions such as heart failure and central or complex sleep apnoea [240]. Central to understanding stability in an individual is the

measurement of loop gain. One half of this loop relates to controller sensitivity, essentially how ventilation changes as arterial P_{CO_2} and P_{O_2} are varied, and for which there are many dynamic models and estimation processes for tailoring them to individuals, e.g. [241]. The second half of the loop relates to the plant sensitivity, which is how arterial P_{CO_2} and P_{O_2} change as ventilation is varied. Here there are far fewer models, and the present study helps to fill this gap. Importantly, our model can both be tailored to specific individuals and integrates both CO_2 and O_2 stores enabling a single loop gain to be calculated as both of these respiratory stimuli vary simultaneously.

A second potential application is in multi-breath washout testing. Multi-breath washout tests are increasingly being used in clinical studies to delineate the lung physiology of individual patients [175]. In these studies, it is generally the case that no correction is made for the amounts of gas entering and leaving the lung through the pulmonary circulation. This is a significant limitation, as the results have been shown to depend on the solubility of the test gas [242], and in the case of a nitrogen washout that is accomplished by breathing pure oxygen, the results are also likely to be affected by changes in oxygen uptake. Finally, the duration of a MBW is typically a few minutes. This period is both too short to ignore the delays associated with circulatory transit times, but it is also too long to ignore changes in the tissue gas stores of the body. The CBGS model provides a potential way to correct for these effects.

A third potential application relates to improving respiratory techniques for determining cardiac output. These techniques, as reviewed by Laszlo [243], typically involve the use of a soluble tracer gas such as nitrous oxide or acetylene and measuring the rate of its disappearance from the lungs. While the subsequent calculation of cardiac output has the advantage of being firmly rooted in mass balance, it nevertheless assumes no recirculation of the tracer gas back to the lungs. The CBGS model suggests a possible approach whereby recirculation could be taken into account in the estimation of cardiac output by these methods, so making the calculation more accurate and also offering the possibility of allowing a somewhat longer measurement period.

10.3 Concluding remarks

This thesis has demonstrated that highly accurate respiratory measurements combined with detailed modelling of both the lungs and circulatory system can accurately recreate underlying cardiopulmonary physiology and pathology with future potential for useful clinical measures that have advantages over existing techniques.

Appendix A

Arterial tree values

Table A.1. *Standard man arterial tree*

Vessel #	Artery Name	Length /cm	Radius /cm	Volume /ml
	Myocardium			
0	Right coronary	5.3	0.16	0.40
0	Left main coronary	0.5	0.24	0.09
0	Left ant. desc. coronary	4.7	0.13	0.26
0	Left circumflex	2.6	0.17	0.22
	Great vessels			
1	Ascending aorta	4	1.45	26.42
1	Aortic arch (1)	2	1.12	7.88
2	Aortic arch (2)	3.9	1.07	14.03
2	Thoracic aorta (1)	5.2	1.00	16.34
3	Thoracic aorta (2)	10.4	0.95	29.49
4	Abdominal aorta (1)	5.3	0.87	12.60
5	Abdominal aorta (2)	10.6	0.57	10.82
6	Left subclavian artery	3.4	0.42	1.88
7	Brachiocephalic artery	3.4	0.62	4.11
	Left lower body and legs			
8	Common iliac	5.8	0.52	4.93
8	External iliac (1)	8.3	0.29	2.19
8	Internal iliac	5	0.20	0.63
8	External iliac (2)	6.1	0.27	1.40
8	Femoral artery (1)	12.7	0.24	2.30
8	Profundis artery	12.6	0.23	2.09
8	Femoral artery (2)	12.7	0.24	2.30
8	Popliteal artery	18.8	0.20	2.36
8	Anterior tibial artery (1)	2.5	0.13	0.13
8	Anterior tibial artery (2)	30	0.10	0.94
8	Posterior tibial artery	32.2	0.18	3.28
8	Peroneal artery	31.8	0.13	1.69

		Right lower body and legs		
8	vessels as for left lower body and legs			
		Left upper body and arm		
9	Subclavian artery	6.8	0.40	3.42
9	Internal mammary	15	0.10	0.47
9	Costo-cervical artery	5	0.10	0.16
9	Axilliary artery (1)	6.1	0.36	2.48
9	Suprascapular	10	0.20	1.26
9	Thyrocervical	5	0.10	0.16
9	Thoraco-acromial	3	0.15	0.21
9	Axillary artery (2)	5.6	0.31	1.69
9	Circumflex scapular	5	0.10	0.16
9	Subscapular	8	0.15	0.57
9	Brachial artery (1)	6.3	0.28	1.55
9	Profunda brachi	15	0.15	1.06
9	Brachial artery (2)	6.3	0.26	1.34
9	Brachial artery (3)	6.3	0.25	1.24
9	Superior ulnar collateral	5	0.07	0.08
9	Inferior ulnar collateral	5	0.06	0.06
9	Brachial artery (4)	4.6	0.24	0.83
9	Ulnar artery (1)	6.7	0.21	0.93
9	Radial artery	11.7	0.16	0.94
9	Interossea artery	7.9	0.09	0.20
9	Radial artery	11.7	0.16	0.94
9	Ulnar artery (2)	17	0.19	1.93
		Right upper body and arm		
10	vessels as for left upper body and arm			
		Left head		
24	Superior thyroid artery	4	0.07	0.06
24	External carotid	5.9	0.18	0.60
24	Lingual artery	3	0.10	0.09
24	Facial artery	4	0.10	0.13
24	External carotid (1)	5.9	0.13	0.31
24	External carotid (2)	5.9	0.08	0.12
24	Superficial temporal	4	0.06	0.05
24	Maxilliary artery	5	0.07	0.08
		Right head		
25	vessels as for left head			
		Kidneys		
11	Left renal artery	3.2	0.26	0.68
11	Right renal artery	3.2	0.26	0.68

		Liver		
12	Coeliac artery	1	0.39	0.48
13	Hepatic artery	6.6	0.22	1.00
		GI tract and spleen		
14	Gastric artery	7.1	0.18	0.72
14	Splenic artery	6.3	0.28	1.55
15	Superior mesenteric	5.9	0.43	3.43
16	Inferior mesenteric	5	0.16	0.40
17	Portal vein	5.8	0.50	4.56
		Left brain		
18	Left common carotid	20.9	0.37	8.99
22	Internal carotid	11.8	0.15	0.83
22	Middle cerebral	3	0.06	0.03
22	Cerebral artery	5.9	0.08	0.12
22	Opthalmic artery	3	0.07	0.05
20	Vertebral artery	14.8	0.19	1.68
		Right brain		
19	Right common carotid	17.8	0.37	7.66
23	Internal carotid	11.8	0.15	0.83
23	Opthalmic artery	3	0.07	0.05
23	Cerebral artery	5.9	0.08	0.12
23	Middle cerebral	3	0.06	0.03
21	Vertebral artery	14.8	0.19	1.68

Bibliography

[1] S. R. M. Magor-Elliott, C. J. Fullerton, G. Richmond, G. A. D. Ritchie, and P. A. Robbins, "A dynamic model of the body gas stores for carbon dioxide, oxygen, and inert gases that incorporates circulatory transport delays to and from the lung," *Journal of Applied Physiology*, vol. 130, no. 5, pp. 1383–1397, 2021.

[2] S. Barco, S. H. Mahmoudpour, L. Valerio, F. A. Klok, T. Münzel, S. Middeldorp, W. Ageno, A. T. Cohen, B. J. Hunt, and S. V. Konstantinides, "Trends in mortality related to pulmonary embolism in the European Region, 2000–15: analysis of vital registration data from the WHO Mortality Database," *The Lancet Respiratory Medicine*, vol. 8, no. 3, pp. 277–287, 2020.

[3] R. Puranik, C. K. Chow, J. A. Duflou, M. J. Kilborn, and M. A. McGuire, "Sudden death in the young," *Heart rhythm*, vol. 2, no. 12, pp. 1277–1282, 2005.

[4] N. I. for Health Care Excellence, "Venous thromboembolic diseases: diagnosis, management and thrombophilia testing NICE guideline [NG158]," March 2020. https://www.nice.org.uk/guidance/ng158.

[5] G. Lippi, L. Bonfanti, C. Saccenti, and G. Cervellin, "Causes of elevated D-dimer in patients admitted to a large urban emergency department," *European journal of internal medicine*, vol. 25, no. 1, pp. 45–48, 2014.

[6] A. Manara, W. D'hoore, and F. Thys, "Capnography as a diagnostic tool for pulmonary embolism: a meta-analysis," *Annals of emergency medicine*, vol. 62, no. 6, pp. 584–591, 2013.

[7] S. Verscheure, P. B. Massion, F. Verschuren, P. Damas, and S. Magder, "Volumetric capnography: lessons from the past and current clinical applications," *Critical care*, vol. 20, no. 1, pp. 1–9, 2016.

[8] L. Ciaffoni, D. P. O'Neill, J. H. Couper, G. A. D. Ritchie, G. Hancock, and P. A. Robbins, "In-airway molecular flow sensing: A new technology for continuous, noninvasive monitoring of oxygen consumption in critical care," *Science Advances*, vol. 2, no. 8, 2016.

[9] J. E. Mountain, P. Santer, D. P. O'Neill, N. M. J. Smith, L. Ciaffoni, J. H. Couper, G. A. D. Ritchie, G. Hancock, J. P. Whiteley, and P. A. Robbins, "Potential for noninvasive assessment of lung inhomogeneity using highly precise, highly time-resolved measurements of gas exchange," *J Appl Physiol*, vol. 124, pp. 615–631, Mar 2018. 29074714[pmid].

[10] N. Herring and D. J. Paterson, *Levick's introduction to cardiovascular physiology*. CRC Press, 2018.

[11] A. Einstein, "Über die von der molekularkinetischen Theorie der Wärme geforderte Bewegung von in ruhenden Flüssigkeiten suspendierten Teilchen," *Annalen der physik*, vol. 4, 1905.

[12] C. C. Miller, "The Stokes-Einstein law for diffusion in solution," *Proceedings of the Royal Society of London. Series A, Containing Papers of a Mathematical and Physical Character*, vol. 106, no. 740, pp. 724–749, 1924.

[13] D. J. Randall, D. Randall, D. Randall, W. Burggren, K. French, and R. Eckert, *Animal physiology*. Macmillan, 2002.

[14] H. W. Vliegen, A. Van der Laarse, C. J. Cornelisse, and F. Eulderink, "Myocardial changes in pressure overload-induced left ventricular hypertrophy: A study on tissue composition, polyploidization and multinucleation," *European heart journal*, vol. 12, no. 4, pp. 488–494, 1991.

[15] J. Valentin, "Basic anatomical and physiological data for use in radiological protection: reference values: ICRP Publication 89," *Annals of the ICRP*, pp. 1–277, 2002.

[16] B. Alberts, A. Johnson, J. Lewis, M. Raff, K. Roberts, and P. Walter, "Blood vessels and endothelial cells," in *Molecular Biology of the Cell. 4th edition*, Garland Science, 2002.

[17] H. Darcy, *Les fontaines publiques de la ville de Dijon: exposition et application...* Victor Dalmont, 1856.

[18] J. L. M. Poiseuille, "Recherches experimentales sur le movements des liquides dans les tubes de tres petits diametres," *Comptes rend. Acad d. sc.*, vol. 11, no. 961, p. 1041, 1840.

[19] R. Chaudhry, J. H. Miao, and A. Rehman, "Physiology, cardiovascular," *StatPearls [Internet]*, 2020.

[20] F. L. Powell, P. D. Wagner, and J. B. West, "Ventilation, blood flow, and gas exchange," in *Murray and Nadel's textbook of respiratory medicine*, pp. 44–75, Elsevier, 2016.

[21] P. S. Hasleton, "The internal surface area of the adult human lung," *Journal of anatomy*, vol. 112, no. Pt 3, p. 391, 1972.

[22] R. M. Berne and M. N. Levy, *Principles of physiology*. Mosby, 2000.

[23] C. Charalampidis, A. Youroukou, G. Lazaridis, S. Baka, I. Mpoukovinas, V. Karavasilis, I. Kioumis, G. Pitsiou, A. Papaiwannou, K. Karavergou, Anastasia Tsakiridis, N. Katsikogiannis, E. Sarika, K. Kapanidis, L. Sakkas, I. Korantzis, S. Lampaki, K. Zarogoulidis, , and P. Zarogoulidis, "Pleura space anatomy," *Journal of thoracic disease*, vol. 7, no. Suppl 1, p. S27, 2015.

[24] G. Miserocchi and D. Negrini, "Pleural space: pressures and fluid dynamics," *The lung: scientific foundations*, vol. 1, pp. 1217–1225, 1997.

[25] G. Miserocchi, "Mechanisms controlling the volume of pleural fluid and extravascular lung water," *European Respiratory Review*, vol. 18, no. 114, pp. 244–252, 2009.

[26] M. G. Levitzky, *Pulmonary physiology, 4th edition.* No. 1, McGraw-Hill Education,, 1995.

[27] J. Wanger, J. Clausen, A. Coates, O. Pedersen, V. Brusasco, F. Burgos, R. Casaburi, R. Crapo, P. Enright, C. Van Der Grinten, *et al.*, "Standardisation of the measurement of lung volumes," *European respiratory journal*, vol. 26, no. 3, pp. 511–522, 2005.

[28] J. B. West, "Regional differences in gas exchange in the lung of erect man," *Journal of Applied Physiology*, vol. 17, no. 6, pp. 893–898, 1962.

[29] N. S. Cherniack and G. S. Longobardo, "Oxygen and Carbon Dioxide Gas Stores of the Body," *Physiol Rev*, vol. 50, no. 2, pp. 196–243, 1970.

[30] P. K. Weathersby and L. D. Homer, "Solubility of inert gases in biological fluids and tissues: a review," *Undersea Biomed Res*, vol. 7, no. 4, pp. 277–96, 1980.

[31] W. Henry, "III. Experiments on the quantity of gases absorbed by water, at different temperatures, and under different pressures," *Philosophical Transactions of the Royal Society of London*, no. 93, pp. 29–274, 1803.

[32] L. E. Farhi and H. Rahn, "Dynamics of changes in carbon dioxide stores," *Anesthesiology*, vol. 21, no. 6, pp. 604–614, 1960.

[33] H. Rahn, "The gas stores of the body, with particular reference to carbon dioxide," *Man's dependence on the earthly atmosphere*, pp. 297–304, 1962.

[34] F. H. Freeman and W. O. Fenn, "Changes in carbon dioxide stores of rats due to atmospheres low in oxygen or high in carbon dioxide," *American Journal of Physiology-Legacy Content*, vol. 174, no. 3, pp. 422–430, 1953.

[35] F. B. Jensen, "Red blood cell pH, the Bohr effect, and other oxygenation-linked phenomena in blood O_2 and CO_2 transport," *Acta Physiologica Scandinavica*, vol. 182, no. 3, pp. 215–227, 2004.

[36] F. J. W. Roughton, "Some recent work on the chemistry of carbon dioxide transport by the blood," *Harvey lectures*, vol. 39, no. 96, p. 44, 1943.

[37] H. J. Hamburger, *Osmotischer Druck und Ionenlehre in den medicinischen Wissenschaften*. Ripol Classic, 1902.

[38] J. Christiansen, C. Douglas, and J. Haldane, "The absorption and dissociation of carbon dioxide by human blood," *The Journal of physiology*, vol. 48, no. 4, pp. 244–271, 1914.

[39] D. P. O'Neill and P. A. Robbins, "A mechanistic physicochemical model of carbon dioxide transport in blood," *J Appl Physiol (1985)*, vol. 122, no. 2, pp. 283–295, 2017.

[40] K. Permentier, S. Vercammen, S. Soetaert, and C. Schellemans, "Carbon dioxide poisoning: a literature review of an often forgotten cause of intoxication in the emergency department," *International journal of emergency medicine*, vol. 10, no. 1, pp. 1–4, 2017.

[41] N. Ikeda, H. Takahashi, K. Umetsu, and T. Suzuki, "The course of respiration and circulation in death by carbon dioxide poisoning," *Forensic science international*, vol. 41, no. 1-2, pp. 93–99, 1989.

[42] N. J. Langford, "Carbon dioxide poisoning," *Toxicological reviews*, vol. 24, no. 4, pp. 229–235, 2005.

[43] S. M. Tenney and T. W. Lamb, "Physiological consequences of hypoventilation and hyperventilation," *Handbook of physiology, Section*, vol. 3, pp. 979–1010, 1965.

[44] L. Giosa, M. Busana, M. Bonifazi, F. Romitti, F. Vassalli, I. Pasticci, M. M. Macrì, R. D'Albo, F. Collino, A. Gatta, *et al.*, "Mobilizing Carbon Dioxide Stores. An Experimental Study," *American Journal of Respiratory and Critical Care Medicine*, vol. 203, no. 3, pp. 318–327, 2021.

[45] L. L. Hamm, N. Nakhoul, and K. S. Hering-Smith, "Acid-base homeostasis," *Clinical Journal of the American Society of Nephrology*, vol. 10, no. 12, pp. 2232–2242, 2015.

[46] W. J. Waddell and R. G. Bates, "Intracellular pH," *Physiological Reviews*, vol. 49, no. 2, pp. 285–329, 1969.

[47] G. Nichols, "Serial changes in tissue carbon dioxide content during acute respiratory acidosis," *The Journal of clinical investigation*, vol. 37, no. 8, pp. 1111–1122, 1958.

[48] H. Rahn, "Oxygen stores of man," in *Oxygen in the animal organism*, pp. 609–619, Elsevier, 1964.

[49] A. R. Fanelli, E. Antonini, and A. Caputo, "Hemoglobin and myoglobin," *Advances in protein chemistry*, vol. 19, pp. 73–222, 1964.

[50] H. T. Andersen, "Physiological adaptations in diving vertebrates," *Physiological Reviews*, vol. 46, no. 2, pp. 212–243, 1966.

[51] L. Irving, "Respiration in diving mammals," *Physiological Reviews*, vol. 19, no. 1, pp. 112–134, 1939.

[52] G. Biorck, *On myoglobin and its occurrence in man*. Ivar Haeggströms Boktryckeri, 1949.

[53] J. B. Wittenberg and B. A. Wittenberg, "Myoglobin function reassessed," *Journal of Experimental Biology*, vol. 206, no. 12, pp. 2011–2020, 2003.

[54] J. T. Edsall, "Hemoglobin and the origins of the concept of allosterism," in *Federation proceedings*, vol. 39, pp. 226–235, 1980.

[55] C. Bohr, K. Hasselbalch, and A. Krogh, "Ueber einen in biologischer Beziehung wichtigen Einfluss, den die Kohlensäurespannung des Blutes auf dessen Sauerstoffbindung übt 1," *Skandinavisches Archiv Für Physiologie*, vol. 16, no. 2, pp. 402–412, 1904.

[56] W. E. Siri, D. C. Van Dyke, H. S. Winchell, M. Pollycove, H. G. Parker, and A. S. Cleveland, "Early erythropoietin, blood, and physiological responses to severe hypoxia in man," *Journal of applied physiology*, vol. 21, no. 1, pp. 73–80, 1966.

[57] L. E. Farhi, "Gas stores of the body," *Handbook of physiology*, vol. 1, pp. 873–885, 1964.

[58] A. B. Otis, "Quantitative relationships in steady-state gas exchange," *Handbook of physiology. Respiration*, vol. 1, pp. 681–698, 1964.

[59] P. C. Caldwell and E. J. Harris, "Metabolic control by intracellular pH," *The Biochemical journal*, vol. 51, no. 5, p. XLI, 1952.

[60] A. S. E. Fowle and J. M. Campbell, "The immediate carbon dioxide storage capacity of man," *Clin Sci*, vol. 27, pp. 41–49, 1964.

[61] F. S. Grodins, J. S. Gray, K. R. Schroeder, A. L. Norins, and R. W. Jones, "Respiratory responses to CO_2 inhalation. A theoretical study of a nonlinear biological regulator," *Journal of applied physiology*, vol. 7, no. 3, pp. 283–308, 1954.

[62] J. W. Vance and W. S. Fowler, "Adjustments of the stores of CO_2 during voluntary hyperventilation," *Diseases Chest*, vol. 37, pp. 304–313, 1960.

[63] N. S. Cherniack, G. S. Longobardo, I. Staw, and M. Heymann, "Dynamics of carbon dioxide stores changes following an alteration in ventilation," *J Appl Physiol*, vol. 21, no. 3, pp. 785–93, 1966.

[64] N. S. Cherniack, G. S. Longobardo, F. P. Palermo, and M. Heymann, "Dynamics of oxygen stores changes following an alteration in ventilation," *J Appl Physiol*, vol. 24, no. 3, pp. 809–816, 1968.

[65] A. B. Baker and A. D. Farmery, "Inert gas transport in blood and tissues," *Compr Physiol*, vol. 1, no. 2, pp. 569–592, 2011.

[66] W. W. Mapleson and N. R. Davis, "STRUCTURE AND QUANTIFICATION OF A PHYSIOLOGICAL MODEL OF THE DISTRIBUTION OF INJECTED AGENTS AND INHALED ANAESTHETICS," *Br J Anaesth*, vol. 53, p. 399, 1981.

[67] R. P. Brown, M. D. Delp, L. D. Lindstedt, L. R. Rhomberg, and R. P. Beliles, "Physiological parameter values for physiologically based pharmacokinetic models.," *Toxicol Ind Health*, vol. 13, no. 4, pp. 407–484, 1997.

[68] V. F. Tapson, "Acute pulmonary embolism," *New England Journal of Medicine*, vol. 358, no. 10, pp. 1037–1052, 2008.

[69] C. Kearon and J. Hirsh, "The diagnosis of pulmonary embolism," *Pathophysiology of Haemostasis and Thrombosis*, vol. 25, no. 1-2, pp. 72–87, 1995.

[70] J. L. Carson, M. A. Kelley, A. Duff, J. G. Weg, W. J. Fulkerson, H. I. Palevsky, J. S. Schwartz, B. T. Thompson, J. Popovich Jr, T. E. Hobbins, M. A. Spera, A. Alavi, and M. L. Terrin, "The clinical course of pulmonary embolism," *New England Journal of Medicine*, vol. 326, no. 19, pp. 1240–1245, 1992.

[71] M. M. A. Hamad, P. Bhatia, E. Ellidir, M. M. Abdelaziz, and V. Connolly, "Diagnostic approach to pulmonary embolism and lessons from a busy acute assessment unit in the UK," *Breathe*, vol. 7, no. 4, pp. 315–323, 2011.

[72] E. J. R. van Beek, E. M. J. Brouwers, B. Song, P. D. Stein, and M. Oudkerk, "Clinical validity of a normal pulmonary angiogram in patients with suspected pulmonary embolism—a critical review," *Clinical radiology*, vol. 56, no. 10, pp. 838–842, 2001.

[73] A. N. Whitaker, M. J. Elms, P. P. Masci, P. G. Bundesen, D. B. Rylatt, A. J. Webber, and I. H. Bunce, "Measurement of cross linked fibrin derivatives in plasma: an immunoassay using monoclonal antibodies," *Journal of clinical pathology*, vol. 37, no. 8, pp. 882–887, 1984.

[74] M. J. H. A. Kruip, M. J. Slob, J. H. E. M. Schijen, C. van der Heul, and H. R. Buller, "Use of a clinical decision rule in combination with D-dimer concentration in diagnostic workup of patients with suspected pulmonary embolism: a prospective management study," *Archives of Internal Medicine*, vol. 162, no. 14, pp. 1631–1635, 2002.

[75] K. Shahir, L. R. Goodman, A. Tali, K. M. Thorsen, and R. S. Hellman, "Pulmonary embolism in pregnancy: CT pulmonary angiography versus perfusion scanning," *American journal of roentgenology*, vol. 195, no. 3, pp. W214–W220, 2010.

[76] H. Nazaroglu, C. A. Ozmen, H. O. Akay, I. Kilinc, and A. Bilici, "64-MDCT pulmonary angiography and CT venography in the diagnosis of thromboembolic disease," *American Journal of Roentgenology*, vol. 192, no. 3, pp. 654–661, 2009.

[77] F. A. Mettler, "Medical effects and risks of exposure to ionising radiation," *Journal of Radiological Protection*, vol. 32, no. 1, p. N9, 2012.

[78] G. Bourjeily, M. Paidas, H. Khalil, K. Rosene-Montella, and M. Rodger, "Pulmonary embolism in pregnancy," *The Lancet*, vol. 375, no. 9713, pp. 500–512, 2010.

[79] Y. J. Feng, W. R. Chen, T. P. Sun, S. Y. Duan, B. S. Jia, and H. L. Zhang, "Estimated cosmic radiation doses for flight personnel," *Space medicine & medical engineering*, vol. 15, no. 4, pp. 265–269, 2002.

[80] J. Hirsh and A. Y. Y. Lee, "How we diagnose and treat deep vein thrombosis," *Blood, The Journal of the American Society of Hematology*, vol. 99, no. 9, pp. 3102–3110, 2002.

[81] E. J. R. Van Beek, B. E. Schenk, B. C. Michel, B. Van Den Ende, D. P. M. Brandjes, Y. T. Van Der Heide, P. M. M. Bossuyt, and H. R. Buller, "The role of plasma D-dimer concentration in the exclusion of pulmonary embolism," *British journal of haematology*, vol. 92, no. 3, pp. 725–732, 1996.

[82] P. Investigators *et al.*, "Value of the ventilation/perfusion scan in acute pulmonary embolism. Results of the prospective investigation of pulmonary embolism diagnosis (PIOPED)," *Jama*, vol. 263, no. 20, pp. 2753–2759, 1990.

[83] P. D. Stein, R. D. Hull, H. A. Saltzman, and G. Pineo, "Strategy for diagnosis of patients with suspected acute pulmonary embolism," *Chest*, vol. 103, no. 5, pp. 1553–1559, 1993.

[84] A. H. James, "Pregnancy-associated thrombosis," *ASH Education Program Book*, vol. 2009, no. 1, pp. 277–285, 2009.

[85] A. H. James, "Venous thromboembolism in pregnancy," *Arteriosclerosis, Thrombosis, and Vascular Biology*, vol. 29, no. 3, pp. 326–331, 2009.

[86] B. S. Andersen, F. H. Steffensen, H. T. Sorensen, G. L. Nielsen, and J. Olsen, "The cumulative Incidence of venous thromboembolism during pregnancy and puerperium - An 11 year Danish population-based study of 63,300 pregnancies," *Acta Obstetricia et Gynecologica Scandinavica*, vol. 77, pp. 170 – 173, 06 2003.

[87] F. A. Anderson, H. B. Wheeler, R. J. Goldberg, D. W. Hosmer, N. A. Patwardhan, B. Jovanovic, A. Forcier, and J. E. Dalen, "A Population-Based Perspective of

the Hospital Incidence and Case-Fatality Rates of Deep Vein Thrombosis and Pulmonary Embolism: The Worcester DVT Study," *JAMA Internal Medicine*, vol. 151, no. 5, pp. 933–938, 1991.

[88] J. Heit, C. Kobbervig, A. James, T. Petterson, K. Bailey, and L. Melton, "Trends in the Incidence of Venous Thromboembolism During Pregnancy or Postpartum: A 30-Year Population-Based Study," *Annals of internal medicine*, vol. 143, pp. 697–706, 11 2005.

[89] J. G. Ray and W. S. Chan, "Deep vein thrombosis during pregnancy and the puerperium: a meta-analysis of the period of risk and the leg of presentation," *Obstetrical & gynecological survey*, vol. 54, no. 11, pp. 169–175, 1999.

[90] C. J. Berg, J. Chang, L. Elam-Evans, L. Flowers, J. Herndon, K. A. Seed, and C. J. Syverson, "Pregnancy-related mortality surveillance–United States, 1991–1999," 2003.

[91] M. Knight, S. Kenyon, P. Brocklehurst, J. Neilson, J. Shakespeare, and J. Kurinczuk, "Saving lives, improving mothers' care: lessons learned to inform future maternity care from the UK and Ireland confidential enquiries into maternal deaths and morbidity 2009-2012," 2017.

[92] A. Panting-Kemp, S. Geller, T. Nguyen, L. Simonson, B. Nuwayhid, and L. Castro, "Maternal deaths in an urban perinatal network, 1992-1998.," *American journal of obstetrics and gynecology*, vol. 183 5, pp. 1207–12, 2000.

[93] S. V. Konstantinides, G. Meyer, C. Becattini, H. Bueno, G. Geersing, V. Harjola, M. V. Huisman, M. Humbert, C. S. Jennings, D. Jiménez, *et al.*, "2019 ESC Guidelines for the diagnosis and management of acute pulmonary embolism developed in collaboration with the European Respiratory Society (ERS) The Task Force for the diagnosis and management of acute pulmonary embolism of the European Society of Cardiology (ESC)," *European heart journal*, vol. 41, no. 4, pp. 543–603, 2020.

[94] P. S. Wells, D. R. Anderson, M. Rodger, I. Stiell, J. F. Dreyer, D. Barnes, M. Forgie, G. Kovacs, J. Ward, and M. J. Kovacs, "Excluding Pulmonary Embolism at the

Bedside without Diagnostic Imaging: Management of Patients with Suspected Pulmonary Embolism Presenting to the Emergency Department by Using a Simple Clinical Model and D-dimer," *Annals of Internal Medicine*, vol. 135, no. 2, pp. 98–107, 2001. PMID: 11453709.

[95] S. Goodacre, K. Horspool, C. Nelson-Piercy, M. Knight, N. Shephard, F. Lecky, S. Thomas, B. Hunt, G. Fuller, and D. R. Group, "The Di PEP study: an observational study of the diagnostic accuracy of clinical assessment, D-dimer and chest x-ray for suspected pulmonary embolism in pregnancy and postpartum," *BJOG: An International Journal of Obstetrics & Gynaecology*, vol. 126, no. 3, pp. 383–392, 2019.

[96] P. Chabloz, G. Reber, F. Boehlen, P. Hohlfeld, and P. De Moerloose, "TAFI antigen and D-dimer levels during normal pregnancy and at delivery," *British journal of haematology*, vol. 115, no. 1, pp. 150–152, 2001.

[97] L. M. Van der Pol, A. T. A. Mairuhu, C. Tromeur, F. Couturaud, M. V. Huisman, and F. A. Klok, "Use of clinical prediction rules and D-dimer tests in the diagnostic management of pregnant patients with suspected acute pulmonary embolism," *Blood reviews*, vol. 31, no. 2, pp. 31–36, 2017.

[98] F. Boehlen, M. Epiney, M. Boulvain, O. Irion, and P. de Moerloose, "Changes in D-dimer levels during pregnancy and the postpartum period: results of two studies," *Revue medicale suisse*, vol. 1, no. 4, pp. 296–298, 2005.

[99] R. Ramsay, L. Byrd, C. Tower, J. James, M. Prescott, and J. Thachil, "The problem of pulmonary embolism diagnosis in pregnancy," *British Journal of Haematology*, vol. 170, no. 5, pp. 727–728, 2015.

[100] J. K. Pahade, D. Litmanovich, I. Pedrosa, J. Romero, A. A. Bankier, and P. M. Boiselle, "Imaging pregnant patients with suspected pulmonary embolism: what the radiologist needs to know," *Radiographics*, vol. 29, no. 3, pp. 639–654, 2009.

[101] S. K. Doshi, I. S. Negus, and J. M. Oduko, "Fetal radiation dose from CT pulmonary angiography in late pregnancy: a phantom study," *The British Journal of Radiology*, vol. 81, no. 968, pp. 653–658, 2008.

[102] J. R. Russell, M. G. Stabin, R. B. Sparks, and E. Watson, "Radiation absorbed dose to the embryo/fetus from radiopharmaceuticals," *Health physics*, vol. 73, no. 5, pp. 756–769, 1997.

[103] L. M. Hurwitz, T. T. Yoshizumi, R. E. Reiman, E. K. Paulson, D. P. Frush, G. T. Nguyen, G. I. Toncheva, and P. C. Goodman, "Radiation dose to the female breast from 16-MDCT body protocols," *American Journal of Roentgenology*, vol. 186, no. 6, pp. 1718–1722, 2006.

[104] A. J. Einstein, M. J. Henzlova, and S. Rajagopalan, "Estimating risk of cancer associated with radiation exposure from 64-slice computed tomography coronary angiography," *Jama*, vol. 298, no. 3, pp. 317–323, 2007.

[105] L. E. Simcox, L. Ormesher, C. Tower, and I. A. Greer, "Pulmonary thromboembolism in pregnancy: diagnosis and management," *Breathe*, vol. 11, no. 4, pp. 282–289, 2015.

[106] R. L. Riley and A. Cournand, "Ideal Alveolar Air and the Analysis of Ventilation-Perfusion Relationships in the Lungs," *Journal of Applied Physiology*, vol. 1, no. 12, pp. 825–847, 1949. PMID: 18145478.

[107] R. L. Riley and A. Cournand, "Analysis of factors affecting partial pressures of oxygen and carbon dioxide in gas and blood of lungs: theory," *Journal of applied physiology*, vol. 4, no. 2, pp. 77–101, 1951.

[108] M. A. Rodger, M. Carrier, G. N. Jones, P. Rasuli, F. Raymond, H. Djunaedi, and P. S. Wells, "Diagnostic value of arterial blood gas measurement in suspected pulmonary embolism," *American journal of respiratory and critical care medicine*, vol. 162, no. 6, pp. 2105–2108, 2000.

[109] P. Egermayer, G. I. Town, J. G. Turner, D. C. Heaton, A. L. Mee, and M. E. J. Beard, "Usefulness of D-dimer, blood gas, and respiratory rate measurements for excluding pulmonary embolism," *Thorax*, vol. 53, no. 10, pp. 830–834, 1998.

[110] N. Gravenstein and M. B. Jaffe, "Capnography," in *Anesthesia Equipment*, pp. 239–252, Elsevier, 2021.

[111] D. Prentice, C. B. Deroche, and D. D. Wipke-Tevis, "Excluding Pulmonary Embolism with End-tidal Carbon Dioxide: Accuracy, Cost, and Harm Avoidance," *Western journal of nursing research*, vol. 42, no. 12, pp. 1022–1030, 2020.

[112] M. J. McFarlane and T. F. Imperiale, "Use of the alveolar-arterial oxygen gradient in the diagnosis of pulmonary embolism," *The American journal of medicine*, vol. 96, no. 1, pp. 57–62, 1994.

[113] O. Cvitanic and P. L. Marino, "Improved use of arterial blood gas analysis in suspected pulmonary embolism," *Chest*, vol. 95, no. 1, pp. 48–51, 1989.

[114] P. D. Stein, S. Z. Goldhaber, and J. W. Henry, "Alveolar-arterial oxygen gradient in the assessment of acute pulmonary embolism," *Chest*, vol. 107, no. 1, pp. 139–143, 1995.

[115] J. G. Hardman and A. R. Aitkenhead, "Estimating alveolar dead space from the arterial to end-tidal CO2 gradient: a modeling analysis," *Anesthesia & Analgesia*, vol. 97, no. 6, pp. 1846–1851, 2003.

[116] J. W. Severinghaus and M. Stupfel, "Alveolar dead space as an index of distribution of blood flow in pulmonary capillaries," *Journal of Applied Physiology*, vol. 10, no. 3, pp. 335–348, 1957.

[117] C. for Systems Science and E. at John Hopkins University, "Coronavirus resource centre COVID-19 Dashboard," 2021.

[118] W. H. Organisation, "WHO Coronavirus (COVID-19) Dashboard," 2021.

[119] R. Lu, X. Zhao, J. Li, P. Niu, B. Yang, H. Wu, W. Wang, H. Song, B. Huang, N. Zhu, *et al.*, "Genomic characterisation and epidemiology of 2019 novel coronavirus: implications for virus origins and receptor binding," *The lancet*, vol. 395, no. 10224, pp. 565–574, 2020.

[120] Z. Wu and J. M. McGoogan, "Characteristics of and important lessons from the coronavirus disease 2019 (COVID-19) outbreak in China: summary of a report of 72 314 cases from the Chinese Center for Disease Control and Prevention," *Jama*, vol. 323, no. 13, pp. 1239–1242, 2020.

[121] P. Zhou, X.-L. Yang, X.-G. Wang, B. Hu, L. Zhang, W. Zhang, H.-R. Si, Y. Zhu, B. Li, C.-L. Huang, *et al.*, "A pneumonia outbreak associated with a new coronavirus of probable bat origin," *Nature*, vol. 579, no. 7798, pp. 270–273, 2020.

[122] R. Yan, Y. Zhang, Y. Li, L. Xia, Y. Guo, and Q. Zhou, "Structural basis for the recognition of SARS-CoV-2 by full-length human ACE2," *Science*, vol. 367, no. 6485, pp. 1444–1448, 2020.

[123] M. L. Holshue, C. DeBolt, S. Lindquist, K. H. Lofy, J. Wiesman, H. Bruce, C. Spitters, K. Ericson, S. Wilkerson, A. Tural, *et al.*, "First case of 2019 novel coronavirus in the United States," *New England Journal of Medicine*, 2020.

[124] N. Van Doremalen, T. Bushmaker, D. H. Morris, M. G. Holbrook, A. Gamble, B. N. Williamson, A. Tamin, J. L. Harcourt, N. J. Thornburg, S. I. Gerber, *et al.*, "Aerosol and surface stability of SARS-CoV-2 as compared with SARS-CoV-1," *New England journal of medicine*, vol. 382, no. 16, pp. 1564–1567, 2020.

[125] P. Anfinrud, V. Stadnytskyi, C. E. Bax, and A. Bax, "Visualizing speech-generated oral fluid droplets with laser light scattering," *New England Journal of Medicine*, vol. 382, no. 21, pp. 2061–2063, 2020.

[126] R. Huang, J. Xia, Y. Chen, C. Shan, and C. Wu, "A family cluster of SARS-CoV-2 infection involving 11 patients in Nanjing, China," *The Lancet Infectious Diseases*, vol. 20, no. 5, pp. 534–535, 2020.

[127] C. Wang, Z. Wang, G. Wang, J. Y.-N. Lau, K. Zhang, and W. Li, "COVID-19 in early 2021: current status and looking forward," *Signal Transduction and Targeted Therapy*, vol. 6, no. 1, pp. 1–14, 2021.

[128] M. Nicola, Z. Alsafi, C. Sohrabi, A. Kerwan, A. Al-Jabir, C. Iosifidis, M. Agha, and R. Aghaf, "The socio-economic implications of the coronavirus pandemic (COVID-19): A review [Internet]. Vol. 78," *International Journal of Surgery. IJS Publishing Group Ltd*, pp. 185–193, 2020.

[129] L. Thunström, S. C. Newbold, D. Finnoff, M. Ashworth, and J. F. Shogren, "The benefits and costs of using social distancing to flatten the curve for COVID-19," *Journal of Benefit-Cost Analysis*, vol. 11, no. 2, pp. 179–195, 2020.

[130] S. Pokhrel and R. Chhetri, "A literature review on impact of COVID-19 pandemic on teaching and learning," *Higher Education for the Future*, vol. 8, no. 1, pp. 133–141, 2021.

[131] D. Wang, B. Hu, C. Hu, F. Zhu, X. Liu, J. Zhang, B. Wang, H. Xiang, Z. Cheng, Y. Xiong, *et al.*, "Clinical characteristics of 138 hospitalized patients with 2019 novel coronavirus–infected pneumonia in Wuhan, China," *Jama*, vol. 323, no. 11, pp. 1061–1069, 2020.

[132] W. He, G. Y. Yi, and Y. Zhu, "Estimation of the basic reproduction number, average incubation time, asymptomatic infection rate, and case fatality rate for COVID-19: Meta-analysis and sensitivity analysis," *Journal of medical virology*, vol. 92, no. 11, pp. 2543–2550, 2020.

[133] K. Mizumoto, K. Kagaya, A. Zarebski, and G. Chowell, "Estimating the asymptomatic proportion of coronavirus disease 2019 (COVID-19) cases on board the Diamond Princess cruise ship, Yokohama, Japan, 2020," *Eurosurveillance*, vol. 25, no. 10, p. 2000180, 2020.

[134] H. Nishiura, T. Kobayashi, T. Miyama, A. Suzuki, S.-m. Jung, K. Hayashi, R. Kinoshita, Y. Yang, B. Yuan, A. R. Akhmetzhanov, *et al.*, "Estimation of the asymptomatic ratio of novel coronavirus infections (COVID-19)," *International journal of infectious diseases*, vol. 94, p. 154, 2020.

[135] M. Chung, A. Bernheim, X. Mei, N. Zhang, M. Huang, X. Zeng, J. Cui, W. Xu, Y. Yang, Z. A. Fayad, *et al.*, "CT imaging features of 2019 novel coronavirus (2019-nCoV)," *Radiology*, vol. 295, no. 1, pp. 202–207, 2020.

[136] W. Guan, Z. Ni, Y. Hu, W. Liang, C. Ou, J. He, L. Liu, H. Shan, C. Lei, D. S. C. Hui, *et al.*, "Clinical characteristics of coronavirus disease 2019 in China," *New England journal of medicine*, vol. 382, no. 18, pp. 1708–1720, 2020.

[137] H. Y. F. Wong, H. Y. S. Lam, A. H. Fong, S. T. Leung, T. W. Chin, C. S. Y. Lo, M. M. Lui, J. C. Y. Lee, K. W. Chiu, T. W. Chung, *et al.*, "Frequency and distribution of chest radiographic findings in patients positive for COVID-19," *Radiology*, vol. 296, no. 2, pp. E72–E78, 2020.

[138] B. Gallo Marin, G. Aghagoli, K. Lavine, L. Yang, E. J. Siff, S. S. Chiang, T. P. Salazar-Mather, L. Dumenco, M. C. Savaria, S. N. Aung, *et al.*, "Predictors of COVID-19 severity: A literature review," *Reviews in medical virology*, p. e2146, 2020.

[139] F. Zhou, T. Yu, R. Du, G. Fan, Y. Liu, Z. Liu, J. Xiang, Y. Wang, B. Song, X. Gu, *et al.*, "Clinical course and risk factors for mortality of adult inpatients with COVID-19 in Wuhan, China: a retrospective cohort study," *The lancet*, vol. 395, no. 10229, pp. 1054–1062, 2020.

[140] V. Surveillances, "The epidemiological characteristics of an outbreak of 2019 novel coronavirus diseases (COVID-19)—China, 2020," *China CDC weekly*, vol. 2, no. 8, pp. 113–122, 2020.

[141] Q. Ruan, K. Yang, W. Wang, L. Jiang, and J. Song, "Clinical predictors of mortality due to COVID-19 based on an analysis of data of 150 patients from Wuhan, China," *Intensive care medicine*, vol. 46, no. 5, pp. 846–848, 2020.

[142] R. H. Kallet, "THE YEAR IN REVIEW: MECHANICAL VENTILATION DURING THE FIRST YEAR OF THE COVID-19 PANDEMIC," *Respiratory Care*, 2021.

[143] J. R. Navas-Blanco and R. Dudaryk, "Management of Respiratory Distress Syndrome due to COVID-19 infection," *BMC anesthesiology*, vol. 20, no. 1, pp. 1–6, 2020.

[144] M. Busana, L. Giosa, M. Cressoni, A. Gasperetti, L. Di Girolamo, A. Martinelli, A. Sonzogni, L. Lorini, M. M. Palumbo, F. Romitti, *et al.*, "The impact of ventilation–perfusion inequality in COVID-19: a computational model," *Journal of Applied Physiology*, vol. 130, no. 3, pp. 865–876, 2021.

[145] L. Camporota, J. N. Cronin, M. Busana, L. Gattinoni, and F. Formenti, "Pathophysiology of coronavirus-19 disease acute lung injury," *Current opinion in critical care*, vol. 28, no. 1, p. 9, 2022.

[146] R. K. Reddy, W. N. Charles, A. Sklavounos, A. Dutt, P. T. Seed, and A. Khajuria, "The effect of smoking on COVID-19 severity: A systematic review and meta-analysis," *Journal of Medical Virology*, vol. 93, no. 2, pp. 1045–1056, 2021.

[147] B. M. Popkin, S. Du, W. D. Green, M. A. Beck, T. Algaith, C. H. Herbst, R. F. Alsukait, M. Alluhidan, N. Alazemi, and M. Shekar, "Individuals with obesity and COVID-19: A global perspective on the epidemiology and biological relationships," *Obesity Reviews*, vol. 21, no. 11, p. e13128, 2020.

[148] J. S. Alqahtani, T. Oyelade, A. M. Aldhahir, S. M. Alghamdi, M. Almehmadi, A. S. Alqahtani, S. Quaderi, S. Mandal, and J. R. Hurst, "Prevalence, severity and mortality associated with COPD and smoking in patients with COVID-19: a rapid systematic review and meta-analysis," *PloS one*, vol. 15, no. 5, p. e0233147, 2020.

[149] Y.-J. Kang, "Mortality rate of infection with COVID-19 in Korea from the perspective of underlying disease," *Disaster medicine and public health preparedness*, vol. 14, no. 3, pp. 384–386, 2020.

[150] G. Grasselli, A. Zangrillo, A. Zanella, M. Antonelli, L. Cabrini, A. Castelli, D. Cereda, A. Coluccello, G. Foti, R. Fumagalli, *et al.*, "Baseline characteristics and outcomes of 1591 patients infected with SARS-CoV-2 admitted to ICUs of the Lombardy Region, Italy," *Jama*, vol. 323, no. 16, pp. 1574–1581, 2020.

[151] G. Cai, Y. Bossé, F. Xiao, F. Kheradmand, and C. I. Amos, "Tobacco smoking increases the lung gene expression of ACE2, the receptor of SARS-CoV-2," *American journal of respiratory and critical care medicine*, vol. 201, no. 12, pp. 1557–1559, 2020.

[152] M. N. Gong, E. K. Bajwa, B. T. Thompson, and D. C. Christiani, "Body mass index is associated with the development of acute respiratory distress syndrome," *Thorax*, vol. 65, no. 1, pp. 44–50, 2010.

[153] E. Hernández-Garduño, "Obesity is the comorbidity more strongly associated for Covid-19 in Mexico. A case-control study," *Obesity research & clinical practice*, vol. 14, no. 4, pp. 375–379, 2020.

[154] E. A. Karlsson, J. J. Milner, W. D. Green, J. Rebeles, S. Schultz-Cherry, and M. A. Beck, "Influence of obesity on the response to influenza infection and vaccination," in *Mechanisms and Manifestations of Obesity in Lung Disease*, pp. 227–259, Elsevier, 2019.

[155] N. Báez-Ferrer, A. Bompart-Cairós, D. López-Rial, P. Abreu-González, D. Hernández-Vaquero, and A. Domínguez-Rodríguez, "Mortality with ECMO in critically ill patients with SARS-CoV-2 infection during the COVID-19 pandemic. A systematic review," *REC Interv Cardiol*, 2021.

[156] E. K. McCreary and J. M. Pogue, "Coronavirus disease 2019 treatment: a review of early and emerging options," in *Open forum infectious diseases*, vol. 7, p. ofaa105, Oxford University Press US, 2020.

[157] Y. K. Ratre, N. Kahar, L. Bhaskar, A. Bhattacharya, and H. K. Verma, "Molecular mechanism, diagnosis, and potential treatment for novel coronavirus (COVID-19): a current literature review and perspective," *3 Biotech*, vol. 11, no. 2, pp. 1–24, 2021.

[158] M. W. Tenforde, S. S. Kim, C. J. Lindsell, E. B. Rose, N. I. Shapiro, D. C. Files, K. W. Gibbs, H. L. Erickson, J. S. Steingrub, H. A. Smithline, *et al.*, "Symptom duration and risk factors for delayed return to usual health among outpatients with COVID-19 in a multistate health care systems network—United States, March–June 2020," *Morbidity and Mortality Weekly Report*, vol. 69, no. 30, p. 993, 2020.

[159] S. Lopez-Leon, T. Wegman-Ostrosky, C. Perelman, R. Sepulveda, P. A. Rebolledo, A. Cuapio, and S. Villapol, "More than 50 Long-term effects of COVID-19: a systematic review and meta-analysis," *Available at SSRN 3769978*, 2021.

[160] L. Townsend, J. Dowds, K. O'Brien, G. Sheill, A. H. Dyer, B. O'Kelly, J. P. Hynes, A. Mooney, J. Dunne, C. Ni Cheallaigh, *et al.*, "Persistent Poor Health Post-COVID-

19 Is Not Associated with Respiratory Complications or Initial Disease Severity," *Annals of the American Thoracic Society*, no. ja, 2020.

[161] J. Mountain, *The lognormal lung: quantifying inhomogeneity of ventilation*. PhD thesis, University of Oxford, 2016.

[162] M. Folke, L. Cernerud, M. Ekström, and B. Hök, "Critical review of non-invasive respiratory monitoring in medical care," *Medical and Biological Engineering and Computing*, vol. 41, no. 4, pp. 377–383, 2003.

[163] C. G. Douglas, "A method for determining the total respiratory exchange in man," *Journal of Physiology*, vol. 42, pp. 17–18, 1911.

[164] C. Stuart-Andrews, P. Peyton, G. Robinson, and B. Lithgow, "Continuous indirect calorimetry - a laboratory simulation of a new method for non-invasive metabolic monitoring of patients under anaesthesia or in critical care," *Physiological measurement*, vol. 27, no. 2, p. 155, 2006.

[165] T. Walsh, "Recent advances in gas exchange measurement in intensive care patients," *British journal of Anaesthesia*, vol. 91, no. 1, pp. 120–131, 2003.

[166] W. L. Beaver, N. Lamarra, and K. Wasserman, "Breath-by-breath measurement of true alveolar gas exchange," *Journal of Applied Physiology*, vol. 51, no. 6, pp. 1662–1675, 1981.

[167] J. Takala, O. Keinänen, P. Väisänen, and A. A. R. N. O. Kari, "Measurement of gas exchange in intensive care: laboratory and clinical validation of a new device.," *Critical care medicine*, vol. 17, no. 10, pp. 1041–1047, 1989.

[168] B. Cummings, M. L. Hamilton, L. Ciaffoni, T. R. Pragnell, R. Peverall, G. A. Ritchie, G. Hancock, and P. A. Robbins, "Laser-based absorption spectroscopy as a technique for rapid in-line analysis of respired gas concentrations of O_2 and CO_2," *Journal of applied physiology*, vol. 111, no. 1, pp. 303–307, 2011.

[169] G. Berden, R. Peeters, and G. Meijer, "Cavity ring-down spectroscopy: Experimental schemes and applications," *International Reviews in Physical Chemistry*, vol. 19, no. 4, pp. 565–607, 2000.

[170] J. C. Hogg, "Pathophysiology of airflow limitation in chronic obstructive pulmonary disease," *The Lancet*, vol. 364, no. 9435, pp. 709–721, 2004.

[171] P. D. Wagner, R. B. Laravuso, R. R. Uhi, and J. B. West, "Continuous distributions of ventilation-perfusion ratios in normal subjects breathing air and 100% O_2," *The Journal of clinical investigation*, vol. 54, no. 1, pp. 54–68, 1974.

[172] P. D. Wagner, H. A. Saltzman, and J. B. West, "Measurement of continuous distributions of ventilation-perfusion ratios: theory," *Journal of applied physiology*, vol. 36, no. 5, pp. 588–599, 1974.

[173] P. D. Wagner, "The multiple inert gas elimination technique (MIGET)," *Applied physiology in intensive care medicine*, pp. 29–36, 2009.

[174] R. C. Sá, A. C. Henderson, T. Simonson, T. J. Arai, H. Wagner, R. J. Theilmann, P. D. Wagner, G. K. Prisk, and S. R. Hopkins, "Measurement of the distribution of ventilation-perfusion ratios in the human lung with proton MRI: comparison with the multiple inert-gas elimination technique," *Journal of Applied Physiology*, vol. 123, no. 1, pp. 136–146, 2017.

[175] P. D. Robinson, P. Latzin, S. Verbanck, G. L. Hall, A. Horsley, M. Gappa, C. Thamrin, H. G. Arets, P. Aurora, S. I. Fuchs, G. G. King, S. Lum, K. Macleod, M. Paiva, J. J. Pillow, S. Ranganathan, F. Ratjen, F. Singer, S. Sonnappa, J. Stocks, P. Subbarao, B. R. Thompson, and P. M. Gustafsson, "Consensus statement for inert gas washout measurement using multiple- and single- breath tests," *Eur Respir J*, vol. 41, no. 3, pp. 507–22, 2013.

[176] R. Rodríguez-Roisin, M. Drakulovic, D. A. Rodríguez, J. Roca, J. A. Barbera, and P. D. Wagner, "Ventilation-perfusion imbalance and chronic obstructive pulmonary disease staging severity," *Journal of applied physiology*, vol. 106, no. 6, pp. 1902–1908, 2009.

[177] A. J. Swan and M. H. Tawhai, "Evidence for minimal oxygen heterogeneity in the healthy human pulmonary acinus," *Journal of applied physiology*, vol. 110, no. 2, pp. 528–537, 2011.

[178] J. Mountain, P. Santer, D. P. O'Neill, L. Ciaffoni, J. H. Couper, G. Hancock, G. A. D. Ritchie, J. P. Whiteley, and P. A. Robbins, "Measuring lung inhomogeneity in early chronic lung disease." 2016.

[179] A. R. Clark, M. H. Tawhai, E. A. Hoffman, and K. S. Burrowes, "The interdependent contributions of gravitational and structural features to perfusion distribution in a multiscale model of the pulmonary circulation," *Journal of applied physiology*, vol. 110, no. 4, pp. 943–955, 2011.

[180] A. J. Swan, A. R. Clark, and M. H. Tawhai, "A computational model of the topographic distribution of ventilation in healthy human lungs," *Journal of theoretical biology*, vol. 300, pp. 222–231, 2012.

[181] N. M. J. Smith, J. Couper, C. J. Fullerton, G. Richmond, N. P. Talbot, G. Hancock, I. Pavord, G. A. D. Ritchie, P. A. Robbins, and N. Petousi, "Novel measure of lung function for assessing disease activity in asthma," *BMJ open respiratory research*, vol. 7, no. 1, p. e000531, 2020.

[182] J. S. Haldane and J. I. Graham, *Methods of air analysis*. Griffin, 1912.

[183] W. S. C. Snyder, M. J. Cook, E. S. Nasset, L. R. Karhausen, G. Parry-Howells, and I. H. Tipton, "International Commission on Radiological Protection No. 23. Report of the Task Group on Reference Man," report, International Commission on Radiological Protection, 1975.

[184] J. J. K. Cutnell, *Physics, Fourth Edition*. Wiley, 1998.

[185] R. W. Leggett and L. R. Williams, "Reference values for resting blood flow to organs of man," *Clin Phys Physiol Meas*, vol. 13, pp. 187–217, 1989.

[186] R. W. Leggett and L. R. Williams, "Suggested reference values for regional blood volumes in humans.," *Health Phys*, vol. 60, no. 2, pp. 139–154, 1991.

[187] R. W. Leggett and L. R. Williams, "A proposed blood circulation model for reference man," *Health Phys*, vol. 69, p. 187–201, 1995.

[188] R. M. Berne and M. N. Levy, *Cardiovascular Physiology*. St Louis: Mosby, 1992.

[189] J. R. Levick, *An Introduction to Cardiovascular Physiology.* London: Butterworth & Co Ltd, 1991.

[190] A. P. Avolio, "Multi-branched model of the human arterial system," *Med Biol Eng Comput*, vol. 18, no. 6, pp. 709–718, 1980.

[191] M. F. O'Rourke and A. P. Avolio, "Pulsatile flow and pressure in human systemic arteries. Studies in man and in a multibranched model of the human systemic arterial tree," *Circ Res*, vol. 46, no. 3, pp. 363–372, 1980.

[192] P. Reymond, F. Merenda, F. Perren, D. Rüfenacht, and N. Stergiopulos, "Validation of a one-dimensional model of the systemic arterial tree," *Am J Physiol Heart Circ Physiol*, vol. 297, no. 1, pp. 208–222, 2009.

[193] G. Geleto, W. Getnet, and T. Tewelde, "Mean Normal Portal Vein Diameter Using Sonography among Clients Coming to Radiology Department of Jimma University Hospital, Southwest Ethiopia," *Ethiopian J Health Sci*, vol. 26, no. 3, pp. 237–242, 2016.

[194] N. Ongoiba, F. Sissoko, I. Ouologuem, S. Berete, A. K. Traore, S. Sidibe, M. Toure, A. D. Keita, and A. K. Koumare, "Portal vein: echographic anatomy," *Morphologie*, vol. 87, no. 277, pp. 29–32, 2003.

[195] H. G. Bogren and M. H. Buonocore, "Blood flow measurements in the aorta and major arteries with MR velocity mapping," *J Magn Reson Imaging*, vol. 4, no. 2, pp. 119–30, 1994.

[196] Z. Wang, Z. Ying, A. Bosy-Westphal, J. Zhang, B. Schautz, W. Later, S. B. Heymsfield, and M. J. Muller, "Specific metabolic rates of major organs and tissues across adulthood: evaluation by mechanistic model of resting energy expenditure," *Am J Clin Nutr*, vol. 92, no. 6, pp. 1369–77, 2010.

[197] M. Elia, *Organ and tissue contribution to metabolic rate.* New York: Raven Press, 1992.

[198] P. Deurenberg, J. Weststrate, and J. Seidell, "Body mass index as a measure of body fatness: age- and sex-specific prediction formulas," *Br J Nutr*, vol. 65, no. 2, pp. 105–114, 1991.

[199] K. M. Flegal, J. A. Shepherd, A. C. Looker, B. I. Graubard, L. G. Borrud, C. L. Ogden, T. B. Harris, J. E. Everhart, and N. Schenker, "Comparisons of percentage body fat, body mass index, waist circumference, and waist-stature ratio in adults," *Am J Clin Nutr*, vol. 89, no. 2, pp. 500–508, 2009.

[200] D. J. Goldsmith and P. J. Hilton, "Relationship between intracellular proton buffering capacity and intracellular pH," *Kidney Int*, vol. 41, no. 1, pp. 43–9, 1992.

[201] E. Do, D. Ellis, and J. Noireaud, "Intracellular pH and intrinsic H+ buffering capacity in normal and hypertrophied right ventricle of ferret heart," *Cardiovascular Research*, vol. 31, no. 5, pp. 729–738, 1996.

[202] G. Nichols Jr., "Solubility of carbon dioxide in body fat," *Science*, vol. 126, no. 3285, pp. 1244–5, 1957.

[203] J. A. Campbell and L. Hill, "Concerning the amount of nitrogen gas in the tissues and its removal by breathing almost pure oxygen," *J Physiol*, vol. 71, no. 3, p. 309–322, 1931.

[204] O. Siggaard-Andersen, *The Acid-Base Status of Blood, 4th Edn*, p. 32. Baltimore: Williams & Wilkins, 1974.

[205] J. P. Whiteley, D. J. Gavaghan, and C. E. W. Hahn, "A tidal breathing model of the inert gas sinewave technique for inhomogeneous lungs," *Resp Physiol*, vol. 124, no. 1, pp. 65–83, 2000.

[206] G. Musch, J. D. H. Layfield, R. S. Harris, M. F. V. Melo, T. Winkler, R. J. Callahan, A. J. Fischman, and J. G. Venegas, "Topographical distribution of pulmonary perfusion and ventilation, assessed by PET in supine and prone humans," *J Appl Physiol (1985)*, vol. 93, no. 5, pp. 1841–1851, 2002.

[207] A. Roos and W. F. Boron, "Intracellular pH," *Physiological Reviews*, vol. 61, no. 2, pp. 296–434, 1981. PMID: 7012859.

[208] S. E. Rees and S. Andreassen, "Mathematical models of oxygen and carbon dioxide storage and transport: the acid-base chemistry of blood," *Crit Rev Biomed Eng*, vol. 33, no. 3, pp. 209–264, 2005.

[209] M. B. Wolf, "Physicochemical Models of Acid-Base," *Seminars in Nephrology*, vol. 39, no. 4, pp. 328–339, 2019.

[210] V. Fiserova-Bergerova and M. L. Diaz, "Determination and prediction of tissue-gas partition coefficients.," *Int Arch Occup Environ Health*, vol. 58, no. 1, pp. 75–87, 1986.

[211] M. H. Abraham, J. M. Gola, A. Ibrahim, W. E. Acree Jr, and X. Liu, "A simple method for estimating in vitro air-tissue and in vivo blood-tissue partition coefficients," *Chemosphere*, vol. 120, pp. 188–91, 2015.

[212] M. H. Abraham, A. Ibrahim, and W. E. Acree Jr, "Partition of compounds from gas to water and from gas to physiological saline at 310 K: Linear free energy relationships," *Fluid Phase Equilibria*, vol. 251, no. 2, pp. 93–109, 2007.

[213] A. C. Groom, R. Morin, and L. E. Farhi, "Determination of dissolved N_2 in blood and investigation of N_2 washout from the body," *J Appl Physiol*, vol. 23, no. 5, pp. 706–712, 1967.

[214] C. M. Stock, J. Q. Schisler, and T. D. McSweeney, "The $PaCO_2$ Rate of Rise in Anesthetized Patients with Airway Obstruction," *J Clin Anesth*, vol. 1, no. 5, pp. 328–332, 1989.

[215] M. H. Al-Abrak, C. E. Briscoe, and J. P. Payne, "THE EFFECT OF HALOTHANE ANAESTHESIA ON THE UPTAKE OF OXYGEN AND ON THE RESPIRATORY PATTERN IN MAN," *Br J Anaesth*, vol. 47, no. 6, pp. 679–685, 1975.

[216] J. Frumin, R. M. Epstein, and G. Cohen, "Apneic Oxygenation in Man," *Anesthesiology*, vol. 20, no. 6, pp. 789–798, 1959.

[217] J. Ibanez and J. M. Raurich, "Normal Values of Functional Residual Capacity in the Sitting and Supine positions," *Intensive Care Med*, vol. 8, pp. 173–177, 1982.

[218] P. H. Quanjer, G. J. Tammeling, J. E. Cotes, O. F. Pedersen, R. Peslin, and J. C. Yernault, "Lung volumes and forced ventilatory flows. Report Working Party Standardization of Lung Function Tests, European Community for Steel and Coal. Official Statement of the European Respiratory Society," *Eur Respir J Suppl*, vol. 16, pp. 5–40, 1993.

[219] H. Rahn, "A CONCEPT OF MEAN ALVEOLAR AIR AND THE VENTILATION-BLOODFLOW RELATIONSHIPS DURING PULMONARY GAS EXCHANGE," *American Journal of Physiology-Legacy Content*, vol. 158, no. 1, pp. 21–30, 1949.

[220] J. B. West, *Pulmonary gas exchange. Vol. 1.* 1980.

[221] R Core Team, *R: A Language and Environment for Statistical Computing*. R Foundation for Statistical Computing, Vienna, Austria, 2016.

[222] B. Winter, *Linear models and linear mixed effects models in R with linguistic applications*. 2013.

[223] E. Forno, Y. Han, J. Mullen, and J. C. Celedón, "Overweight, obesity, and lung function in children and adults—a meta-analysis," *The Journal of Allergy and Clinical Immunology: In Practice*, vol. 6, no. 2, pp. 570–581, 2018.

[224] C. Brandenberger and C. Mühlfeld, "Mechanisms of lung aging," *Cell and tissue research*, vol. 367, no. 3, pp. 469–480, 2017.

[225] J. L. Wright and A. Churg, "Effect of long-term cigarette smoke exposure on pulmonary vascular structure and function in the guinea pig," *Experimental lung research*, vol. 17, no. 6, pp. 997–1009, 1991.

[226] R. T. Dhawan, D. Gopalan, L. Howard, A. Vicente, M. Park, K. Manalan, I. Wallner, P. Marsden, S. Dave, H. Branley, *et al.*, "Beyond the clot: perfusion imaging of the pulmonary vasculature after COVID-19," *The Lancet Respiratory Medicine*, vol. 9, no. 1, pp. 107–116, 2021.

[227] L. Chen, R. Tang, H. Chen, Y. Huang, S. Yi, Q. Bai, Y. Zhu, C. Hong, C. Liu, N. Zhang, *et al.*, "Pulmonary vasculature: a target for COVID-19," *American journal of respiratory and critical care medicine*, vol. 203, no. 2, pp. 260–261, 2021.

[228] S. Provencher, F. Potus, and S. Bonnet, "COVID-19 and the pulmonary vasculature," *Pulmonary Circulation*, vol. 10, no. 3, p. 2045894020933088, 2020.

[229] Z. Varga, A. J. Flammer, P. Steiger, M. Haberecker, R. Andermatt, A. S. Zinkernagel, M. R. Mehra, R. A. Schuepbach, F. Ruschitzka, and H. Moch, "Endothelial cell infection and endotheliitis in COVID-19," *The Lancet*, vol. 395, no. 10234, pp. 1417–1418, 2020.

[230] X. Han, Y. Fan, O. Alwalid, N. Li, X. Jia, M. Yuan, Y. Li, Y. Cao, J. Gu, H. Wu, *et al.*, "Six-month follow-up chest CT findings after severe COVID-19 pneumonia," *Radiology*, vol. 299, no. 1, pp. E177–E186, 2021.

[231] R. J. van Gassel, J. L. Bels, A. Raafs, B. C. van Bussel, M. C. van de Poll, S. O. Simons, L. W. van der Meer, H. A. Gietema, R. Posthuma, and S. van Santen, "High prevalence of pulmonary sequelae at 3 months after hospital discharge in mechanically ventilated survivors of COVID-19," *American journal of respiratory and critical care medicine*, vol. 203, no. 3, pp. 371–374, 2021.

[232] C. Baratto, S. Caravita, A. Faini, G. B. Perego, M. Senni, L. P. Badano, and G. Parati, "Impact of COVID-19 on exercise pathophysiology: a combined cardiopulmonary and echocardiographic exercise study," *Journal of Applied Physiology*, vol. 130, no. 5, pp. 1470–1478, 2021.

[233] P. J. Hantzidiamantis and E. Amaro, "Physiology, Alveolar to Arterial Oxygen Gradient (Aa Gradient)," *Treasure Island (FL): StatPearls*, 2019.

[234] R. D. Pollock, C. J. Jolley, N. Abid, J. H. Couper, L. Estrada-Petrocelli, P. D. Hodkinson, S. Leonhardt, S. Magor-Elliott, T. Menden, G. Rafferty, G. Richmond, P. A. Robbins, G. A. D. Ritchie, M. J. Segal, A. T. Stevenson, H. D. Tank, and T. G. Smith, "Pulmonary effects of sustained periods of high-G acceleration relevant to suborbital spaceflight," *Aerospace medicine and human performance*, vol. 92, no. 8, pp. 633–641, 2021.

[235] I. Frerichs, T. Dudykevych, J. Hinz, M. Bodenstein, G. Hahn, and G. Hellige, "Gravity effects on regional lung ventilation determined by functional EIT during parabolic flights," *J Appl Physiol*, vol. 91, no. 1, pp. 39–50, 2001. PMID: 11408411.

[236] D. H. Glaister, *The effect of positive acceleration on the inequality of ventilation and perfusion in the lung*, p. 11. London: Flying Personnel Research Committee, 1964.

[237] D. H. Glaister, "Regional ventilation and perfusion in the lung during positive acceleration measured with Xe-133," *J Physiol*, vol. 177, pp. 73–74, 1965.

[238] D. H. Glaister, *The Effects of Gravity and Acceleration on the Lung.* Slough, England: Technivision Services, 1970.

[239] C. C. Dobler, "Overdiagnosis of pulmonary embolism: definition, causes and implications," *Breathe*, vol. 15, no. 1, pp. 46–53, 2019.

[240] J. E. Orr, A. Malhotra, and S. A. Sands, "Pathogenesis of central and complex sleep apnoea," *Respirology*, vol. 22, no. 1, pp. 43–52, 2017.

[241] M. E. F. Pedersen, M. Fatemian, and P. A. Robbins, "Identification of fast and slow ventilatory responses to carbon dioxide under hypoxic and hyperoxic conditions in humans," *J Physiol*, vol. 521, no. 1, pp. 273–287, 1999.

[242] L. Guglani, A. Kasi, M. Starks, K. E. Pedersen, J. G. Nielsen, and D. J. Weiner, "Difference between SF_6 and N_2 Multiple Breath Washout kinetics is due to N2 back diffusion and error in N_2 offset," *J Appl Physiol*, 2018.

[243] G. Laszlo, "Respiratory measurements of cardiac output: from elegant idea to useful test," *J Appl Physiol*, vol. 96, no. 2, pp. 428–437, 2004. PMID: 14715674.